Crystallographic analysis of twin variant selection and twin-twin junctions in commercially pure titanium

Shun Xu

UNIVERSITÉ DE LORRAINE

DISSERTATION

Presented at
Université de Lorraine

Shun Xu

To obtain the doctor's degree of
University of Lorraine

SPECIAL FIELD: Engineering Sciences
OPTION: Materials Science

Crystallographic analysis of twin variant selection and twin-twin junctions in commercially pure titanium

---

Defended on 28th August, 2017 in front of the jury:

Salima Bouvier	Professor	Université de Technologie de Compiègne, France	Rapporteur
Véronique Doquet	DR -CNRS	Ecole Polytechnique, France	Rapporteur
Irene J. Beyerlein	Professor	University of California, USA	Examinateur
Jian Wang	Professor	University of Nebraska-Lincoln, USA	Examinateur
Laszlo S. Toth	Professor	Université de Lorraine, France	Examinateur
Christophe Schuman	Doctor HDR	Université de Lorraine, France	Directeur
Jean-Sébastien Lecomte	Doctor HDR	Université de Lorraine, France	Directeur

Laboratoire d'Étude des Microstructures et de Mécanique des Matériaux, LEM3
Île du Saulcy, 57045 Metz Cedex 01, France

Contents

Abstract

Titanium and its alloys have been extensively investigated due to their wide application in chemical industry, medical implants and aerospace industries. As a significant role in plastic deformation, twinning has been widely studied in hexagonal metals. The local stress state may be modified by twinning, which influences sequential plastic deformation modes such as slips, twinning and secondary twinning. Thus, there is also an urgent demand for understanding the mechanism associated with the twinning-induced deformation, which is useful for the development of predictive capabilities that can describe twinning and twinning-induced sequential events, and their correlations with microstructures.

In this work, crystallographic analysis of twin variant selection and twin-twin junctions is applied in commercially pure titanium. A new sequential twinning mechanism that $\{10\bar{1}2\}$ twins are stimulated by the $\{11\bar{2}1\}$ twin-twin junctions (TTJs) is observed by quasi in-situ EBSD. Another sequential twinning mechanism that a $\{11\bar{2}2\}$ compression twin adjoins a $\{10\bar{1}2\}$ extension twin is found at high angle grain boundaries. Displacement gradient accommodation is used to determine the sequential twin variant while the classical Schmid factor (SF) is not sufficient. Besides, a detailed analysis of the detected 425 $\{10\bar{1}2\}$ double twins inside primary $\{11\bar{2}2\}$ twins reveals that the double twin variants that exhibit specific misorientation with respect to the parent grains are the most frequent. The prevalence of double twins is possible to justify with the prismatic-dislocation mediated nucleation mechanism. When complemented with an apparent SF analysis, the criterion can accurately predict the selection between two variants within the group of the popular double twins. When multiple twin variants are active in the same grain, twin-twin interactions may happen. $\{11\bar{2}2\}$ TTJs can be divided into three types according to the crystallography of $\{11\bar{2}2\}$ twins. A statistical analysis of $\{11\bar{2}2\}$ TTJs reveals that one type is the most popular while other types are rarely activated. The frequency of TTJs can be evaluated by using an apparent SF analysis. The interesting finding is that twin-twin boundaries (TTBs) form in one side of the incoming twin as a TTJ forms. Corresponding to the formation of TTBs based on the interactions of twinning dislocations, interface dislocations in the observed TTBs have lower line energy than those in the un-observed TTBs. Similar operation is applied to the analysis of $\{11\bar{2}1\}$ TTJs.

Keywords: Titanium; Twinning; Variant; Accommodation; Schmid Factor.

Résumé

Le titane et ses alliages sont très largement étudiés en raison de leur grande utilisation dans l'industrie chimique, les implants médicaux et les industries aérospatiales. Vu le rôle important dans la déformation plastique, le maclage a été largement étudié dans les métaux hexagonaux L'état de contrainte locale peut être modifié par maclage, ce qui influence les modes séquentiels de déformation tels que le glissement, le maclage et le maclage secondaire Ainsi, il existe une demande urgente pour comprendre le mécanisme associé à la déformation induite par maclage, utile pour le développement de modèles prédictifs qui peuvent décrire les événements ultérieurs induits par maclage, ainsi que leurs corrélations avec les microstructures.

Dans ce travail, l'analyse cristallographique de la sélection de variantes de macles et des jonctions macle-macle (TTJ= twin-twin junction) est appliquée sur du titane commercialement pur. Un nouveau mécanisme de maclage séquentiel, où les macles $\{10\bar{1}2\}$ sont stimulées par des jonctions macle $\{11\bar{2}1\}$-macle, est observée par EBSD quasi in situ. Un autre mécanisme de maclage séquentiel a été trouvé lorsque le maclage de compression $\{11\bar{2}2\}$ contient une macle d'extension $\{10\bar{1}2\}$ près des joints de grain à forte désorientation. L'accommodation est utilisée pour déterminer le variant de macle séquentiel lorsque le facteur de Schmid classique (SF) n'est pas suffisant. En outre, une analyse détaillée des 425 macles secondaires $\{10\bar{1}2\}$ détectées dans les macles $\{11\bar{2}2\}$ primaires révèle que les deux variants de macles qui présentent une désorientation spécifique par rapport aux grains parents sont les plus fréquentes. Il est possible de justifier la prévalence des macles secondaires avec un mécanisme de nucléation aidée par les dislocations prismatiques. Lorsqu'il est complété par une analyse SF généralisée, le critère peut prédire avec précision la sélection entre deux variants dans le groupe des macles secondaires les plus fréquentes. Lorsque plusieurs variants de macles sont actifs dans le même grain, des interactions macle-macle peuvent se produire. Les jonctions macle $\{11\bar{2}2\}$-macle peuvent être divisés en trois types selon la cristallographie des macles $\{11\bar{2}2\}$. Une analyse statistique de ces interfaces révèle qu'un seul type est le plus fréquent tandis que les autres types sont rarement activés. La fréquence des TTJ peut être évaluée en utilisant une analyse SF généralisée. Il en ressort que les interfaces macle-macle (TTB= twin-twin boundary) ne se forment que d'un côté de la macle. Concernant la formation de TTBs basée sur les interactions des dislocations de macle, les dislocations d'interface dans les TTBs observées ont une énergie de ligne inférieure à celles des TTB non observées. Une opération similaire est appliquée à l'analyse de $\{11\bar{2}1\}$ TTJs.

Mots-clés: Titane; maclage; variante; Accommodation; Facteur de Schmid.

List of Abbreviations

$Angle_{GDT}$	Misorientation angle between the grain and double twin
$Axis_{GDT}$	Misorientation axis between the grain and double twin
B <***a***>	{0002}<11$\bar{2}$0> basal slip
BP / PB	Basal-Prismatic / Prismatic-Basal interface
BS	Bright side
C_i^I	{11$\bar{2}$2}<11$\bar{2}\bar{3}$> compression twinning
C_i^{II}	{11$\bar{2}$4} compression twinning
C_i^{III}	{10$\bar{1}$1} compression twinning
CRSS	Critical resolved shear stress
CTB	Coherent twin boundary
DS	Dark side
EBSD	Electron Backscattered Diffraction
E_{tw}	Displacement gradient tensor in the twinning reference frame
g	The metric tensor in direct space
g^*	The metric tensor in reciprocal space
GB	Grain boundary
HCP	Hexagonal Close-Packed
M_{43}	Transformation matrix from Millar lattice frame to Millar-Bravais frame
M_{3o}	Transformation matrix from crystal orthonormal coordinate to Millar lattice frame
M_o	Transformation matrix from crystal orthonormal coordinate to Millar-Bravais frame
M_{ct}	Transformation matrix from crystal orthonormal frame to twinning reference frame
Msy	Symmetric matrices in crystal orthonormal coordinate for HCP
ND	Normal direction of rolled sheets
P <***a***>	{10$\bar{1}$0}<1$\bar{2}$10> prismatic slip
Py_1<***a***>	{10$\bar{1}$1}<1$\bar{2}$10> pyramidal slip
Py_1<***c***+***a***>	{10$\bar{1}$1}<11$\bar{2}\bar{3}$> pyramidal slip
Py_2<***c***+***a***>	{11$\bar{2}$2}<11$\bar{2}\bar{3}$> pyramidal slip
PTW	Primary twin boundary

R	Transformation matrix from sample frame to crystal orthonormal frame
R_{tw}	The matrix for rotation of 180° around the twin plane normal
R_{gt}	Transformation matrix between the crystal orthonormal frames in a grain and a twin inside the grain
RD	Rolling direction
SD	Shear direction
SEI	Secondary electron imaging
SEM	Scanning electron microscope
SF	Schmid factor
STB	Secondary twin boundary
T_i^I	$\{10\bar{1}2\}\langle\bar{1}011\rangle$ extension twinning
T_i^{II}	$\{11\bar{2}1\}$ extension twinning
TB	Twin boundary
TD	Transverse direction
TTBs	Twin-twin boundaries
TTB_A	Twin-twin boundaries in the acute region
TTB_O	Twin-twin boundaries in the obtuse region
TTJ	Twin-twin junction
TPN	Twin plane normal

List of Figures

List of Tables

Acknowledgements

This work is completed at LEM3 (Laboratoire d'Étude des Microstructures et de Mécanique des Matériaux), Université de Lorraine. I would like to sincerely thank this laboratory for offering me opportunity to use the advanced equipment and giving me their kind help. I also gratefully acknowledge the Ministry of National Éducation, Higher Éducation and Research of France for providing the Doctoral Contract.

I would like to thank my supervisor Dr. Christophe Schuman, who gave me much help in my research. In order to communicate with the technician in French, he took me to do compression and tension tests. We also have discussed so much about my experiments. Many ideas and methods were suggested in my work. I am deeply indebted to my co-supervisor Dr. Jean-Sébastien Lecomte for his concern and friendly help. He has a good understanding of the equipment and taught me a lot about how to use them during my PhD research. I am also grateful to Dr. Yudong Zhang for fruitful discussions about crystal calculation. Her optimistic attitude, critical thinking and rigorous working style encourage me a lot. I also would like to thank some collaborators. Prof. Laszlo Toth in our lab was so patient to discuss with me and helped me a lot in simulation by applying VPSC. Prof. Matthew Barnett in Deakin University in Australia enlightened me to use dislocation dissociation mechanism in my research. Prof. Jian Wang in University of Nebraska-Lincoln in USA guided me to understand dislocation reactions and invited me to USA to work with him for half year. I will benefit from their broad perspective and fruitful knowledge in my research for the whole life.

I greatly thank Mr. Patrick Moll for helping me to do compression tests and Mr. Laurent Peltier for carrying out heat treatment. I also would like to express my thanks to Mr. Jérôme Slowensky, Ms. Auriane Mandrelli, Ms. Jacqueline Decker, Ms. Nathalie Kasprzak, Ms. Anne-martine Blum and Ms. Arlette Jacquierre at LEM3, France for their technical and administrative help and support to my Ph. D. work.

I am also grateful to all the staffs and students in LEM3 and University of Nebraska-Lincoln in USA, and my friends who shared their experiences with me and offered help to my study, especially to Dr. Haile YAN, Dr. Xiaorui Liu, Dr. Cai Chen, Dr. Yajun Zhao, Dr. Jiangkun Fan, Dr. Jing Wen, Dr. Liang Cheng, Mr. Jie Yang, Mr. Naifu Zou, Dr. Chunyang Zhang, Ms. Chunqing Lin, Ms. Dan Zhao, Mr. Yuqi Zhang, Ms. Li Zuo, Mr. Ke Hua, Ms. Xiaomeng Liu, Ms. Meishuai Liu. Special thanks are shown to Dr. Cai Chen for his help in my daily life and Dr. Yajun Zhao for his help in ex-situ compression, and my young friend Ms. Pengru Zhao for endless help in my daily life. Dr. Qing Su, Mr. Mingyu Gong, Mr. Chao Gu,

Ms. Xinyan Xie and Ms. Lin Chen, Mr. Junfei Tong, Ms. Zhe Zhang, Mr. Pengfei Dong in University of Nebraska-Lincoln are greatly thanked for their help during my stay in USA.

Finally, I would give my hearted thanks to my parents Dagen Xu and Shuangjie Li and my sister Li Xu for their patience, encouragement and support.

General introduction

Titanium (Ti) and its alloys attract wide application in aerospace, chemical industry and medical implants due to their excellent physical and mechanical properties, such as high specific strength, excellent corrosion resistance and good biocompatibility [1]. However, the complexity of extraction process, the difficulty of melting and the problems in fabrication and machining result in high expense for application of these metals. In order to reduce the cost of titanium components, several methods have been introduced such as castings, isothermal forging and powder metallurgy [2-4]. Conventional machining methods are still widely used for the production of titanium parts. Machining operations, such as turning, milling, drilling, reaming, tapping, sawing, and grinding, are employed in producing aerospace components [5]. Turning and drilling are the major machining operations to produce gas turbine engines [6]. For reducing the cost, an important issue is to improve the machinability of titanium and its alloys, which arouses extensive researches on the deformability of these metals in recent decades. In consideration of the characteristics of the metal and its alloys, desirable production rates and high quality of products can be achieved with conventional machining [7]. Especially for α-Ti, it can plastically deform by slips and twinning as hexagonal close packed structure (HCP). Since there are a limited number of independent slip systems in HCP metals, twinning is a major deformation mode that can accommodate strains along the *c*-axis of the crystal. For the purpose of clarifying the deformation mechanism of HCP metals such α-Ti, magnesium, zirconium and zinc, a large number of researchers dedicate to the exploration of the role of twinning in the deformation by applying scanning electron microscopy (SEM) [8-13], transmission electron microscopy (TEM) [14-16], and theory and modelling [17-25]. A tremendous amount of experimental work has been carried out for α-Ti and other hexagonal metals to understand mechanisms and mechanics of slips and twins in the context of temperatures and strain rates [11, 26], cyclic loading [27-29], strain path changes [30], textures [31, 32], twinning modes [33], grain size effects [34, 35], and sample size effects [36, 37].

Twinning plays a significant role in the deformation of pure titanium. Crystal plasticity models at meso- and macro- scales are developed in recent years to deal with twinning in hexagonal metals, especially in magnesium and its alloys. During cyclic loading or strain-path changes, a twin interacts with another twin, resulting in the formation of twin-twin junctions that influence sequential plastic deformation modes, slips, twinning, secondary twinning, and de-twinning. Thus, there is also an urgent demand for the development of predictive capabilities that can describe twinning and twinning-induced sequential events, and their

correlations with microstructures, temperatures, and loading conditions. These predictive models will enable engineers to optimize mechanical forming processes of hexagonal metals for specific applications.

Based on such a background, this work is mainly focused on deformation twinning in commercially pure titanium subjected to uniaxial compression along the normal direction of a rolled sheet. By using crystallographic analysis, the current work aims to conduct a statistical analysis of the sequential twinning stimulated by other twins in commercially pure titanium. In addition, the variant selection for double twinning will be investigated as well as the crystallographic feature of twin-twin junctions. The preference of various types of twin-twin junctions and the formation mechanism based on dislocation reactions will be discussed. Unless particularly mentioned, crystallographic calculation have been applied throughout the thesis based on the computer codes self-developed in MATLAB. The main contents of this work can be summarized as below:

In Chapter 1, slip and twinning modes will be introduced. Then, a literature review of the studies on twinning in HCP crystal structure materials will be summarized to present the main results that have been declared, which includes twin nucleation and growth, variables on twinning, interfaces associated with twins and the criterions that are used for the prediction of twinning variants.

In Chapter 2, the calculation methods used in the thesis will be introduced such as transformation of displacement gradient tensor of a twin, trace analysis and texture reorientation associated with the twin variant selection.

In Chapter 3, sequential primary twinning stimulated by other primary twins in rolled pure titanium. The geometrical relation between the twins and the sequential twins is examined in this work and the selection criterion will be established for the sequential twins. In this chapter, two physical conditions of sequential primary twins will be discussed, i.e., $\{10\bar{1}2\}$ twins stimulated by $\{11\bar{2}1\}$ twin-twin junctions and accommodative $\{10\bar{1}2\}$ twins stimulated by $\{11\bar{2}2\}$ twins at high angle grain boundaries. Classical Schmid factor (SF) criterion fails to explain the activation of these anomalous $\{10\bar{1}2\}$ twinning. To understand the mechanism, displacement gradient tensor based local accommodation will be proposed for the selection of these $\{10\bar{1}2\}$ twins.

In Chapter 4, dislocation mediated variant selection for double twinning in compression of pure titanium. There are 36 possibilities that $\{10\bar{1}2\}$ double twinning occurs inside $\{11\bar{2}2\}$ primary twins, which can be classified into three groups according to the misorientation

between the double twins and the corresponding parent grains. In this Chapter, a specific group of $\{10\bar{1}2\}$ double twins are found to dominate the proportion of all the detected double twins. Dislocation mediated nucleation is proposed for the occurrence of double twinning, which can successfully select the popular group of double twins. In combination of an apparent SF analysis, a specific twinning variant within two possibilities can be predicted in agreement with the experimental result. The orientation of the parent grains is closely related to the activation of one double twin variant or both double twin variants in the popular group.

In Chapter 5, the crystallographic characters of twin-twin interactions in commercially pure titanium will be introduced such as $\{11\bar{2}2\}$ twin-twin junctions and $\{11\bar{2}1\}$ twin-twin junctions. Based on crystallography, six twin variants can produce three types of twin-twin junction. Beside, a twin-twin junction can form two twin-twin boundaries. Mainly, there are two interesting points about the twin-twin junctions, i.e., only one type of twin-twin junctions is the most popular in the detected twins and the formation of only one twin-twin boundary is facilitated. The former point will be addressed by using an apparent SF analysis and the latter one will be discussed with the help of dislocation reaction.

.

Chapter 1 Literature review

Contents

1.1 Deformation modes

1.1.1 Slip

In hexagonal structure materials, basal <***a***> slip $\{0002\}\langle 11\bar{2}0\rangle$, prismatic <***a***> slip $\{10\bar{1}0\}\langle 1\bar{2}10\rangle$, pyramidal <***c***+***a***> slip $\{10\bar{1}1\}\langle 11\bar{2}\bar{3}\rangle$, pyramidal <***a***> slip $\{10\bar{1}1\}\langle 1\bar{2}10\rangle$ and pyramidal <***c***+***a***> slip $\{11\bar{2}2\}\langle 11\bar{2}\bar{3}\rangle$ are the most commonly observed slip modes. They are depicted in Fig. 1. 1. Diverse slip systems in HCP metals with various *c/a* ratios exhibit different activities, which results in the formation of specific texture in wrought materials. The texture with basal poles tilted from the normal direction (ND) to the transverse direction (TD) for titanium and zirconium results from the dominating $\{10\bar{1}0\}\langle 1\bar{2}10\rangle$ prismatic and $\{0002\}\langle 1\bar{2}10\rangle$ basal slip, while in cadmium and zinc the component with basal poles tilted from the ND towards the rolling direction (RD) is attributed to $\{11\bar{2}2\}\langle 11\bar{2}\bar{3}\rangle$ pyramidal and $\{0002\}\langle 1\bar{2}10\rangle$ basal slip. In magnesium, $\{0002\}\langle 1\bar{2}10\rangle$ basal slip assists the formation of the basal texture (*c*-axis parallel to the ND), where the *c/a* ratio is close to 1.633 [38-40]. Slip systems and corresponding shear strain are listed in Table 1. 1. By four-point bending of

commercial purity titanium, prismatic <***a***> slip is the most frequently observed mode while basal and pyramidal slips are rarely detected [41]. Prismatic <***a***> slip is more active during tension along the RD [42].

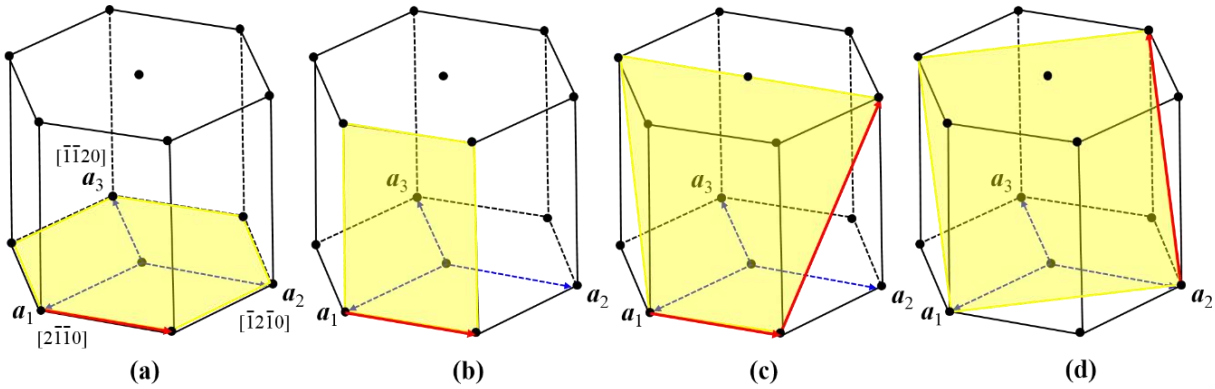

Fig. 1. 1 Main slip systems in α-titanium: (a) Basal {0001} <***a***> slip, (b) Prismatic {10$\bar{1}$0} <***a***> slip, (c) Pyramidal {10$\bar{1}$1} <***a***> and <***c***+***a***> slip, (d) Pyramidal {11$\bar{2}$2} <***c***+***a***> slip.

Table 1. 1 Main slip systems and corresponding strain in α-titanium.

Slip plane	Slip Direction	Number	Abbreviation
{0002}	<11$\bar{2}$0>	3	B <***a***>
{10$\bar{1}$0}	<1$\bar{2}$10>	3	P <***a***>
{10$\bar{1}$1}	<1$\bar{2}$10>	6	Py_1<***a***>
{10$\bar{1}$1}	<11$\bar{2}\bar{3}$>	12	Py_1<***c***+***a***>
{11$\bar{2}$2}	<11$\bar{2}\bar{3}$>	6	Py_2<***c***+***a***>

1.1.2 Twinning

The limited number of independent slip systems in HCP metals requires the participation of twinning in deformation. As a result of twinning, the crystal is reoriented around an axis with respect to the parent grain and may facilitate the activation of slip and/or twinning systems in the new crystal that are unfavorable in the initial orientation. Twinning shear happens along the twinning direction and twinning are characterized by twinning elements as shown in Fig. 1. 2 [43]. In the classical theory of deformation twinning, the original (parent) lattice is reoriented by atom displacements which are equivalent to a simple shear of the lattice points or of some integral fraction of these points. Since a parent crystal and its twin remain in contact at the interface plane during the formation of the twin, the relation between the structures must be such that this plane is invariant in any deformation carrying one lattice into the other [43].

The invariant plane of this shear is called $\mathbf{K_1}$ plane and the shear direction $\boldsymbol{\eta_1}$. $\mathbf{K_2}$ represents the second undistorted but rotated plane. Shear plane **P** contains $\boldsymbol{\eta_1}$ and the normal of $\mathbf{K_1}$. The intersection plane between **P** and $\mathbf{K_2}$ is the conjugate shear direction $\boldsymbol{\eta_2}$. Twins are usually classified into three types: type I ($\mathbf{K_1}$ and $\boldsymbol{\eta_2}$ represent a rational plane and a rational direction of the parent lattice, respectively), type II ($\mathbf{K_2}$ and $\boldsymbol{\eta_1}$ are rational) and compound twins ($\mathbf{K_1}$, $\mathbf{K_2}$, $\boldsymbol{\eta_1}$ and $\boldsymbol{\eta_2}$ are all rational). The orientation of the new twin lattice relative to the original lattice can be achieved by a reflection in $\mathbf{K_1}$ for a type I twin and by a rotation of 180° about $\boldsymbol{\eta_1}$ for a type II twin. Both operations are applicable to a compound twin. The important feature of twinning as a mode of deformation is the shape change resulting from the simple shear, so that a twin might be regarded as any reoriented region produced by a simple shear of the parent lattice.

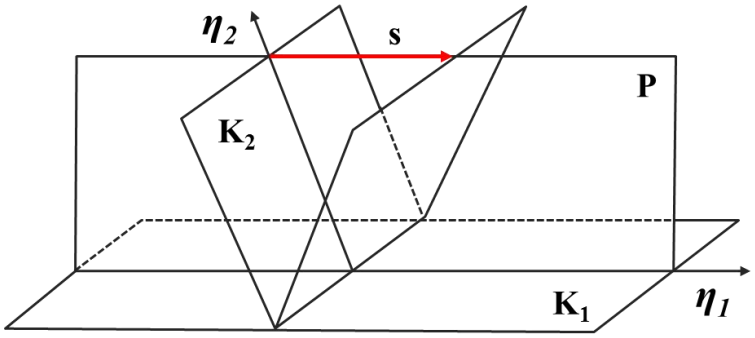

Fig. 1. 2 The four twinning elements [43].

Table 1. 2 Main twinning systems and corresponding parameters in α-Ti.

Type	$\mathbf{K_1}$	$\boldsymbol{\eta_1}$	$\mathbf{K_2}$	$\boldsymbol{\eta_2}$	Shear strain	Misorientation axis	Misorientation angle	Notation (i=1…6)
Compression twinning	$\{11\bar{2}2\}$	$<11\bar{2}\bar{3}>$	$\{\bar{1}\bar{1}24\}$	$<\bar{2}\bar{2}43>$	0.22	$<\bar{1}100>$	~64°	C_i^I
	$\{11\bar{2}4\}$	$<\bar{2}\bar{2}43>$	$\{\bar{1}\bar{1}22\}$	$<\bar{1}\bar{1}2\bar{3}>$	0.22	$<\bar{1}100>$	~77°	C_i^{II}
	$\{10\bar{1}1\}$	$<10\bar{1}\bar{2}>$	$\{\bar{1}013\}$	$<\bar{3}03\bar{2}>$	0.09	$<\bar{1}2\bar{1}0>$	~57°	C_i^{III}
Extension twinning	$\{10\bar{1}2\}$	$<\bar{1}011>$	$\{\bar{1}012\}$	$<10\bar{1}1>$	0.18	$<\bar{1}2\bar{1}0>$	~85°	T_i^I
	$\{11\bar{2}1\}$	$<\bar{1}\bar{1}26>$	$\{0001\}$	$<11\bar{2}0>$	0.63	$<\bar{1}100>$	~35°	T_i^{II}

Twinning systems and corresponding parameters are listed in Table 1. 2. The notation of the twinning systems are used in the following chapters. As listed in Fig. 1. 3, the relation between the twinning shear and *c/a* ratio is plotted [44]. Twinning direction $\boldsymbol{\eta_1}$ is dependent on

the *c/a* ratio. The shear direction of $(10\bar{1}2)$ twin is along $[10\bar{1}\bar{1}]$ and thus is a compression twin for cadmium and zinc with *c/a* $>\sqrt{3}$ while it is along $[\bar{1}011]$ and thus it is an extension twin for all the other metals with *c/a* $<\sqrt{3}$. It can also be seen that there are several available twinning systems for titanium such as $\{10\bar{1}2\}$, $\{11\bar{2}2\}$, $\{11\bar{2}4\}$ and $\{10\bar{1}1\}$ twinning. $\{11\bar{2}1\}$ twins were observed in our experiments especially in the samples with large grain size.

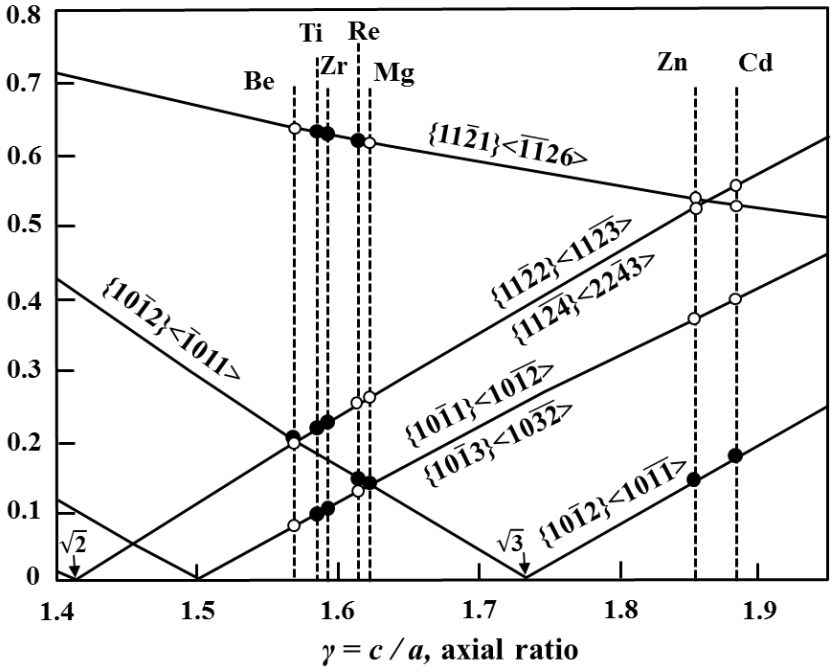

Fig. 1. 3 Variation of twinning shear with the axial ratio for the seven hexagonal metals. A filled symbol indicates that the twin mode is an active mode [44].

In magnesium, $\{10\bar{1}2\}<\bar{1}011>$ extension twinning is extensively reported and the high popularity is attributed to its quite low CRSS [29]. Due to the strong texture of wrought magnesium and the polar nature of deformation twinning [45], $\{10\bar{1}2\}<\bar{1}011>$ extension twinning is easily activated under compression perpendicular to the *c*-axis of the crystal and under tension parallel to the *c*-axis [46]. De-twinning happens when reversal loading is applied under low stress [47]. During cyclic loading, the fraction of the residual twins, i.e. the twins that fail to de-twin completely, gradually increases with increasing cycles [29]. At room temperature, $\{10\bar{1}2\}<\bar{1}011>$ extension twinning and $\{11\bar{2}2\}<11\bar{2}\bar{3}>$ compression twinning are most commonly observed in pure titanium [10, 48, 49]. Other twinning modes, $\{11\bar{2}1\}<\bar{1}\bar{1}26>$ extension twinning [50-52], $\{11\bar{2}4\}<22\bar{4}\bar{3}>$ compression twinning which are conjugate to $\{11\bar{2}2\}$ twinning [43, 53, 54], and $\{10\bar{1}1\}<10\bar{1}\bar{2}>$ compression twining [22, 55], can occur depending on temperature and loading conditions. Extension twinning relates to the aspect of

introducing a positive strain along the *c*-axis of the parent grain and compression refers to a negative component along the *c*-axis. Twinning planes are depicted in Fig. 1. 4.

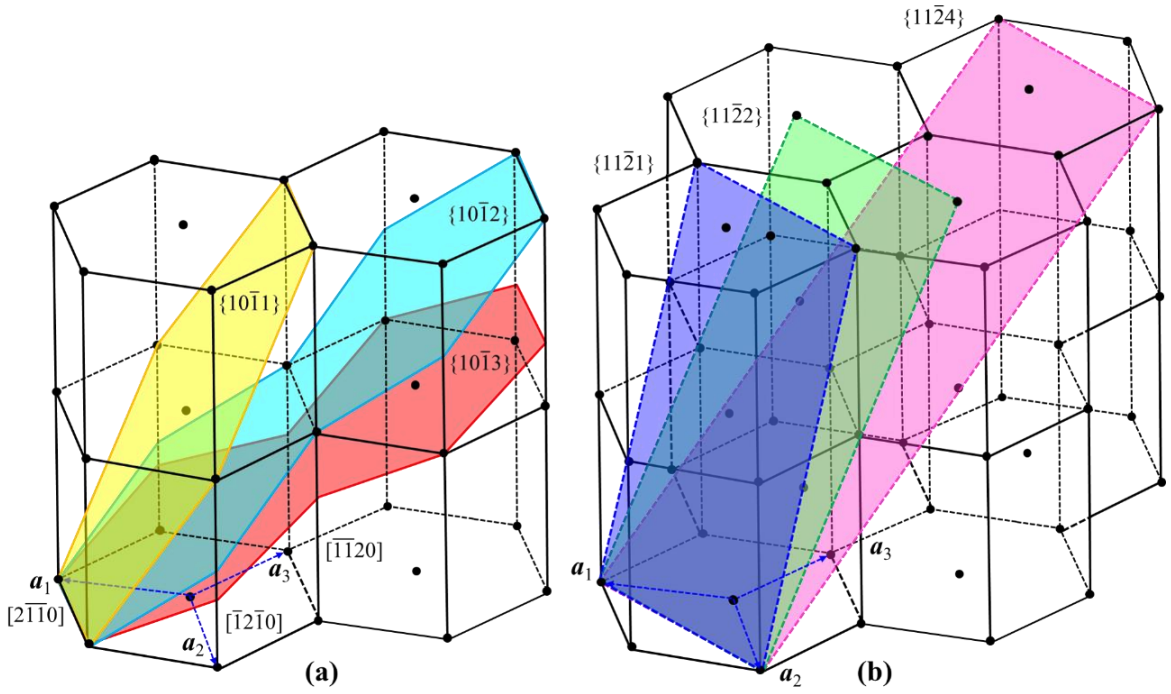

Fig. 1. 4 Main twinning systems in α-titanium: (a) {10$\bar{1}$1} twinning plane in yellow, {10$\bar{1}$2} twinning plane in light blue and {10$\bar{1}$3} twinning plane in red (b) {11$\bar{2}$1} twinning plane in blue, {11$\bar{2}$2} twinning plane in green and {11$\bar{2}$4} twinning plane in pink.

1.2 Multi-scale studies on deformation twins

Twins play a significant role in the deformation of HCP metals. It has been reported that strain hardening in the stress-strain curves during plastic deformation of polycrystalline pure titanium at various strain rates and temperature can be divided into three stages, i.e. stage I characterized by a decreasing slope of the stress-strain curve, stage II with an increasing slope and stage III exhibiting a decreasing slope [56]. Experiments were performed in order to understand the meaning and the deformation mechanism in each stage. Gray [57] suggested that deformation twinning plays a significant role in the strain hardening response because they attribute the higher hardening rates in the high-purity titanium with large grain size to deformation twins which acts as barriers to slip via a Hall-Petch type hardening mechanism. The appearance of stage II with an increasing strain hardening rate is related to the dynamic strain aging effects and caused by the interaction between moving dislocations and mobile point defects, such as vacancies and solute atoms. However, Doner and Conrad [58] have previously shown that the temperature and strain rate range that dynamic strain aging occurred

in titanium does not correspond to the temperature used in [56], which requires further research on the exploration of the deformation mechanism corresponding to stage II. Salem et al. [49, 59] conducted various deformation modes of high purity polycrystalline α-titanium and constructed the relation between the three stages of strain hardening curves (Fig. 1.5) and the microstructural evolution, indicating that the occurrence of deformation twinning results in a sudden increase of strain hardening rate (stage II) and the following decrease of the rate is attributed to the saturation of twinning. This mechanism was incorporated into constitutive laws and implemented to Taylor-type crystal-plasticity modelling, which was used to accurately capture three stages of stress-strain hardening curve [60].

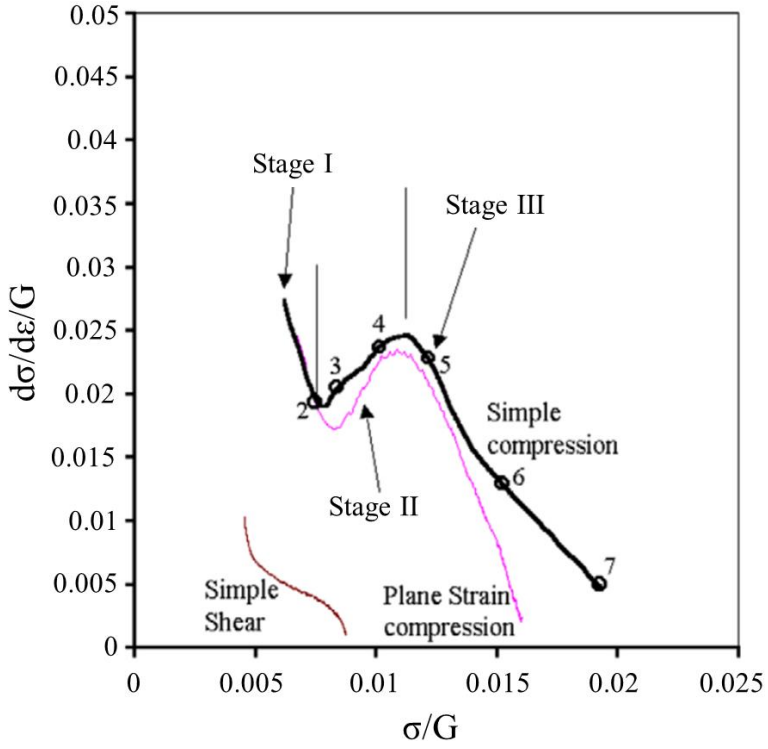

Fig. 1.5 Normalized strain hardening responses of α-titanium in simple compression, plane-strain compression, and simple shear [49].

In response to the stress-strain curve, deformation twinning causes hardening through reducing the effective slip length and softening through reorientation of the twinned crystal [61]. Under tension along the RD of a rolled commercial pure titanium, Becker et al. [62] examined the work-hardening behavior and identified three different work-hardening stages depending on the work-hardening rate. Plastic deformation in the first stage is dominated primarily by prismatic and basal slip and additionally by pyramidal $<\boldsymbol{c}+\boldsymbol{a}>$ slip, whereas $\{11\bar{2}2\}$ compression twinning and $\{10\bar{1}2\}$ twinning are active in the second and third stages, respectively.

1.2.1 Twin nucleation and growth

Twin nucleation, propagation and thickening are involved in twinning process [21, 43, 63]. It is well-known that the glide of twinning dislocations on their twin planes attributed to the twinning mechanisms [64-67]. The concept of a twinning dislocation in HCP crystals was introduced by Thompson and Millard [68], and later by Kronberg [69], Westlake [70] and Serra et al. [71]. Pond and Hirth [72] characterized a disconnection by a dislocation **b** and a step of height **h**. The height of the step is dependent on the type of twinning dislocation and usually consists of several crystallographic planes [73]. Unlike slip, twinning shear happens only in one direction. Twin nucleation was suggested to most likely occur at grain boundaries [21] and strongly depends on the structure of grain boundaries and local stress state [17]. Beyerlein et al. [17] also gave a theoretical study of twin nucleation from grain boundaries in HCP metals, indicating the relation between the propensity for twin nucleation and grain boundary properties.

Mendelson [65, 74] reported the production of glissile twinning dislocations on their respective twin planes through the dissociation of <***a***>, <***c***+***a***> or <***c***> dislocations. By atomistic simulations using density function theory, Wang et al. [23, 24] investigated the atomic structures of the nucleus of a $(10\bar{1}2)[\bar{1}011]$ twin in Mg. The normal-twinning mechanism and a zonal-twinning mechanism were proposed. A stable twin nucleus of the former mechanism is created by simultaneous glide of multiple twinning dislocations while that of the latter mechanism is created by simultaneous glide of a zonal dislocation, which consists of partial dislocation and multiple twinning dislocations. The nucleus consists of one partial dislocation with a Burgers vector of -50/107 $[\bar{1}011]$ together with multiple twinning dislocations with a Burgers vector of 1/15 $[\bar{1}011]$. Eight twinning dislocations and one partial dislocation are involved for the minimum and stable nucleus, which corresponds to a thickness of 17 crystallographic planes. Compared with the normal-twinning mechanism, the zonal-twinning mechanism is energetically favorable due to a much lower elastic energy. A pure-shuffle mechanism was proposed for $(10\bar{1}2)[\bar{1}011]$ twinning in [25], which shows that the twin grows via the glide of twinning dislocations along the coherent twin boundaries (CTB). The pure-shuffle nucleation of twins at grain boundaries can be ascribed to a high-stress concentration and pre-existing grain boundary dislocations [30].

Serra et al. [71, 75-77] examined the topology and mobility of $\{10\bar{1}1\}$ and $\{10\bar{1}3\}$ twinning dislocations by applying atomic scale simulation. They proposed the occurrence of a 2-layer mixed twinning dislocation and a 4-layer edge twinning dislocation. In [22, 55], the

kinetics and energetics associated with the nucleation and propagation of $\{10\bar{1}1\}$ and $\{10\bar{1}3\}$ twinning dislocations were studied in Mg by atomistic simulations. The interaction of a mixed 60° basal dislocation with the twin boundary provides a 2-layer twinning dislocation nucleation by dislocation dissociation. Even though the 4-layer twinning dislocation has a lower shear and a smaller Burgers vector, the higher mobility of the 2-layer twinning dislocation of mixed character attributes to its favorability over a 4-layer twinning dislocation of edge character [22], which is also declared in [55, 71]. Experimental observation of the 4-layer twinning dislocation should result from the combination of two 2-layer mixed twinning dislocations with opposite-signed screw components.

1.2.2 Variables on deformation twinning

In recent decades, EBSD was extensively applied to fully understand the evolution of microstructure and texture during different deformation processes. Ex-situ and in-situ EBSD methods were utilized to track the evolution of local microstructure and orientation. The effect of temperatures and strain rates [11, 26], cyclic loading [27-29] and loading path [30], initial texture [31, 32], and size effect such as grain size [34, 35], and sample size [36, 37] were investigated on twinning in HCP metals such as α-titanium, magnesium, and zirconium.

1.2.2.1 Temperature and strain rate effect

The twinning stress was measured to slightly decrease with decreasing temperature for most HCP modes, except for $\{10\bar{1}1\}$ twinning [43]. Paton et al. [78] reported that $\{10\bar{1}1\}$ compressive twinning is possible at high temperature and its activity is difficult at temperatures below 300 ºC. The low frequency of $\{10\bar{1}1\}$ compression twinning and $\{11\bar{2}1\}$ extension twinning are attributed to a large shuffling parameter and high twinning shear strain, respectively [79]. Twinning is more prevalent at high strain rate and low temperature. Zeng et al. [80] investigated the deformation of pure titanium at temperatures ranging from 673 to 973 K. The result indicates that flow stress is sensitive to deformation strain rate and temperature. Stress softening occurs when temperature is higher and strain rate is lower while work hardening happens under lower temperature and higher strain rate. Glavicic et al. [81] established the deformation mechanisms of textured pure titanium subjected to rolling at various temperatures. The volume fraction of twinning decreased rapidly in the rolled samples as the deformation temperature is increased. At room temperature, twinning accommodated 40.5% of the total imposed strain while less than 5% of the imposed total strain is accommodated by twinning above 300°C, which implies that the strain accommodated by

crystallographic slip increases sharply with the increase of temperature. The deduced slip system activity and densities imply the transition in deformation behavior from the heavily-twinned to the untwinned mode with an increase in deformation temperature for commercially pure titanium.

Under quasi-static and dynamic loading conditions, Gurao et al. [82] studied the microstructure and texture evolution of commercially pure titanium with four different initial orientations subjected to compression at various strain rates. The results reveal that deformation at high strain rate is characterized by extensive twinning and additional texture component is produced. For the samples with different orientations, the differences in the strain hardening response are reduced at the high strain rate. Mechanical response of α-titanium at high strain rate is examined for the discovery of the deformation mechanisms that are reflected by the macroscopic behavior [83]. In comparison of quasi-static compression testing and dynamic compression testing and high rate, α-titanium exhibits substantial rate sensitivity of the flow stress and pronounced strain hardening. Greater strain-hardening is obtained at high strain rates than at low strain rates. Microstructure observation shows that both dislocations and twins occur and the density of twins increases with both strain and strain rate. Twin-dislocation interactions play an important role in strain hardening. The deformation of commercially pure titanium with different strain rates by using the split Hopkinson pressure bar was investigated in Ref [84], demonstrating that the quantities of the deformation twins at the high strain rates are more pronounced than those at the low to medium speed deformation. Besides, the content of $\{11\bar{2}2\}$ twin increases with the strain rate, while the quantity of $\{11\bar{2}1\}$ twins decreases slightly with the increasing strain rate. The semi-quantitative relationship between twin density and strain rates is derived and discussed, which indicates that twin density is nonlinearly proportional to the strain rate. Recently, Zhou et al. [85] concerned the interactions between $\{11\bar{2}1\}$ twins and other twin modes such as $\{10\bar{1}2\}$, $\{11\bar{2}2\}$ and $\{11\bar{2}4\}$ twins at high strain rate. $\{11\bar{2}1\}$ and $\{11\bar{2}4\}$ twins are activated under such a high strain rate condition. This finding is in agreement with the result reported in [54] that these four types of twins are generated under dynamic deformation condition (high strain rate) while only three of the four twin types except $\{11\bar{2}4\}$ are detected in the sample subjected to quasi-static compression (low strain rate).

1.2.2.2 Loading path effect

{11$\bar{2}$2} compression twins in α-titanium are frequently generated in rolled pure titanium under compression along the ND [86, 87], under rolling [88], under tension along the RD [89, 90], and under monotonic simple shear tests [91, 92]. Prismatic slip {10$\bar{1}$0}<1$\bar{2}$10> in α-titanium is the most easily activated slip family at room temperature while basal slip {0002}<1$\bar{2}$10> and pyramidal slip {10$\bar{1}$1}<1$\bar{2}$10> can also be active [41, 56, 83, 93-95]. In order to satisfy the Von Mises criterion [44], another independent deformation mode should be provided. It has been reported that pyramidal <***c***+***a***> slip such as {10$\bar{1}$1}<11$\bar{2}\bar{3}$> slip and {11$\bar{2}$2}<11$\bar{2}\bar{3}$> [78, 96, 97], and twinning [43, 78, 79, 89, 94] are potential deformation systems. In consideration of strong basal texture generally developed in commercially pure titanium sheets, the active twin mode may be different between tension and compression. Under uniaxial tension along the RD [89], Mullins et al. found {11$\bar{2}$2} twinning and {11$\bar{2}$4} twinning. They also detected {10$\bar{1}$2} twinning when uniaxial tension was applied along the TD. By interrupted tension along the RD of rolled pure titanium, Wang et al. [53] found that the incompatible strain induced by slip in neighboring grains can stimulate the formation of twins regardless of the SFs. Certain accommodative deformation (twinning and slip) in their immediate neighborhoods is preferred to accommodate the strain caused by the deformation twins. By compression of a wire-drawn commercial pure titanium, Stanford et al. [98] demonstrated that {10$\bar{1}$2} twinning is the most active mode also with the observation of {11$\bar{2}$2} twinning and {11$\bar{2}$1} twinning. Deng et al. [99] analysed the twinning behaviors in pure titanium, indicating that {10$\bar{1}$2} twinning is easier to be activated than {11$\bar{2}$2} twinning while {11$\bar{2}$1} twinning is the most difficult among these three twinning modes, which is also reported in Ref [100] in pure titanium subjected to a monotonic simple shear. The poor activity of {11$\bar{2}$1} twinning is declared by Wang et al. [52] under tension imposed by four-point bending. Mullins et al. [89] reported that twinning is active only at the latter stage of deformation under tension. Bozzolo et al. [88] observed {11$\bar{2}$2}<11$\bar{2}\bar{3}$> twinning and {10$\bar{1}$2}<$\bar{1}$011> twinning in commercial pure titanium subjected to cold rolling as well as the frequent generation of {10$\bar{1}$2}<$\bar{1}$011> double twinning inside primary {11$\bar{2}$2}<11$\bar{2}\bar{3}$> twins.

1.2.2.3 Initial texture effect

Gurao et al. [82] investigated the deformation behavior of commercially pure titanium with different orientations, revealing that the sample with basal orientations undergoes minimum twinning and exhibits least hardening. The activation of harder pyramidal slip system results in a higher yield strength. A Taylor-type rate sensitive crystal plasticity model was

employed to simulate the deformation behavior of titanium. The effect of initial orientation has been investigated mostly on two different orientations, namely the through-thickness orientation with strong basal texture and the in-plane orientation with prismatic texture [82, 101, 102]. Different mechanical responses are produced due to different initial textures. The basal orientation exhibits higher yield strength but lower strain hardening rate, while the prismatic orientation shows a lower yield strength and a higher strain hardening rate. Crystal plasticity models are able to predict different mechanical responses with respect to the initial orientations. The mechanical response of different initial orientations can be indirectly influenced by the value of stacking fault energy (SFE), which is different for different planes in HCP metals like titanium [103]. Battaini et al. [104] investigated the effect of initial orientations on the mechanical properties of commercially pure titanium under plane-strain compression. In their experiments, $\{11\bar{2}2\}$ twins and $\{10\bar{1}2\}$ twins accounted for the most frequency of all twins while no $\{10\bar{1}1\}$ twins were detected. Besides, the contribution of $\{11\bar{2}1\}$ twinning was very small. The effect of initial orientations on flow stress was also studied, showing that the samples with the majority of *c*-axes aligned near the compression direction have the highest flow stresses, while those with the majority of *c*-axes normal to the compression direction have the lowest flow stresses in the strain range tested, but a noticeably higher hardening rate. The samples with *c*-axis alignment intermediate to former two conditions also have intermediate flow stresses.

1.2.2.4 Size effect

Much attention has been paid to investigating the effect of grain size and sample size on deformation twinning in hexagonal metals such as magnesium and α-titanium. For polycrystalline materials, the strength (σ) is increased with decreasing the grain size (d). The relation is described by the Hall-Petch equation: $\sigma = \sigma_0 + kd^{-1/2}$ [105, 106], where σ is the flow strength, σ_0 and k are size-independent constants. The Hall-Petch slope (k) is much larger for deformation twinning-mediated plasticity than that for ordinary dislocation plasticity [98, 107, 108]. Grain size has been declared to affect the twinning and slip behaviors [11, 34, 43, 98, 109, 110] while twining is known to be more easily influenced by grain size than slip [108]. It is well recognized that large grains facilitate the activity of deformation twinning [110-112]. Stanford et al. [98] investigated the effect of grain size and temperature on the behavior of wire-drawn α-titanium during compression. Interestingly, the flow stress exhibits a negative Hall–Petch slope at strains of 0.3, which results from the prevalence of twinning during the

compressive deformation. The region in which a negative slope is obtained is the transitional region between slip-dominated and twin-dominated flow as shown in Fig. 1.6. EBSD characterization revealed that $\{10\bar{1}2\}$ is the most prolific twin type across all the deformation temperatures and grain sizes examined. Of the twinning modes observed, $\{11\bar{2}2\}$ twinning is the most sensitive to the grain size and deformation temperature. The transition from twinning to slip is readily discovered in Mg [109] and α-titanium [98]. By means of electron microscopy techniques, Sun et al. [113] investigated the deformation behavior of ultrafine-grained HCP titanium processed by dynamic plastic deformation, showing that the deformation twinning propensity in ultrafine-grained titanium decreases monotonously. The number of dislocations having the <***c***> component increases with decreasing grain size, which indicates the transition of the deformation mechanism from twinning to slip without the change of twinning mechanism in their examined grain size range. The studies on single crystals illustrated that the ordinary dislocation dominated deformation is strongly influenced by the sample dimension [114-116]. The critical resolved shear stress (CRSS) and activation of twinning in magnesium and titanium single crystals was observed to be dependent on the sample size.

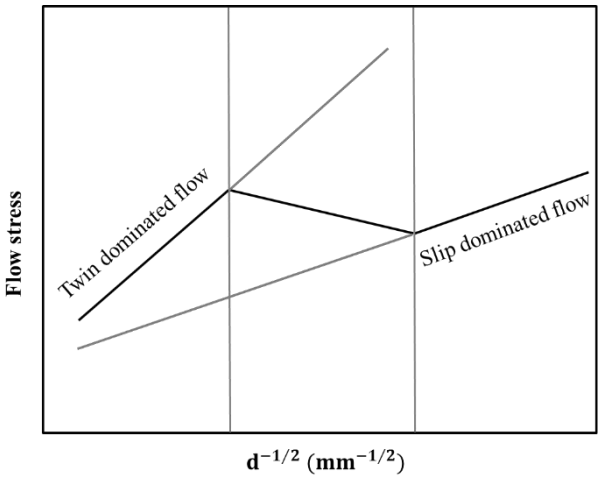

Fig. 1. 6 Schematic representation of the flow stress resulting from slip-dominated and twin-dominated flow. The transitional region between these two flow behaviors is also shown and indicates the region in which a negative Hall–Petch slope may be obtained [98].

1.2.3 Boundaries and interfaces associated with deformation twins

1.2.3.1 Twin interfaces

A $(10\bar{1}2)$ twin rotates the crystal around $[\bar{1}2\bar{1}0]$ axis by 86.3° for Mg, which results in 3.7° misalignment between the (0002) plane of the parent grain and the $(10\bar{1}0)$ plane of the twinned crystal as shown in Fig. 1.7 [117]. If a $(10\bar{1}2)$ twin rotates the crystal by θ = 90° with respect

to $[\bar{1}2\bar{1}0]$ axis, the (0002) basal plane of one crystal will become parallel to the $(10\bar{1}0)$ prismatic plane of the other, which is regarded as the basal-prismatic (BP or PB) interface [118].

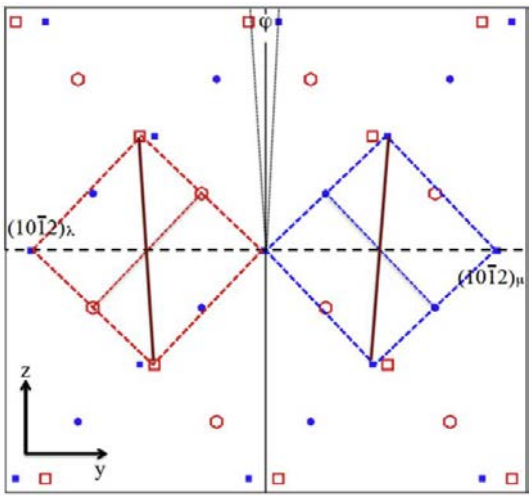

Fig. 1. 7 Coherent dichromatic complexes for a $(10\bar{1}2)$ twin. The $(1\bar{1}00)$ prism plane on the right and the equivalent $(\bar{1}100)$ on the left are shown as solid lines. Both transposed to the centre with rotation angle φ shown [117].

BP interface is widely characterized by TEM and high resolution TEM (HRTEM) in recent years [15, 36, 118-122]. A typical HRTEM pattern of $\{10\bar{1}2\}$ twin boundary in titanium is shown in Fig. 1.8a [122]. Twin boundaries consist of coherent twinning boundaries (CTB) and BP interfaces. The yellow solid lines correspond to the theoretical $\{10\bar{1}2\}$ planes and the red dash lines correspond to the BP interfaces. The migration of twin boundaries involves the glide of twin dislocations on the CTBs and the climb of interface dislocations on the PBs/BPs [15]. The accumulation of residual dislocations due to the migration of the BPs/PBs can hinder the motion of twin boundaries and can dissociate into basal dislocations or partial dislocations on the basal plane. As a result, the migration of the BP interface attributes to the observation of the abundant basal stacking faults in association with $\{10\bar{1}2\}$ twins. Wang et al. [118] demonstrated that the formation of BP is geometrically and energetically preferred in the serrated coherent twin boundaries, which migrates by glide and climb of twinning dislocations, combined with atomic shuffling. Particularly, the climb mechanism, combined with the density and the height of parallel basal-prismatic planes serrations in the serrated CTBs plays a significant role in controlling strain hardening related to twinning and de-twinning. Fig. 1.8b shows a HRTEM micrograph of a $\{\bar{1}\bar{1}22\}$ twin boundary in deformed Zirconium [123]. The observed facets highlighted in orange align the $\{1\bar{2}12\}$ pyramidal planes in the matrix with basal planes in the twin, and simultaneously basal planes in the matrix with $\{1\bar{2}12\}$ pyramidal planes in the twin. Twin boundary consists of coherent $\{11\bar{2}2\}$ twin boundaries and {0002}-

$\{1\bar{2}12\}$ interface. Fig. 1.8c shows a HRTEM micrograph of a $\{11\bar{2}1\}$ twin in deformed Zirconium [123]. It reveals that twin boundary consists of coherent $\{11\bar{2}1\}$ twin boundaries and $\{11\bar{2}2\}$-$\{1\bar{2}10\}$ interface.

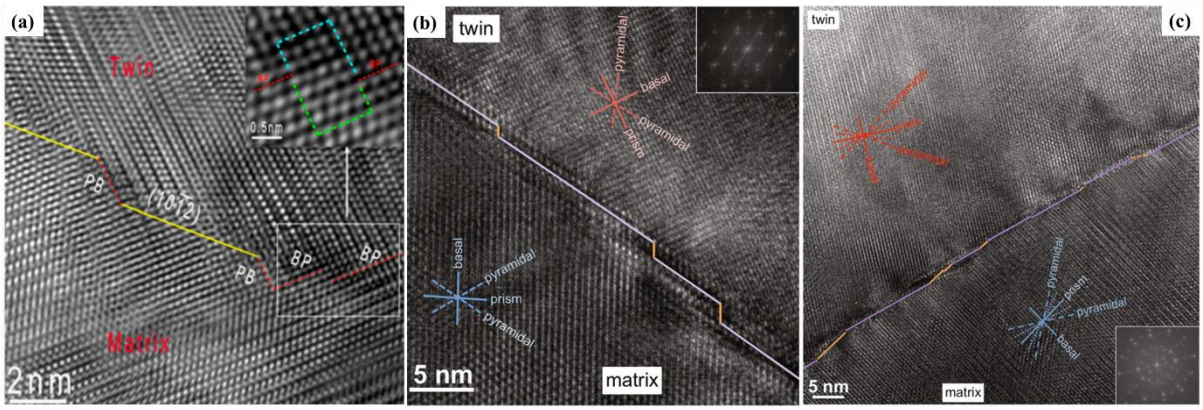

Fig. 1. 8 (a) HRTEM image of a $\{10\bar{1}2\}$ twin boundary along the $[1\bar{2}10]$ zone axis in titanium [122]. The straight $\{10\bar{1}2\}$ twin boundaries and the basal-prismatic (BP) interfaces are denoted by the yellow and red lines, respectively [122]. (b) A HRTEM micrograph showing $\{11\bar{2}2\}$ compression twin boundary in zirconium. Beam direction is $[10\bar{1}0]$ [123]. (c) A HRTEM micrograph showing $\{11\bar{2}1\}$ extension twin boundary in zirconium. Beam direction is $[10\bar{1}0]$ [123].

Zhang et al. [120] found that the actual $\{10\bar{1}2\}$ twin boundaries can largely deviate from the $\{10\bar{1}2\}$ twinning planes in HCP metals such as Co (Fig. 1.9a-b) and Mg (Fig. 1.9c). The twin boundaries are coherent and match well the twinning plane on the atomic scale since the twinning dislocations of some twinning modes in HCP [22, 23, 124] and FCC metals [125-127] are well defined. As presumed previously in [55, 68, 128, 129] that $\{10\bar{1}2\}<\bar{1}011>$ twinning is mediated by twinning dislocations, the twinning dislocations should be strictly bounded in the twinning plane and such a deviation of the twinning plane should not appear on the atomic scale, which encourages the exploration of a twinning mechanism other than the widely accepted twinning dislocation theory. Shuffling mechanism associated with $\{10\bar{1}2\}$ twinning was proposed to result in the deviation of the actual twin boundaries from the twinning plane. Shuffling dominates shear for $\{10\bar{1}2\}$ twinning [120]. Shuffling does not have to be confined in the $\{10\bar{1}2\}$ twinning plane, which permits the deviation of the actual TBs from the $\{10\bar{1}2\}$ twinning plane during twin growth. Therefore, the twin boundaries do not need to keep flat in accordance with the twinning plane. Partridge and Roberts [130] observed abnormal TB migration in Mg. They found that the $\{10\bar{1}2\}$ TB can evolve into extreme incoherency under small stresses.

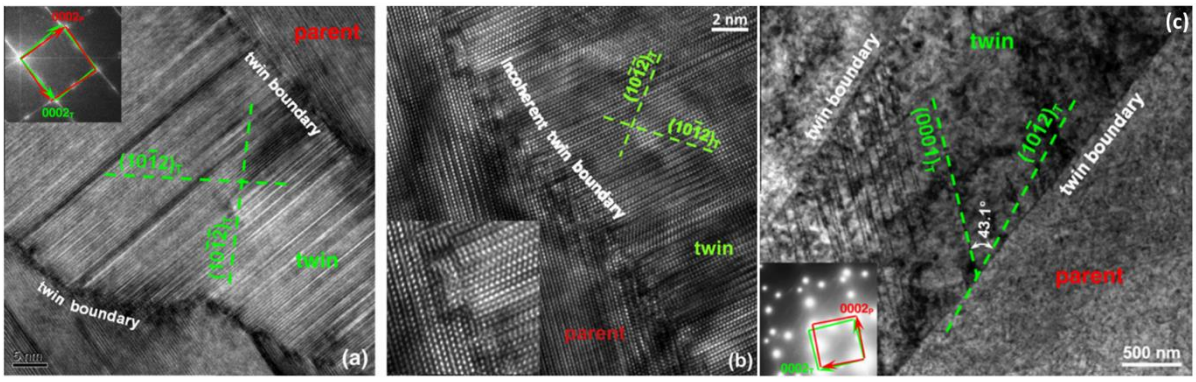

Fig. 1. 9 (a) High-resolution TEM micrographs showing that the twin boundaries near the twin tip in Co conspicuously deviate from the twinning planes. The diffraction pattern in the inset indicates that the twin and the parent indeed satisfy the $\{10\bar{1}2\}\langle\bar{1}011\rangle$ twin relationship (zone axis $[1\bar{2}10]$). In this orientation, the two possible twinning planes $\{10\bar{1}2\}$ are marked with broken lines. (b) A higher magnification showing the lattice fringes near the twin boundary evidencing a very rough interface as can be better seen in the higher-magnified inset. The twin boundary is actually incoherent. (c) TEM micrograph of deformed Mg shows that the actual twin boundary deviates (~10°) from the trace of the twinning plane. The diffraction pattern in the inset identifies the twinning mode as $\{10\bar{1}2\}\langle\bar{1}011\rangle$ since the [0002] axes of the parent and the twin are nearly perpendicular to each other (zone axis $[1\bar{2}10]$). The straight dark lines inside the twin are the traces of the stacking faults and coincide with the trace of the basal plane (0002) [120].

TEM observation of twins are usually applied with the beam direction parallel to the zone direction of the twins. The propagation of $\langle\bar{1}011\rangle$ twinning dislocations in alternating $\{10\bar{1}2\}$ planes, combined with an atomic shuffle, has the effect of growing twins perpendicular to the $\{10\bar{1}2\}$ plane and along the $\langle\bar{1}011\rangle$ twinning direction. Due to the difficulty of characterizing twins along the shear direction, not much effort was done about the lateral growth of the twin, although such mobility can be expected to condition greatly the overall propagation of the twin and its ability to accommodate shear in a meaningful volume of the grain. Liu et al. [14] identified $\{10\bar{1}2\}$ twins using HRTEM and atomistic simulations with view direction parallel to the shear direction of the twins. Experimental characterizations using EBSD or TEM in two dimensional sections show an approximately elliptical twin shape, with the long axis along the twinning shear direction $\boldsymbol{\eta_1}$ (Fig. 1.10a). This view is called bright side and represented by BS. Thus, the three-dimensional (3D) shape is approximately ellipsoidal (Fig. 1.10b). Fig. 1.10c shows the coherent twin boundaries parallel to the twinning plane and BP interfaces observed along a direction perpendicular to the twinning shear direction $\boldsymbol{\eta_1}$ and the normal to the twin plane $\mathbf{K_1}$. When the twin domain is observed along the twinning direction $\boldsymbol{\eta_1}$ (this view is called dark side and represented by DS) in Fig. 1.10d, it can be seen that the matrix and the twin domain have identical atom columns.

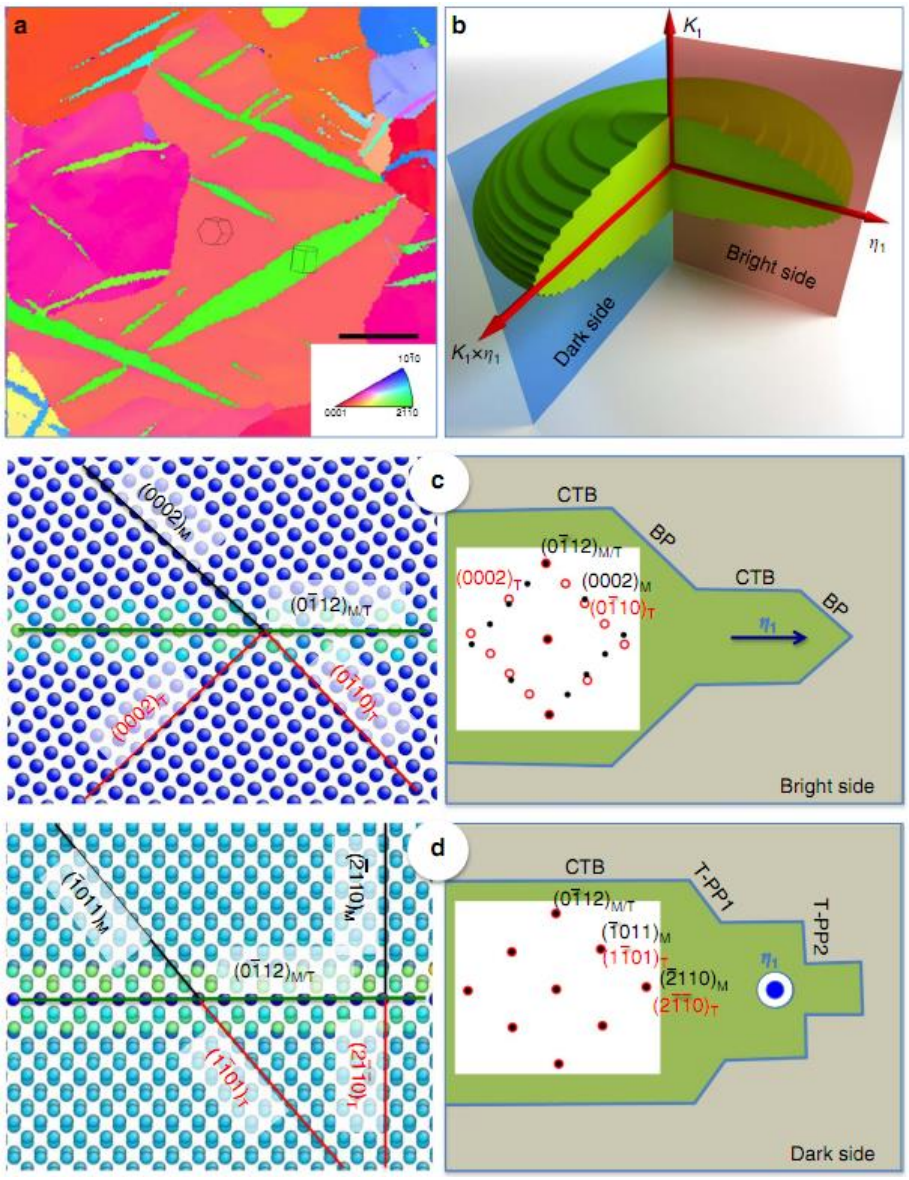

Fig. 1. 10 Three-dimensional twin boundaries of $\{10\bar{1}2\}$ twins. (a) EBSD analysis of deformed polycrystalline magnesium shows twins of elliptical shape with the long axis along the twinning direction. (b) Speculated ellipsoidal morphology of a three dimensional twin. The bright side refers to the observation along a direction perpendicular to both the twinning shear direction ($\boldsymbol{\eta_1}$) and the normal to the twin plane ($\boldsymbol{K_1}$). The dark side refers to the observation along $\boldsymbol{\eta_1}$. (c) The bright side of a $\{10\bar{1}2\}$ twin domain shows two types of boundaries: CTB and BP interface. A schematic of these twin boundaries (CTBs and PB/BPs) and corresponding electron diffraction pattern is on right side (d) Speculated characteristics of the dark side of a $\{10\bar{1}2\}$ twin domain: CTBs twist pyramidal-pyramidal (T-PP1) and twist prismatic–prismatic (T-PP2) boundaries with high atomic areal density. A schematic of these twin boundaries and corresponding electron diffraction pattern is on right side [14].

The DS of twins might be revealed by TEM at the atomic level if twist TBs in the DS view relax to form semi-coherent interfaces associated with the formation of misfit dislocations.

These misfit dislocations will cause local elastic distortion and, as a consequence, the twin and matrix across the coherent boundary will deviate locally from the perfect twin orientation [14].

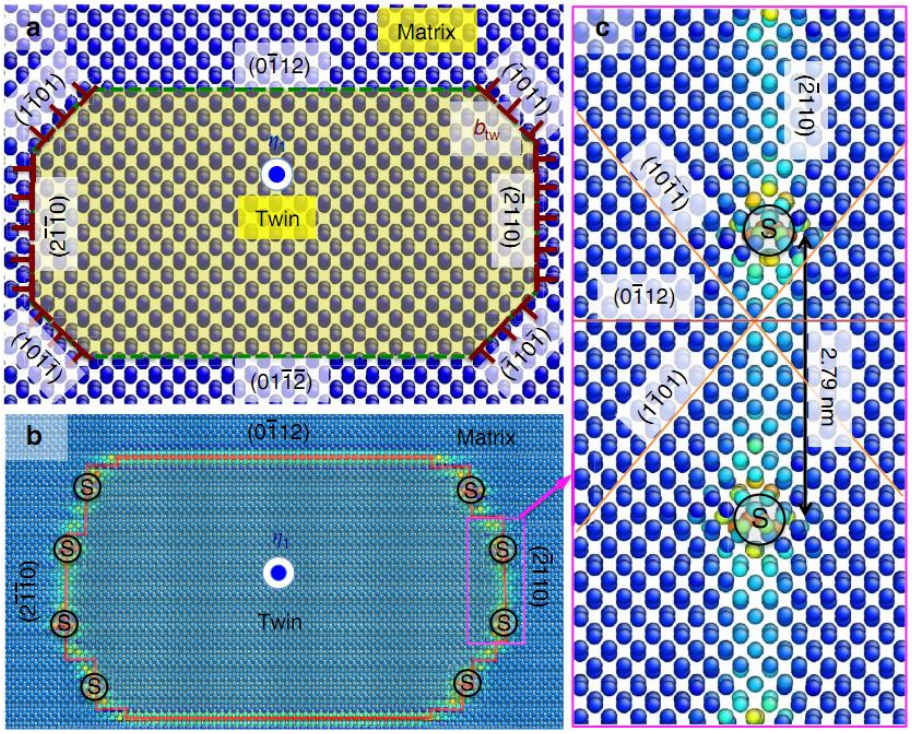

Fig. 1. 11 Atomistic simulation of atomic structures of the dark side. (a) The atomic structure of the dark side along the twinning direction ($\boldsymbol{\eta}_1$). Three atomic planes, $\{0\bar{1}12\}$ (CTB), $\{1\bar{1}01\}$ (T-PP1) and $\{\bar{2}110\}$ (T-PP2), with high atomic areal density are chosen to be potential low-energy interfaces between the matrix and the twin. (b) Atomic structure of a relaxed twin nucleus, showing $\{0\bar{1}12\}$ CTBs, $\{\bar{2}110\}$ semi-coherent boundaries and discrete misfit dislocations (denoted by the black symbol 'S'). (c) Atomic structure of T-PP2 $\{\bar{2}110\}$ semi-coherent boundary containing coherent interface and discrete misfit dislocations [14].

Twin boundaries under DS consist of $\{10\bar{1}2\}$ coherent twin boundary, $\{1\bar{1}01\}$ (T-PP1) interface and $\{\bar{2}110\}$ (T-PP2) interface in magnesium as depicted in Fig. 1.11a. Atomic structure of a relaxed twin nucleus in Fig. 1.11b reveals the energies and atomic structures of the three interfaces: CTB has the lowest formation energy of 125 mJ m^{-2}, T-PP2 has a formation energy of 212 mJ m^{-2}, which is lower than most tilt grain boundaries (GBs), and T-PP1 has a formation energy of 318 mJ m^{-2}, which is higher than most tilt GBs. Fig. 1.11c shows the atomic structures of the T-PP2 interface, indicating the formation of a semi-coherent interface and misfit dislocations. TBs in the DS can be represented by CTB + T-PP2, where the additional twist rotation 3.78° associated with a perfect twin orientation is accommodated by misfit dislocations. This suggests that selected area diffraction patterns could show additional spots associated with the coherent interface, and so provide a signature of the DS.

1.2.3.2 Twin-twin interfaces

When multiple twin variants are activated in one grain, twin-twin interactions can happen. Reed-Hill and Buchanan investigated twin-twin interactions in HCP metals [131]. Twin-twin interactions were found to correlate with mechanical hardening [12, 132, 133]. De-twinning is blocked due to the formation of twin-twin interactions [134], which is ascribed to the unfavorable dissociation of twin-twin boundary (TTBs) dislocations. Roberts and Partridge experimentally characterized TTBs between two $\{10\bar{1}2\}$ twins in Mg [135]. They suggested that the twin-twin boundaries are the common interface bisecting two twinning planes.

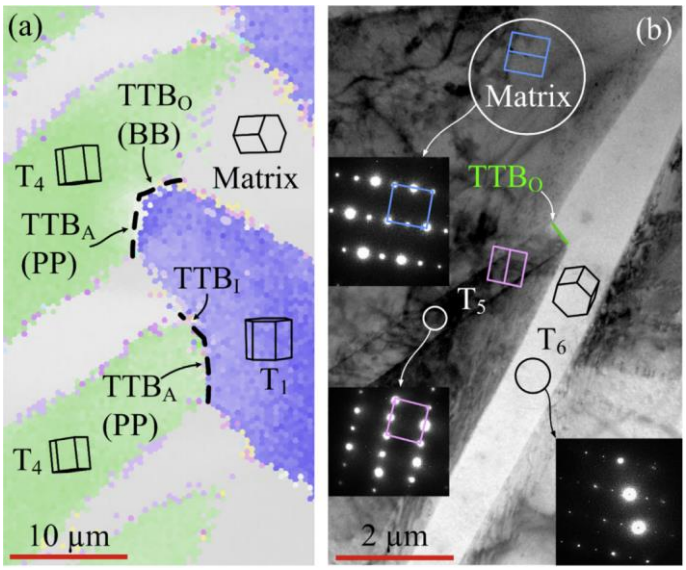

Fig. 1. 12 Experimentally observed TTBs: (a) EBSD orientation map of low-angle TTBs, TTB_A (BB) and TTB_O (PP), in Type I co-zone twin interaction under compression in $[10\bar{1}0]$ Mg single crystal; (b) TEM bright field micrograph showing TTB_O in Type II(a) twin–twin interaction [136].

Recently, Yu et al. [136] investigated the interaction structures and twin transmission associated with $\{10\bar{1}2\}$ twin-twin interactions by conducting two cyclic loading tests in Mg single crystals along the [0001] and $[10\bar{1}0]$ directions, respectively. Three types of twin-twin structures were detected according to the geometrical relation between the two intersected twinning planes: Type I with the intersection line along $[\bar{1}2\bar{1}0]$, Type II (a) with the intersection line along $[\bar{2}\bar{2}43]$, and Type II (b) with the intersection line along $[0\bar{2}21]$. In Fig. 1.12a, TTBs belonging to Type I is presented. Twin-twin boundaries on the acute (TTB_A) side and on the obtuse side (TTB_O) are characterized, indicating that the trace of the TTB_A is nearly parallel to the traces of prismatic planes in both twins and referred to as PP boundary while that of TTB_O boundary is near the basal plane traces in both twins and referred to as the BB boundary. Fig.

1.12b shows a TTB_O boundary belonging to a Type II (a) twin-twin interaction. It can be seen that twin transmission does not happen.

1.2.4 Criterions for twin variant selection

The Schmid factor (SF) is conveniently used as a reference point for examining variant selection. It is based on the idealized hypothesis that the stress direction in a grain is exactly the same as the one applied on the whole sample. From this hypothesis one obtains the following simple formula for the SF:

$$SF = cos\lambda \cdot cos\theta \tag{1-1}$$

Here λ is the angle between the loading direction (LD) and the twin plane normal (TPN) while θ is the angle between the LD and the twin shear direction (SD). It is expected that twin variants with high SFs will tend to be more active. This classical law has been applied to successfully predict the generation of twins [137, 138]. Due to the reorientation effect induced by twinning, the local stress may be largely deviated from the external one. Low SF twins or anomalous twins may happen that do not meet the SF law, which leads to the exploration of new criterions to explain their activation. Compression along the $<11\bar{2}0>$ direction of Mg single crystals, $\{10\bar{1}2\}$ twinning resulted in the formation of soft orientations for slip and additional twinning in the form of secondary and tertiary twinning [139]. Yang et al. [140] studied the twinning behavior in extruded bars and rolled plates deformed at 97 ºC by channel die compression. Twin strain tensor of each twin variant was computed and explained the selection of twin variants. This method was also taken to explain the activation of second twin variant with low SF in one grain [141]. It has been reported that some $\{10\bar{1}2\}$ twins in opposition of the external strain can happen [142, 143]. It has been speculated that their formation is caused due to the inhomogeneity of the internal stress distribution during unloading. Based on the calculation of strain tensor, the occurrence of anomalous $\{10\bar{1}2\}$ twinning in rolled sheets of AZ31 Mg alloy deformed at room temperature in tension along the RD can completely cancel the diagonal strain components associated with the localized basal slip [144]. Molodov et al. [145] characterized anomalous $\{10\bar{1}2\}$ twins in Mg single crystals that had negative SFs and produced an opposite strain to the external deformation, demonstrating that the active variants correspond to the ones that involve a lattice rotation opposite to that induced by basal slip.

Schuman et al. [146, 147] put forward a new selection criterion based on the calculation of the deformation energy to create a primary twin in commercially pure titanium deformed by

channel-die compression. In their method, the effect of the grain size was taken into account using a Hall-Petch type relation to explain the activation of the twinning variant. This criterion was extended into the case when commercially pure titanium was subjected to rolling in one step with 10% reduction [148]. A good prediction can be obtained for the variant selection.

Recently, Jonas et al. [13] investigated the twinning behaviors in AM30 and AZ31 magnesium alloys deformed in tension at room temperature and a strain rate of 0.1 s^{-1} to strains of 0.08 and 0.15. Nearly half proportion of detected $\{10\bar{1}1\}$ twins have low SFs while some potential twins with high SF do not form. The absence of potential high SF twins and the presence of the low SF twins are explained in terms of the accommodation strains, which are obtained by rotating the twinning shear displacement gradient tensor into the crystallographic reference frame of the neighboring grain. It indicates that the twin variants that are accommodated by easy accommodation systems preferentially take place while those that need accommodation from difficult systems cannot happen, indicating that basal glide and extension twins belong to easy accommodation systems while accommodation from prismatic slip is considered to be generally avoided. This method was employed to the analysis of primary, secondary and tertiary twinning in AZ31 magnesium alloy deformed under channel-die compression at 100 ºC and a strain rate of 5×10^{-3} s^{-1} [149]. The primary twin selected is not necessarily the one with the highest SF but the one that requires the least accommodation work in most of the neighboring grains. With respect to the secondary and tertiary twins, potential high SF twins that require the accommodation from hard systems do not form. Similar attention was paid to the analysis of twinning in commercially pure titanium subjected to uniaxial compression at room temperature [86, 87]. The absence of the potential high SF twins is attributed to the requirement of accommodation from basal glide, pyramidal glide, and twinning. Prismatic glide is considered as the easiest accommodation system that facilitates the appearance of the low SF twins. In AZ31Mg alloy, the CRSS of prismatic slip is only 1.1-5.5 times of that of basal slip [150, 151]. The activity of prismatic slip can be enhanced by stress concentration caused by strain incompatibility in AZ31 [152]. The role of prismatic slip in accommodating the strain induced by twinning was further studied by Shi et al. [153]. They proposed that the favorable twin variants require not only the most or more accommodation through basal slip or prismatic slip with low CRSS, but also the least or less accommodation through pyramidal slip with high CRSS in the neighbors. CRSS ratios relative to P <***a***> slip in commercially pure titanium at room temperature are listed in Table 1. 3 [154]. In order to examine the role of each deformation system in accommodating the strain caused by twinning in commercially pure titanium, Wang et al. [53] conducted interrupted in-situ tensile tests along

the RD of rolled commercially pure titanium. Accommodative slips and twins have different impacts on the further development of the initiating twins. It has been found that high SF twins that are accommodated by twins have a higher capacity to propagate and repeatedly nucleate while those with low SF that are accommodated by slips have less power and are comparatively static. Their strain contributions of the twins with positive SFs are consistent with the macroscopic strains. In contrast, the twins with negative SFs formed due to the unbalanced local constraints induced by high SF twinning or slip, are unstable. They impose a negative contribution to the external strain.

Table 1. 3 Non-exhaustive literature data for CRSS ratios relative to P <***a***> slip in commercially pure or highly pure -titanium at room temperature. For P <***a***> systems, the absolute values of CRSS are given. The CRSSs stand for to the values of resolved shear stress when slip initiates on a system [154].

Method	P <***a***>	B <***a***>	Py_1<***a***>	Py_1<***c***+***a***>	Py_2<***c***+***a***>	O(wt.%)	Ref.
Slip line analysis	90 MPa	1.2	1.1	-	-	0.10	[155]
	14 MPa	3.0	-	-	-	0.01	
	-	3.6	25.4	22.5	-	0.25	[156]
TEM observations	-	-	< 13	-	-	0.10	[157]
Slip line analysis + TEM observations	120 MPa	1.5	1.2	2	-	0.16	[158]
	192 MPa	1.5	1.2	1.8	-	0.32	
FEM modelling of single crystals	181 MPa	1.2	-	2.6	-	0.07	[159]
	150 MPa	2.3	-	7.4	-		[160]
Taylor-type modelling		6.0	-	9.0	-	0.11	[161]
	37 MPa	1.3	-	5.3	-	< 0.0002	[60]
	30 MPa	5.0	-	4.0	-	< 0.0002	[102]
Self-consistent modelling	90 MPa	2.5	-	9.4	-		[82]
	80 MPa	1.1	1.4	3.3	-	0.06	[95]
	57 MPa	4.8	2.9	5.4	4.1	0.13	[162]
	68 MPa	2.6	1.8	3.7	-	0.12	[163]
	98 MPa	-	-	2.3	-	< 0.001	[164]
	141 MPa	1.8	1.4	2.4	2.5	0.11	[154]

1.3 Chapter conclusion

In this chapter, researches on twinning in HCP metals in recent years are introduced. Atomic-scale simulations are mainly used to study twin nucleation and growth. A large number of researchers utilize EBSD and TEM characterizations to investigate the effect of temperature, strain rate, grain size, initial texture and loading paths on twinning behaviors as well as the character of twin boundaries. In order to analyze the experimental results, a brief introduction of calculation principles used in this work will be given in the next chapter.

Chapter 2 Basic crystallographic calculations

Contents

2.1 Crystal coordinate system

For hexagonal structure materials, the Bravais lattice is shown in Fig. 2. 1a and Miller indices can be obtained (3-index system). The basis vectors are established as: $\boldsymbol{a}_1 \parallel [2\bar{1}\bar{1}0]$, $\boldsymbol{a}_2 \parallel [\bar{1}2\bar{1}0]$, $\boldsymbol{c} \parallel [0001]$. In consideration of symmetry of hexagonal structure, the Miller-Bravais system is used as shown in Fig. 2.1b (4-index system). The basis vectors are set up as: $\boldsymbol{a}_1 \parallel [2\bar{1}\bar{1}0]$, $\boldsymbol{a}_2 \parallel [\bar{1}2\bar{1}0]$, $\boldsymbol{a}_3 \parallel [\bar{1}\bar{1}20]$, $\boldsymbol{c} \parallel [0001]$. In Equation (2-1), M_{43} can enable us to obtain Miller indices of crystallographic directions when Miller-Bravais indices are known.

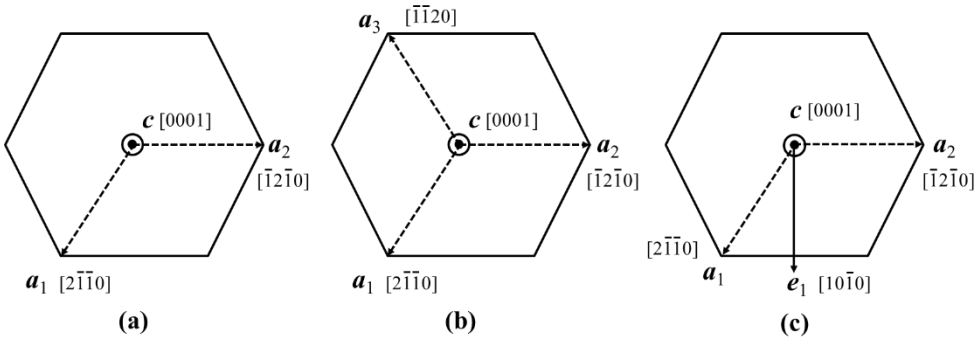

Fig. 2. 1 (a) Bravais lattice, (b) Miller-Bravais system, (c) Crystal orthonormal coordinate.

According to the HKL-Channel 5 acquisition systems, crystal orthonormal coordinate is established as drawn in Fig. 2. 1c. The basis vectors are fixed as: $\boldsymbol{e}_1 \parallel [10\bar{1}0]$, $\boldsymbol{e}_2 \parallel \boldsymbol{a}_2$, $\boldsymbol{e}_3 \parallel \boldsymbol{c}$. In Equation (2-2), M_{3o} can help us to obtain the indices of crystallographic directions expressed in crystal orthonormal coordinate when the Miller indices are given. Then, the coordinate transformation matrix for directions from crystal orthonormal coordinate to Miller-Bravais system is represented by M_o (Equation (2-3)), which equals to the dot product of M_{43} and M_{3o}.

It should be mentioned that all calculations associated with the matrices used in this thesis are expressed in matrix notation.

$$M_{43}=\begin{bmatrix}2 & 1 & 0\\ 1 & 2 & 0\\ 0 & 0 & 1\end{bmatrix} \tag{2-1}$$

$$M_{3o}=\begin{bmatrix}\sqrt{3}/2 & 0 & 0\\ -1/2 & 1 & 0\\ 0 & 0 & c/a\end{bmatrix} \tag{2-2}$$

$$M_{o}=\begin{bmatrix}\sqrt{3} & \sqrt{3}/2 & 0\\ 0 & 3/2 & 0\\ 0 & 0 & c/a\end{bmatrix} \tag{2-3}$$

In the above equations, *c/a* is the axial ratio.

Crystallographic orientation is detected by SEM microscope equipped with an EBSD camera and the AZtec acquisition software package (Oxford Instruments). The most commonly used Euler angles (φ_1, Φ, φ_2) are formulated in Bunge convention [165]. The rotation matrix (R) from the sample frame to the crystal orthonormal frame is given by Equation (2-4):

$$R=\begin{bmatrix}cos(\varphi_1) & -sin(\varphi_1) & 0\\ sin(\varphi_1) & cos(\varphi_1) & 0\\ 0 & 0 & 1\end{bmatrix}\cdot\begin{bmatrix}0 & 0 & 1\\ 0 & cos(\Phi) & -sin(\Phi)\\ 0 & sin(\Phi) & cos(\Phi)\end{bmatrix}\cdot\begin{bmatrix}cos(\varphi_2) & -sin(\varphi_2) & 0\\ sin(\varphi_2) & cos(\varphi_2) & 0\\ 0 & 0 & 1\end{bmatrix} \tag{2-4}$$

The metric tensor in direct space is represented by g as shown in Equation (2-5).

$$g=\begin{bmatrix}1 & -1/2 & 0\\ -1/2 & 1 & 0\\ 0 & 0 & c^2/a^2\end{bmatrix} \tag{2-5}$$

The metric tensor in reciprocal space is represented by g^* as shown in Equation (2-6).

$$g^*=\begin{bmatrix}4/3 & 2/3 & 0\\ 2/3 & 4/3 & 0\\ 0 & 0 & a^2/c^2\end{bmatrix} \tag{2-6}$$

They can be used to achieve the coordinate transformation between the two spaces. The indices of a plane in direct space are the same as the ones of the plane normal direction in reciprocal space.

2.2 Twinning reference frame

For a twinning system, the twinning reference frame is set up as: X || shear direction (SD), Y || shear plane normal (SPN), Z || twinning plane normal (TPN), SPN (**p**) is the cross product of HPN (**m**) and SD (**n**) [13, 153, 166].

$$M_{ct}=\begin{bmatrix} n_1 & p_1 & m_1 \\ n_2 & p_2 & m_2 \\ n_3 & p_3 & m_3 \end{bmatrix} \tag{2-7}$$

For a compound twin, twinning operation is equivalent to a rotation of 180° around the TPN. This rotation matrix (R_{tw}) can be obtained by giving an Euler angle of (180°, 0°, 0°):

$$R_{tw}=\begin{bmatrix} -1 & 0 & 0 \\ 0 & -1 & 0 \\ 0 & 0 & 1 \end{bmatrix} \tag{2-8}$$

As illustrated in Fig. 2.2, the transformation matrix between the crystal orthonormal coordinates of the twin and the corresponding parent grain is:

$$R_{gt}=M_{ct}\cdot R_{tw}\cdot M_{ct}^{-1} \tag{2-9}$$

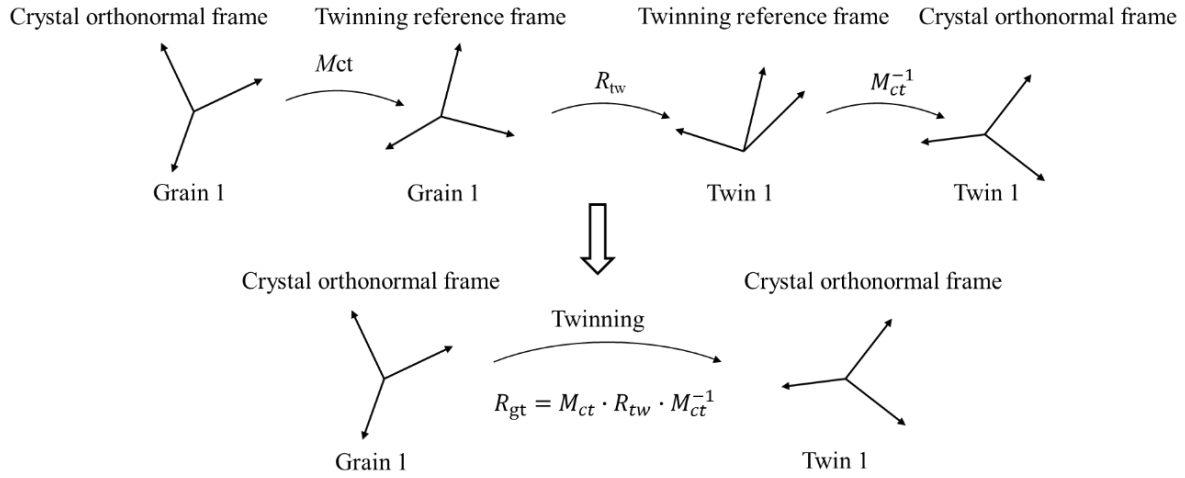

Fig. 2. 2 Schematics of operation between grain and a twinning inside the grain.

The indices of a plane *(h, k, i, l)* expressed in the twinning reference frame can be transformed into the Bravais lattice frame of the corresponding parent grain as:

$$\mathbf{P} = (M_{3o}^{-1} \cdot (M_{ct} \cdot (R_{tw} \cdot (M_{ct}^{-1} \cdot (M_{3o} \cdot ([h\ k\ l] \cdot g^{*})^{T})))))^{T} \cdot (g^{*})^{-1} \quad (2\text{-}10)$$

Similarly, the indices of a direction [*u, v, t, w*] expressed in the twinning reference frame can be transformed into the Bravais lattice frame of the corresponding parent grain as:

$$\mathbf{D} = M_{o}^{-1} \cdot (M_{ct} \cdot (R_{tw} \cdot (M_{ct}^{-1} \cdot (M_{o} \cdot [u\ v\ w]^{T})))) \quad (2\text{-}11)$$

2.3 Displacement gradient tensor

The displacement gradient tensor of a twin has a simple form in the twinning reference frame established by Equation (2-7):

$$E_{tw} = \begin{bmatrix} 0 & 0 & s \\ 0 & 0 & 0 \\ 0 & 0 & 0 \end{bmatrix} \quad (2\text{-}12)$$

In Equation (2-12), s=0.218, 0.175 and 0.63 for $\{11\bar{2}2\}$, $\{10\bar{1}2\}$ and $\{11\bar{2}1\}$ twinning (*c/a*=1.587), respectively. With the help of transformation matrix in Equation (2-9), this displacement gradient tensor of a twin can be expressed into the crystal orthonormal coordinate of the corresponding parent grain as:

$$E_{ij} = R_{gt} \cdot E_{tw} \cdot R_{gt}^{-1} \quad (2\text{-}13)$$

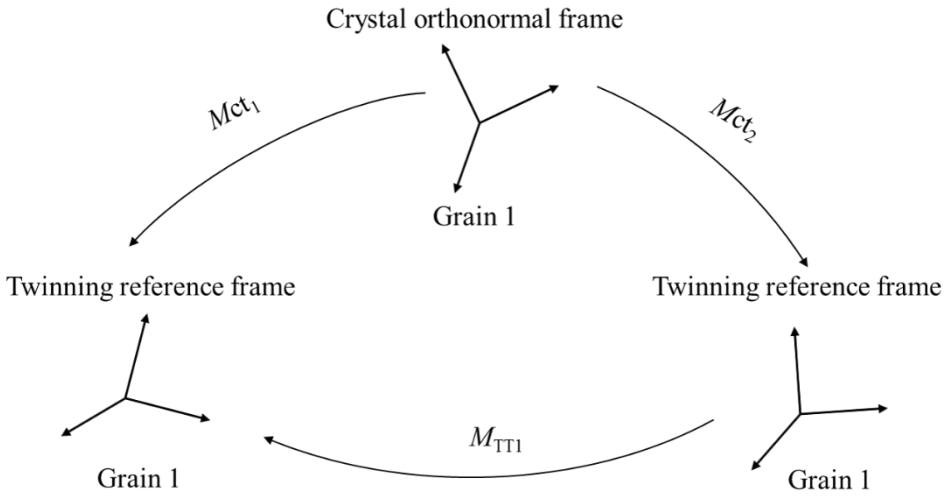

Fig. 2. 3 Schematics of operation matrix between two twinning systems in the same grain.

In Chapter 3, the displacement gradient tensor a twin (T_1) will be expressed in another twinning reference frame (T_2) in the same grain. As illustrated in Fig. 2. 3, M_{ct1} and M_{ct2} are

supposed to represent the twinning reference frames of T_1 and T_2 twins in the same grain, respectively. The displacement gradient tensor of T_1 twin (E_{tw}) can be expressed in the T_2 twinning reference frame (E_{ij}) in the same parent grain as:

$$E_{ij}=M_{ct2}^{-1}\cdot M_{ct1}\cdot E_{tw}\cdot M_{ct1}^{-1}\cdot M_{ct2} \tag{2-14}$$

In the obtained tenor (E_{ij}), E_{13} component will be used to evaluate the capacity of T_2 twin to accommodate the strain induced by T_1 twin. Both T_1 and T_2 twins are activated in the same grain.

In Chapter 3, the displacement gradient tensor a twin (T_1) will also be expressed in another twinning reference frame (T_2) in the neighboring grain. T_1 twin forms in grain 1 (G_1) and T_2 in G_2. As illustrated in Fig. 2.4, M_{ct1} and M_{ct2} represent the twinning reference frames of T_1 and T_2 twins, respectively. R_1 and R_2 represent the rotation matrix from the sample frame to the crystal orthonormal frame of G_1 and G_2, respectively.

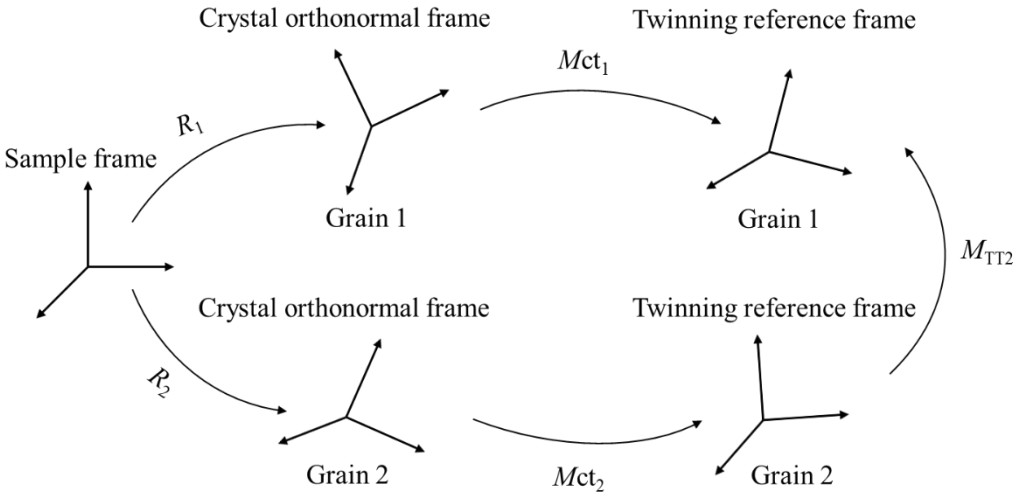

Fig. 2. 4 Schematics of operation matrix between two twinning systems in neighboring grains.

As shown in Fig. 2.4, the displacement gradient tensor (E_{tw}) of T_1 twin in G_1 can be expressed in the twinning reference frame (E_{ij}) of T_2 in G_2 as:

$$E_{ij}=M_{ct2}^{-1}\cdot R_2^{-1}\cdot R_1\cdot M_{ct1}\cdot E_{tw}\cdot M_{ct1}^{-1}\cdot R_1^{-1}\cdot R_2\cdot M_{ct2} \tag{2-15}$$

In the obtained tenor (E_{ij}), E_{13} component will be used to evaluate the capacity of T_2 twin to accommodate the strain induced by T_1 twin. In this case, T_1 and T_2 twins happen in two neighboring grains.

2.4 Trace analysis

As shown in Fig. 2. 5a, a twinning plane is represented by **TP** (in blue). **ON** is the normal direction of **TP**. According to the principle of pole figure, point **N′** is intersection point between **NS** and the equatorial plane (in yellow). Thus, point **N′** is the projection point of **ON** in the macroscopic frame. **TB** indicated by a red line is the trace of the **TP** in the observation plane (**OP**) during EBSD characterization and also represents the twin boundary. It can be noticed that **TB**⊥**OS** and **TB**⊥**ON**, which can lead to the conclusion that **TB** is perpendicular to the **ONS** plane. Therefore, **TB**⊥**ON′**. That is why the trace of a twinning plane in the EBSD scanning surface is perpendicular to the line between circle centre of twinning plane pole figure and the projection point of the twinning plane.

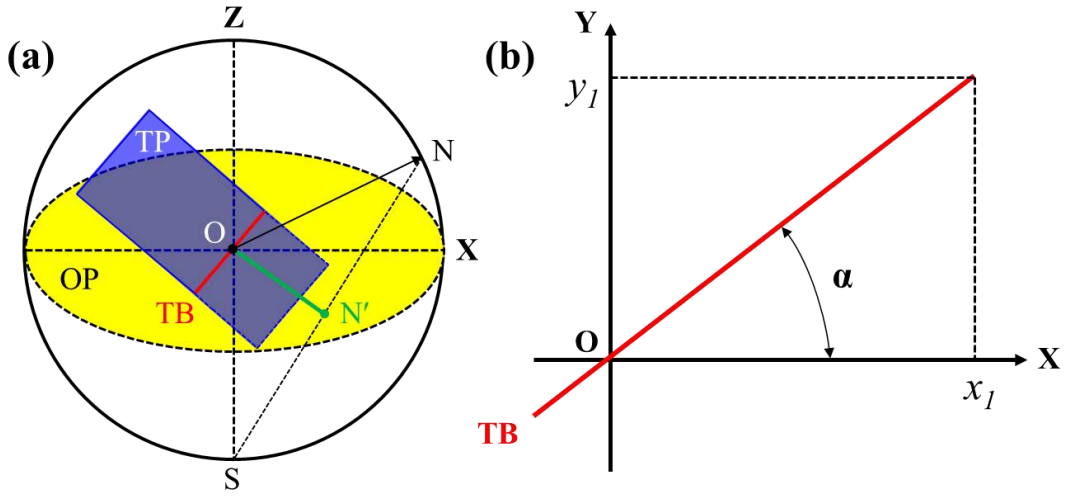

Fig. 2. 5 illustration of pole figure of planes and corresponding trace in external frame.

As shown in Fig. 2.5b, the angle between the trace of twinning plane and the X-axis in the sample frame (**XOY**) can be calculated. The components of **ON** in the sample frame are represented by (m_1, n_1, p_1):

$$\mathbf{ON} = \begin{pmatrix} m_1 \\ n_1 \\ p_1 \end{pmatrix} \tag{2-16}$$

The components of **TB** are represented by (x_1, y_1, z_1):

$$\mathbf{TB} = \begin{pmatrix} x_1 \\ y_1 \\ z_1 \end{pmatrix} \tag{2-17}$$

Since this vector is in the observation plane, $z_1 = 0$. Then, the condition **TB** $\perp$ **ON** can also be written as **TB**·**ON** = 0,

$$m_1 x_1 + n_1 y_1 = 0 \Longrightarrow \frac{y_1}{x_1} = -\frac{m_1}{n_1} \tag{2-18}$$

If α is the angle between **TB** and **X**, we can obtain the angle α:
When $n_1 \neq 0$,

$$\alpha = tan^{-1}(-m_1/n_1) \tag{2-19}$$

When $n_1 = 0$ and $m_1 \neq 0$, the trace of the twinning plane is Y-axis.
When $n_1 = 0$ and $m_1 = 0$, the twinning plane is parallel to the observation plane.

In order to identify the slip systems that are activated during plastic deformation, the observed traces in the secondary electron images are the intersection lines between slip planes and the observation plane. In this method, only slip planes are considered regardless of slip directions. If two slip systems happen in the same slip plane along two directions, they cannot be distinguished. For example, the distinction between $\{10\bar{1}1\}<1\bar{2}10>$ and $\{10\bar{1}1\}<11\bar{2}\bar{3}>$ slip systems cannot be verified by trace analysis.

2.5 Misorientation

In order to calculate the misorientation between a double twin and the associated parent grain, the transformation between the grain and the doubly-oriented region should be established. M_{PT} and M_{DT} represent the twinning reference frames of primary twins and double twins, respectively. R_1 indicates the rotation matrix from the sample frame to the crystal orthonormal frame of the grain where twins form. The rotation matrix from the sample frame to the crystal orthonormal frame of the primary and secondary twins can be expressed as R_{SPT} and R_{SDT}, respectively:

$$R_{SPT}=R_1 \cdot M_{PT} \cdot R_{tw} \cdot M_{PT}^{-1} \tag{2-20}$$

$$R_{SDT}=R_1 \cdot M_{PT} \cdot R_{tw} \cdot M_{PT}^{-1} \cdot M_{DT} \cdot R_{tw} \cdot M_{DT}^{-1} \tag{2-21}$$

There are 12 symmetric matrices (*Msy*) in HCP metals as listed in Table 2. 1. Therefore, the rotation between the crystal orthonormal frames of the grain and the double twin (R_{GDT}) can be achieved by 12 operations:

$$R_{GDT}=M_{PT}\cdot R_{tw}\cdot M_{PT}^{-1}\cdot M_{DT}\cdot R_{tw}\cdot M_{DT}^{-1}\cdot M_{sy} \tag{2-22}$$

Equation (2-22) should be normalized in order to calculate the axis-angle relation ($Axis_{GDT}$ - $Angle_{GDT}$) between the grain and the double twin. $Angle_{GDT}$ and $Axis_{GDT}$ can be obtained as:

$$Angle_{GDT}=cos^{-1}\left(\left(R_{GDT}(1,1)+R_{GDT}(2,2)+R_{GDT}(3,3)\right)/2\right) \tag{2-23}$$

(1) If $Angle_{GDT}=0$,

$$Axis_{GDT}=[100] \tag{2-24}$$

(2) If $0°<Angle_{GDT}<180°$,

$$Axis_{GDT}(1,1)=R_{GDT}(2,3)-R_{GDT}(3,2)/2sin\left(Angle_{GDT}\right) \tag{2-25}$$

$$Axis_{GDT}(2,1)=R_{GDT}(3,1)-R_{GDT}(1,3)/2sin\left(Angle_{GDT}\right) \tag{2-26}$$

$$Axis_{GDT}(3,1)=R_{GDT}(1,2)-R_{GDT}(2,1)/2sin\left(Angle_{GDT}\right) \tag{2-27}$$

(3) If $Angle_{GDT}=180°$,

$$Axis_{GDT}=\left[\pm\sqrt{\frac{R_{GDT}(1,1)+1}{2}},\ \pm\sqrt{\frac{R_{GDT}(2,2)+1}{2}},\ \pm\sqrt{\frac{R_{GDT}(3,3)+1}{2}}\right] \tag{2-28}$$

$$\text{with}\begin{pmatrix}\left|Axis_{GDT_m}\right|=max\left(\left|Axis_{GDT_i}\right|,\ i=1,2,3\right)\\ Axis_{GDT_m}>0\\ \forall i\neq m,\ Axis_{GDT_i}=sign\left(R_{GDT_{im}}\right)\cdot\left|Axis_{GDT_i}\right|\end{pmatrix}.$$

In Equation (2-28), the indices of the axis are expressed in the crystal orthonormal frame. The Miller-Bravais indices ($(Axis_{GDT})_B$) of this axis can be obtained according to Equation (2-29).

$$(Axis_{GDT})_B = M_o^{-1} \cdot Axis_{GDT} \tag{2-29}$$

Table 2. 1 Rotation symmetry matrices (*Msy*) in orthogonal coordinate for HCP metals

$\begin{bmatrix}1&0&0\\0&1&0\\0&0&1\end{bmatrix}$	$\begin{bmatrix}1/2&\sqrt{3}/2&0\\-\sqrt{3}/2&1/2&0\\0&0&1\end{bmatrix}$	$\begin{bmatrix}1&0&0\\0&-1&0\\0&0&-1\end{bmatrix}$
$\begin{bmatrix}-1/2&\sqrt{3}/2&0\\-\sqrt{3}/2&-1/2&0\\0&0&1\end{bmatrix}$	$\begin{bmatrix}1/2&-\sqrt{3}/2&0\\-\sqrt{3}/2&-1/2&0\\0&0&-1\end{bmatrix}$	$\begin{bmatrix}1/2&\sqrt{3}/2&0\\\sqrt{3}/2&-1/2&0\\0&0&-1\end{bmatrix}$
$\begin{bmatrix}-1&0&0\\0&-1&0\\0&0&1\end{bmatrix}$	$\begin{bmatrix}-1/2&-\sqrt{3}/2&0\\-\sqrt{3}/2&1/2&0\\0&0&-1\end{bmatrix}$	$\begin{bmatrix}-1/2&\sqrt{3}/2&0\\\sqrt{3}/2&1/2&0\\0&0&-1\end{bmatrix}$
$\begin{bmatrix}1/2&-\sqrt{3}/2&0\\\sqrt{3}/2&1/2&0\\0&0&1\end{bmatrix}$	$\begin{bmatrix}-1/2&-\sqrt{3}/2&0\\\sqrt{3}/2&-1/2&0\\0&0&1\end{bmatrix}$	$\begin{bmatrix}-1&0&0\\0&1&0\\0&0&-1\end{bmatrix}$

If the transformation matrix between the sample frame and a crystal is: $\Delta g = \begin{bmatrix}u&v&w\\r&s&t\\h&k&l\end{bmatrix}$, the Euler angle can be obtained by:

$$\varphi_1 = cos^{-1}\frac{-t}{\sqrt{w^2+t^2}}, \in [0, 2\pi] \tag{2-30}$$

$$\Phi = cos^{-1}\frac{l}{\sqrt{h^2+k^2+l^2}}, \in [0, \pi] \tag{2-31}$$

$$\varphi_2 = cos^{-1}\frac{k}{\sqrt{h^2+k^2}}, \in [0, 2\pi] \tag{2-32}$$

Based on this calculation, the orientations of six equivalent twins can be obtained, which can be used to predict the effect of twin variant selection on texture evolution.

2.6 Apparent Schmid factor analysis

In order to take into account the local stress, apparent SF analysis will be applied to analyse the twinning activity. This method can establish the relation between the SF of a twinning variant and the orientation of the parent grain. Under a loading direction, the SF of a twin variant can be calculated. Then, the loading direction can be plotted into an inverse pole

figure, which is set up as: X-axis || [10$\bar{1}$0], Y-axis || [$\bar{1}$2$\bar{1}$0], Z-axis || [0001]. The color of the projection point represents the value of the obtained SF. Take (10$\bar{1}$2)[$\bar{1}$011] twin variant in pure titanium (*c/a* = 1.587) for example. As shown in Fig. 2.6a, point 1 is the projection point of the loading direction [0001]. When compression is applied along this direction, the SF of (10$\bar{1}$2)[$\bar{1}$011] twin variant is -0.4981. This value is indicated by a blue point in Fig. 2.6a. Similarly, point 2 is the projection point of the loading direction [10$\bar{1}$0]. The SF of (10$\bar{1}$2)[$\bar{1}$011] twin variant under compression along this direction is 0.4981. This value is indicated by red in Fig. 2.6a. According to this method, all loading directions can be plotted into the inverse pole figure and the SFs of the twin variant are revealed by the color as shown in Fig. 2.6b.

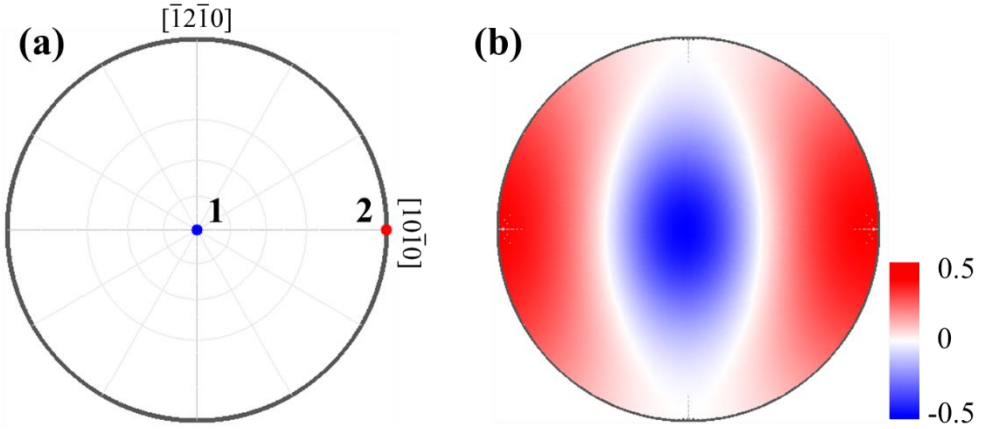

Fig. 2.6 (a) Projection of [0001] (Point 1) and [10$\bar{1}$0] (Point 2) loading directions into the inverse pole figure, (b) Projection of all loading directions into the inverse pole figure in terms of the SFs of (10$\bar{1}$2)[$\bar{1}$011] twin variant under compression.

The methods introduced above will be used in the following chapters. In Chapter 3, two new mechanisms are found that {10$\bar{1}$2} twins are stimulated by other twins in rolled pure titanium. In the section about {10$\bar{1}$2} twins stimulated by {11$\bar{2}$1} twin-twin junctions, the displacement gradient tensor of a twin will be expressed into other twinning reference frames in the same grain. In the section about {10$\bar{1}$2} twins stimulated by {11$\bar{2}$2} twins at high angle grain boundaries, the displacement gradient tensor of a twin will be expressed into other twinning reference frames in the neighboring grain. In Chapter 4, the orientation of {11$\bar{2}$2} → {10$\bar{1}$2} double twins will be calculated in terms of the variant selection. The displacement gradient tensor of the primary twin will be expressed into twinning reference frames of potential secondary twin variants. In Chapter 5, the crystallographic characters of twin-twin junctions will be introduced. The indices of the planes where twin-twin lies will be expressed in different coordinates. Apparent SF analysis will be used in all chapters.

Chapter 3 Sequential {10$\bar{1}$2} twinning stimulated by other twins in pure titanium

Contents

3.1 Introduction

The formation of twins may modify the local stress state and facilitate the activities of twinning and slip systems that are inactive initially. Attention should be paid to the twinning-induced sequential plastic deformation modes such as slips, twinning, secondary twinning, and de-twinning, which is useful for the development of predictive capabilities that can describe twinning and twinning-induced sequential events, and their correlations with microstructures, temperatures, and loading conditions. In this work, a statistical analysis of the sequential {10$\bar{1}$2}

primary twinning stimulated by other twins is investigated in commercially pure titanium subjected to uniaxial compression. Two new sequential twinning mechanisms were found. In Section 3.2, we experimentally characterized sequential {10$\bar{1}$2} (T_i^I) twinning stimulated by the twin-twin junction (TTJ) of two primary {11$\bar{2}$1} extension twins T_{i-1}^{II} and T_i^{II}, which holds a certain relation $T_{i-1}^{II}T_i^{II} \rightarrow T_i^I$ (referred to as {11$\bar{2}$1} TTJ $\rightarrow$ {10$\bar{1}$2}). The mechanism is investigated in terms of SF and displacement gradient accommodation. The apparent SF analysis, as the local stress is taken into account, is able to determine the group of sequential twin variants, but cannot determine the twin variant in the group of two twin variants. Displacement gradient accommodation is further used to determine the twin variant. In Section 3.3, {10$\bar{1}$2} (T_i^I) extension twins stimulated by {11$\bar{2}$2} (C_i^I) compression twins in the neighboring grain were detected. The twin pairs were found at grain boundaries with misorientation angles close to 90°. The mechanism accounting for the formation of these adjoined {10$\bar{1}$2} is examined in terms of SF and local displacement gradient accommodation.

3.2 {10$\bar{1}$2} twinning stimulated by {11$\bar{2}$1} TTJ

3.2.1 Experiment details

In the whole work, the as-received material was hot-rolled and then annealed commercially pure titanium T40 sheet (ASTM grade 2) with a thickness of 1.5 mm. The composition is shown in Table 3.1. After the samples were cut, heat treatment was carried out at different temperatures in order to obtain samples with various grain size.

Table 3.1 Chemical composition of the commercially-pure titanium T40 used in the study.

element	H	C	N	O	Fe	Ti
Composition (wt. ppm)	3	52	41	1062	237	Balance

In this section, the samples from the sheet were annealed in a vacuum furnace at 800 ºC for 3 hours. At room temperature, the annealed sample was compressed with reduction of 7% at a strain rate 1×10^{-3} s^{-1} using a Zwick 120T machine. The compression direction was along the ND.

After compression, the surface of the deformed sample was ground with SiC papers of grits from $1200^{\#}$ to $4000^{\#}$. Electrolytic polishing was performed using a solution of 10% perchloric acid and 90% methanol at 35 V for 5 s at 5 ºC for EBSD measurements, which were performed on a JEOL 6500F field emission gun and on a JSM 6490 SEM microscope equipped

with an EBSD camera and the AZtec acquisition software package (Oxford Instruments). In order to save some time, EBSD scanning was applied on JSM 6490 SEM with a large step size (several μm) to detect the grain size and texture of the initial material. Specifically, EBSD patterns were acquired on a JEOL 6500F field emission gun for obtaining more detailed examination of twins at a small step size. During EBSD characterizations, the sample was tilt by an angle of 70° and a voltage of 15 kV was used. The data that indicates next-neighbor grain to grain misorientation was processed by using ATOM software [169]. Pole figures were processed by using JTEX software [170].

3.2.2 Microstructure evolution

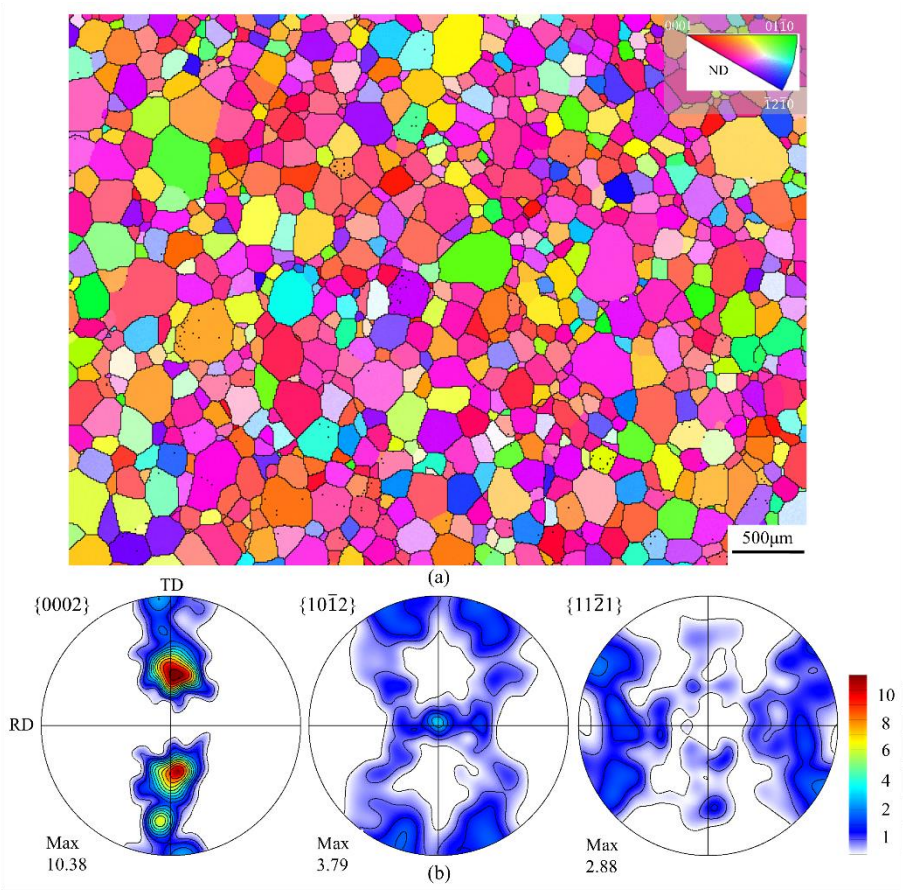

Fig. 3. 1 (a) IPF of the initial sample, (b) {0002}, {10$\bar{1}$2} and {11$\bar{2}$1} pole figures from (a)

After annealing, the sheet is fully recrystallized with an average grain size of ~200 μm and no twins appear as shown in Fig. 3. 1. The EBSD analysis of the sheet that is displayed in {0002}, {10$\bar{1}$2} and {11$\bar{2}$1} pole figures indicates a typical texture of a rolled titanium sheet where the *c*-axes are oriented ±40° from the ND of the plate towards the TD. The microstructure of the deformed sample is presented in Fig. 3. 2 as well as the neighboring grain-

to-grain misorientation. Fig. 3. 2a shows an EBSD pattern of the polished surface with a step size of 0.5 μm. It can be noticed that a large number of twins with lamellar shape are detected, including primary twins and double twins within primary twins. Fig. 3. 2b shows the twin boundaries that are characterized with a tolerance of ± 5° deviation from the ideal crystallographic axis and angle.

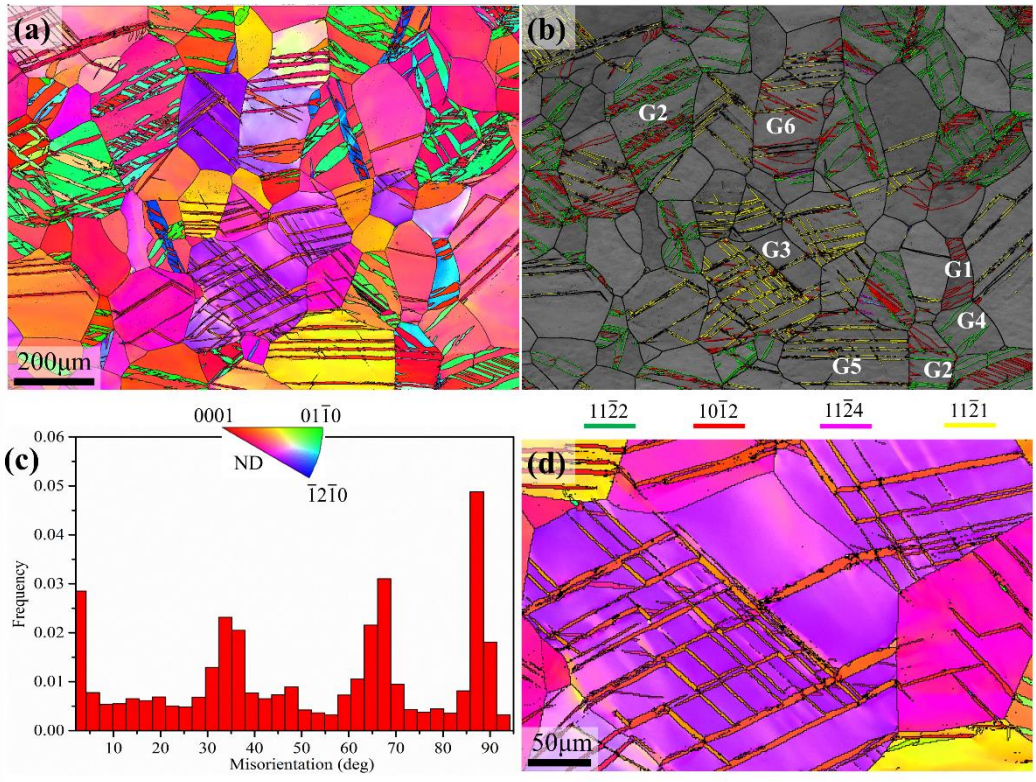

Fig. 3. 2 (a) EBSD patterns of the deformed Ti, (b) the next-neighbor grain to grain misorientation analysis, (c) the distribution of grain misorientation angles, and (d) the magnified EBSD pattern of the region G3 in (b). The yellow and red lines indicate {11$\bar{2}$1} and {10$\bar{1}$2} twin boundaries; the blue and pink lines indicate {11$\bar{2}$2} and {11$\bar{2}$4} twin boundaries.

Corresponding to the crystallography of twins in α-titanium, {11$\bar{2}$1} extension twinning rotates the twinned domain by ~35° around a <1$\bar{1}$00> axis; {10$\bar{1}$2} extension twinning rotates the twinned domain by ~87° around a <1$\bar{2}$10> axis; {11$\bar{2}$2} compression twinning rotates the twinned domain by ~64° around a <1$\bar{1}$00> axis; {11$\bar{2}$4} compression twinning rotates the twinned domain by ~77° around a <1$\bar{1}$00> axis, with respect to the parent. The meaning of the colors that indicate specific twin boundaries is shown in Fig. 3.2b. We statistically analyzed the next-neighbor grain-to-grain misorientation (Fig. 3. 2c). The peaks at ~35° and ~64° are attributed to the formation of {11$\bar{2}$1} and {11$\bar{2}$2} twins, respectively. The {11$\bar{2}$4} compression twins do not produce an obvious peak at ~77° due to their small volume fraction. The maximum

peak at ~87° is associated with {10$\bar{1}$2} extension twins. {10$\bar{1}$2} twins are activated either as primary twin in grain (G1 in Fig. 3. 2b) or as secondary twin associated with {11$\bar{2}$2} → {10$\bar{1}$2} double twinning (G2 in Fig. 3. 2b) and {11$\bar{2}$1} twin-twin junction → {10$\bar{1}$2} twinning (G3 in Fig. 3. 2b and d). {11$\bar{2}$2} compression twins are either only one twin variant in grains (G4 in Fig. 3. 2b) or coexistent with secondary {10$\bar{1}$2} extension twin (G2 in Fig. 3. 2b). {11$\bar{2}$1} extension twins in grains are either as single twin variant (G5 in Fig. 3. 2b), coexistent with {10$\bar{1}$2} extension twin (G6 in Fig. 3. 2b) or associated with two variants interaction (G3 in Fig. 3. 2b). The interesting finding is that the interaction between two {11$\bar{2}$1} extension twins stimulates new {10$\bar{1}$2} twins.

3.2.3 Crystallographic character

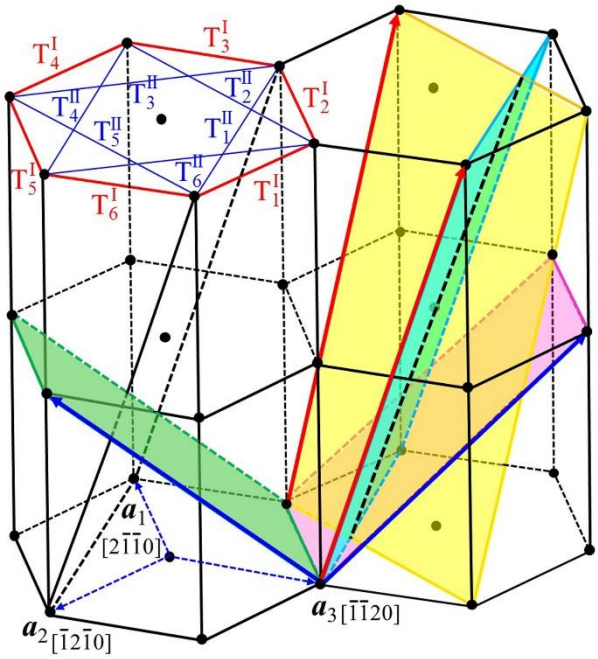

Fig. 3. 3 The crystallography of twins in hexagonal structure. Four shadow planes are twin planes associated with two {11$\bar{2}$1} twins, T_1^{II} (light green) and T_2^{II} (yellow), and two {10$\bar{1}$2} twins T_2^I (pink) and T_5^I (green). Two red arrows indicate the twinning shear directions of {11$\bar{2}$1} twins, and the blue arrows represent the twinning shear directions of {10$\bar{1}$2} twins.

In hexagonal structure, 12 rotational symmetry matrices result in 6 equivalent variants for each twinning system. We denote twin variants in Fig. 3. 3 as T_i^I for six {10$\bar{1}$2} twin variants and T_i^{II} for six {11$\bar{2}$1} twin variants where i =1…6. The subscript *i* increases by a counter-clockwise rotation around the *c*-axis of the crystal. The zone axis <10$\bar{1}$0> associated with a T_i^{II}

twin variant is the vector summation of two zone axes $\frac{1}{3}$<11$\bar{2}$0> associated with T_i^I and T_{i+1}^I twins. The red and blue arrows indicate the twinning directions of the two twins.

To characterize the {10$\bar{1}$2} twin variant stimulated by {11$\bar{2}$1} TTJ, the EBSD pattern in Fig. 3.4a was acquired at a step size of 0.2 μm. The next-neighbor grain-to-grain misorientation is depicted in Fig. 3. 4b. The peaks at ~35° and ~90° are attributed to the formation of {11$\bar{2}$1} and {10$\bar{1}$2} twins, respectively. As signed by white arrows in Fig. 3. 4a, many twin-twin junctions appear and other twins meet the twin-twin junctions.

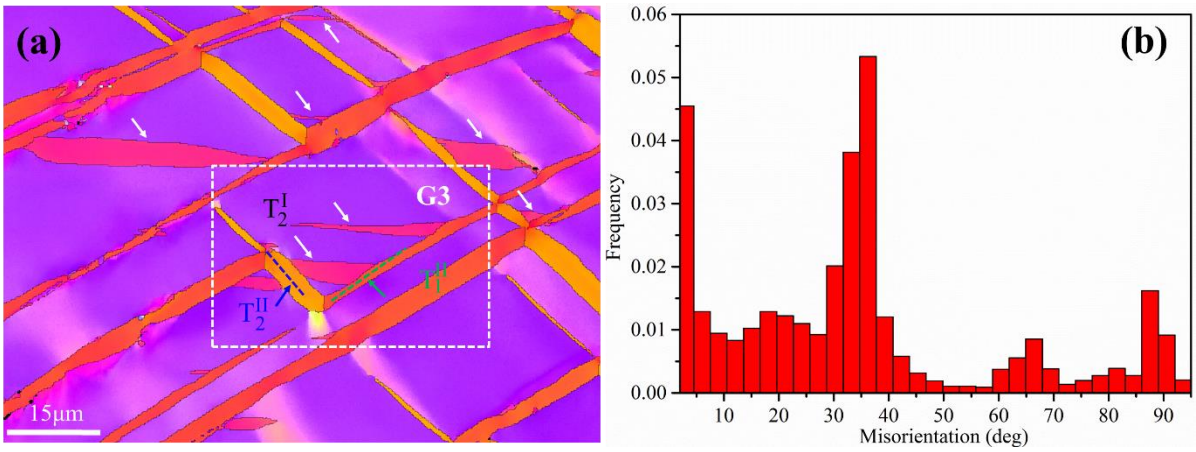

Fig. 3. 4 (a) EBSD characterization of {10$\bar{1}$2} twins and {11$\bar{2}$1} twin-twin junctions, (b) the next-neighbor grain to grain misorientation of (a).

A typical case of a twin intersecting a twin-twin junction is labelled by a white box in Fig. 3. 4a. In order to identify the twin variants, six {11$\bar{2}$1} planes in the matrix and in the twin are plotted into the pole figure corresponding to the orientation of the observed grain (Fig. 3. 5a). The misorientation angle between (11$\bar{2}$1) plane in T_1^{II} twin and in the matrix is 1.05°, and the misorientation angle between ($\bar{1}$2$\bar{1}$1) plane in T_2^{II} twin and the matrix is 2.06°. Thus the two primary twin variants are ($\bar{1}$2$\bar{1}$1)[1$\bar{2}$16] (T_2^{II}) and (11$\bar{2}$1)[$\bar{1}\bar{1}$26] (T_1^{II}). The sequential extension twin variant is determined according to the pole figures of {10$\bar{1}$2} twin planes and of <$\bar{1}$011> twin directions. The misorientation angle between (01$\bar{1}$2) planes in the twin and in the matrix is 0.23°, and between (0$\bar{1}$12) twin planes in the twin and in the matrix is 10.08°, as shown in Fig. 3. 5b. The misorientation angle between [0$\bar{1}$11] directions in the T_2^I twin and the matrix is 1.04°, and that between [01$\bar{1}$1] directions in the T_5^I and in matrix is 10.03° as shown in Fig. 3. 5c. According to the crystallography of {10$\bar{1}$2}<$\bar{1}$011> twins, twin variant (01$\bar{1}$2)[0$\bar{1}$11] (T_2^I) is a good fit. The red, green and black dashed lines in Fig. 3. 4a and b indicate the traces of the

three twin planes on the observed surface. The three twins hold a relation of $T_1^{II}T_2^{II} \rightarrow T_2^{I}$. Fig. 3. 5d shows the illustration of sequential twinning relations.

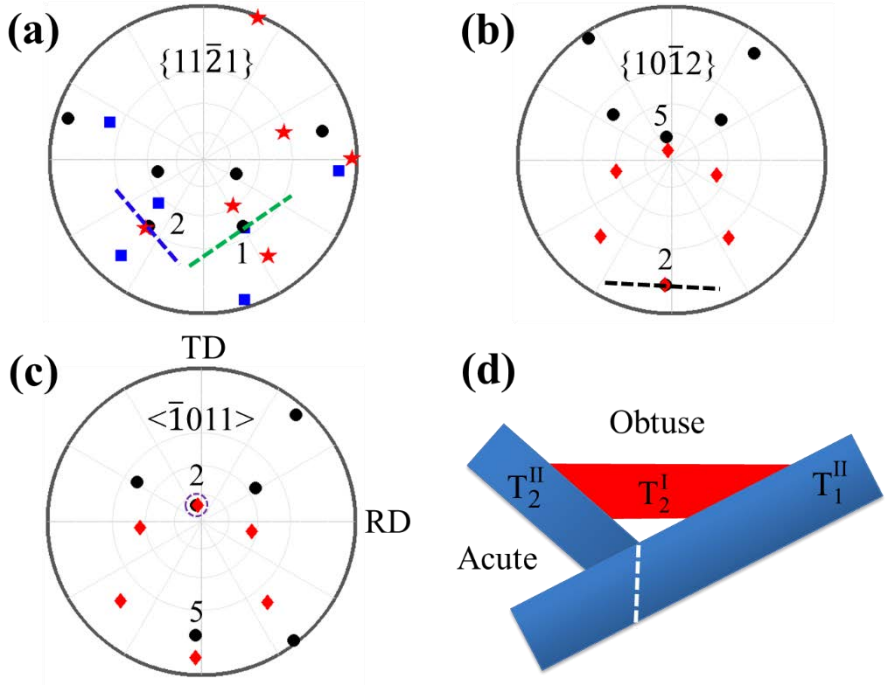

Fig. 3. 5 (a) The pole figure of (a) {11$\bar{2}$1} plane, (b) {10$\bar{1}$2} plane, (c) <$\bar{1}$011> direction with respect to the orientation of the observed grain as indicated by white box in Fig. 3. 4a. In (a), the black dots represent six {11$\bar{2}$1} twin planes in the matrix, the blue squares and red stars represent six {11$\bar{2}$1} twin variants in two twins. In (b), the black dots represent six {10$\bar{1}$2} twin planes in the matrix, the red diamonds represent six {10$\bar{1}$2} twin planes in the twin, and (c) the black dots represent six <$\bar{1}$011> twin directions in the matrix, the red diamonds represent six <$\bar{1}$011> twin directions in the twin, (d) Schematics of {11$\bar{2}$1} TT Junction → {10$\bar{1}$2} sequential twinning.

There are several geometry features associated with $T_1^{II}T_2^{II} \rightarrow T_2^{I}$ sequential twinning. The common axis between T_1^{II} and T_2^{II} is parallel to <0$\bar{1}$13> as indicated by a dashed line in Fig. 3. 5d. A twin-twin boundary (TTB) produced by the {11$\bar{2}$1} twin-twin junction is identified to lie in ($\bar{2}$110) plane in the grain with the assumption that the interface bisects two intersected twinning planes of T_1^{II} and T_2^{II} twins [135]. We conducted statistical analysis in our sample and identified 96 {10$\bar{1}$2} twins associated with 46 {11$\bar{2}$1} twin-twin junctions. The obvious TTB always forms in the obtuse corner between the two primary twinning planes and lie in {$\bar{2}$110} planes. They hold the relationship that T_i^{I} forms in the obtuse region between T_{i-1}^{II} and T_i^{II}, where the zone axis associated with T_i^{I} is a shared vector in describing the zone axis of the two primary twins. Thus such a sequential twinning mechanism can be described by $T_{i-1}^{II}T_i^{II} \rightarrow T_i^{I}$. To understand such a sequential twinning mechanism, we conduct the analysis of SF,

displacement gradient accommodation, and local stress fields, associated with the T_{i-1}^{II} and T_i^{II} junction. To confirm such a sequential twinning mechanism, we conducted quasi in-situ EBSD analysis by applying two steps of compression along the ND on a pre-polished sample. In the first step, a reduction of 6.2% was applied, followed by EBSD characterization with a step size of 0.2 μm as shown in Fig. 3. 6a.

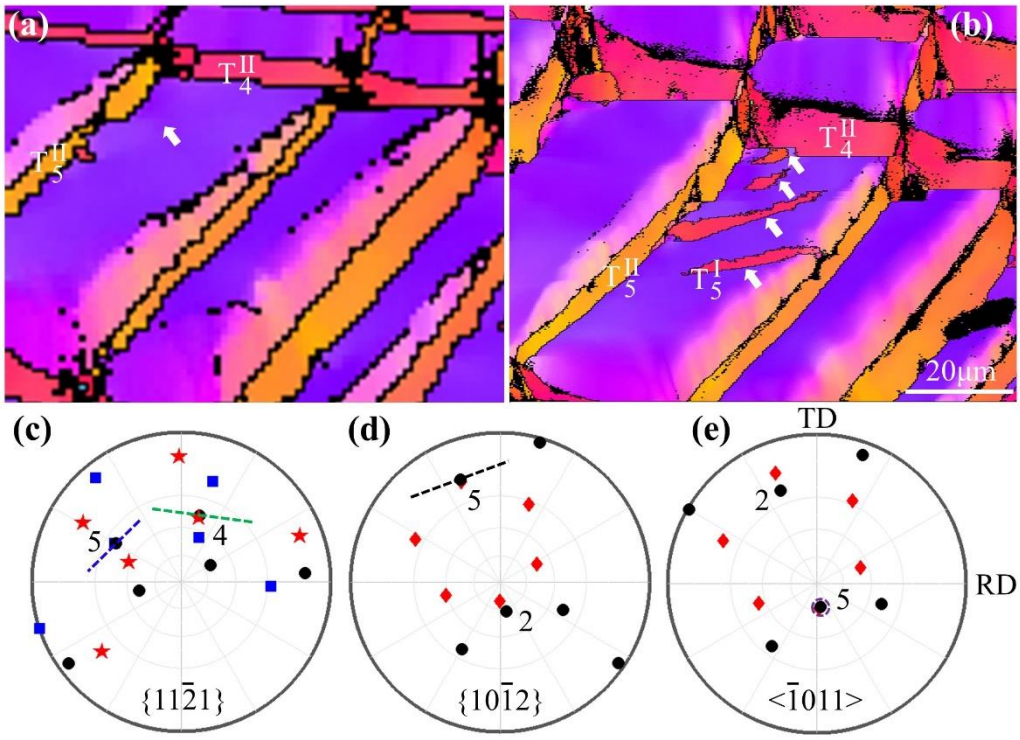

Fig. 3. 6 Quasi in-situ EBSD maps of {11$\bar{2}$1} twin-twin junctions and sequential {10$\bar{1}$2} twins with a reduction of: (a) 6.2%, (b) 9.5% as well as the pole figure of (c) {11$\bar{2}$1} plane, (d) {10$\bar{1}$2} plane, (e) <$\bar{1}$011> direction with respect to the orientation of the observed grain. In (c), the black dots represent six {11$\bar{2}$1} twin planes in the matrix, the blue squares and red stars represent six {11$\bar{2}$1} twin variants in two twins. In (d), the black dots represent six {10$\bar{1}$2} twin planes in the matrix, the red diamonds represent six {10$\bar{1}$2} twin planes in the twin, and (e) the black dots represent six <$\bar{1}$011> twin directions in the matrix, the red diamonds represent six <$\bar{1}$011> twin directions in the twin.

It can be seen that {11$\bar{2}$1} twin-twin junctions were generated in Fig. 3. 6a. Then, second step of compression was done with a further reduction of 3.3% along the same direction, followed by EBSD mapping on the same position. Fig. 3. 6b shows the EBSD pattern and the white arrows indicate that new {10$\bar{1}$2} twins were activated in the obtuse region. In order to identify the twin variants, six {11$\bar{2}$1} planes in the matrix and in the twin are plotted into the pole figure corresponding to the orientation of the observed grain. The misorientation angle between ($\bar{1}\bar{1}$21) plane in T_4^{II} twin and in the matrix is 1.15°, and the misorientation angle

between (1$\bar{2}$11) plane in T_5^{II} twin and the matrix is 1.06°. Thus, the two primary twin variants are ($\bar{1}\bar{1}$21)[11$\bar{2}$6] (T_4^{II}) and (1$\bar{2}$11)[$\bar{1}$2$\bar{1}$6] (T_5^{II}). Dashed lines in Fig. 3. 6c mark the traces of the two twin planes. The sequential {10$\bar{1}$2} extension twin variant is determined according to the pole figures of {10$\bar{1}$2} planes in Fig. 3. 6d and of <$\bar{1}$011> twin directions in Fig. 3. 6e. The misorientation angle between (0$\bar{1}$12) planes in the twin and in the matrix is 0.96°, and between (01$\bar{1}$2) twin planes in the twin and in the matrix is 6.16°, as shown in Fig. 3. 6d. The misorientation angle between <01$\bar{1}$1> directions in the T_5^I twin and the matrix is 1.04°, and that between <0$\bar{1}$11> directions in the T_2^I and in matrix is 6.95° as shown in Fig. 3. 6e. According to the crystallography of {10$\bar{1}$2}<$\bar{1}$011> twins, twin variant (0$\bar{1}$12)[01$\bar{1}$1] (T_5^I) is a good fit. The SF of T_4^{II} and T_5^{II} twins in Fig. 3.6a is 0.424 and 0.369, respectively. They carry the highest and second highest SF among six {11$\bar{2}$1} variants. The SF of active T_5^I and absent T_2^I in Fig. 3.6b is 0.277 (the second highest) and 0.345 (the highest), respectively. The three twins hold a relation of $T_4^{II}T_5^{II} \rightarrow T_5^I$.

3.2.4 Selection criteria for {10$\bar{1}$2} twinning stimulated by {11$\bar{2}$1} TTJ

3.2.4.1 Location selection of sequential twins

Why the sequential twin always presents in the obtuse region is firstly examined according to stress fields due to the two primary twins using finite element method (FEM). In the FEM model shown in Fig. 3. 7a, two {11$\bar{2}$1} twin domains T_1^{II} and T_2^{II} were embedded in a 40*40*8 matrix through the thickness along the z-axis in the model. In order to conveniently analyze the resolved shear stress on twin planes associated with sequential twinning, the matrix adopts the coordinates with the x-axis along [1$\bar{2}$10], the y-axis normal to ($\bar{3}$032) and the z-axis along [$\bar{1}$01$\bar{3}$]. The z direction is parallel to the intersection line of T_1^{II} and T_2^{II} twin planes. Correspondingly, the trace of the twin plane associated with the sequential twin variant T_2^I or T_5^I is parallel to the x-axis or the y-axis. Two twins have an elliptical shape in the cross-sectional plane along the z-axis. For T_1^{II} twin, the long axis was 22.7 μm and short axis was 3.7 μm. For T_2^{II} twin, the long axis was 15.8 μm and the short axis was 3.1 μm. Anisotropic elastic modulus was assigned into the three regions corresponding to the local orientation [171]. Eigenstrains that mimic the corresponding twinning shear were applied to two twin domains. The model was meshed with 127328 hexahedron elements for better accuracy. To obtain the feature of the elastic stress field, here we conducted linear elastic calculation with free boundaries while ignoring plasticity relaxation associated with slips or twins in the matrix. A thin slice in the

middle of the model depicted in Fig. 3. 7a was chosen for the analysis of back-stress that is caused by the two primary twins. Due to the near 90 degrees between the two twin planes associated with twin variants T_2^I and T_5^I, the resolved shear stress associated with T_2^I and T_5^I twins are approximately same. We only show the resolved shear stress field associated with twin variant T_2^I in the matrix in Fig. 3. 7b. Fig. 3. 7c shows the variation of the resolved shear stress along two directions in the acute and obtuse region. The result shows that the resolved shear stress associated with twin variants T_2^I and T_5^I are negative, i.e., opposite to the twin shear direction. However, the resolved shear stress due to the back-stress is smaller in the obtuse region than in the acute region. Under an applied stress, the net resolved shear stress in the obtuse region is thus greater than that in the acute region, favoring sequential extension twinning in the obtuse region. However, the stress analysis could not identify the twin variant between T_2^I and T_5^I.

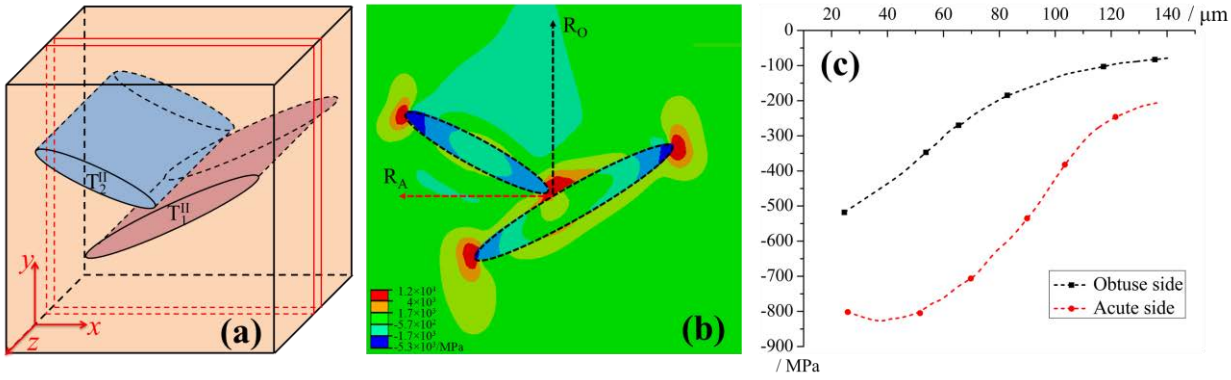

Fig. 3. 7 (a) Schematic of the FEM model. (b) Resolved shear stress fields associated with twin variants T_2^I and T_5^I in the matrix. (c) The variation of the resolved shear stress (MPa, in the vertical axis) along two directions Ro and R_A (μm, in the horizontal axis). The resolved shear stress is caused by the back-stress due to the TT junction.

3.2.4.2 SF analysis

Corresponding to crystallography of twins in Fig. 3. 4a, SFs associated with T_5^I and T_2^I twins are found to be 0.277 and 0.201, respectively. T_5^I and T_2^I variants carry the highest and second highest SF, but the second high SF twin T_2^I was only activated without the presence of T_5^I variant. There is a question whether the activated twin variant is always associated with the second high SF among six twin variants. Without loss of generality, an apparent SF analysis is conducted under uniaxial compressive stresses that favor two primary twins T_{i-1}^{II} and T_i^{II} among six {11$\bar{2}$1} twin variants. All loading directions that satisfy this condition are grouped into one loading domain (referred to as the $T_{i-1}^{II}T_i^{II}$ loading domain). An apparent SF analysis

in Fig. 3. 8a shows the $T^{II}_{i-1}T^{II}_{i}$ loading domain in which the T^{II}_{1} and T^{II}_{2} twins are subjected to the highest and secondary higher SF among six {11$\bar{2}$1} twin variants. The red means that both twins have SFs near 0.5, orange and pink mean that the SF of one twin is close to 0.5. We also checked our samples and found that the loading acting on the grain that have two {11$\bar{2}$1} twin variants is in the loading domain. The black pentagram in Fig. 3. 8a indicates the loading direction of the grain G3 along [0.0501, 0.4705 $\overline{0.5206}$, $\overline{0.3197}$]. Secondly, we calculate SFs associated with six T^{I}_{i} twins as the grain is subjected to uniaxial compression within the $T^{II}_{i-1}T^{II}_{i}$ loading domain. Due to the approximate 90 degrees between the twin planes of T^{I}_{i} and T^{I}_{i+3}, a pair of T^{I}_{i} and T^{I}_{i+3} is subjected to the same resolved shear stress. Fig. 3. 8b, c and d show the SFs associated with T^{I}_{1} and T^{I}_{4}, T^{I}_{2} and T^{I}_{5}, and T^{I}_{3} and T^{I}_{6}, respectively. The blue color represents negative SFs, and red represents positive SFs. The SFs associated with T^{I}_{2} and T^{I}_{5} are always greater than that for other two pairs, implying that T^{I}_{2} and T^{I}_{5} are mechanically preferred if sequential twinning occurs.

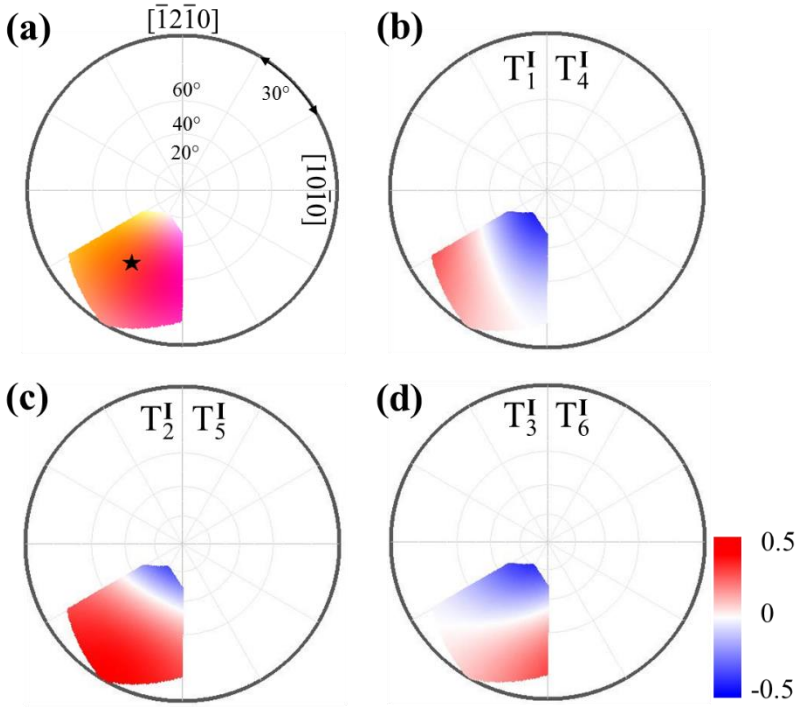

Fig. 3. 8 Inverse pole figures of the Schmid factor of twinning systems subjected to compression: (a) the loading domain in which SFs of T^{II}_{1} and T^{II}_{2} twins are positive and are greater than other four equivalent variants. Under this loading domain, the SF associated with sequential twin variants (b) T^{I}_{1} and T^{I}_{4}, (c) T^{I}_{2} and T^{I}_{5}, and (d) T^{I}_{3} and T^{I}_{6}. The blue color represents negative SFs, and red represents positive SFs (shown by the colorbar).

However, the result does not determine the preference between two variants T^{I}_{2} and T^{I}_{5}. We further compare the SFs associated with the two twin variants and find that the SF

associated with T_5^I is always higher than that associated with T_2^I for any applied compression in the loading domain, except only one specific loading direction along [0$\bar{1}$10] direction, under which T_2^I and T_5^I have the largest and identical SF as listed in Table 3.2 (Spe. SFs). This is contradictory to the EBSD analysis where T_2^I always occurs. Therefore, the apparent SF analysis can determine the group of sequential twins, but cannot help determine the sequential twin variant.

3.2.4.3 Deformation gradient accommodation

From elastic deformation view, the same shear strain may be associated with different crystal rotation that depends on displacement gradients. Corresponding to the simple shear model associated with twinning, we calculate the deformation gradient caused by T_1^{II} and T_2^{II} twinning. The displacement gradient tensor of a twin has a simple form in the twinning system frame, i.e., x || the twinning shear direction ($\boldsymbol{\eta}$), z || the normal of the twin plane ($\boldsymbol{n}$), and y || the zone axis ($\boldsymbol{\lambda} = \boldsymbol{n} \times \boldsymbol{\eta}$) [13]. The displacement gradient tensor can be written as

$$E_{ij} = \begin{bmatrix} 0 & 0 & s \\ 0 & 0 & 0 \\ 0 & 0 & 0 \end{bmatrix} \tag{3-1}$$

In this equation, s = 0.63 for {11$\bar{2}$1} twinning (c/a = 1.587) in α-titanium. In order to examine whether the strain induced by the {11$\bar{2}$1} twin can be accommodated by slips and/or other twins in the grain, the displacement gradient tensors of the intersected {11$\bar{2}$1} twins were expressed into the crystal orthonormal frame of the grain, i.e., x'|| [10$\bar{1}$0], y'|| [$\bar{1}$2$\bar{1}$0], z'|| [0001]. $E_{x'z'}$ and $E_{y'z'}$ represent the accommodation by double and single basal slips, respectively; $E_{z'x'}$ and $E_{z'y'}$ indicate the accommodation by twinning; $E_{x'y'}$ and $E_{y'x'}$ are associated with the accommodation by double and single prismatic slips, respectively [13]. For the two primary twins, the obtained displacement gradient tensors are

$$E_{ij}(T_1^{II}) = \begin{pmatrix} -0.135 & -0.078 & -0.049 \\ -0.078 & -0.045 & -0.028 \\ 0.496 & 0.287 & 0.181 \end{pmatrix} \tag{3-2}$$

$$E_{ij}(T_2^{II}) = \begin{pmatrix} 0 & 0 & 0 \\ 0 & -0.181 & -0.057 \\ 0 & 0.573 & 0.181 \end{pmatrix} \tag{3-3}$$

$E_{z'x'}$ and $E_{z'y'}$ have big value, implying that dislocation slips could not efficiently accommodate the displacement gradients, instead, extension twinning corresponding to the positive $E_{z'z'}$ could accommodate them.

We thus evaluate the accommodation capacity of six {10$\bar{1}$2} extension twin variants and other four {11$\bar{2}$1} extension twin variants. The displacement gradient tensors of the activated {11$\bar{2}$1} twins were expressed into the twinning reference frames of {10$\bar{1}$2} variants and {11$\bar{2}$1} variants, respectively. As summarized in Table 3.2, four {11$\bar{2}$1} twin variants do not accommodate the displacement gradient component due to the negative sign. The variant T_2^I has the largest E_{13} among six {10$\bar{1}$2} and four {11$\bar{2}$1} twins, implying that T_2^I twin variant can effectively accommodate the displacement gradient component generated by the two {11$\bar{2}$1} primary twins. T_5^I twin with the highest SF does not accommodate the displacement gradient component because of the negative sign. Other twin variants, T_1^I and T_3^I, can accommodate the displacement gradients, while they often have small SFs, and even negative SFs (Table 3.2). Thus, the combination of SF and displacement gradient accommodation criteria assures the relation of $T_{i-1}^{II} T_i^{II} \rightarrow T_i^I$.

Table 3.2 The expression of displacement gradient tensor of T_1^{II} and T_2^{II} twins into the twinning reference frames of six {10$\bar{1}$2} extension twin variants and other four {11$\bar{2}$1} extension twin variants in the same grain as well as the SFs under macro loading (Exp. SFs) and the SFs under a specific loading along [0$\bar{1}$10] direction (Spe. SFs). The bold fond indicates positive and greater SFs.

Twin variants	Six {10$\bar{1}$2} variants						Four {11$\bar{2}$1} variants			
	T_1^I	T_2^I	T_3^I	T_4^I	T_5^I	T_6^I	T_3^{II}	T_4^{II}	T_5^{II}	T_6^{II}
	(10$\bar{1}$2) [$\bar{1}$011]	(01$\bar{1}$2) [0$\bar{1}$11]	($\bar{1}$102) [1$\bar{1}$01]	($\bar{1}$012) [10$\bar{1}$1]	(0$\bar{1}$12) [01$\bar{1}$1]	(1$\bar{1}$02) [$\bar{1}$101]	($\bar{2}$111) [2$\bar{1}\bar{1}$6]	($\bar{1}\bar{1}$21) [11$\bar{2}$6]	(1$\bar{2}$11) [$\bar{1}$2$\bar{1}$6]	(2$\bar{1}\bar{1}$1) [$\bar{2}$116]
Spe. SFs	0.125	**0.498**	0.125	0.125	**0.498**	0.125	0	0.215	0.215	0
Exp. SFs	-0.029	**0.201**	-0.078	0.015	**0.277**	-0.046	-0.103	-0.224	-0.225	-0.041
T_1^{II} (11$\bar{2}$1) [$\bar{1}\bar{1}$26]	0.41	**0.41**	0.09	-0.10	-0.10	0.09	-0.20	-0.42	-0.20	0.33
T_2^{II} ($\bar{1}$2$\bar{1}$1) [1$\bar{2}$16]	0.09	**0.41**	0.41	0.09	-0.10	-0.10	0.33	-0.20	-0.42	-0.20

3.2.5 Summary

We experimentally studied sequential twinning in rolled pure titanium at room temperature, and identified a new sequential twinning mechanism that {10$\bar{1}$2} (T_i^I) extension twins were stimulated by the primary {11$\bar{2}$1} (T_i^{II}) twin-twin junctions (TTJ). This new sequential twinning mechanism was confirmed by using quasi in-situ EBSD, which was achieved by applying two steps of compression along the ND on a pre-polished sample. Among 96 cases of detected {11$\bar{2}$1} TTJ → {10$\bar{1}$2} twinning, EBSD analysis reveals that the three

extension twins hold a relation of $T_{i-1}^{II} T_i^{II} \rightarrow T_i^I$. Besides, T_i^I is always formed in the obtuse region between two primary {11$\bar{2}$1} twin planes. Corresponding to the crystallography of twins, six twin variants T_i^I are classified into three groups because of the same SF for a pair of twins T_i^I and T_{i+3}^I. An apparent SF analysis in the loading domain where the two primary twins are mechanically preferred was performed to select sequential twins. The results show that the SF analysis made the correct choice for group, but wrong for twin variant in the group. Displacement gradient accommodation analysis correctly selected the twin variant in the group which is determined by the SF analysis. When the local stress associated with twin-twin interactions is taken into account for twin nucleation, the location of sequential twin is well predicted in the obtuse region.

3.3 Accommodative {10$\bar{1}$2} twins at high angle grain boundaries

3.3.1 Introduction

Recently, a {10$\bar{1}$2}<$\bar{1}$011> extension twin in one grain stimulating the generation of another {10$\bar{1}$2}<$\bar{1}$011> twin in a neighboring grain was widely reported in Mg [172, 173] and α-titanium [48]. These two {10$\bar{1}$2} twins forming an intersection at grain boundaries (GBs) were defined as twin pairs, which were found to generally appear at low angle GBs. In pure titanium, {11$\bar{2}$2} contraction twins and {10$\bar{1}$2}<$\bar{1}$011> extension twins were the most commonly found twin modes [87, 100, 174]. Secondary {10$\bar{1}$2}<$\bar{1}$011> extension twins were reported to usually form in {11$\bar{2}$2} contraction twins [86, 175]. By tension along the RD, incompatibility induced by slip in neighboring grains can cause twin formation [53]. Primary twins requiring the accommodation strain from basal glide, pyramidal glide and twinning were reported to be absent [87]. However, in the present study, a {11$\bar{2}$2} twin in one grain accommodated by a {10$\bar{1}$2} twin in an adjacent grain was discovered in rolled pure titanium deformed by compression along the ND. The activity of prismatic slip is not favored under this deformation. The conditions are discussed that produce these adjoined {10$\bar{1}$2} twins stimulated by the neighboring {11$\bar{2}$2} twins, which is meaningful for simulation work to consider these factors.

3.3.2 Experiment details

In this section, rectangle samples from a rolled commercially pure titanium T40 sheet were annealed in a vacuum furnace at 700 ºC for 1 h producing a fully recrystallized microstructure. Compressive strain of 18% was applied along the ND at a strain rate of

$1\times10^{-3}s^{-1}$ using a Zwick 120T machine. Then, sample preparations for electrolytic polishing and EBSD characterizations were conducted according to the procedure in Section 3.2.1.

3.3.3 Microstructure evolution

Fig. 3.9a presents the microstructure of the initial material in form of EBSD inverse pole figure, where the ND axis is projected. A tolerance of ±5° deviation from the axis and the angle was considered in all EBSD maps. The material was obtained with an average grain size of ~18μm and no twins appear. Fig. 3.9b displays the texture of the material in {0002}, {11$\bar{2}$2} and {10$\bar{1}$2} pole figures from Fig. 3.9a. A typical texture of a rolled titanium sheet was achieved with the *c*-axes oriented ±40° from the ND towards the TD. It can be noticed that the grain size obtained here is much smaller than that in Fig. 3. 1.

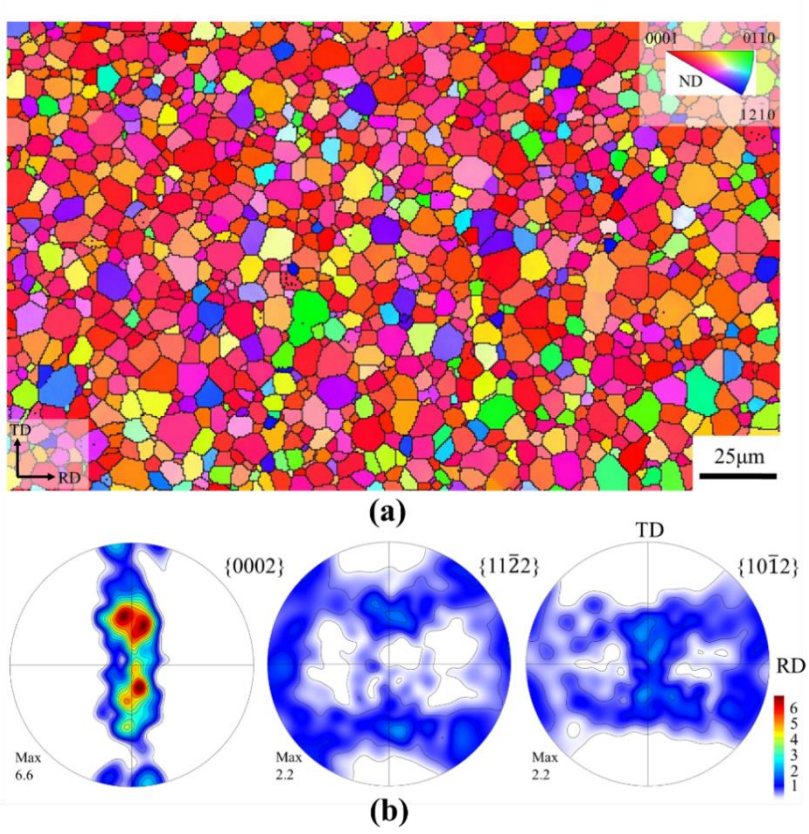

Fig. 3. 9 (a) Microstructure of the initial sample, (b) {0002}, {11$\bar{2}$2} and {10$\bar{1}$2} pole figures from (a).

In Fig. 3. 10a, a typical EBSD pattern on a sample by 18% compression along the ND was acquired at a step size of 0.5 μm, indicating the detection of many twins. The next-neighbor grain-to-grain misorientation is depicted in Fig. 3.10b. The peaks at ~90° and ~65° are attributed to the formation of {10$\bar{1}$2} and {11$\bar{2}$2} twins, respectively. As signed by a white box in Fig. 3. 10a, a twin adjoining another twin at grain boundaries can be seen. In order to obtain

detailed information of the adjoined twins at grain boundaries, the area indicated with a white box in Fig. 3. 10a was further scanned at a step size of 0.2 μm, which is presented in Fig. 3. 11. Three examples of twin transmission consisting of a {11$\bar{2}$2} twin and a {10$\bar{1}$2} twin at the grain boundary are marked with white boxes in Fig. 3. 11b, where the {11$\bar{2}$2} compression twin boundaries with a rotation angle of 64° around a <1$\bar{1}$00> axis are painted green while the {10$\bar{1}$2} extension twin boundaries in red with a rotation angle of 87° around a <11$\bar{2}$0>. The {11$\bar{2}$2} twins traverse the entire grain while the {10$\bar{1}$2} twins terminate within the grain interior. Besides, the former twin also has an obviously larger volume than the latter one. It is reasonably assumed that the {11$\bar{2}$2} twins form first while the {10$\bar{1}$2} twins are generated subsequently. The twin variants are identified by trace analysis and the SF is calculated. In addition, a {11$\bar{2}$2} twin (lamella 6) intersecting another {11$\bar{2}$2} twin (lamella 10) can also be seen in Fig. 3.11b, which is similar as {10$\bar{1}$2} twin pairs reported to occur at low angle GBs [48, 172, 176].

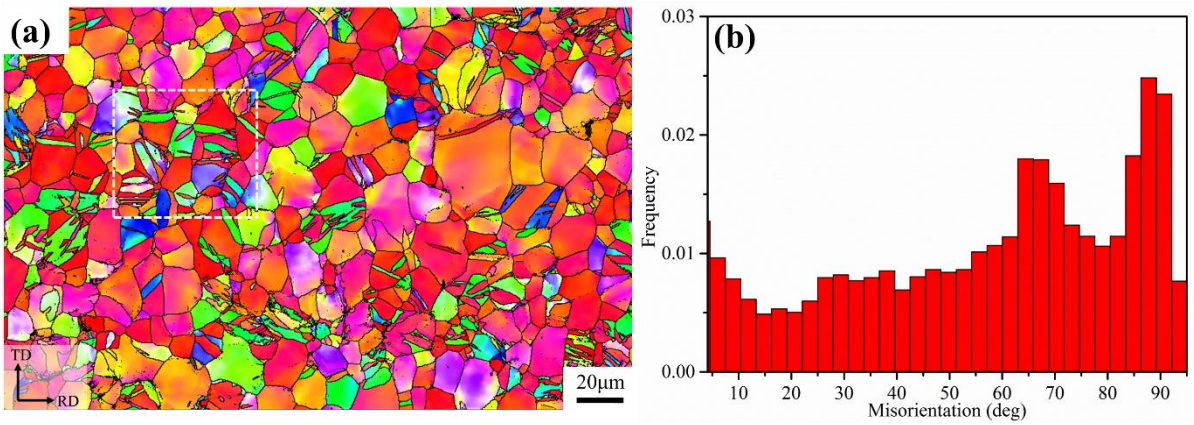

Fig. 3. 10 (a) A typical EBSD pattern of the deformed material, (b) the next-neighbor grain to grain misorientation of (a).

A typical twin transmission is shown in region A in Fig. 3. 11b. Areas 1 and 3 are parent grains. Lamella 2 (4) is a {11$\bar{2}$2} twin ({10$\bar{1}$2} twin) inside grain 1 (3). The pole figure in Fig. 3. 12a illustrates that the basal pole of grain 1 lies in the centre. Lamella 2 with its basal pole near the edge of the pole figure is rotated from the centre by {11$\bar{2}$2} twinning. The {0002} pole of grain 3 largely deviates from the ND. As a result of {10$\bar{1}$2} twinning, lamella 4 forms in grain 3 with *c*-axis aligned in the centre. The active {11$\bar{2}$2} and {10$\bar{1}$2} twinning planes are indicated with a black circle in the {11$\bar{2}$2} pole figure and with a red circle in the {10$\bar{1}$2} pole figure, respectively. The same label is used to display the <$\bar{1}$011> twinning directions. As outlined with a dashed green square in the {10$\bar{1}$2} pole figure, the {10$\bar{1}$2} variant whose twinning plane aligns most closely with that of the observed {11$\bar{2}$2} is not activated. The

criterion for the variant selection of previously-formed twins was proposed by considering the deformation energy [147, 148]. Their formation modifies the local stress to be different from the applied one [177, 178] and stimulates {10$\bar{1}$2} twinning in the neighbors.

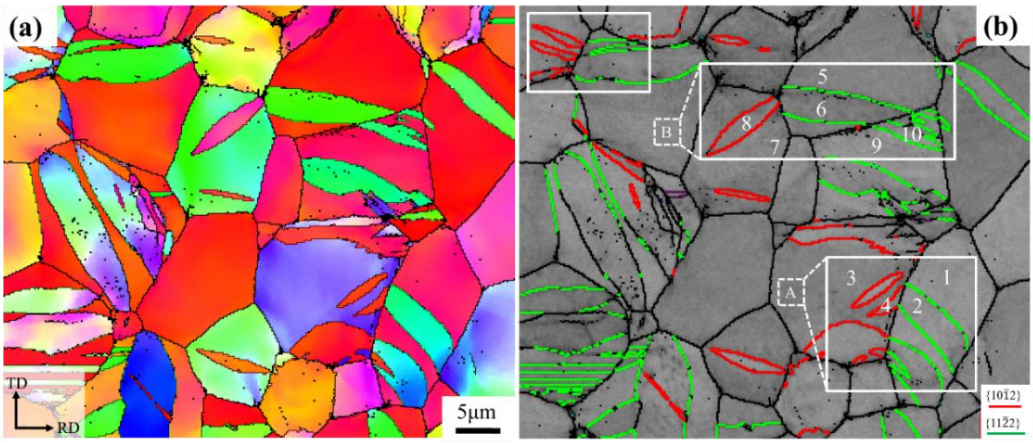

Fig. 3. 11 An EBSD map obtained on a sample after a reduction of 18% along the ND using a step size of 0.2 μm.

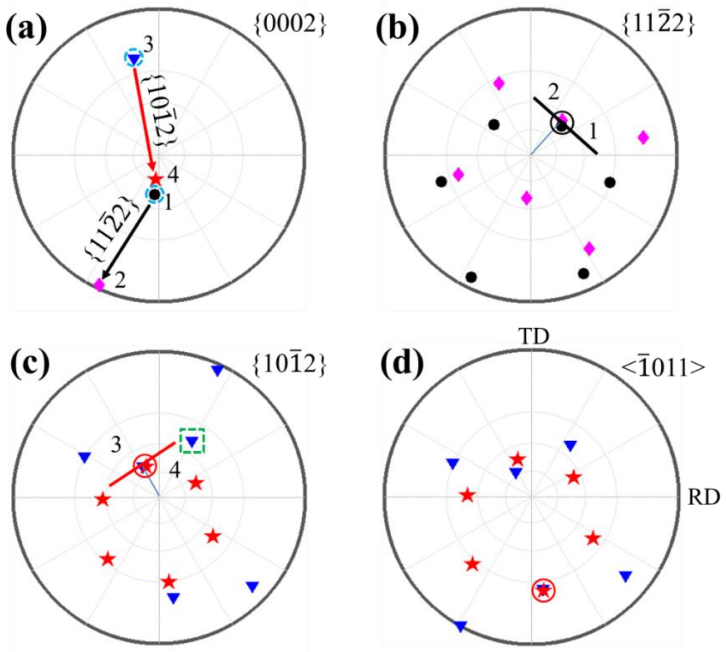

Fig. 3. 12 Pole figures of {0002},{11$\bar{2}$2}, {10$\bar{1}$2} planes, and <$\bar{1}$011> directions associated with the region A in Fig. 3. 11b. In the pole figure, black, pink, blue and red represent grain 1, {11$\bar{2}$2} in grain 1, grain 3 and {10$\bar{1}$2} twin in grain 3, respectively. The black line in (c) and red line in (d) represents the trace of the corresponding twinning plane in the (a).

3.3.4 Character of twin transmission

In all the EBSD patterns, 6300 grains are contained. There are 1272 primary {11$\bar{2}$2} twins and 432 primary {10$\bar{1}$2} twins detected without considering those twins intercepted by the

EBSD scanning border. The GB and basal pole misalignments of the neighboring grains where twin pairs consisting of a {11$\bar{2}$2} twin and a {10$\bar{1}$2} twin are detected are illustrated in Fig. 3. 13. It can be seen that these twin pairs frequently occur at high angle GBs and the highest peak appears near 90°.

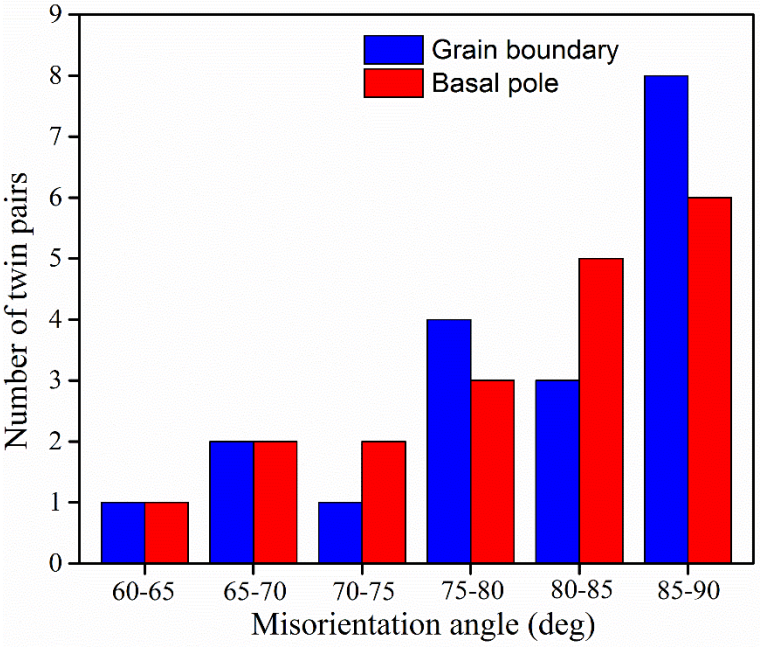

Fig. 3. 13 GB and basal pole misalignments of the neighboring grains containing twin transmission.

3.3.5 Criterion for twin transmission

In order to determine the {10$\bar{1}$2} twin variant in the neighboring grain stimulated by the {11$\bar{2}$2} twinning, SFs of the {10$\bar{1}$2} twins are first evaluated. Besides, the displacement gradient tensor of the detected {11$\bar{2}$2} twins is expressed into the twinning reference frames of six potential {10$\bar{1}$2} twin variants in the adjacent grain. In the obtained tensor E_{ij}, the E_{13} component is considered to evaluate the accommodation ability of each {10$\bar{1}$2} variant. The external compression along the ND results in the external strain of the sample with negative ND and positive RD (TD) components. The contribution of the possible {10$\bar{1}$2} variants to the external strain is evaluated by expressing their displacement gradient tensors into the sample frame (E_{33}).

3.3.5.1 SF analysis

Table 3.3 shows the SFs of the possible {10$\bar{1}$2} twins in the grain 3. It reveals that the active extension twin variant in the grain 3 has the highest SF. A SF analysis of the observed 19 twin pairs is shown in Fig. 3. 14. Not all active {10$\bar{1}$2} twins have the highest SFs. There

are 9 {10$\bar{1}$2} twins (47.4%) carrying low SFs in the 19 detected twin pairs. It can be noticed that two variants with negative SFs are even activated. They expose opposite contribution to the external strain and are not favored by the macroscopic stress. Therefore, the classical SF criterion cannot govern the selection of these {10$\bar{1}$2} twin variants.

Table 3.3 Possible {11$\bar{2}$2} twin variants in grain 1 (Euler angles: φ_1=173.99°, Φ=150.04°, φ_2=24.01°). Value E_{33} is obtained by the expression of the possible {10$\bar{1}$2} twin in grain 3 (Euler angles: φ_1=14.47°, Φ=111.1°, φ_2=38.85°) into the sample frame and E_{13} by the expression of the active {11$\bar{2}$2} twinning shear into possible {10$\bar{1}$2} twin variants in grain 3 (Euler angles: φ_1=13.75°, Φ=101.23°, φ_2=51.19°). The variant in bold is active.

{11$\bar{2}$2} twin variants in grain 1		{10$\bar{1}$2} twin variants in grain 3			
Twin variants	Schmid factor	Twin variants	Schmid factor	E_{33}	E_{13}
(11$\bar{2}$2)[11$\bar{2}\bar{3}$]	0.114	(10$\bar{1}$2)[$\bar{1}$011]	0.088	-0.015	-0.009
($\bar{1}$2$\bar{1}$2)[$\bar{1}$2$\bar{1}\bar{3}$]	0.074	($\bar{1}$102)[1$\bar{1}$01]	-0.019	0.003	-0.023
($\bar{2}$112)[$\bar{2}$11$\bar{3}$]	0.318	($\bar{1}$012)[10$\bar{1}$1]	0.124	-0.022	0.077
($\bar{1}\bar{1}$22)[$\bar{1}\bar{1}\bar{2}\bar{3}$]	0.416	(1$\bar{1}$02)[$\bar{1}$101]	0.002	0	0.053
(1$\bar{2}$12)[1$\bar{2}\bar{1}\bar{3}$]	**0.415**	(01$\bar{1}$2)[0$\bar{1}$11]	0.330	-0.058	0.001
(2$\bar{1}\bar{1}$2)[2$\bar{1}\bar{1}\bar{3}$]	0.357	**(0$\bar{1}$12)[01$\bar{1}$1]**	**0.388**	**-0.069**	**0.162**

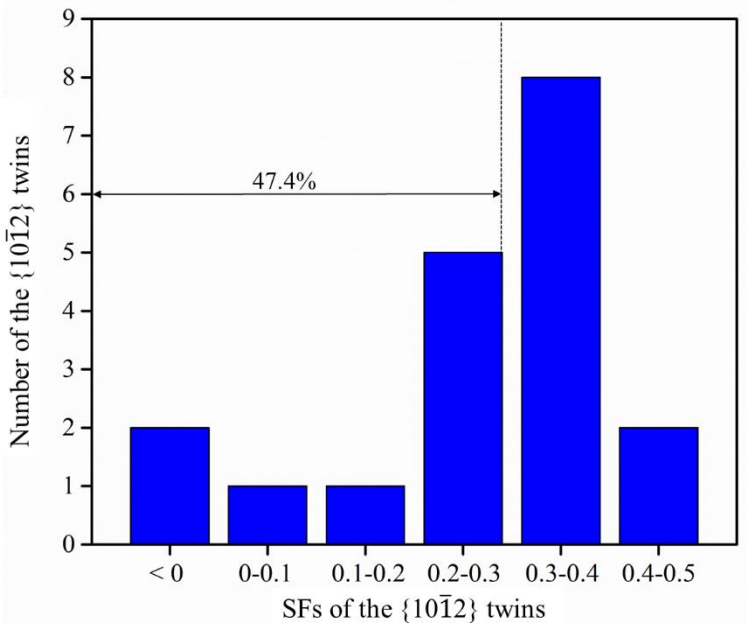

Fig. 3. 14 Schmid factors of the adjoined {10$\bar{1}$2} twins.

3.3.5.2 Displacement gradient accommodation

In order to consider the twinning effect on the external strain along the ND, the displacement gradient tensor of a twin expressed in its twinning frame was expressed into the sample frame and E_{33} component was used. Besides, the displacement gradient tensor of a twin expressed in its twinning frame was also expressed into the twinning system frames of possible adjoined twin variants in the neighboring grain for evaluating the accommodation ability of the potential adjoined twins and E_{13} component was taken.

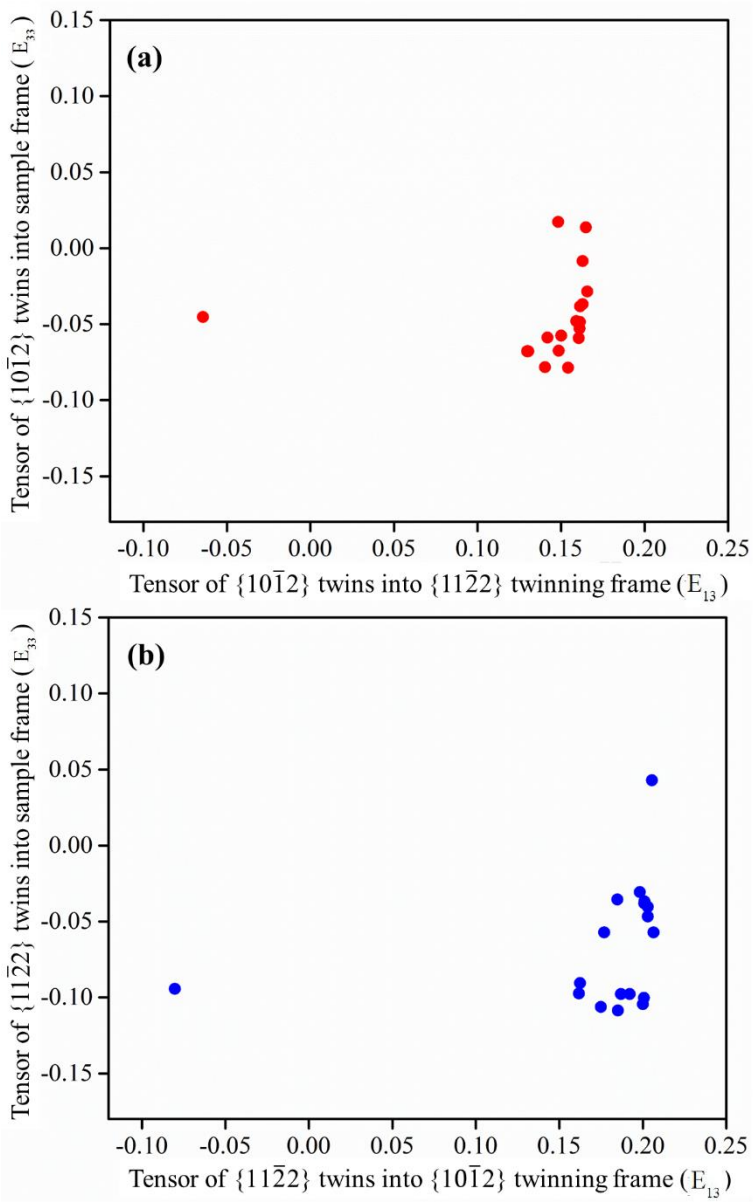

Fig. 3. 15 An analysis of the detected 19 twin pairs: (a) displacement gradient tensor of {11$\bar{2}$2} twins expressed into the sample frame and the twinning frame of adjoined {10$\bar{1}$2} twins, (b) displacement gradient tensor of {10$\bar{1}$2} twins expressed into the sample frame and the twinning frame of adjoined {11$\bar{2}$2} twins.

In Fig. 3. 15a, the E_{13} (the displacement gradient tensor of the active {10$\bar{1}$2} twins was expressed into the twinning reference frame of the {11$\bar{2}$2} twins in the neighboring grain) in

these twin pairs concentrates at the right side while E_{33} (the displacement gradient tensor of the active {10$\bar{1}$2} twins was expressed into the sample frame) varying between -0.1 and 0.05 exhibits large difference, revealing that the formation of some {10$\bar{1}$2} has little even negative contribution to the external strain. In Fig. 3. 15b, the expression of the displacement gradient tensor of the {11$\bar{2}$2} twins was done into the sample frame and the twinning reference frame of the adjoined {10$\bar{1}$2} twin variants. It can be noticed that the generation of {11$\bar{2}$2} twins in the 18 twin pairs tends to require the accommodation from the neighboring {10$\bar{1}$2} variant with the highest E_{13} among all the possibilities, even though the SFs of the active {10$\bar{1}$2} twins show that their orientations are not favorable for the activation and two accommodative {10$\bar{1}$2} twins are generated with negative SFs. Therefore, at these high angle GBs, the selection of the {10$\bar{1}$2} variants in the neighbouring grains is strongly determined by the accommodation ability of the potential {10$\bar{1}$2} variants rather than by the external stress. The {10$\bar{1}$2} variant with the largest E_{13} is favorably activated to accommodate the strain caused by the neighboring {11$\bar{2}$2} twins.

3.3.6 Discussion

As discussed above, Fig. 3. 15 shows an exception that there is an adjoined {10$\bar{1}$2} twin with negative E_{13} as labelled in Fig. 3. 11b (region B).

Table 3. 4 Possible {11$\bar{2}$2} twin variants in grain 5 (Euler angles: φ1=151.15°, Φ=8.54°, φ2=22.65°). Value E_{33} is obtained by the expression of the possible {10$\bar{1}$2} twin in grain 7 into the sample frame and E_{13} by the expression of the active {11$\bar{2}$2} twinning shear into possible {10$\bar{1}$2} twin variants in grain 7 (Euler angles: φ1=13.75°, Φ=101.23°, φ2=51.19°). The variant in bold is the active one.

{11$\bar{2}$2} twin variants in grain 5		{10$\bar{1}$2} twin variants in grain 7			
Twin variants	Schmid factor	Twin variants	Schmid factor	E_{33}	E_{13}
(11$\bar{2}$2)[11$\bar{2}\bar{3}$]	0.485	**(10$\bar{1}$2)[$\bar{1}$011]**	**0.259**	**-0.045**	**-0.080**
($\bar{1}$2$\bar{1}$2)[$\bar{1}$2$\bar{1}\bar{3}$]	0.491	($\bar{1}$102)[1$\bar{1}$01]	-0.010	0.002	0.015
($\bar{2}$112)[$\bar{2}$11$\bar{3}$]	0.449	($\bar{1}$012)[10$\bar{1}$1]	0.285	-0.050	0.100
($\bar{1}\bar{1}$22)[$\bar{1}\bar{1}$2$\bar{3}$]	0.384	(1$\bar{1}$02)[$\bar{1}$101]	-0.005	0	-0.024
(1$\bar{2}$12)[1$\bar{2}$1$\bar{3}$]	0.374	(01$\bar{1}$2)[0$\bar{1}$11]	0.382	-0.067	-0.020
(2$\bar{1}\bar{1}$2)[2$\bar{1}\bar{1}$3]	**0.433**	(0$\bar{1}$12)[01$\bar{1}$1]	0.413	-0.072	0.121

In Table 3.4, the active {10$\bar{1}$2} twin variant only has a moderate SF among the six possible variants. The expression of the detected {11$\bar{2}$2} displacement in grain 5 into six possible {10$\bar{1}$2} twinning frames in grain 7 illustrates that the accommodated {10$\bar{1}$2} variant does not have the largest E_{13} value while the variant that has the largest e_{13} value is absent. It seems this variant should not be favored in the variant selection according to the mechanism we proposed above. Actually, the detailed reason leading to the activation of such an unfavourable adjoined {10$\bar{1}$2} twin variant is not clear. This twin pair appears at the triple junction. It can be assumed that the local stress at triple junctions should determine the variant selection.

3.3.7 Summary

To be concluded, a {11$\bar{2}$2} compression twin adjoining a {10$\bar{1}$2} extension twin was investigated in rolled pure titanium subjected to compression along the ND. These twin pairs were observed at high angle GBs close to 90°. Classical SF analysis is invalid to explain the occurrence of some adjoined {10$\bar{1}$2} because they have low even negative SFs. Local accommodation mechanism is applied by expressing the displacement gradient tensor of the {11$\bar{2}$2} twins into the twinning reference frames of all potential {10$\bar{1}$2} twins in the neighboring grain. The results show that the shear induced by the {11$\bar{2}$2} twins can be accommodated by the active {10$\bar{1}$2} twins in the neighboring grains. Among all six possible {10$\bar{1}$2} twinning variants, the active {10$\bar{1}$2} twin is the one that has the largest capacity to accommodate the shear induced by the {11$\bar{2}$2} twins. The selection of the {10$\bar{1}$2} twin variants is dependent on the accommodation ability of the potential {10$\bar{1}$2} twin variants while it is not controlled by the external stress.

3.4 Chapter conclusion

In this chapter, we analysed the mechanism for two types of sequential {10$\bar{1}$2} primary twinning stimulated by other twins. Firstly, sequential {10$\bar{1}$2} (T_i^I) twinning was found to be stimulated by the twin-twin junction (TTJ) of two primary {11$\bar{2}$1} extension twins T_{i-1}^{II} and T_i^{II}, which holds a certain relation $T_{i-1}^{II}T_i^{II} \rightarrow T_i^I$ (referred to as {11$\bar{2}$1} TTJ $\rightarrow$ {10$\bar{1}$2}). The mechanism was investigated in terms of SF and displacement gradient accommodation. The SF analysis, as the local stress is taken into account, is able to determine the position of sequential twin variant, but cannot determine the twin variant in the group of twin variants. Displacement gradient accommodation is further used to determine the twin variant. Secondly, {10$\bar{1}$2} (T_i^I) extension twins stimulated by {11$\bar{2}$2} (C_i^I) compression twins in the neighboring

grain were detected. The twin pairs appear at grain boundaries with misorientation angles close to 90°. The mechanism accounting for the formation of these adjoined {10$\bar{1}$2} twins is examined in terms of SF and local displacement gradient accommodation, revealing that the selection of the stimulated {10$\bar{1}$2} twins is not controlled by external stress. Local accommodation can effectively explain their activation.

Besides, many {10$\bar{1}$2} twins are detected inside {11$\bar{2}$2} twins, especially in the samples with large grain size. The external stress favorable for {11$\bar{2}$2} compression twinning also facilitates the activation of {10$\bar{1}$2} extension twinning inside the {11$\bar{2}$2} compression twins. In the next chapter, a statistical analysis of {11$\bar{2}$2}-{10$\bar{1}$2} double twins will be given. The criterion for variant selection of {11$\bar{2}$2}-{10$\bar{1}$2} double twins is established by using dislocation dissociation mechanism and an apparent SF method.

Chapter 4 Dislocation mediated variant selection for double twinning in compression of pure titanium

Contents

4.1 Introduction

Secondary $\{10\bar{1}2\}$ extension twins inside primary $\{11\bar{2}2\}$ type compression twins ($\{11\bar{2}2\}$ → $\{10\bar{1}2\}$ double twins) were easily generated in deformed pure titanium. Several compression tests were carried out on commercially pure titanium to study $\{11\bar{2}2\}$ → $\{10\bar{1}2\}$ double twins in Refs [86, 88, 148]. Recently, the preferred secondary twins were found with a misorientation relation of 41° around a $<5\bar{1}\bar{4}3>$ axis compared to the matrix in commercially pure titanium subjected to cold-rolling [88]. The activation of secondary twinning induced by channel-die compression was recently reported and found to be reasonably consistent with a simplified SF criterion [175]. Based on a range of findings and interpretations in the literature, the present work aims to test their applicability to secondary $\{10\bar{1}2\}$ twining within primary $\{11\bar{2}2\}$ twins in compressed pure titanium. It is found in the present work that the only SF based and also the accommodation based secondary twin selection criteria [86] cannot explain the experimental observations. However, the habit plane orientation based criterion - originally proposed for magnesium [8] - applies also to titanium; i.e., it selects the right group (Group II). It does not, however, select the right variant within the group.

In this chapter, samples from rolled pure titanium sheet were subjected to compression along the ND. Primary $\{11\bar{2}2\}$ compression twins were observed, followed by secondary $\{10\bar{1}2\}$ extension twins. The latter can be classified into three groups according to their misorientation with respect to the parent matrix grains: 41.34° around $<5\bar{1}\bar{4}3>$ (Group I), 48.44° around $<\bar{5}503>$ (Group II), and 87.85° around $<7\bar{4}\bar{3}0>$ (Group III). 425 secondary $\{10\bar{1}2\}$ twins were detected. The SF of the observed $\{10\bar{1}2\}$ double twins indicates that Group II is the most frequent followed by Group I, and only a few secondary twins can be seen for Group III. An apparent SF analysis successfully predicts the smallest activity for Group III, while fails to distinguish between Group I and Group II variants. In order to disclose the preference for Group II variant over Group I and Group III, a new approach is proposed based on the geometrical condition that the intersection line of the primary and secondary twin planes lies in an active prismatic plane in the primary twin, which cannot be found in Group I. Consequently, prismatic-dislocation mediated can explain why Group III is difficult to happen even though the geometrical condition for the dissociation of prismatic $<\boldsymbol{a}>$ type dislocations also applies to Group III. Therefore, the preference of Group II over Group I and Group III can be clarified only by prismatic-dislocation mediated nucleation mechanism. With the help of an apparent SF analysis, the stress domains in which only one or two Group II double twin variants can be activated are found, which is in agreement with experiments.

4.2 Experimental procedure

In the current study, the material used was also rolled commercially pure titanium T40 sheet (ASTM grade 2) with a thickness of 1.5 mm. It is generally understood that deformation twinning is more active with a larger grain size [110-112]. Therefore, samples with a large grain size were prepared by annealing in a vacuum furnace at 800 ºC for 2 h, leading to a fully-recrystallized microstructure. By using a Zwick 120T machine, the samples were deformed at room temperature with 8.1% reduction at a strain rate of $1\times10^{-3}s^{-1}$. The compression direction (CD) was parallel to the ND. After compression, sample preparations for electrolytic polishing and EBSD characterizations were conducted according to the procedure in Section 3.2.1.

Crystal plasticity simulations were carried out to obtain information on the required slip systems for accommodating the twin shears that are produced by the secondary twins at the grain boundary of the parent grain. The fully imposed Taylor approach is suitable for such calculation in which the twin shear is imposed on the parent orientation. The approach based on rate sensitive slip proposed in Ref [180] was used for this purpose.

4.3 Microstructure in the initial and deformed states

Fig. 4. 1a presents the microstructure of the initial material in form of EBSD inverse pole figure where the ND axis was projected with the shown color code. The material was fully recrystallized with an average grain size of ~160 μm and presented no twins. Fig. 4. 1b displays the texture of the material in {0002}, {11$\bar{2}$0} and {11$\bar{2}$2} pole figures obtained from Fig. 4. 1a.

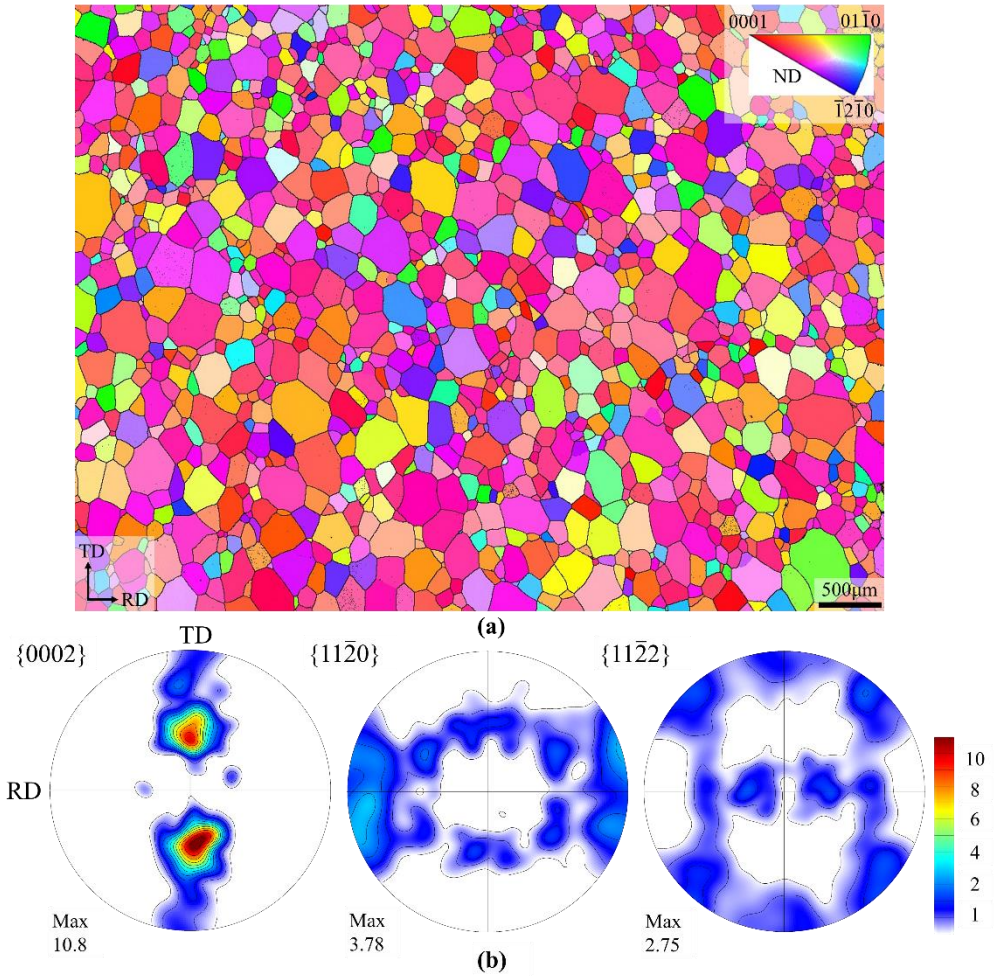

Fig. 4. 1 (a) IPF of the initial material, (b) the corresponding {0002}, {11$\bar{2}$0} and {11$\bar{2}$2} pole figures.

A typical EBSD map obtained on a sample after a compressive strain of 8.1% along the ND is shown in Fig. 4.2a and b. The main twin systems detected in this work are listed in Table 4. 1. Boundaries with a tolerance of ± 5° deviation from the axis and the angle are plotted. This enables detection of {11$\bar{2}$2} and {11$\bar{2}$4} compression twins as well as {10$\bar{1}$2} and {11$\bar{2}$1} extension twins. In Fig. 4.2b, random boundaries with misorientations larger than 5° are traced in black. The {11$\bar{2}$2} compression twins are shown in green (64° rotations around <1$\bar{1}$00>), while the {10$\bar{1}$2} extension twins are depicted in red (87° misorientations around <11$\bar{2}$0>). The green lines correspond chiefly to primary {11$\bar{2}$2} compression twins formed in the parent

grains or secondary {11$\bar{2}$2} compression twins in primary {10$\bar{1}$2} twins. Red lines are typically primary {10$\bar{1}$2} extension twins in the parent grains or secondary {10$\bar{1}$2} extension twins in primary {11$\bar{2}$2} compression twins. Yellow and pink lines correspond to {11$\bar{2}$1} and {11$\bar{2}$4} twins, respectively.

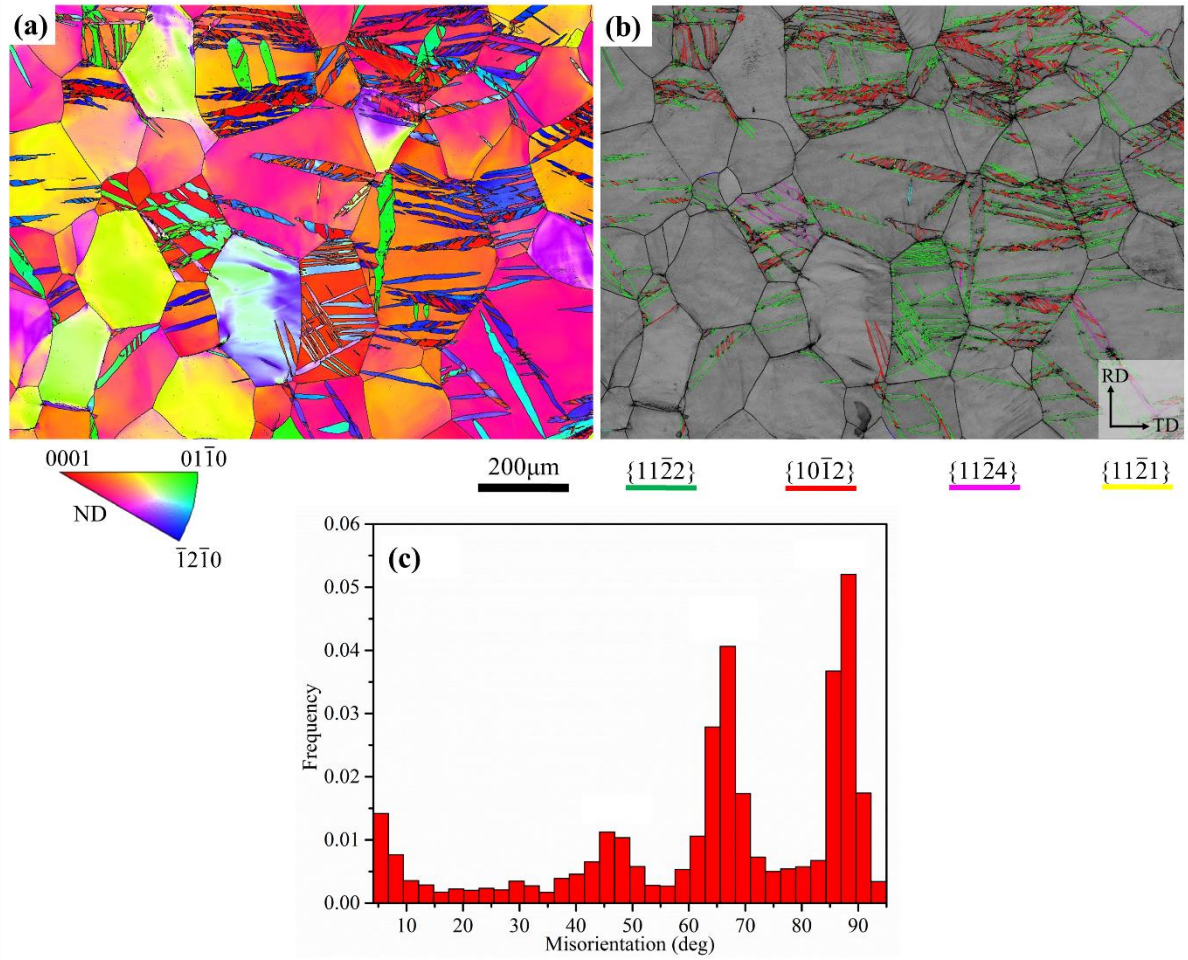

Fig. 4. 2 A typical EBSD result of a sample compressed by 8.1% in IPF map (a) and in band contrast (b). Colour coded lines are used to identify the type of twins in (b). (c): The grain-to-grain misorientation angle distribution corresponding to the map.

Table 4. 1 Main deformation twin systems in titanium.

Type	Compression twins		Extension twins	
K$_1$ plane	{11$\bar{2}$2}	{11$\bar{2}$4}	{10$\bar{1}$2}	{11$\bar{2}$1}
Rotation angle	~64°	~77°	~87°	~35°
Rotation axis	<$\bar{1}$100>	<$\bar{1}$100>	<1$\bar{2}$10>	<$\bar{1}$100>

Fig. 4. 2c shows the next-neighbor grain to grain misorientation distribution and reveals that there are strong peaks at ~65° and ~87°, which can be attributed to the formation of {11$\bar{2}$2}

and $\{10\bar{1}2\}$ twins, respectively. A large number of primary twins form in the parent grains and many secondary twins can also be seen within these primary twins. The two peaks identified as $\{11\bar{2}2\}$ twins and $\{10\bar{1}2\}$ twins in Fig. 4.2c belong to both primary and secondary twins (no distinction is made). Another peak can be seen between 40° and 50°. This angle is not listed in Table 4. 1 because it arises from boundaries between $\{11\bar{2}2\} \rightarrow \{10\bar{1}2\}$ or $\{10\bar{1}2\} \rightarrow \{11\bar{2}2\}$ double twins and the parent matrix. In the present study, $\{10\bar{1}2\} \rightarrow \{11\bar{2}2\}$ double twins were not observed while a large amount of $\{11\bar{2}2\} \rightarrow \{10\bar{1}2\}$ double twins were detected. The $\{11\bar{2}1\}$ extension and $\{11\bar{2}4\}$ compression twins do not produce peaks in Fig. 4.2c at ~35° and ~77°, respectively, because of their small frequency. This is consistent with the characteristics of the texture because such initial texture favors the formation of $\{11\bar{2}2\}$ twins under the ND compression [86].

4.4 Crystallography and classification of $\{11\bar{2}2\} \rightarrow \{10\bar{1}2\}$ double twins

For simplicity in describing twins later, we denote twin variants in Fig. 4. 3 as T_i^I for six $\{10\bar{1}2\}$ twin variants and C_i^I for six $\{11\bar{2}2\}$ twin variants, where i=1…6. The subscript i increases by a counter-clockwise rotation around the *c*-axis of the crystal. The zone axis $<10\bar{1}0>$ associated with a C_i^I twin variant is the vector summation of two zone axes $\frac{1}{3}<11\bar{2}0>$ associated with T_i^I and T_{i+1}^I twins.

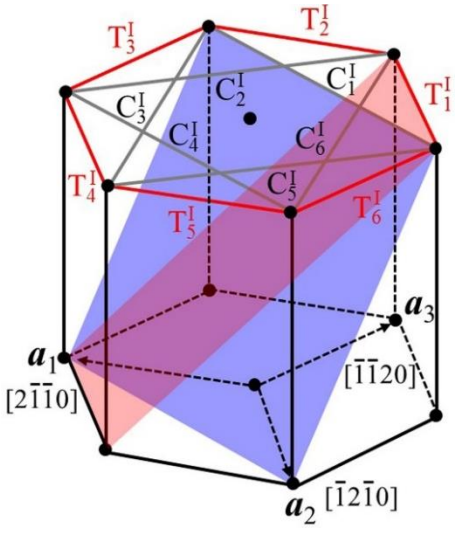

Fig. 4. 3 The crystallography of hexagonal structure. Two shadow planes are twin planes associated with contraction twin $\{11\bar{2}2\}$, C_1^I (blue), and extension twin $\{10\bar{1}2\}$, T_1^I (pink).

Comparing the parent grain orientation to secondary twins inside, there are 36 possible combinations as shown in Table 4. 2. The misorientation between a secondary $\{10\bar{1}2\}$ twin

originating from a primary $\{11\bar{2}2\}$ twin and its parent grain was determined by rotating the orientation of the parent grain around the respective normal directions of primary and secondary twinning planes by 180°. Then, the 12 symmetry operations of the hexagonal lattice were applied and the minimum misorientation angle and corresponding axis were computed between the orientation matrix of the parent and the 12 equivalent matrices of the secondary twins.

Table 4. 2 The 36 possible combinations of secondary $\{10\bar{1}2\}$ extension twins and their minimum misorientations with respect to the parent grains. The same color indicates same group of secondary twin variants.

$\{11\bar{2}2\}$-$\{10\bar{1}2\}$ double twins		Secondary $\{10\bar{1}2\}$ twin variants in primary twins					
		$\{10\bar{1}2\}$ $<\bar{1}011>$	$\{01\bar{1}2\}$ $<0\bar{1}11>$	$\{\bar{1}102\}$ $<1\bar{1}01>$	$\{\bar{1}012\}$ $<10\bar{1}1>$	$\{0\bar{1}12\}$ $<01\bar{1}1>$	$\{1\bar{1}02\}$ $<\bar{1}101>$
Primary $\{11\bar{2}2\}$ twin variants	$\{11\bar{2}2\}$ $<11\bar{2}3>$	$<50\bar{5}3>$ 48.44°	$<0\bar{5}5\bar{3}>$ 48.44°	$<34\bar{7}0>$ 87.85°	$<41\bar{5}3>$ 41.34°	$<\bar{1}45\bar{3}>$ 41.34°	$<\bar{4}\bar{3}70>$ 87.85°
	$\{\bar{1}2\bar{1}2\}$ $<\bar{1}2\bar{1}3>$	$<3\bar{7}40>$ 87.85°	$<0\ 5\bar{5}3>$ 48.44°	$<5\bar{5}0\bar{3}>$ 48.44°	$<\bar{4}7\bar{3}0>$ 87.85°	$<\ \bar{1}5\bar{4}3>$ 41.34°	$<4\bar{5}1\bar{3}>$ 41.34°
	$\{\bar{2}112\}$ $<\bar{2}11\bar{3}>$	$<5\bar{1}\bar{4}\bar{3}>$ 41.34°	$<7\bar{4}\bar{3}0>$ 87.85°	$<\bar{5}503>$ 48.44°	$<50\bar{5}\bar{3}>$ 48.44°	$<\bar{7}340>$ 87.85°	$<\bar{5}413>$ 41.34°
	$\{\bar{1}\bar{1}22\}$ $<\bar{1}\bar{1}2\bar{3}>$	$<\bar{4}\bar{1}53>$ 41.34°	$<14\bar{5}\bar{3}>$ 41.34°	$<43\bar{7}0>$ 87.85°	$<\bar{5}053>$ 48.44°	$<0\bar{5}\bar{5}\bar{3}>$ 48.44°	$<\bar{3}\bar{4}70>$ 87.85°
	$\{1\bar{2}12\}$ $<1\bar{2}1\bar{3}>$	$<4\bar{7}30>$ 87.85°	$<1\bar{5}43>$ 41.34°	$<\bar{4}5\bar{1}\bar{3}>$ 41.34°	$<\bar{3}7\bar{4}0>$ 87.85°	$<0\bar{5}53>$ 48.44°	$<\bar{5}50\bar{3}>$ 48.44°
	$\{2\bar{1}\bar{1}2\}$ $<2\bar{1}\bar{1}\bar{3}>$	$<\bar{5}05\bar{3}>$ 48.44°	$<7\bar{3}\bar{4}0>$ 87.85°	$<54\bar{1}\bar{3}>$ 41.34°	$<\bar{5}143>$ 41.34°	$<\bar{7}340>$ 87.85°	$<55\bar{0}3>$ 48.44°

Table 4. 3 Classification of secondary twin variants from Table 4.2 into three groups.

Group	Axis-angle (minimum)	Number of variants
I	$<5\bar{1}\bar{4}3>$ 41.34°	12
II	$<\bar{5}503>$ 48.44°	12
III	$<7\bar{4}\bar{3}0>$ 87.85°	12

According to misorientation between the matrix and the secondary twins, six $\{10\bar{1}2\}$ secondary twins inside one primary $\{11\bar{2}2\}$ twin were categorized into 3 groups as listed in Table 4.3: $C_i^I \rightarrow T_{i+3}^I$ and T_{i+4}^I (Group I), $C_i^I \rightarrow T_i^I$ and T_{i+1}^I (Group II), and $C_i^I \rightarrow T_{i+2}^I$ and T_{i+5}^I (Group III). In each primary $\{11\bar{2}2\}$ twin, there are two secondary variants for each group. In Table 4. 3 the three groups are defined; each group of secondary twins has the same number of 12 variants. In Group I, the angle between two twin planes is 95.9° and the angle between two

twin shear directions is 76.6 °. In Groups II and III, the angle between two twin planes is 27.4° and 66.9 °, respectively, and the angle between two twin shear directions is 24.2° and 55.2°, respectively.

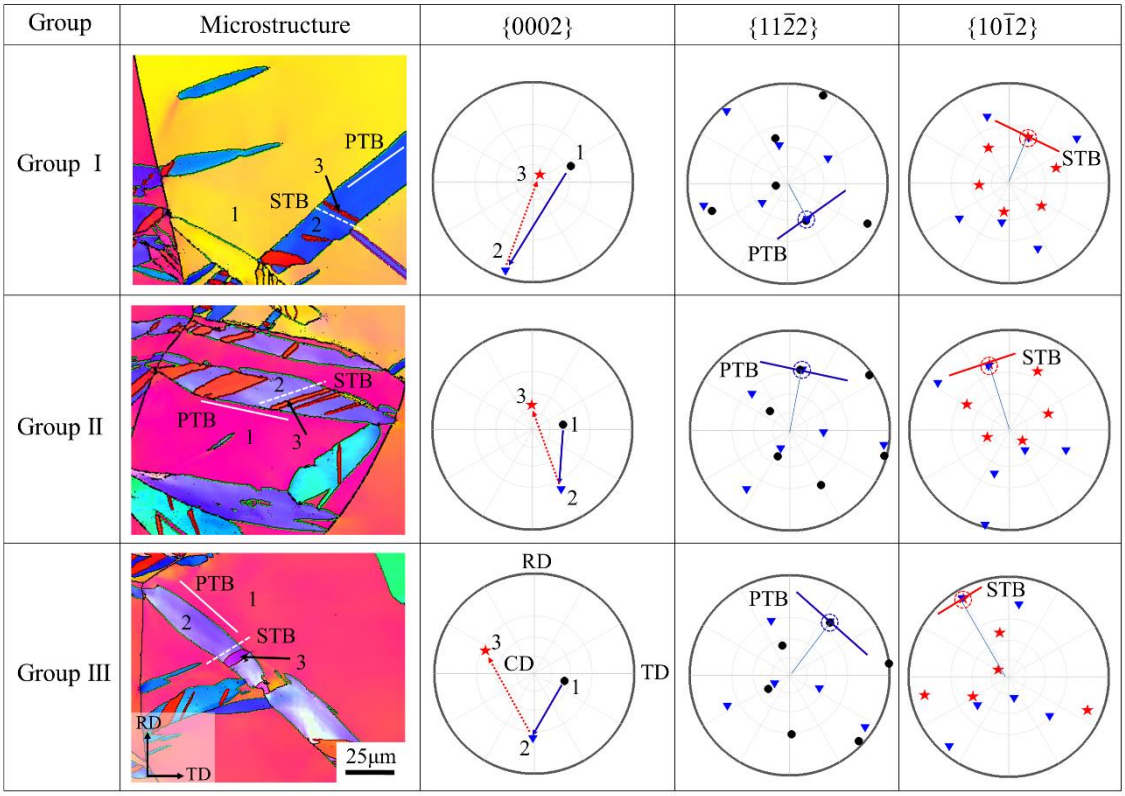

Fig. 4. 4 EBSD examples of three secondary twinning variants revealed in Table 4. 3. The compression direction is indicated by CD. Lamellas 1, 2 and 3 represent the parent grains, primary {11$\bar{2}$2} twins and secondary {10$\bar{1}$2} twins, respectively. In the following {0002} pole figures, black solid points, blue triangles and red stars represent the c-poles of the parent grains, primary twins and secondary twins, respectively. In the {11$\bar{2}$2} pole figures, the active {11$\bar{2}$2} twin planes are showed by blue circles and the traces of primary twin boundaries (PTB) are manifested by blue lines. In the {10$\bar{1}$2} pole figures, the active {10$\bar{1}$2} twin planes are marked by red circles and the traces of secondary twin boundaries (STB) are displayed by red lines.

Fig. 4. 4 displays one example of primary and secondary twin variants for each of the three groups listed in Table 4. 3 in form of EBSD orientation maps and pole figures. For each group, the {0002} poles of the parent grains are located in the vicinity of the center of the pole figure, which enables {11$\bar{2}$2} twinning to be readily activated. A common characteristic between the three groups is that primary twinning takes the c-axis of the twinned part away from the center region. As for the secondary twins, the c-poles are returned near the center region for Groups I and II while those for group III variants, they are oriented in a position largely deviating from the ND. The {11$\bar{2}$2} pole figures in Fig. 4. 4 display both the poles of the parent and the selected primary twin. The common pole belongs to the primary twin plane

and is labeled by a small blue circle. A line segment is drawn in the figure perpendicular to the projected twin plane normal direction. This line segment lies both in the RD-TD and in the primary twin planes, so it indicates the orientation of the twin boundary line in the micrograph. Indeed, for all three groups, the orientation of this boundary line is nearly parallel to the twin-platelet (it is indicated with PTB and also traced in the IPF micrographs by white line)[1]. Similar construction indicates the orientation of the secondary twin boundary in the $\{10\bar{1}2\}$ pole figures where the secondary twin plane normal is indicated with a red circle and the twin boundary with STB.

4.5 Texture variations due to primary and secondary twinning

Using the EBSD grain orientation data obtained for the matrix grains as well as for the twins, it is possible to visualize the changes that occur in the texture due to twinning. The result of such analysis is displayed in Fig. 4. 5 in forms of {0002} pole figures, separately for the matrix grains (Fig. 4. 5a), for the primary active $\{11\bar{2}2\}$ twins (Fig. 4. 5b) and for the secondary $\{10\bar{1}2\}$ twins (Fig. 4. 5c). The parent grains and primary twins included in the texture are those where secondary twins were seen. The initial texture with the *c*-axes aligned near to the center of the pole figure favors the activation of $\{11\bar{2}2\}$ twinning by compression in the ND. Primary $\{11\bar{2}2\}$ twinning reorients the basal plane of the matrix by ~64° around a $<1\bar{1}00>$ direction.

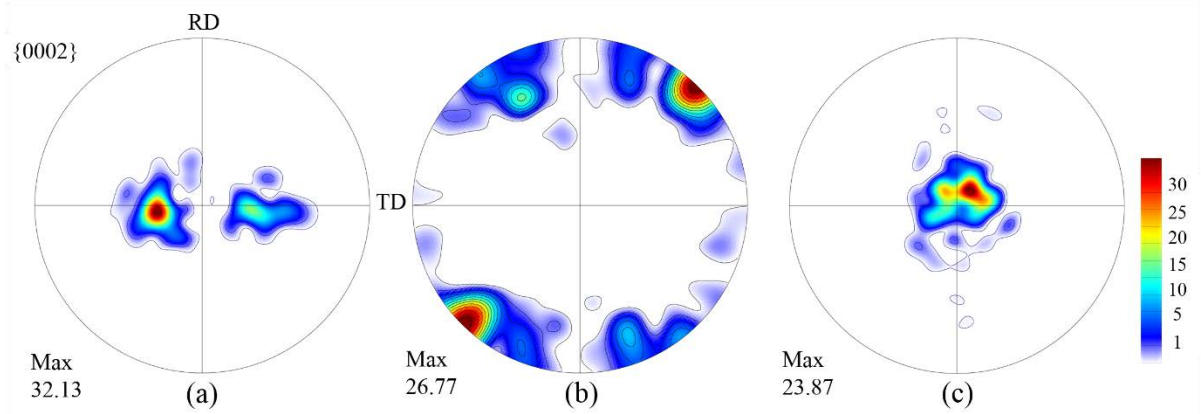

Fig. 4. 5 {0002} pole figures from the EBSD statistics. (a): parent grains, (b): primary twins where secondary twins were found, (c): secondary $\{10\bar{1}2\}$ twins.

As a result of $\{11\bar{2}2\}$ twinning, the basal poles of the primary twins are located away from the ND as shown in Fig. 4. 5b. The stress state favorable for primary $\{11\bar{2}2\}$ twinning in the parent grains also supports the occurrence of secondary $\{10\bar{1}2\}$ twinning in the identified

[1] Note that perfect parallel is only expected for very thin platelets because for thick twins the growth rate of the twin boundary is generally not uniform. Usually lenticular shapes appear because of the pile-up of twinning dislocations against the grain boundaries.

primary twins. Due to secondary $\{10\bar{1}2\}$ twinning, the basal poles of the primary twins are rotated by ~86° around a $<11\bar{2}0>$ axis. In the present case, this leads to basal poles in the centre of the pole figure. With reference to Fig. 4. 4, this suggests that Group I and/or II double twins are dominant because these types return the *c*-axis to the ND.

4.6 Frequency of the detected $\{10\bar{1}2\}$ double twins

As displayed in Table 4. 3, the 36 possible $\{11\bar{2}2\}$-$\{10\bar{1}2\}$ double twin variants involve three groups. In the present statistics, 425 secondary $\{10\bar{1}2\}$ twins were detected by EBSD. For this population of secondary twins, the frequency of the three groups is shown in Fig. 4. 6. This figure indicates clearly that Group II (i.e., $<\bar{5}503>$ 48.44°) accounts for 85.6% of the total twin population. Only 10.6% and 3.8% of the secondary twins belong to Group I and Group III, respectively. Group II secondary twin variants are clearly preferentially selected in the primary twins.

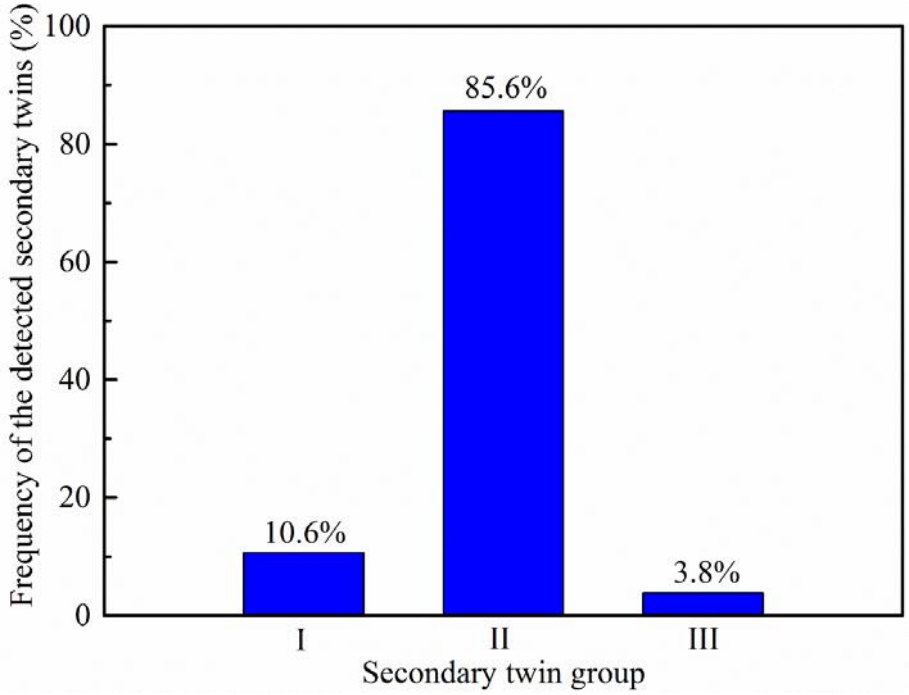

Fig. 4. 6 The observed group-frequency of 425 measured secondary twins.

4.7 Selection criteria for $\{11\bar{2}2\} \rightarrow \{10\bar{1}2\}$ double twins

4.7.1 A Schmid factor based evaluation of the secondary $\{10\bar{1}2\}$ twins

The SF is conveniently used as a reference point for examining variant selection. It is based on the idealized hypothesis that the stress direction in a grain is exactly the same as the one applied on the whole sample. It is helpful to normalize the SF [181]; all twinning SF values

in a given grain are divided by the highest SF value found in that grain to obtain the normalized Schmid factor, NSF(i):

$$NSF(i) = \frac{SF(i)}{SF_{\max}}, \quad i = 1...6 \tag{4-1}$$

Since there are six possible variants for one twin in one grain, the twin with an "absolutely" low positive SF might be the one with a "relatively" high SF, compared with the SFs of the other possible twin variants in the same grain. With the help of this parameter NSF, the twin variant with actually high SFs can be defined. The maximum possible value of NSF is 1.

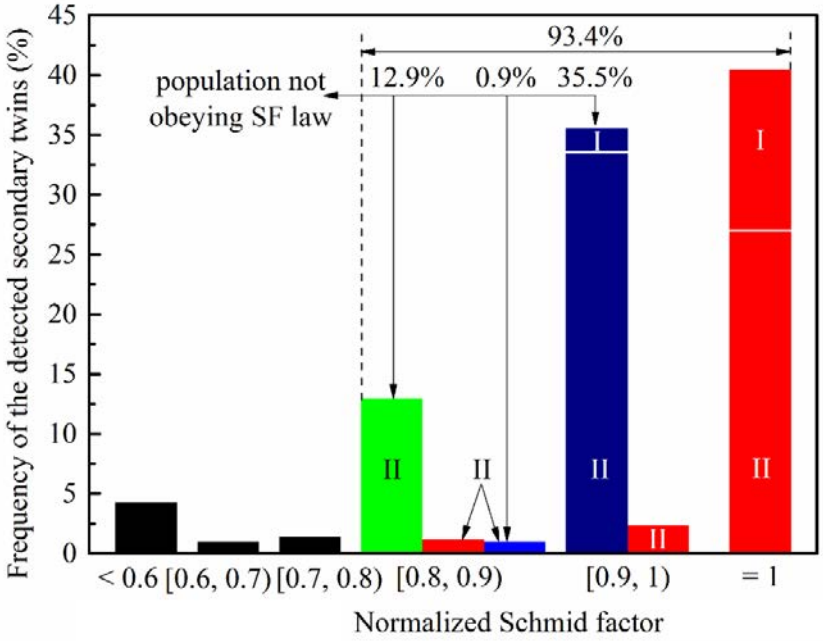

Fig. 4. 7 Frequency distribution of the 425 measured secondary twins as a function of the normalized Schmid factor. Red color means the highest SF variant is activated. Blue and green colors indicate variants with NSF < 1 in primary twins where the highest SF variant is absent.

The distribution of the NSF values of the 425 secondary twins measured in the present study is shown in Fig. 4. 7. As indicated in the figure, 93.4% of the twins have an NSF factor higher than 0.8. Only one secondary twin variant is activated in most primary twins. 4.5% of the secondary twins are found in the primary twins where two variants are activated. A color code is used in Fig. 4. 7 to identify twins of different categories starting from NSF = 0.8. Red color indicates that the highest SF variant is activated, so the SF rule is respected. For a few cases marked by red, the second highest NSF variant is also active in the same primary twin - they are counted in the other NSF intervals according to their NSF factors (between [0.8, 0.9) and [0.9, 1)). There was no case when the first three highest NSF variants were all active in the same primary twin. The blue colored column indicates the proportion of twins that are present

in the material with NSF < 1, moreover, the variant corresponding to NSF = 1 is absent in those primary twins. The meaning of the green color is similar: it shows the population of twins that have even smaller NSF factors, without the presence of other twin variants with higher NSF in those primary twins. Thus, the blue and green color columns together indicate the proportion of twins that do not obey the classical Schmid law. Totally, we can identify 49.3% of the secondary twin variants that do not obey Schmid law. Fig. 4. 7 also indicates the proportion of twins belonging to the three possible groups defined in Table 4. 3. Only Group I and Group II appear in the colored regions because Group III is present only with NSF factors less than 0.8. As can be seen from Fig. 4. 7, Group II is particularly disobeying the Schmid law because it represents (count in the blue and green color columns) 47.5% of the total twins and 96.2% of the non-Schmid twins. The non-Schmid part of Group I is 1.9% and for Group III it is 3.8% of the total population.

Without loss of generality, we conducted an apparent SF analysis. Firstly, we determine the loading domain in which one primary contraction twin is activated. $\{11\bar{2}2\}$ twin variant C_1^I is chosen to be the primary twin in this study. The grain is subjected to uniaxial compression. The loading domain is determined according to the SF associated with C_1^I twin. When the SF is greater than 0.3 and is the greatest among six equivalent variants, the loading directions are plotted into an inverse pole figure as shown in Fig. 4. 8a. Due to the approximate 90 degrees between secondary twin variants T_i^I and T_{i+3}^I, they have nearly same SF. At a given loading direction within the loading domain in Fig. 4. 8a, we calculated the SFs associated with six $\{10\bar{1}2\}$ twin variants T_j^I (j=1...6), and plotted them in Fig. 4. 8b-d. The results show that twin variants T_3^I and T_6^I in Group III have smaller SFs than twin variants in Group II and Group I. The SFs in Group II and I are similar and there is no significant difference, because T_1^I in Group II has the same SF as T_4^I in Group I, and T_2^I in Group II has the same SF as T_5^I in Group I. This could address the lower activity of twin variants in Group III than other two groups, while this could not distinguish the activity of twin variants in Group II and I. The same feature is associated with other contraction twin variants. For example, the loading domain associated with C_2^I is obtained by counterclockwise rotating the C_1^I loading domain 60 degrees around the <0001>. Three typical loading directions are marked by A, B and C in Fig. 4. 8a. SFs of six secondary twin variants at the three points are given in Table 4. 4. T_1^I and T_4^I have the largest SFs when the loading is along the A; T_2^I and T_5^I have the largest SFs when the loading is along the C. Four variants in Group II and Group I have the largest SFs when the loading is along the B. We further compared SFs associated with two equivalent twin variants belonging to Group

II. When the difference in the SFs associated with two variants in Group II is smaller than 0.05, we treated them equal. Correspondingly, we re-plotted the loading domain in Fig. 4. 8e and f for Group II associated with the primary contraction twin C_5^I and C_4^I, respectively. In a small loading domain (marked by the red color), two variants share the equal SF. In the rest region of the loading domain, one is greater than the other. The same feature is also observed for Group I. This could address why most primary twins only contain one secondary twin variant.

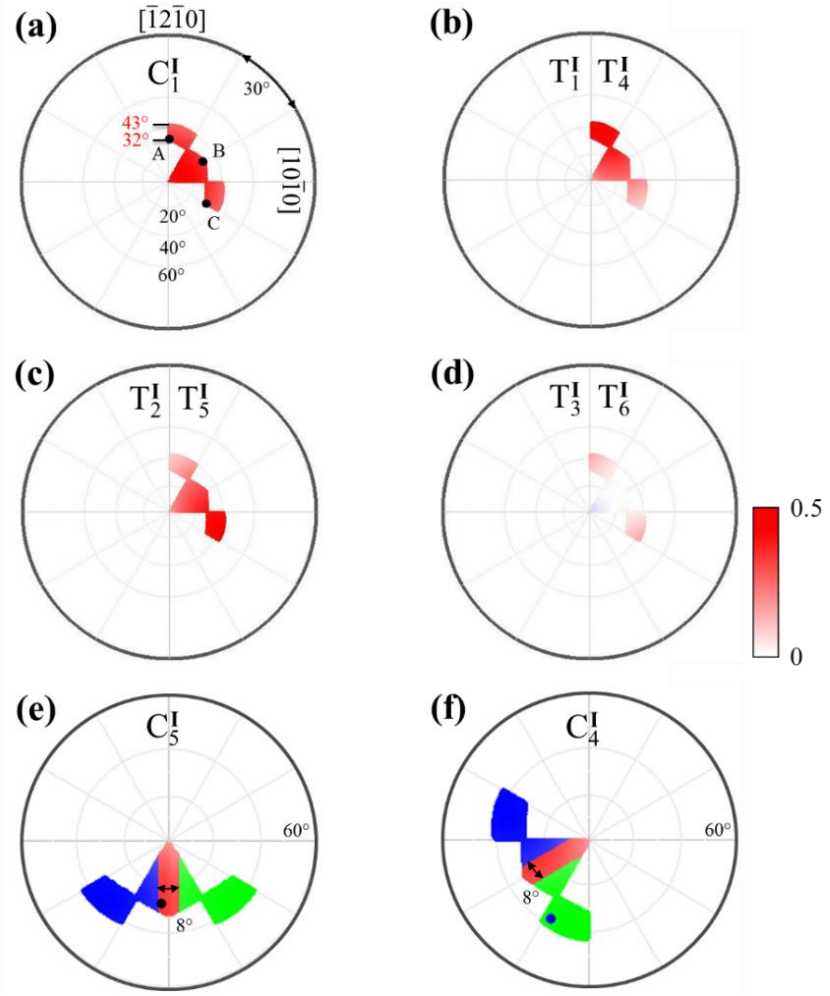

Fig. 4. 8 Inverse pole figures of the Schmid factor of twinning systems subjected to compression: (a) Stress domain where SF of C_1^I primary twin variant is positive and is the largest among the six possibilities. Under this stress domain, the SF of: (b) T_1^I and T_4^I secondary twin variants, (c) T_2^I and T_5^I secondary twin variants, (d) T_3^I and T_6^I secondary twin variants. Distribution of SFs of Group II variants T_i^I and T_{i+1}^I in the loading domain associated with contraction twin (e) C_5^I and (f) C_4^I. Green means the SF associated with variant T_i^I is larger than the variant T_{i+1}^I. Blue means the SF associated with variant T_i^I is smaller than the variant T_{i+1}^I. Red means the difference in the SFs of two variants is less than 0.05.

Table 4. 4 Comparison of selection criteria for $\{11\bar{2}2\} \rightarrow \{10\bar{1}2\}$ double twins. SFs associated with six twin variants correspond to three loading directions A, B and C in Fig. 4.8a. DGA means displacement gradient accommodation, and NDD represents nucleation based on dislocation dissociation.

	In primary twin (C_1^I) $(11\bar{2}2)[11\bar{2}\bar{3}]$					
Secondary $\{10\bar{1}2\}$ variants	T_4^I	T_5^I	T_1^I	T_2^I	T_3^I	T_6^I
	$(\bar{1}012)$ $[10\bar{1}1]$	$(0\bar{1}12)$ $[01\bar{1}1]$	$(10\bar{1}2)$ $[\bar{1}011]$	$(01\bar{1}2)$ $[0\bar{1}11]$	$(\bar{1}102)$ $[1\bar{1}01]$	$(1\bar{1}02)$ $[\bar{1}101]$
Group	I, <41$\bar{5}$3> 41.34°		II, <50$\bar{5}$3> 48.34°		III, <34$\bar{7}$0> 87.85°	
Experiments	10.6%		85.6%		3.8%	
SFs (A)	0.490	0.138	**0.474**	0.129	0.101	0.093
SFs (B)	0.357	0.357	**0.370**	**0.370**	-0.006	-0.006
SFs (C)	0.138	0.490	0.129	**0.474**	0.093	0.101
Apparent SFs	One high, One moderate		One high, One moderate		Two are same and low	
DGA	-0.01	-0.01	**0.18**	**0.18**	0.05	0.05
NDD	Very difficult unless dislocations climb		Energetically favored by prismatic <***a***> dislocations		Facilitated by prismatic <***a***> dislocations	

Fig. 4. 7 is the experimental situation, so that it should be compared to the theoretical prediction based on the SFs by respecting the activation of high NSF twin systems. For this purpose a full analysis was carried out considering all possible secondary twins that potentially can form in the detected primary twins. We consider only those variants that carry the first and second highest SFs. Smaller SF variants are omitted because generally one or two variants appear in a primary twin.

Fig. 4. 9 shows the result of such analysis: Group III variants constitute only 0.5% of all possible variants, while Group I and II account for 50.2% and 49.3%, respectively. This is in agreement with the results indicated in Fig. 4. 8 that only Group I and Group II double twin variants have high SFs. The small population of group III twins concurs with the experimental observations, so their absence can be convincingly attributed to their relatively low SFs. However, our analysis predicts similar proportions for Group I and II twins. This is not consistent with the experiment: Group II twins alone represent 85.6% of the total population of the detected secondary twins (Fig. 4.6). Even though the active secondary twin variants carry high SFs in [175], this classical law is found to be invalid in explaining the occurrence of secondary twinning in our work.

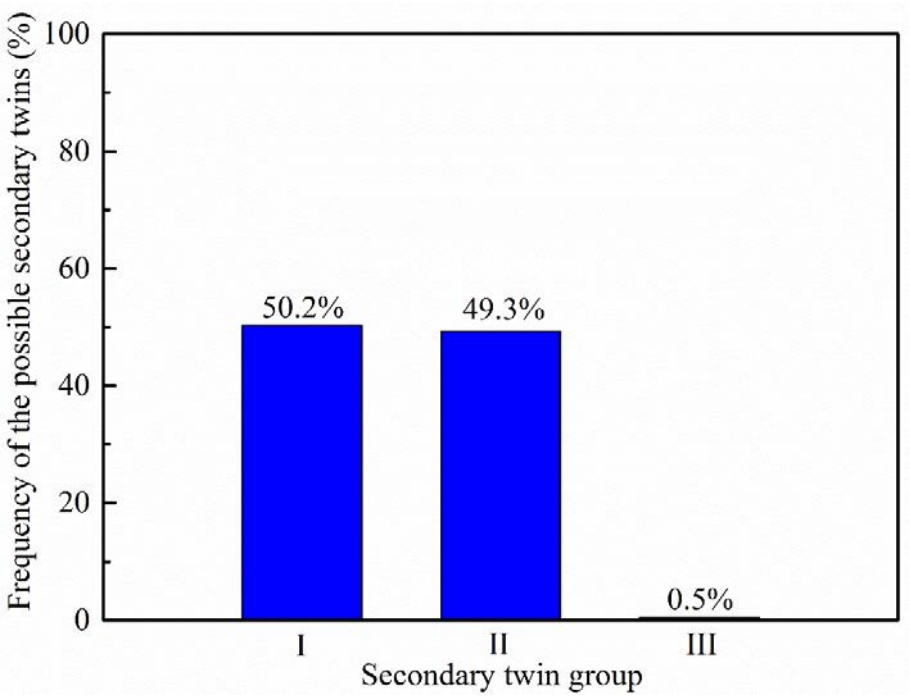

Fig. 4. 9 Predicted active frequency of the possible secondary twins using the highest and second highest Schmid factors.

Since only one secondary twin variant is activated in majority of the primary twins, it is a simple matter to simulate the effect of activating different secondary twin variants on the evolution of secondary twin textures. The orientations of possible secondary twins were artificially calculated within the detected primary twins to reveal particular secondary twin variants. Each group includes two secondary twin variants. The reorientation of the texture by the secondary twin variant with a higher SF is shown in the first row of Fig. 4. 10. The *c*-poles of the secondary twins induced by Group I and Group II variants are located close to the center of the pole figure, which is similar to the experimental result. Those secondary twins by Group III variants are largely misaligned with the observed secondary twin texture as indicated in Fig. 4. 5c. However, the other variant carrying a lower SF in each group reorients the texture as presented in the secondary row of Fig. 4. 10, which reveals that these secondary twins are not in agreement with the detected results because the texture is away from the center of the pole figures. This is true for the three groups. Therefore, the texture evolution illustrates that the selection between two secondary twin variants in the same group is controlled by the SF criterion. Only one variant is favored for Group I and Group II if they have high SFs, respectively. It is clear that a SF based selection rule is only effective to resolve the absence of Group III variants as well as one variant in Group I, and also one in Group II.

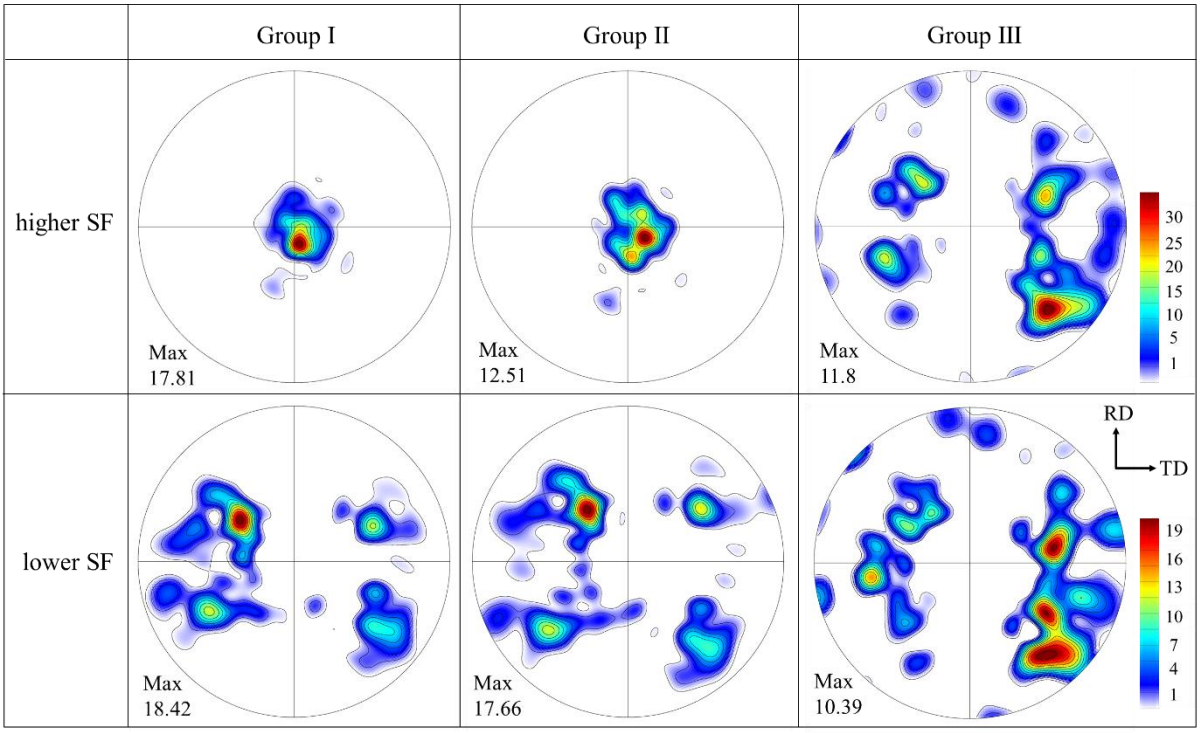

Fig. 4. 10 {0002} pole figures showing simulated secondary twin textures. The activation of only one secondary twin variant is assumed for each case. There are two possible variants for each group in every primary twin which are clearly differentiated by the values of their Schmid factors leading to preference for the higher Schmid factor variants in both Groups I and II.

In conclusion, it follows from the above SF analysis that there remain only two possible variants that can explain the experimental observation. They are: the higher SF cases in Group I and Group II. Therefore, further selection rule is needed because Group II is much more favored than Group I. This will be established with the help of dislocation mediated mechanisms.

4.7.2 Local accommodation

The apparent SF analysis predicts the low activity of Group III twin variants, while the competition of variants between Group II and Group I cannot be accessed. We thus tested displacement gradient accommodation. Displacement gradient tensor of a $(11\bar{2}2)[11\bar{2}\bar{3}]$ twin expressed in its twinning reference frame was expressed into the twinning reference frames of six $\{10\bar{1}2\}$ twins. The component E_{13} is summarized in Table 4. 4. Two variants in Group II have the largest E_{13}, which means that the strain induced by the primary twin can be effectively accommodated by Group II twins. Twin variants in Group I are also observed in experiments, but the component E_{13} is negative. As to twin variants in Group III, the component E_{13} is positive but they are rarely observed in experiments. This implies that displacement gradient

accommodation is not the necessity in accessing the variant, but can predict the relative activity when multiple variants have positive SF in the case of $C_i^I \rightarrow T_j^I$ double twins (j= i or i+1).

As a consideration of the accommodation in the parent grain required by the double twins, the next step is then to examine the applicability of the recently proposed accommodation based selection criterion [86] on our measurements. In Ref. [86], the displacement gradient tensor of a possible secondary twinning variant was expressed into the neighbor mother grain. The components of the obtained tensor correspond to different slip systems. Then that secondary twin variant was admitted which was the best compatible with the displacement gradients produced by basal or prismatic slip in the neighbor grain.

Table 4. 5 Slip systems and the corresponding critical resolved shear stress in pure titanium.

Slip systems	$\{10\bar{1}0\}$ $<1\bar{2}10>$	$\{0002\}$ $<1\bar{2}10>$	$\{10\bar{1}1\}$ $<1\bar{2}10>$	$\{10\bar{1}1\}$ $<11\bar{2}\bar{3}>$	$\{11\bar{2}2\}$ $<11\bar{2}\bar{3}>$
Notation	P<***a***>	B<***a***>	Py_1<***c***+***a***>	Py_1<***c***+***a***>	Py_2<***c***+***a***>
CRSS / MPa	141	254	197	338	353

In our analysis, we applied this approach in the following way introduced in the Appendix. First, for each experimentally observed primary twin orientation containing secondary twins, we expressed the velocity gradients of the shears corresponding to the six possible secondary twins in the sample reference system of the EBSD measurement. Then these velocity gradients were imposed on the mother grain, one by one. All possible slip families of HCP crystals were considered in the mother grains for possible accommodation of the secondary twin shears; they are listed in Table 4. 5. The CRSS values of these systems were taken from Ref [154] where the material of the same composition was studied. The single crystal plasticity problem was solved to obtain the necessary slip distribution within the mother grain by employing the full constraints conditions of crystal plasticity with visco-plastic slip according to the approach published in [180]. The value of the strain rate sensitivity index for slip was m=0.05. The calculation was done in the sample reference system in full constraints conditions, which is the only possible approach that can be considered at a grain boundary between the primary twin and the mother grain. The resulting slip distribution was examined for each secondary twin variant. Note that this accommodation approach is more rigorous than the one employed in [86], because the accommodation is possible for any shear caused by secondary twins and produces precise values for the slips in the mother grain.

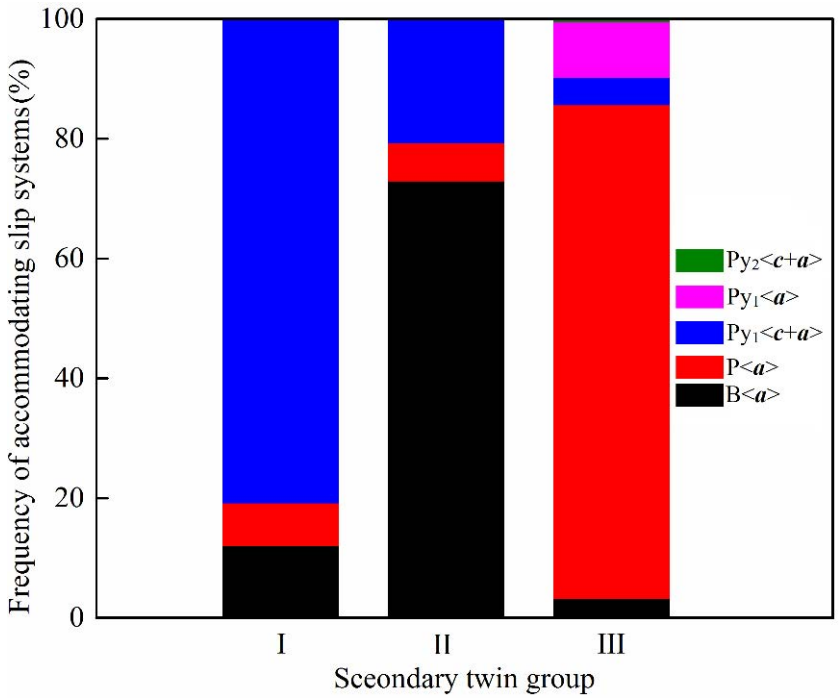

Fig. 4. 11 Classification of the possible secondary twins when prismatic slip in the parent grains is assumed to accommodate the secondary twin shear.

The simulation result is displayed in Fig. 4. 11: twinning shear in Group I is mainly accommodated by Py_1<***c***+***a***> slip. For a small fraction of cases, basal and prismatic slip are the most active. For Group II - which is the most frequently observed experimentally - basal slip is the major accommodating slip mode, in a few cases prismatic slip, and in 22% Py_1 <***c***+***a***> slip. Group III requires mostly prismatic slip (80%) and in a few cases basal slip, Py_1<***c***+***a***> as well as <***a***> type pyramidal. The accommodation by Py_2<***c***+***a***> slip is very rare. In conclusion, the twin-shear accommodation based approach selects Group III where the easiest slip (prismatic) is the most active. Although Group II can be accommodated by basal slip – a possible selection variant according to the principles in Ref. [86]. It cannot be applied to select only Group II because Group III is accommodated more easily by prismatic slip. Therefore, the selection criteria based on the prismatic or basal slip accommodation of the secondary twin shear is not validated by our experiments and simulations. In the following section, another dislocation mediated mechanism is proposed, which is able to account for the experimental observations.

4.7.3 Nucleation based on dislocation dissociation

The particularity of the secondary extension twins is that their *c*-axes are nearly perpendicular to the primary twin *c*-axis. A consequence of this is a large difference in the

stress state between the twinned and matrix grain regions. Indeed, crystal plasticity simulations show that the stress state in a grain can be very different from the macroscopic applied stress [177]. Internal stresses arising from the twins and from the neighboring grains can also play a significant role [182, 183]. These are probably responsible for the variation in NSFs for active Group II twins, but the effect is unlikely capable to explain the striking difference between Group I and II variants. In looking elsewhere for an explanation without going into detailed crystal plasticity simulations, we examine dislocation reaction based mechanism, using the principles developed for magnesium in Ref [184]. As discussed above, in each primary $\{11\bar{2}2\}$ twin, three distinct secondary twin variants can be created which can be characterized by the misorientation between the parent grains and secondary twins; they are referred to Group I, II and III (Table 4. 3).

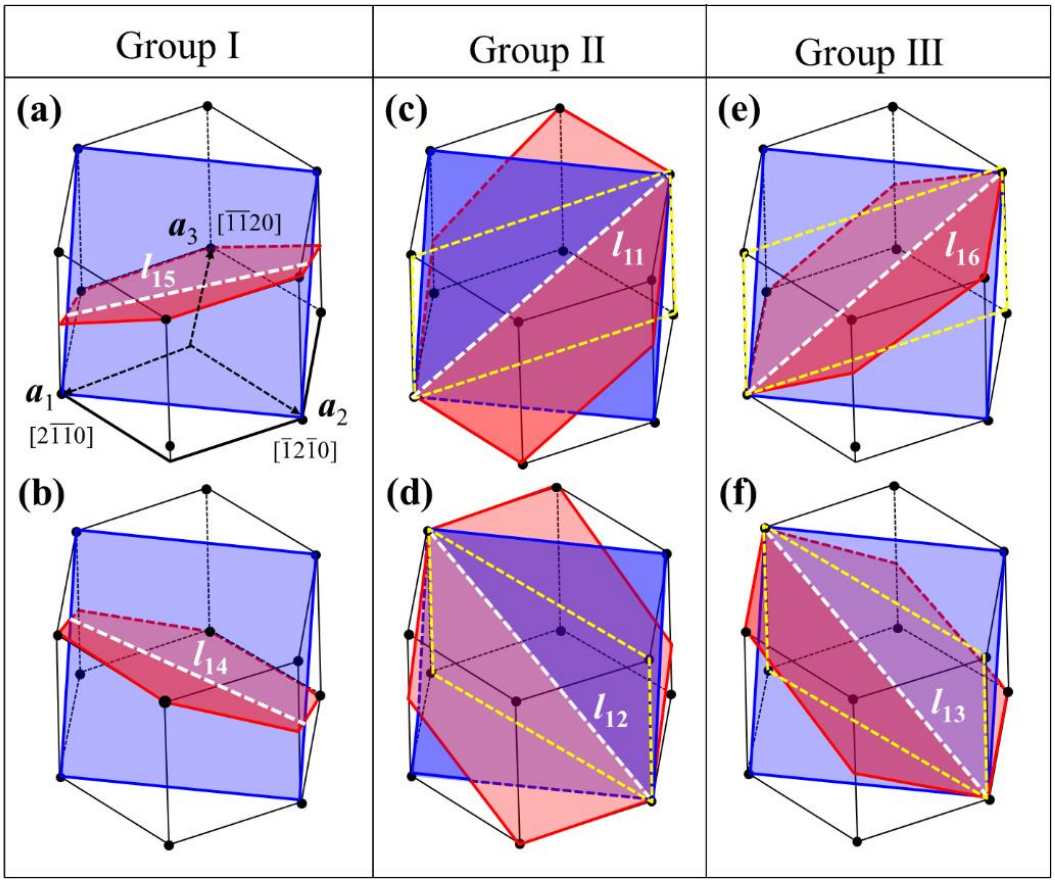

Fig. 4. 12 Crystallography of $\{11\bar{2}2\} \rightarrow \{10\bar{1}2\}$ double twins. The blue plane denotes the primary twin C_i^I, and the pink plane represents the secondary twin T_j^I. The white dashed line indicates the intersection, l_{ij}, between the primary twin C_i^I and the secondary twin T_j^I. The yellow dashed lines outline a $\{10\bar{1}0\}$ prismatic plane.

The crystallographic feature of $C_i^I \rightarrow T_j^I$ double twins is illustrated in Fig. 4. 12. The blue plane denotes the primary twin C_i^I, and the pink plane represents the secondary twin T_j^I. The

white dashed line indicates the intersection l_{ij}, between the primary twin C_i^I and the secondary twin T_j^I. The intersection lines, l_{14} and l_{15} in Group I are along [8 $\bar{1}0$ 2 3] and [$\bar{1}0$ 8 2 3], respectively. The intersection lines l_{11} and l_{12} in Group II are along [$\bar{4}$223] and [2$\bar{4}$23], respectively. The same intersection lines are identified for l_{13} and l_{16} along [$\bar{4}$223] and [2$\bar{4}$23] in Group III, respectively. The intersection lines in Groups II and III lie in a $\{10\bar{1}0\}$ prismatic plane, as outlined by the yellow dashed lines.

The Miller-Bravais indices of the intersection lines between the primary twin plane and three groups of secondary twin planes, as well as of the corresponding prismatic planes in the primary twin are listed in Table 4. 6. As determined graphically, for Group II twins, the common direction is in a prismatic plane, offering good geometrical conditions for the possible dissociation of prismatic <***a***> dislocations [65, 74]. <***a***> type prismatic glide $\{10\bar{1}0\}<1\bar{2}10>$ is favored for titanium and zirconium (c/a < 1.633) [161, 185]. Thus, the nucleation of Group II twins could conceivably originate from reactions of <***a***> type prismatic dislocations in the primary twin that glide into the primary twin boundary. Such reactions are facilitated by the shared zone axis of the prismatic slip and Group II twinning planes lying in the primary twin boundary.

Table 4. 6 The Miller-Bravais indices of the common direction between a primary $(11\bar{2}2)$ twin, the six secondary twins as well as the corresponding prismatic plane for the three secondary twin groups.

Primary twin variant	$(11\bar{2}2)$ $[11\bar{2}\bar{3}]$					
Group	I		II		III	
Secondary twin variants	I_1 $(0\bar{1}12)$	I_2 $(\bar{1}012)$	II_1 $(01\bar{1}2)$	II_2 $(10\bar{1}2)$	III_1 $(1\bar{1}02)$	III_2 $(\bar{1}102)$
Common axis	[8 $\bar{1}0$ 2 3]	[$\bar{1}0$ 8 2 3]	[$\bar{4}$223]	[2$\bar{4}$23]	[$\bar{4}$223]	[2$\bar{4}$23]
Prismatic plane	-	-	$(10\bar{1}0)$	$(01\bar{1}0)$	$(01\bar{1}0)$	$(10\bar{1}0)$

Taking the similar analysis in Ref [64], we investigate the dissociation or reflection of prismatic <***a***> dislocation at the primary twin plane into twinning dislocations associated with $\{10\bar{1}2\}$ twins. As shown in Fig. 4. 13a, secondary T_2^I (in red) and T_3^I (in green) variants intersect the C_1^I (in blue) primary twin plane along the [2$\bar{4}$23] axis, which lies in $(10\bar{1}0)$ prismatic plane (in yellow). When $(10\bar{1}0)[1\bar{2}10]$ dislocations approach the primary twin boundary as depicted in Fig. 4. 13b, they could dissociate into twinning dislocations associated with Group II and Group III secondary twins. Here, the feasibility of the dislocation dissociation into twinning partials for Group II and Group III is examined.

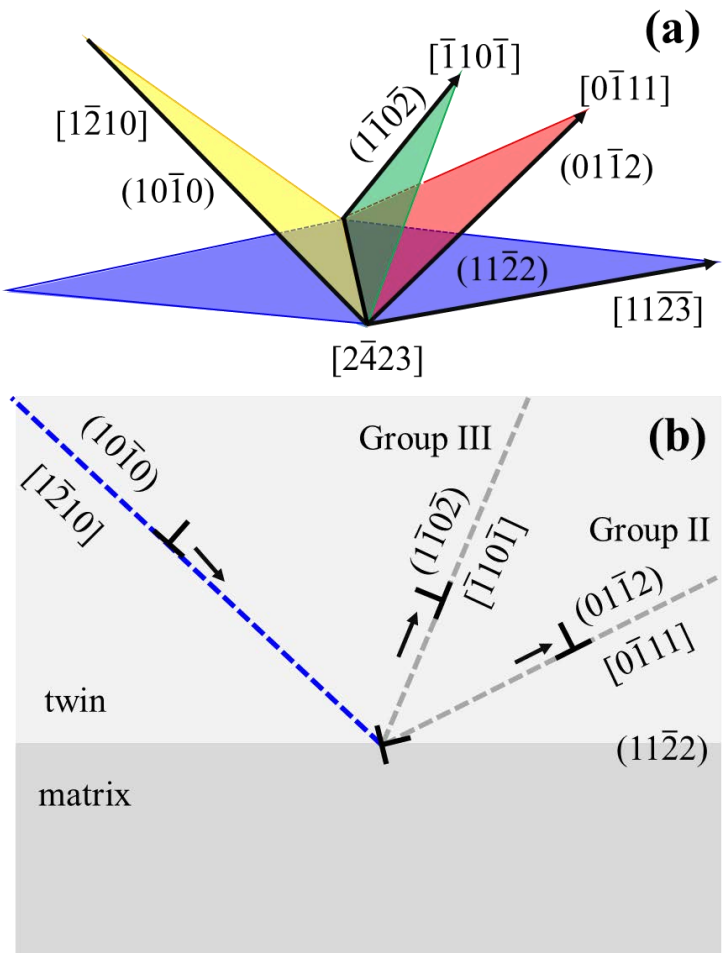

Fig. 4. 13 (a) Illustration of the common line between a prismatic plane, a Group II twinning plane, a Group III twinning plane and a primary twin plane along [2$\bar{4}$23]. (b) Schematic of reaction of a prismatic dislocation at a primary twin boundary into a Group II or a Group III twin dislocation plus a residual dislocation.

For Group II, a (10$\bar{1}$0)[1$\bar{2}$10] dislocation, b_a can be dissociated into three secondary twining dislocations $3b_t^{(01\bar{1}2)}$, and a residual one b_r^1,

$$b_a \Rightarrow b_r^1 + 3b_t^{(01\bar{1}2)} \tag{4-2}$$

according to the Frank's law $\left(|b_a|^2 > |b_r^1|^2 + \left|3b_t^{(01\bar{1}2)}\right|^2\right)$. However, a prismatic dislocation (10$\bar{1}$0)[1$\bar{2}$10] can dissociate into only one twining dislocation associated with Group III twin,

$$b_a \Rightarrow b_r^2 + b_t^{(1\bar{1}0\bar{2})} \tag{4-3}$$

The dissociation is energetically unfavourable according to the Frank's law, $|b_a|^2 < |b_r^2|^2 + \left|b_t^{(1\bar{1}0\bar{2})}\right|^2$. Where $b_a = \frac{1}{3}[1\bar{2}10]$, 0.295 nm for titanium; The magnitude of Burgers

vector of $\{10\bar{1}2\}$ twinning dislocation is equal to $\frac{3a^2-c^2}{\sqrt{3a^2+c^2}}$, 0.60 nm for Ti ($a$=0.295nm and c=0.4683nm).

If the incoming dislocation b_a is firstly dissociated into twinning dislocation $b_t^{(\bar{1}\bar{1}2\bar{2})}$ on the primary twin plane, and then the residual acts as nucleation source, only one secondary twinning dislocation can be nucleated according to the Frank's law.

$$b_a \Rightarrow b_r^3 + b_t^{(\bar{1}\bar{1}2\bar{2})} + b_t^{(01\bar{1}2)} \tag{4-4}$$

$$b_a \Rightarrow b_r^4 + b_t^{(\bar{1}\bar{1}2\bar{2})} + b_t^{(1\bar{1}0\bar{2})} \tag{4-5}$$

Equation (4-4) was applied for Group II and was energetically favored. Equation (4-5) was applied for Group III and was energetically unfavorable. The magnitude of Burgers vector of $\{11\bar{2}2\}$ twinning dislocation is equal to $\frac{c^2-2a^2}{\sqrt{c^2+a^2}}$, 0.82 nm for titanium.

Looking into the Group I secondary twin configurations with respect to the primary twins, a dislocation dissociation mechanism similar to the one proposed for Group II twins cannot be found. The reason is that the secondary twins belonging to Group I do not benefit from common zone axis in the same way as in Group II variants. They intersect with the primary twin boundary along directions that are not parallel to any prismatic or primary twin planes (see Fig. 4. 12a and b). Moreover, the common lines do not correspond to any crystal direction among the available HCP slip planes and the primary twin boundary. It is also true that for a possible dislocation reaction, <***c***+***a***> type dislocations would be needed which are hard to activate in titanium. Therefore, Group I twins can be expected to be much more difficult to form compared to Group II, as is observed.

In order to confirm the activation of the associated prismatic slip in the primary $\{11\bar{2}2\}$ twin with the preferred secondary $\{10\bar{1}2\}$ Group-II twin, a sample was pre-polished and deformed under compression, followed by the observation of slip traces with the help of secondary electron imaging. Primary $\{11\bar{2}2\}$ and secondary $\{10\bar{1}2\}$ twins were detected as shown in Fig. 4. 14a. Clear slip traces were found in the area identified in the orientation map in Fig. 4. 14a; the corresponding secondary electron image is displayed in Fig. 4. 14b. The primary and secondary twin systems were $(\bar{1}\bar{1}22)[\bar{1}\bar{1}23]$ and $(0\bar{1}12)[01\bar{1}1]$, respectively (all indices are expressed in the primary twin reference frame). Therefore, this secondary twin belongs to Group II. The expected slip-line directions in the observation plane corresponding to the three prismatic planes in the primary twin were computed and plotted in Fig. 4. 14c. As can be seen, one prismatic plane is parallel to the slip lines in Fig. 4. 14b; the $(10\bar{1}0)$ (identified

with a blue line in Fig. 4. 14b-c). Out of the three possible prismatic planes only the observed $(10\bar{1}0)$ prismatic plane satisfies the Group II configuration.

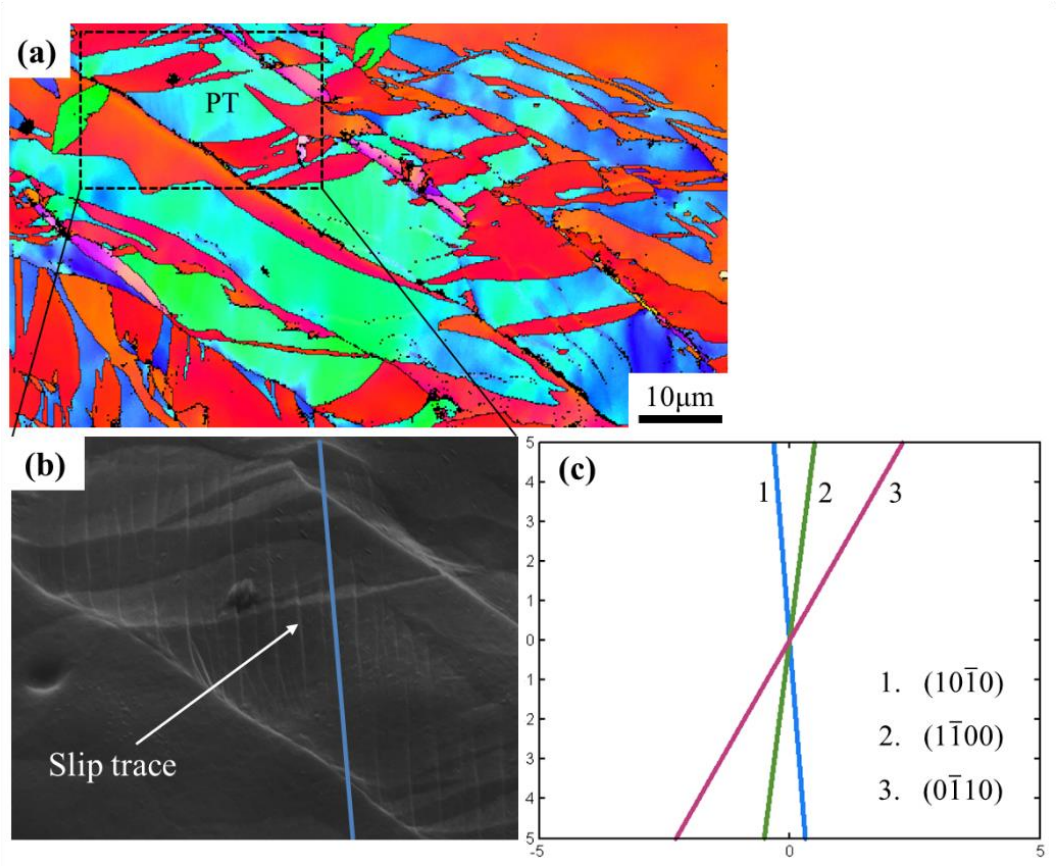

Fig. 4. 14 (a): EBSD map from a pre-polished and deformed sample. (b): Secondary electron imaging of the region enlarged in (a). (c): Orientations of the possible three prismatic plane traces in the primary twin (the primary twin is identified by PT in the insert of (a)). The blue lines in (b) and (c) correspond to the prismatic trace for plane $(10\bar{1}0)$.

Therefore, the presented geometry corresponds to the preferred group; Group II. There are two variants within Group II, out of which the highest SF variant is preferred, see our proposed model above. Indeed, the higher SF variant can be seen in Fig. 4. 14 with a SF of 0.42 in contrast to the other variant which is 0.27. Finally, we note that the predominance of Group II variants in the present case differs from the finding in Ref. [88]**.** In that study, cold rolling was performed and Group I secondary twins were found to be dominant. This difference likely relates to the difference in stress states between the present experiments and those in Ref. [88]**.** In plane strain rolling, prismatic slip is not favored in the primary twin domain, so the present mechanism is not expected to be active.

The above analysis according to the nucleation of twinning dislocations based on the dissociation of prismatic <***a***> dislocation can distinguish the relative activity of three group of

twin variants. Group II is predominant, Group III is secondly activated, and Group I is most unlikely. The mechanism based on the dissociation of prismatic <***a***> type dislocations can explain the preference of Group II over other two Groups. However, the nucleation criterion cannot distinguish the preference of two variants in the same group, due to the approximately same resolved shear stress on two twin variants in a group.

4.7.4 Selection between two variants in Group II

We have examined the selection of $\{11\bar{2}2\}\rightarrow\{10\bar{1}2\}$ double twin variant according to the SF analysis, displacement gradient accommodation, and dislocation dissociation based nucleation. Corresponding to the misorientation between secondary twins and the primary twin, six twin variants T_i^I are conventionally classified into 3 groups — Group I: $C_i^I \rightarrow T_{i+3}^I$ and T_{i+4}^I, Group II: $C_i^I \rightarrow T_i^I$ and T_{i+1}^I, and Group III: $C_i^I \rightarrow T_{i+2}^I$ and T_{i+5}^I. Such classifications show the advantage regarding displacement gradient accommodation, two variants in the same group have the same contribution to displacement gradient accommodation. However, such classification is inconvenient to the discussion of the activity of secondary twins with respect to the SF. Twin variants T_i^I and T_{i+3}^I have similar SF, but they are categorized into two groups, because experimental observations show a strong correlation of twin variant with the SF.

Fig. 4. 15a shows an EBSD pattern where the contraction twin contains two secondary extension twins. The trace of the twinning plane associated with the contraction twin is nearly parallel to the horizontal axis. With the help of pole figures in Fig. 4. 15b, a misorientation angle of the $(1\bar{2}12)$ twin plane between C_5^I twin and the matrix is 3.35°. Therefore, the contraction twin is determined to be twin variant C_5^I. In the pole figure of $\{10\bar{1}2\}$ planes (Fig. 4. 15c), a misorientation angle between $(0\bar{1}12)$ planes in the T_5^I twin and in the matrix is 1.21°, and that between $(1\bar{1}02)$ planes in the T_6^I twin and in the matrix is 0.80°. Fig. 4. 15d shows the pole figure of the corresponding twinning directions. The misorientation angle between $[01\bar{1}1]$ directions in the T_5^I twin and in the matrix is 1.22°, and that between $[\bar{1}101]$ directions in the T_6^I and in the matrix is 0.81°. According to the crystallography of $\{10\bar{1}2\}\langle\bar{1}011\rangle$ twins, the two secondary twin variants are twin variants T_5^I and T_6^I, belonging to Group II. We compared experiment result with the SF analysis. As shown in Fig. 4. 8e, C_5^I is the primary contraction twin, T_5^I and T_6^I are secondary twin. The SFs associated with C_5^I,T_5^I and T_6^I are 0.4295, 0.3511 and 0.3927, respectively. The SF of T_6^I is larger than that of T_5^I and the difference between T_5^I and T_6^I is 0.041, which is smaller than 0.05. This is in agreement with our prediction. The loading direction identified for the grain according to the projection of external ND into the

crystal frame is located at the predicted loading domain, as indicated by a black dot in Fig. 4. 8e. This implies that the SF criterion is satisfied. The displacement gradient accommodation and the nucleation of twinning dislocations based on dislocation dissociation are also satisfied.

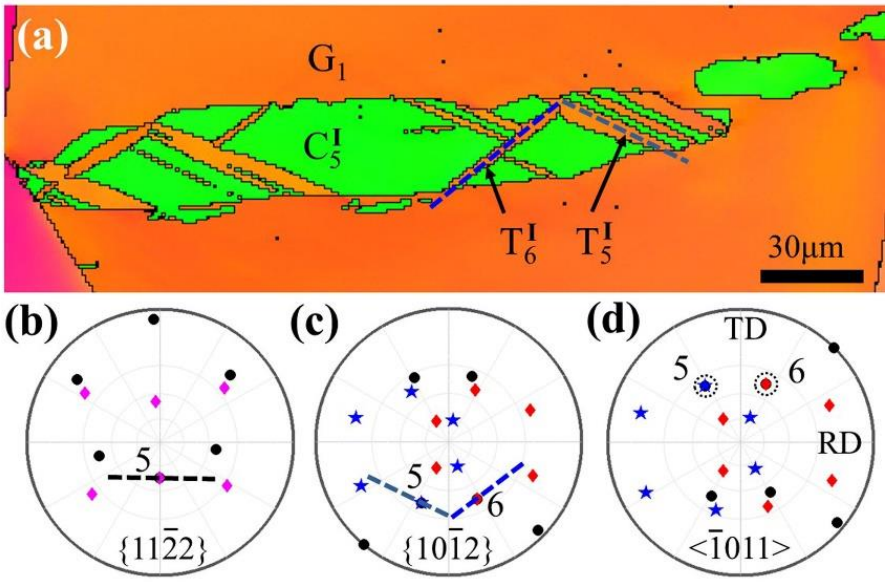

Fig. 4. 15 (a) An EBSD map of two secondary {10$\bar{1}$2} twins in a primary {11$\bar{2}$2} contraction twin as well as pole figures of (b) {11$\bar{2}$2} plane, (c) {10$\bar{1}$2} plane, (d) <$\bar{1}$011> direction. In (b), the black dots represent six {11$\bar{2}$2} twin planes in the matrix, the pink diamonds represent six {11$\bar{2}$2} in the twin. In (c), the black dots represent six {10$\bar{1}$2} twin planes in the matrix, the red diamonds and blue stars represent six {10$\bar{1}$2} twin planes in the two {10$\bar{1}$2} twins, and (d) the black dots represent six <$\bar{1}$011> twin directions in the matrix, the red diamonds and blue stars represent six <$\bar{1}$011> twin directions in the twin.

Fig. 4. 16a shows an EBSD pattern where the contraction twin contains one secondary extension twin variant. With the help of pole figures in Fig. 4. 16b, the misorientation angle between ($\bar{1}\bar{1}$22) planes in the C_4^I twin and in the matrix is 0.85°. Therefore, C_4^I twin variant can be identified as the primary twin. In the pole figure of {10$\bar{1}$2} planes (Fig. 4. 16c), the misorientation angle between ($\bar{1}$012) planes in the T_4^I twin and in the matrix is 0.72°. The misorientation angle between [10$\bar{1}$1] directions in the T_4^I twin and in the matrix is 0.73° as shown in Fig. 4. 16d. T_4^I is thus the active twin variant, belonging to Group II. The same analysis was performed for the case in Fig. 4. 16. We found that the SFs associated with C_4^I and T_4^I are 0.3222 and 0.473. The other twin variant T_5^I in Group II is 0.202, which is much smaller than T_4^I. This explains why it is unfavorable and only one twin variant appears, and T_4^I is activated. The loading direction identified for the grain according to the projection of external ND into the crystal frame is located at the predicted loading domain, as indicated by a blue dot in Fig. 4. 8f, which shows the loading domain for C_4^I variant where the SF of C_4^I variant is

greater than 0.3 and is the greatest among six equivalent variants. This result again demonstrates the SF criterion must be satisfied and predict the selection of twin variants. The displacement gradient accommodation and the nucleation of twinning dislocations based on dislocation dissociation are also satisfied, but cannot predict the selection of the activated twin variant.

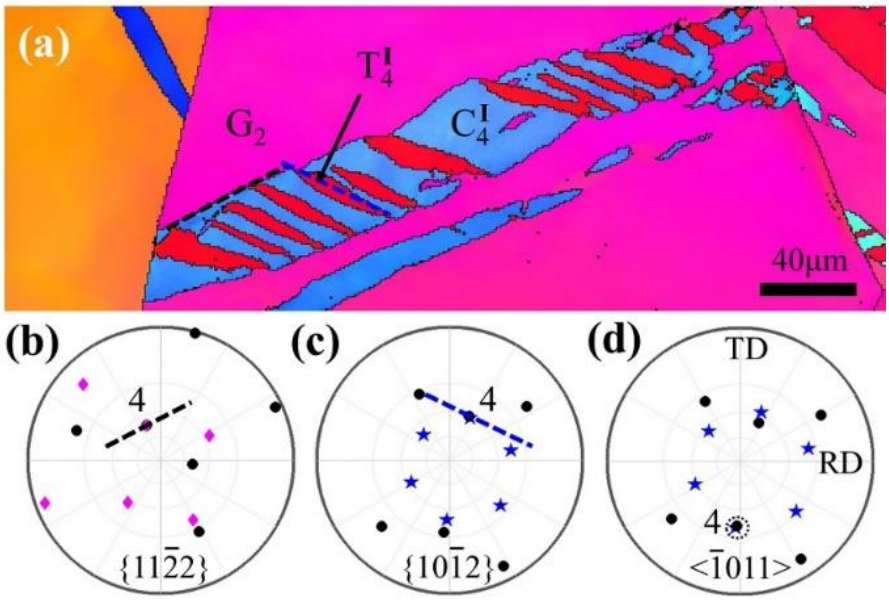

Fig. 4. 16 (a) An EBSD map of one secondary {10$\bar{1}$2} twin in a primary {11$\bar{2}$2} contraction twin as well as pole figures of (b) {11$\bar{2}$2} plane, (c) {10$\bar{1}$2} plane, (d) <$\bar{1}$011> direction. In (b), the black dots represent six {11$\bar{2}$2} twin planes in the matrix, the pink diamonds represent six {11$\bar{2}$2} in the twin. In (c), the black dots represent six {10$\bar{1}$2} twin planes in the matrix, the blue stars represent six {10$\bar{1}$2} twin planes in the {10$\bar{1}$2} twin, and (d) the black dots represent six <$\bar{1}$011> twin directions in the matrix, the blue stars represent six <$\bar{1}$011> twin directions in the twin.

4.8 Chapter conclusion

An experimental study was conducted in the present work for the combination of primary {11 $\bar{2}$ 2} compression and secondary {10 $\bar{1}$ 2} extension twins that were formed during compression in a pure polycrystalline titanium along the normal direction (ND). A detailed analysis of the detected 425 secondary {10$\bar{1}$2} twins has led to the following conclusions:

1. The 36 possible secondary twin variants can be classified into three groups in terms of misorientations between the parents and secondary twins: Group I with a misorientation of 41.34° around axis<5$\bar{1}\bar{4}$3>, Group II with a misorientation of 48.44° around axis <$\bar{5}$503> and Group III with a misorientation of 87.85° around axis <7$\bar{4}\bar{3}$0>. The EBSD statistics revealed

that Group II are far the most frequent (85.6%), while Group I and III variants were only present in a fraction of 10.6% and 3.8%, respectively.

2. Our SF based analysis showed that 93.4% of the detected secondary twins had normalized SFs larger than 0.8, where principally only a single secondary twin variant was activated in the primary compression twins. A small fraction (4.5%) of the secondary twins was found in the primary twins where two variants were observed. There was a very large fraction of secondary twins which did not obey the Schmid law. Group II is particularly disobeying the Schmid law because it represents 47.5% of the total twins and 96.2% of the non-Schmid twins. The non-Schmid part of Group I is 1.9% and for Group III it is 3.8% of the total population.

3. An apparent SF analysis also showed that Group III twins had very low SFs, leading to their low experimental frequency. However, the SF criterion has led to nearly equal theoretical frequencies for twin variants of Groups I and II, which was contradictory to the experimental observations.

4. The prevalence of Group II secondary twins over Group I was possible to justify with dislocation dissociations based on the common direction between the primary and secondary twin planes and a prismatic plane. This prismatic-dislocation mediated nucleation mechanism is applicable to both Group II and Group III double twin variants. Even though the geometrical feature also facilitates the activation of Group III double twins, the dislocation reaction presented clearly shows that a prismatic dislocation dissociating into three secondary twining dislocations for Group II twin is energetically favored while a prismatic dislocation dissociating into only one twining dislocation associated with Group III twin is energetically unfavourable. Prismatic-dislocation mediated nucleation mechanism can clarify the preference of Group II over Group I and Group III. With the help of an apparent SF analysis, the stress domains in which only one or two Group II double twin variants can be activated were in agreement with experiments.

5. With the help of dislocation mediated mechanism, the preference of Group II double twin variants over other two groups is explained. Then, an apparent SF analysis is effective to resolve the competition between two variants in Group II. The stress domain that is calculated to predict the activation of one variant or both variants belonging to Group II is in agreement with the experimental results.

When two or more twin variants are activated in one grain, a twin will meet another twin and twin-twin junctions will be produced, which plays a significant role in stain hardening of materials. However, the crystallographic feature of twin-twin junctions is seldom investigated

in pure titanium. In the next chapter, the crystallographic characters of $\{11\bar{2}2\}$ twin-twin junctions and $\{11\bar{2}1\}$ twin-twin junctions in commercially pure titanium will be introduced. Based on crystallography, six twin variants can produce three types of twin-twin junctions. According to the EBSD results, the preference of only one type of twin-twin junctions is found. An apparent SF analysis will be applied to examine the preference of one type. Besides, the formation mechanism of twin-twin boundaries will be discussed with the help of dislocation reactions.

Chapter 5 Crystallographic characters of twin-twin junctions in pure titanium

Contents

5.1 Introduction

When twin variants interact to each other, twin-twin junctions (TTJ) may form. Recent studies on $\{10\bar{1}2\}$ twin-twin interactions in Mg and Mg alloys reveal the structural features of twin-twin junctions and their influence on sequential plastic deformations [136, 167]. Firstly, one twin does not transmit across the twin boundary and into the other twin. Instead, TTBs form and contain boundary dislocations. These boundary dislocations can be inferred by the

reaction of twinning dislocations associated with the two twin variants. An "apparent crossing" TTJ is thus a consequence of TTB formation. Secondly, back-stresses induced by TTBs hinder the motion of twinning dislocations toward the TTB, producing a strong repulsive force. Further growth of twins thus requires a high stress, resulting in strain hardening during twinning. Under reversed loading, de-twinning may occur as a reversal of the forming process. Atomistic simulations further examined the characters of TTBs that were identified according to crystallography and EBSD analysis. To date, the crystallographic feature of $\{11\bar{2}2\}$ TTJs and $\{11\bar{2}1\}$ TTJs are not studied in pure titanium. Consequently, the contribution of $\{11\bar{2}2\}$ TTJs to the strain hardening was not considered in previous simulations.

In this work, we conduct a statistical analysis of $\{11\,\bar{2}\,2\}$ TTJs in pure titanium. Corresponding to the crystallography of $\{11\bar{2}2\}$ twins (C_i^I, i = 1…6), three types of $\{11\bar{2}2\}$ TTJs form. EBSD analysis among 243 detected TTJs shows that $C_{i,i+1}^I$ TTJs (C_1^I and C_2^I type) account for 79.8%, $C_{i,i+2}^I$ (C_1^I and C_3^I) and $C_{i,i+3}^I$ (C_1^I and C_4^I) TTJs only take up 17.7% and 2.5%, respectively; no twin transmission happens; an incoming twin is blocked by the other in association with the formation of twin-twin boundaries (TTBs) on one side of the incoming twin. These structural features are accounted for by the SF analysis and the reactions of twinning dislocations. The mechanisms are then applied to the analysis of $\{11\bar{2}1\}$ TTJs, which can be classified into three types, i.e., Type I (referred to as $T_{i,i+1}^{II}$), Type II ($T_{i,i+2}^{II}$) and Type III ($T_{i,i+3}^{II}$). The only occurrence of Type I TTJs can be explained by an apparent SF analysis. The preference of TTB_O belonging to Type I rather than TTB_A is examined by dislocation reactions.

5.2 Crystallography of {11$\bar{2}$2} twin-twin interactions

Corresponding to 12 rotational symmetry matrices of HCP structure, each twinning system includes 6 equivalent twin variants. Six $\{11\bar{2}2\}$ twin variants are denoted by C_i^I (the subscript i = 1…6; the superscript I refers to type I compression twin) that the subscript i increases by a counter-clockwise rotation around the *c*-axis of the crystal, as shown in Fig. 5. 1a. The interaction between two $\{11\bar{2}2\}$ twin variants can be classified into three types, as summarized in Fig. 5. 1 and Table 5. 1. Type I is associated with the interaction of C_1^I and C_2^I variants (referred to as $C_{i,i+1}^I$). The intersection line l_{12} between the two twin planes is along $[0\bar{2}23]$. Type II is associated with the interaction of C_1^I and C_3^I variants (referred to as $C_{i,i+2}^I$). The intersection line l_{13} between the two twin planes is along $[2\bar{4}23]$. Type III is associated with

the interaction of C_1^I and C_4^I variants (referred to as $C_{i,i+3}^I$). The intersection line l_{14} between the two twin planes is along $[1\bar{1}00]$.

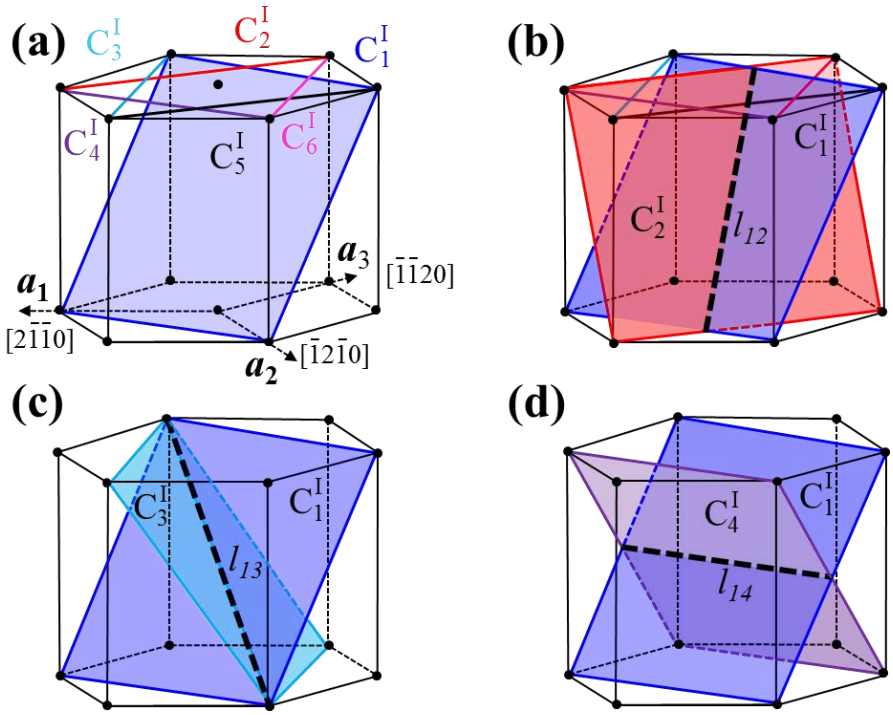

Fig. 5. 1 (a) Six $\{11\bar{2}2\}$ <$11\bar{2}\bar{3}$> (C_i^I) twin variants form three types of twin-twin junctions. (b) Type I $C_{i,i+1}^I$ with the intersection line along $[0\bar{2}23]$; (c) Type II $C_{i,i+2}^I$with the intersection line along $[2\bar{4}23]$; (d) Type III $C_{i,i+3}^I$ with the intersection line along $[1\bar{1}00]$. The bold dashed black lines indicate the intersection line.

Table 5. 1 Crystallographic characters of three types of $\{11\bar{2}2\}$ twin-twin junctions.

TTJs	Intersection line	TTB_A			TTB_O		
		in matrix	in C_1^I	in C_i^I (i=2…4)	in matrix	in C_1^I	in C_i^I (i=2…4)
$C_{i,i+1}^I$	$[0\bar{2}23]$	$(03\bar{3}4)$	$(23\ 2\ \bar{2}5\ 18)$	$(\bar{2}3\ 25\ \bar{2}\ 18)$	$(\bar{2}110)$	$(9\ \bar{1}2\ 3\ \bar{1}0)$	$(9\ 3\ \bar{1}2\ 10)$
			Twist 61.8°			Twist 0.17°	
$C_{i,i+2}^I$	$[2\bar{4}23]$	$(\bar{1}010)$	$(2\ \bar{5}\ 3\ \bar{1}0)$	$(\bar{3}\ 5\ \bar{2}\ 10)$	$(\bar{1}2\bar{1}4)$	$(58\ \bar{3}\ \bar{5}5\ \bar{6})$	$(\bar{5}5\ \bar{3}\ 58\ \bar{6})$
			Twist 8.5°			Twist 76.6°	
$C_{i,i+3}^I$	$[1\bar{1}00]$	$(\bar{1}\bar{1}20)$	$(\bar{3}\ \bar{3}\ 6\ \bar{2}0)$	$(\bar{3}\ \bar{3}\ 6\ 20)$	(0002)	$(22\bar{4}3)$	$(\bar{2}2\bar{4}3)$
			Twist 0°			Twist 0°	

When one twin approaches another twin, TTBs could form with respect to the crystallography of TTJs [136]. Regardless of the formation energy of TTBs, TTBs can be geometrically defined as the bisection plane of the two twin planes [188]. For simplicity of

description later, the TTB in the acute side of the two twinning planes is referred to as TTB_A (marked in pink) while the other in the obtuse side as TTB_O (marked in yellow) as depicted in Fig. 5. 2a. Fig. 5. 2b-d show bisection planes associated with TTJs.

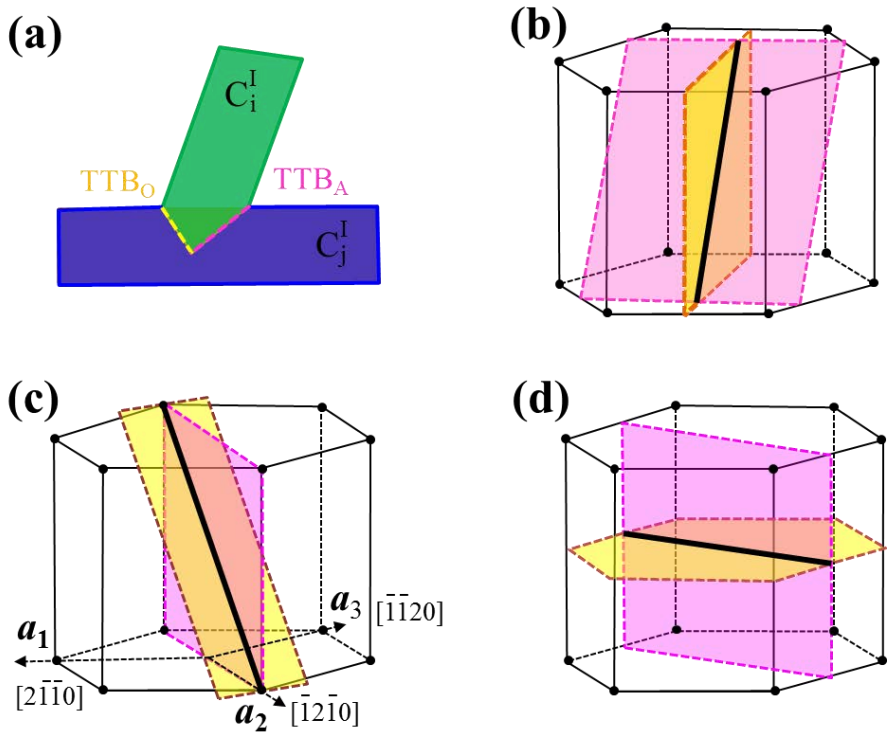

Fig. 5. 2 (a) Schematic of twin-twin boundaries associated with twin-twin junctions, where TTB_A (marked by purple) and TTB_O (marked by yellow) are formed on the acute side and on the obtuse side, respectively. Bisection planes associated with: (b) Type I $C^I_{i,i+1}$, (c) Type II $C^I_{i,i+2}$, (d) Type III $C^I_{i,i+3}$ twin-twin junctions.

For type I TTJs, TTB_A bonds the (23 2 $\overline{25}$ 18) plane in the C_1^I twin and the ($\overline{23}$ 25 $\bar{2}$ 18) plane in the C_2^I twin, and is parallel to (03$\bar{3}$4) plane in the matrix. TTB_O bonds the (9 $\overline{12}$ 3 $\overline{10}$) plane in the C_1^I twin and to the (9 3 $\overline{12}$ 10) plane in the C_2^I twin, and is parallel to the ($\bar{2}$110) in the matrix. In addition, {23 2 $\overline{25}$ 18} planes in the two twin variants are twisted 61.8° about the interface normal, {9 3 $\overline{12}$ 10} planes in the two twin variants are twisted 0.17° about the interface normal. From the geometry view, the TTB_O interface might have lower formation energy than the TTB_A interface because of its high areal density and small twist angle. For Type II TTJ, TTB_A bonds the (2 $\bar{5}$ 3 $\overline{10}$) plane in the C_1^I twin and the ($\bar{3}$ 5 $\bar{2}$ 10) plane in the C_3^I twin, and is parallel to the ($\bar{1}$010) plane in the matrix. TTB_O bonds the (58 $\bar{3}$ $\overline{55}$ $\bar{6}$) plane in the C_1^I twin and the ($\overline{55}$ $\bar{3}$ 58 $\bar{6}$) plane in the C_3^I twin, and is parallel to the ($\bar{1}2\bar{1}4$) plane in the matrix. In addition, {2 $\bar{5}$ 3 $\overline{10}$} planes in the two twin variants are twisted 8.5° about the interface normal, {$\overline{55}$ $\bar{3}$ 58 $\bar{6}$} planes in the two twin variants are twisted 76.6° about the interface normal.

Thus, the TTB_A interface might have lower formation energy. For Type III TTJ, the intersection line is parallel to their zone axis, and the two TTBs are symmetric tilt boundary. TTB_A bonds the $(\bar{3}\ \bar{3}\ 6\ \overline{20})$ plane in the C_1^I twin and the $(\bar{3}\ \bar{3}\ 6\ 20)$ plane in the C_4^I twin, and is parallel to the $(\overline{11}20)$ plane in the matrix. TTB_O bonds the $(22\overline{43})$ plane in the C_1^I twin and the $(\overline{22}4\bar{3})$ plane in the C_4^I twin, and is parallel to the (0002) plane in the matrix. Atomistic simulations showed that TTB_A interface has formation energy (820 mJ/m^2) and TTB_O interface has formation energy (710 mJ/m^2) [189].

5.3 Experiments

In this section, sample preparation is the same as the procedure used in Chapter 4. The samples were annealed in a vacuum furnace at 800 ºC for 2 h. Compression was performed along the ND at a strain rate 1 $\times 10^{-3}$ s^{-1} at room temperature.

5.4 Microstructural evolution

Fig. 5.3 shows one typical EBSD patterns of the polished surface with a step size of 0.5 μm. It can be seen that TTJs form in some grains as indicated by black arrows in Fig. 5.3. The transmission of one twin crossing another twin is not observed.

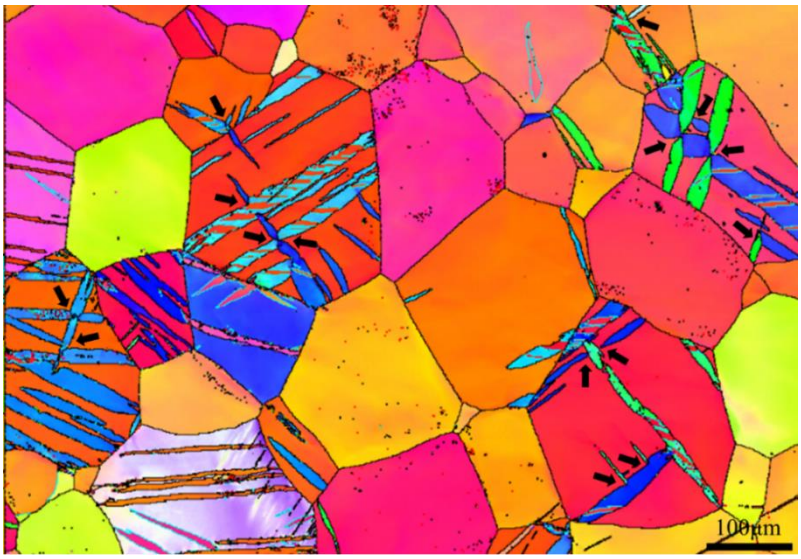

Fig. 5. 3 A typical EBSD map of deformed sample showing twin-twin junctions (indicated by the black arrows).

5.5 Experimental observation of twin–twin structures

EBSD was applied on the rolling surface of the sample subjected to uniaxial compression along the ND. Three typical microstructure was observed: (1) quilted-looking, (2) crossing, (3) double twinning when one twin meets another twin. As shown in Fig. 5.4a, C_2^I and C_6^I twins

were identified to produce C_1^I-C_3^I type junction. In Fig. 5.4b, C_1^I-C_2^I type junction was generated by the interaction of a C_1^I twin and a C_2^I twin. A twin seemly crossing another twin was shown in Fig. 5.4c-d. It can be seen that the seemly crossed region in one twin actually does not activate twinning but experiences a tilt of a small angle. In Fig. 5.4c, C_4^I twin induces a region belonging to C_5^I to be misaligned with C_5^I. The *c*-axis between this tilt region and C_5^I is 4.12°. In Fig. 5.4d, it is obviously seen that in C_1^I, the junction produced by a C_1^I twin and a C_2^I twin induces a region to be tilt. The *c*-axis between this tilt region and C_5^I is 4.15°. The loading stress favorable for the activation of $\{11\bar{2}2\}$ twins also facilitates $\{10\bar{1}2\}$ double twinning inside the $\{11\bar{2}2\}$ twins. There are two typical configurations for twin-twin junction and double twins. In Fig. 5.4e, the double twin in C_2^I connect to C_1^I twin, which forms twin-twin interaction with C_2^I primary twin. In Fig. 5.4f, C_3^I and C_5^I primary twins form an interaction. Double twins are detected within the two primary twins. However, the double twins in one primary twin do not meet the other primary twin while they are located away from the intersected point.

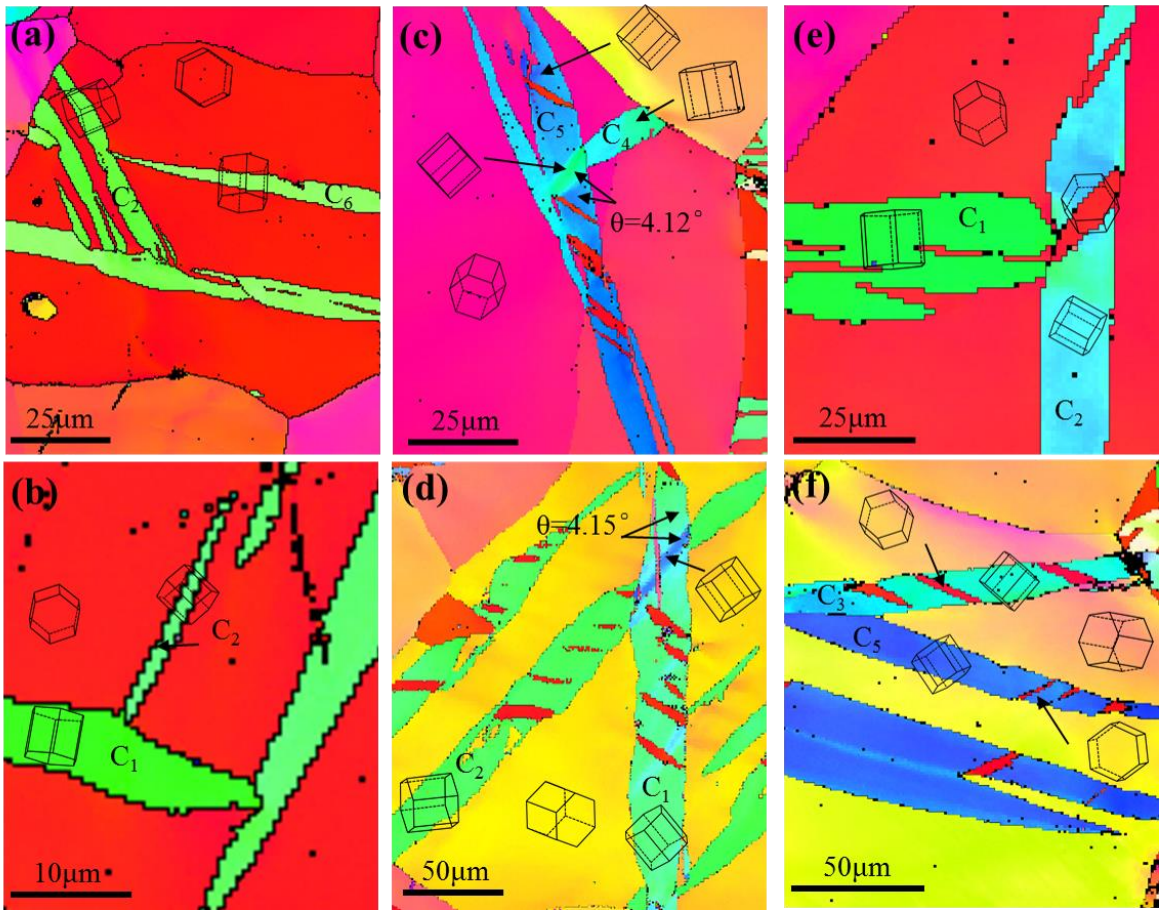

Fig. 5.4 (a-b) "Quilted-looking" sturcture of twin-twin junctions, (c-d) "Crossing" sturcture of twin-twin junctions, (e-f) Double twinning when twin-twin junctions form.

5.6 Twin-twin boundaries

In this section, twin-twin boundaries are characterized by using EBSD. In theory, two twin-twin boundaries exist for each type of twin-twin boundaries, i.e., TTB_A and TTB_O. In experiments, twin-twin boundaries are detected and the growth of intersected twins on both side of twin-twin junctions are analysed.

5.6.1 Statistics of twin-twin boundaries

We detected 243 twin-twin junctions according to EBSD patterns in 4*8 mm^2 surface of the deformed sample. Fig. 5.5a shows their frequency. Type I TTJs account for 79.8%, Type II TTJs and Type III TTJs takes up 17.7% and 2.5%, respectively. In order to further explore the dependence of TTJ Types on stresses, we calculated the SFs of these twins corresponding to the stresses in their parent grains and statistically grouped them according to the order of their SFs (Fig. 5.5b). SF_{ij} (i, j=1…6) indicates the rank of the SFs associated with the two twins among six twin variants. For example, SF_{23} means that one twin variant has the 2nd highest SF and the other twin has the 3rd highest SF. The interesting finding is that two twin variants associated with 93% of TTJs have their SFs to be first, second, or third highest among six variants. Such information enables us to explore the frequency of TTJs in the later discussion.

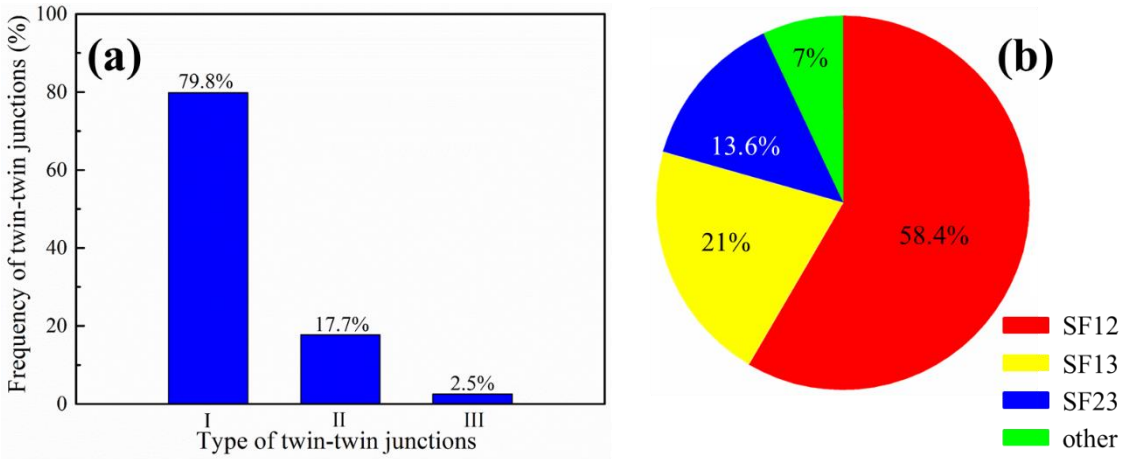

Fig. 5. 5 (a) Statistic plot of frequency of 243 detected twin-twin junctions; (b) Statistic plot of Schmid factors associated with twin-twin junctions. The subscripts ij of SF_{ij} (i, j=1…6) mean the rank of the Schmid factors associated with the two intersected twins.

TTBs form as two twins meet. In order to characterize the feature of TTJs, here we describe a geometrical analysis method based on the traces of boundary planes on the observed surface and corresponding pole figures. Because the normal of the observed surface is along

an arbitrary crystallographic direction, we firstly define the trace of a boundary plane on the observed surface according to EBSD data, then we use the corresponding pole figure to determine which crystallographic plane is a best fit to the trace. As shown in Fig. 5.6a, two planes P_i ($h_i\ k_i\ i_i\ l_i$) and P_j ($h_j\ k_j\ i_j\ l_j$) intersect. The angle θ_{ij} between the two planes can be calculated by:

$$\theta_{ij}=cos^{-1}\left(\frac{h_ih_j+k_ik_j+\frac{1}{2}\left(h_ik_j+h_jk_i\right)+\frac{3a^2}{4c^2}l_il_j}{\sqrt{\left(h_i^2+k_i^2+h_ik_i+\frac{3a^2}{4c^2}l_i^2\right)\left(h_j^2+k_j^2+h_jk_j+\frac{3a^2}{4c^2}l_j^2\right)}}\right) \quad (5\text{-}1)$$

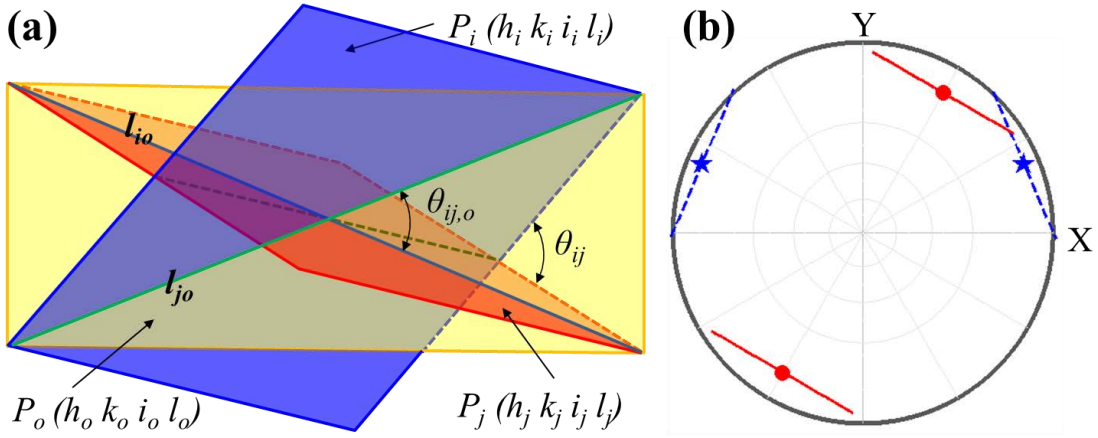

Fig. 5. 6 (a) Schematic of the angle between two twin planes of twins C_i^I and C_j^I on an observed plane Po. (b) A pole figure showing the traces of two twin planes on the observed plane. The red symbols correspond to the observed plane Po = (0002), and the blue symbols correspond to the observed plane Po = $(1\bar{1}02)$.

However, the measured angle between the traces of the two planes on an observed surface varies with respect to the normal of the observed surface. On an observed surface P_o *($h_o\ k_o\ i_o\ l_o$)*, the trace of P_i on P_o is given by

$$l_{io}=\left[\frac{a}{c}k_il_o-\frac{a}{c}k_ol_i,\ \frac{\sqrt{3}a}{3c}l_i(2h_o+k_o)-\frac{\sqrt{3}a}{3c}l_o(2h_i+k_i),\ \frac{2\sqrt{3}a}{3c}h_ik_o-\frac{2\sqrt{3}a}{3c}h_ok_i\right] \quad (5\text{-}2)$$

and the trace of P_j on P_o is given by

$$l_{jo}=\left[\frac{a}{c}k_jl_o-\frac{a}{c}k_ol_j,\ \frac{\sqrt{3}a}{3c}l_j(2h_o+k_o)-\frac{\sqrt{3}a}{3c}l_c\left(2h_j+k_j\right),\ \frac{2\sqrt{3}a}{3c}h_jk_o-\frac{2\sqrt{3}a}{3c}h_ok_j\right] \quad (5\text{-}3)$$

The angle $\theta_{ij,o}$ between the two traces is given by:

$$\theta_{ij,o}=cos^{-1}\left(\frac{l_{io}\cdot l_{jo}}{|l_{io}||l_{jo}|}\right) \quad (5\text{-}4)$$

The angle $\theta_{ij,o}$ represents the measured angle between the two planes P_i and P_j on the observed surface P_o. As illustrated in Fig. 5.6b, the pole figure has Y || the intersection line between the observed surface and (0002) plane, Z || the normal of the observed plane, and X = Y×Z. For two twin planes P_1 $(11\bar{2}2)$ and P_4 $(\bar{1}\bar{1}22)$ in titanium, the angle θ_{14} is 64°. When the observed surface P_o is (0002) plane, the red lines indicate the traces of the two planes on the observed surface and are parallel. Thus, the measured angle $\theta_{14,o}$ is equal to 0°. When P_o is $(1\bar{1}02)$, $\theta_{14,o}$= 46°. The blue dashed lines indicate the traces of the two planes on the observed surface.

5.6.2 Characterizations of twin-twin boundaries

Using the method mentioned above, EBSD data was applied to detect if both twin-twin boundaries can occur for each type. The intriguing feature associated with TTJs is that twin-twin boundary only forms in one side of the incoming twin as one twin meets another twin.

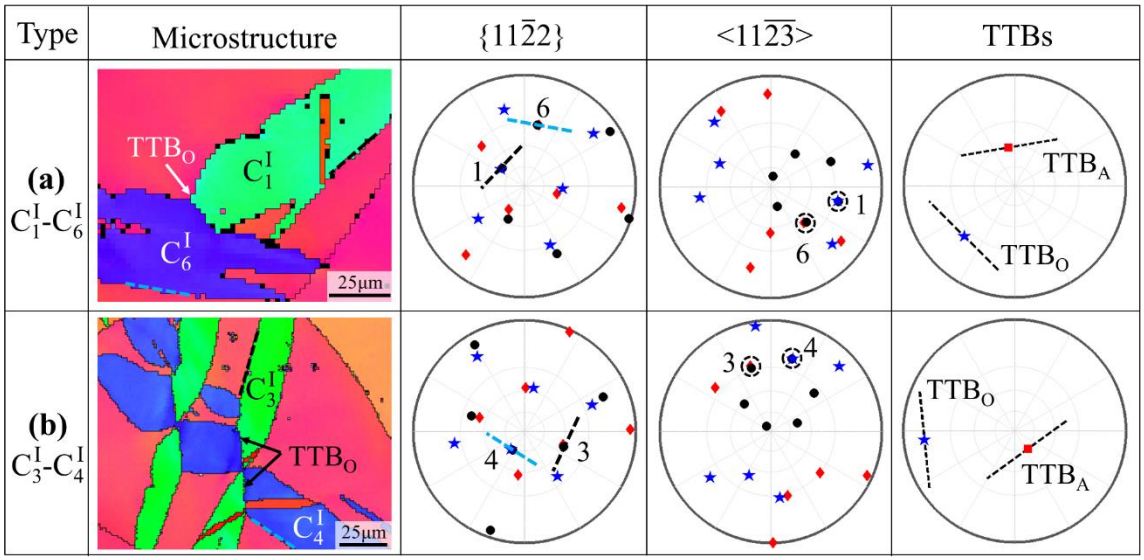

Fig. 5. 7 Microstructure of C_1^I-C_2^I type twin-twin junction as well as {11$\bar{2}$2} and <11$\bar{2}$3> pole figures. The segments in {11$\bar{2}$2} pole figures indicate the trace of the twinning planes. The traces of TTB_A and TTB_O associated with the junction were shown in the pole figures of TTBs.

For Type I TTJs, Fig. 5.7a shows a $C_{1,6}^I$ TTJ, i.e. $(11\bar{2}2)$ $[11\bar{2}3]$ (C_1^I) and $(2\bar{1}\bar{1}2)$ $[2\bar{1}\bar{1}3]$ (C_6^I) twins. Crystallographic planes of TTB_A and TTBo are parallel to $(30\bar{3}4)$ and $(1\bar{2}10)$ in the

matrix, respectively. From the pole figures, we determined the traces of C_1^I and C_6^I twin planes, and the traces of $(30\bar{3}4)$ and $(1\bar{2}10)$ in the matrix (Euler angles of the matrix: φ_1=90.3°, Φ=32.2°, φ_2=38.4°). The angle $\theta_{16,O}$ between C_1^I and C_6^I twin planes on the observed surface P_o (0.2296, 1.2320, $\overline{1.4616}$, 3.9627) is measured to be 64°, which is approximately equal to the measured angle, 63.25° from the EBSD pattern. In addition, the angle θ_{1TTBo} between the traces of C_1^I and the TTB_O plane $(1\bar{2}10)$ is 81.33°, which is close to 81.98° that was measured from the EBSD image. Thus, TTB_O was formed as predicted by the crystallography of the TTJ. However, it can be seen that TTB_A does not form. Another example in Fig. 5.7b is associated with the $C_{3,4}^I$ TTJ, i.e. $(\bar{2}112)$ $[\bar{2}11\bar{3}]$ (C_3^I) and $(\overline{11}22)$ $[\overline{11}2\bar{3}]$ (C_4^I) twin on the observed plane P_o (1.1206, 0.6045, $\overline{1.7251}$, $\overline{3.7693}$). Crystallographic planes of TTB_A and TTBo are $(\bar{3}034)$ and $(1\bar{2}10)$ in the matrix (Euler angles of the matrix: φ_1=170.4°, Φ=35.6°, φ_2=49.4°), respectively. The angle $\theta_{3,TTBo}$ between C_3^I twin plane and TTB_O plane on this observed plane is 27°, which is close to 26.5° measured from the corresponding EBSD image. Again, TTB_A was not observed. The growth of the twins is favorable on the side where TTBs form. It is worth mentioning that TTBo was formed among all type I TTJs while TTB_A was not observed.

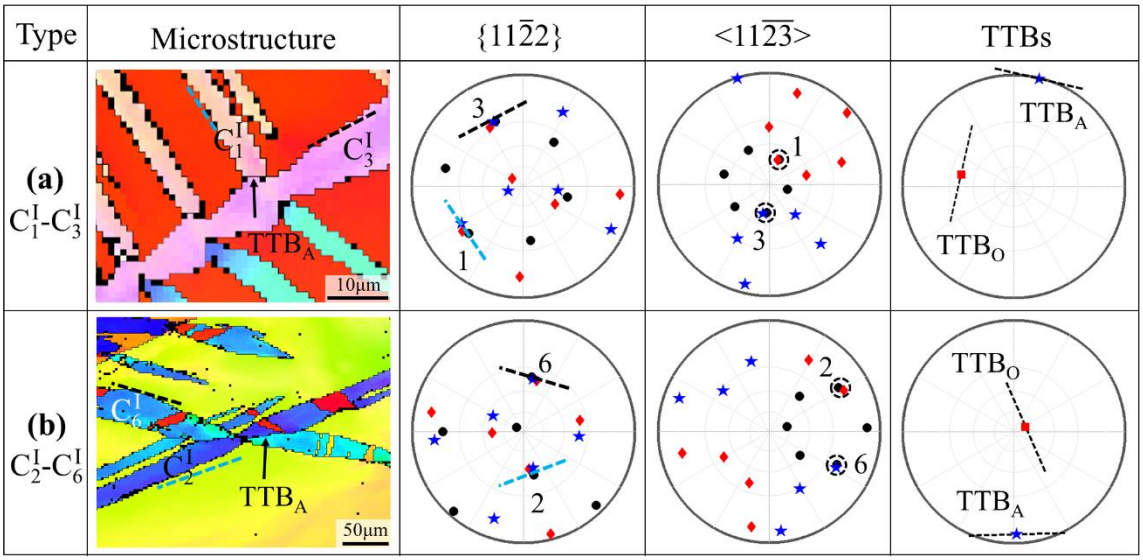

Fig. 5. 8 Microstructure of C_1^I-C_3^I type twin-twin junction as well as {11$\bar{2}$2} and <11$\bar{2}\bar{3}$> pole figures. The segments in {11$\bar{2}$2} pole figures indicate the trace of the twinning planes. The traces of TTB_A and TTB_O associated with the junction were shown in the pole figures of TTBs.

We further analysed other two types of TTJs. For Type II (Fig. 5.8a), a Type II TTJ is $C_{2,6}^I$ associated with $(\bar{1}2\bar{1}2)$ $[\bar{1}2\bar{1}3]$ and $(2\bar{1}\bar{1}2)$ $[2\bar{1}\bar{1}3]$ twins (Euler angles of the matrix: φ_1=79.3°, Φ=166.5°, φ_2=2.4°). On the observed plane ($\overline{0.3191}$, 0.6881, $\overline{0.3690}$, $\overline{4.5536}$), TTB_A was

observed while TTB_O was not observed. Another example in Fig. 5.8b is associated with the $C^I_{2,6}$ TTJ, i.e. $(\bar{1}2\bar{1}2)$ $[\bar{1}2\bar{1}\bar{3}]$ (C^I_2) and $(2\bar{1}\bar{1}2)$ $[2\bar{1}\bar{1}\bar{3}]$ (C^I_6) twin on the observed plane P_o (1.0399, 1.2400, $\overline{2.2799}$, 2.9661) (Euler angles of the matrix: φ_1=94.2°, Φ=50.7°, φ_2=57.1°). Among all type II TTJs, it seemed that only TTB_A was formed. It can also be noticed that the twins preferentially grow on one side of the intersected twins.

Type III TTJs are rarely observed in the EBSD data. Fig. 5.9a shows a Type III TTJ. It consists of a $(\bar{2}112)$ $[\bar{2}11\bar{3}]$ (C^I_3) twin and a $(2\bar{1}\bar{1}2)$ $[2\bar{1}\bar{1}\bar{3}]$ (C^I_6) twin (Euler angles of the matrix: φ_1=77°, Φ=139.8°, φ_2=2.2°). On the observed planes ($\overline{0.8880}$, 1.9027, $\overline{1.0147}$, $\overline{3.5769}$), TTB_A was observed while TTB_O did not appear. Another similar Type III TTJ is presented in Fig. 5.9b, which also corresponds to a $C^I_{3,6}$ TTJ on the observed plane P_o ($\overline{0.3536}$, 0.8487, $\overline{0.4951}$, $\overline{4.4831}$) (Euler angles of the matrix: φ_1=75.3°, Φ=163.2°, φ_2=5.5°).

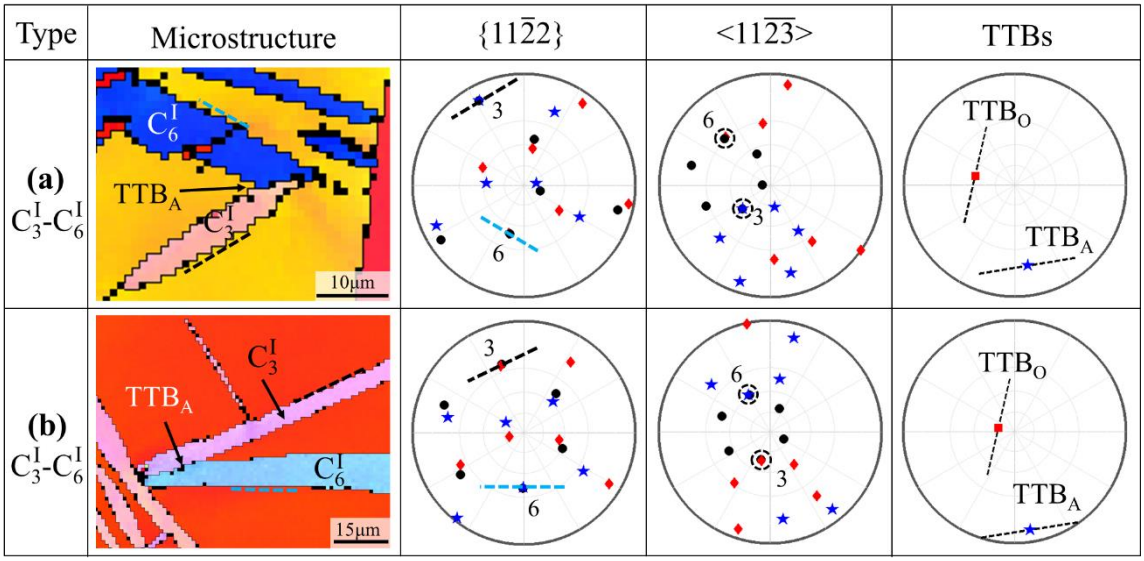

Fig. 5. 9 Microstructure of C^I_1-C^I_4 type twin-twin junction as well as {11$\bar{2}$2} and <11$\bar{2}$3> pole figures. The segments in {11$\bar{2}$2} pole figures indicate the trace of the twinning planes. The traces of TTB_A and TTB_O associated with the junction were shown in the pole figures of TTBs.

5.6.3 Formation of twin-twin boundaries

The formation of TTBs was described as the reaction of twinning dislocations [136]. In order to investigate why only one TTB is preferred while the other one is difficult to occur, the dislocation reactions during the formation of TTBs are examined here. For clear illustration of twin-twin interactions, Fig. 5.10 shows the three-dimensional geometry for the three twin–twin interactions. In the figure, C^I_1 is the pre-existing twin. C^I_2, C^I_3 and C^I_4 are the incoming twins. The coordinate system is established as: X-axis || the twinning shear direction of C^I_1 twin [11$\bar{2}$3],

Y-axis ‖ the normal direction of C_1^I twinning plane $(11\bar{2}2)$ and Z-axis ‖ the zone direction of C_1^I $[1\bar{1}00]$. b^I is the Burgers vector of the impinging twinning dislocation. b^A and b^O represent the Burgers vectors of the twin-twin boundaries on the acute side and obtuse side, respectively.

When two intersected twins grow through the glide of twinning dislocations, these twinning dislocations meet and react, forming TTBs. Therefore, the Burgers vector of the resultant dislocations at the TTB is the sum of the twinning dislocations associated with the two twins, where all dislocation lines are assumed along the intersection line.

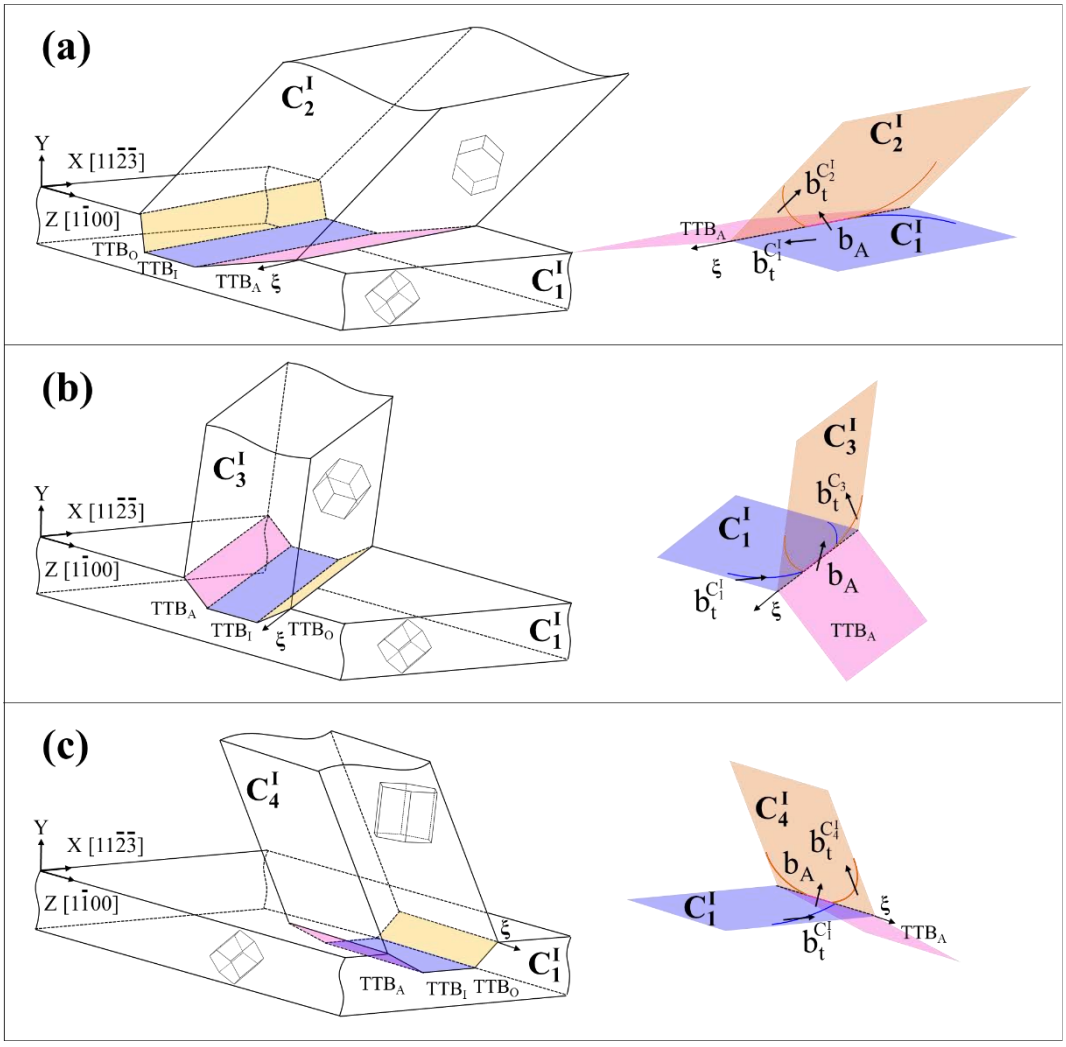

Fig. 5. 10 Illustration of twin-twin interaction for three types of twin-twin junctions.

For TTB_A associated with C_1^I-C_2^I TTJ, the Burgers vector of the resultant interface dislocation is:

$$b_t^{C_2^I} + b_t^{C_1^I} \Rightarrow b_{21}^A$$

$$\lambda[1\bar{2}13]+\lambda[\bar{1}\bar{1}23]\Rightarrow 3\lambda[0\bar{1}12] \tag{5-5}$$

The Burgers vector of the resultant interface dislocation in TTB_O is thus equal to:

$$b_t^{C_2^I} - b_t^{C_1^I} \Rightarrow b_{21}^O$$

$$\lambda[1\bar{2}13]+\lambda[11\bar{2}\bar{3}]\Rightarrow\lambda[2\bar{1}\bar{1}0] \quad (5\text{-}6)$$

In the above equations, $\lambda=\frac{(c/a)^2\text{-}2}{3((c/a)^2+1)}$, 0.0491 for titanium. $b_t^{C_2^I}$ is the Burgers vector of the impinging twinning dislocation. b_{21}^A and b_{21}^O represent the Burgers vectors of the resultant boundary dislocations on the acute side and obtuse side, when C_2^I twin meets primary C_1^I twin. We also analysed other two twin-twin interactions, C_3^I twin meets C_1^I twin and C_4^I twin meets C_1^I twin. The resultant interface dislocations have Burgers vectors: $b_{31}^A = 3\lambda[10\bar{1}0]$, $b_{31}^O = \lambda[1\bar{2}16]$, $b_{41}^A = 2\lambda[11\bar{2}0]$, $b_{41}^O = 6\lambda[0001]$. The elastic energy of these dislocations is proportional to the square of the magnitude of Burgers vector. Table 5. 2 summarizes the elastic energy of these dislocations. According to Frank's law [73], the elastic energy of two twinning dislocations associated with C_2^I and C_1^I twins is proportional to $63.36(\lambda a)^2$. The elastic energy for a resultant interface dislocation in TTBs is proportional to $117.72(\lambda a)^2$ for TTB_A and $9(\lambda a)^2$ for TTB_O, respectively. Thus, TTB_O associated with C_2^I-C_1^I TTJ is energetically preferred than TTB_A. The similar analysis reveals that TTB_A associated with both C_4^I-C_1^I and C_4^I-C_1^I TTJs is energetically preferred than TTB_O. The results are in agreement with experimental observations.

Table 5. 2 Burgers vectors for three types of $\{11\bar{2}2\}$ twin-twin junctions before and after dislocation reaction.

Junction	b^I	b^A	b^O	$2\|b^I\|^2/(\lambda a)^2$	$\|b^A\|^2/(\lambda a)^2$	$\|b^O\|^2/(\lambda a)^2$
$C_2^I \leftrightarrow C_1^I$	$\lambda[\bar{1}2\bar{1}\bar{3}]$	$3\lambda[0\bar{1}12]$	$\lambda[2\bar{1}\bar{1}0]$	63.36	117.72	9.00
$C_3^I \leftrightarrow C_1^I$	$\lambda[\bar{2}11\bar{3}]$	$3\lambda[10\bar{1}0]$	$\lambda[1\bar{2}16]$	63.36	27.00	99.72
$C_4^I \leftrightarrow C_1^I$	$\lambda[\bar{1}\bar{1}2\bar{3}]$	$2\lambda[11\bar{2}0]$	$6\lambda[0001]$	63.36	36.00	90.72

5.7 Discussions

EBSD analysis reveals so far that type I TTJs are prolific among three types of TTJs, twin transmission crossing another twin is not happened, and TTB is formed only on the one side of the incoming twin. These structural features could be addressed according to stress states and dislocation structures of boundaries.

5.7.1 High frequency of Type I TTJs

Without loss of generality, we conducted an apparent SF analysis. According to the SF analysis for detected TTJs, twin variants were activated when their SFs are the top three highest among six variants. Correspondingly, $\{11\bar{2}2\}$ twin variant C_1^I is chosen to be the active one in this study. The grain is subjected to uniaxial compression. We determine the loading domain in which the activated twin has the first, second, or third highest SF among six variants. Fig. 5.11a shows the C_1^I loading domain in which the SF associated with C_1^I is the first, second, or third highest among six twin variants. The similar analysis was conducted for twin variants C_2^I, C_3^I, and C_4^I, as plotted in Fig. 5.11b, c, and d, respectively.

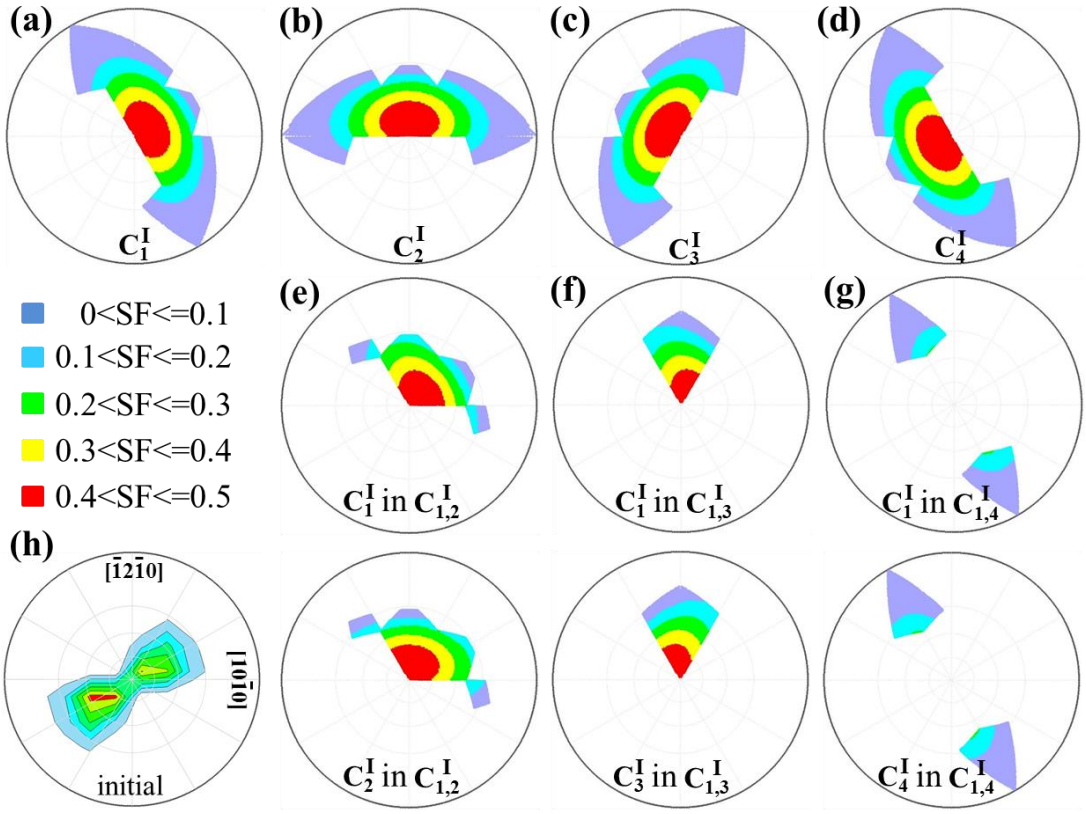

Fig. 5. 11 Loading domains associated with formation of TTJs (a) C_1^I, (b) C_2^I, (c) C_3^I, and (d) C_4^I. The common loading domains associated with the formation of TTJs (e) C_1^I in $C_{1,2}^I$and C_2^I in $C_{1,2}^I$, (f) C_1^I and C_3^I in $C_{1,3}^I$ and (g) C_1^I and C_4^I in $C_{1,4}^I$. (h) Inverse pole figure of the initial grains.

For a pair of twins that form a TTJ, the common loading domain is determined by overlapping their loading domains. Fig. 5.11e, f, and g show the common loading domain associated with the formation of type I $C_{1,2}^I$ TTJ, type II $C_{1,3}^I$ TTJ, and type III $C_{1,4}^I$ TTJ, respectively. It is noticed that type I TTJ will be activated with high SFs under most loadings in the loading domain, while type III TTJ will be activated with small SFs. In addition, under

compression on the ND of rolling Ti sheets with a strong texture (Fig. 5.11h), the formation of Type I TTJs will be profuse, while Type III TTJs will be rarely activated.

5.7.2 Twin transmission

A general analysis for identifying the possibilities of a twin crossing the other twin can be done using the SF criterion [136]. To facilitate this discussion, we refer to the pre-existing twin as C_1^I and the incoming twin as C_j^I (j=2,3,4,5,6). Taking the twin pair C_1^I and C_4^I as an example, Fig. 5.12a and b plot the SF associated with the two twin variants in an inverse pole figure when the parent is subjected to uniaxial compression. A positive SF (red domain) is associated with the stress directions that induce a resolved shear along the positive shear direction and activate C_i^I twinning. The domain with zero SF is depicted in white and with negative SF in blue.

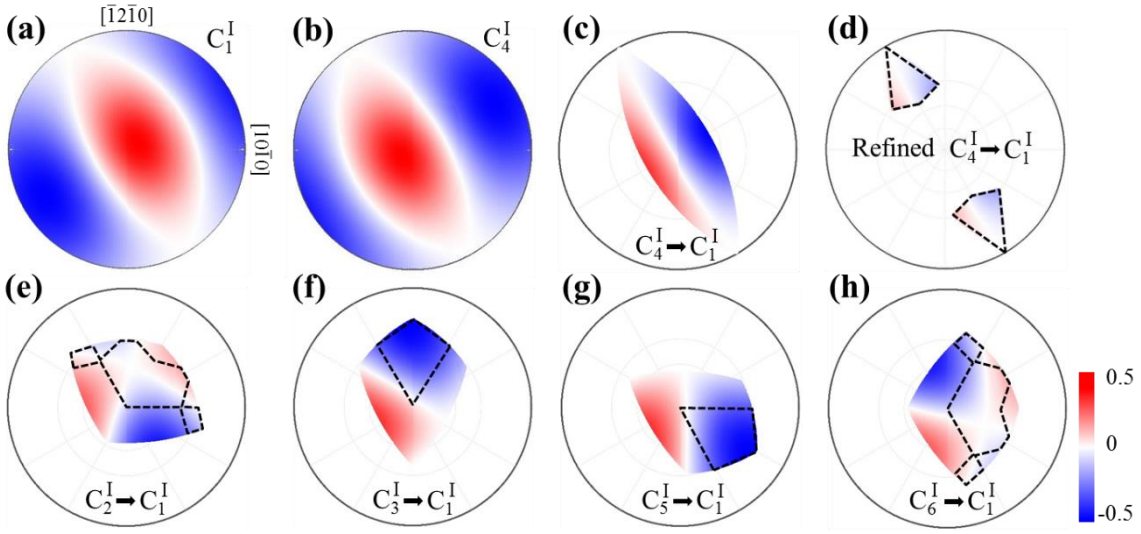

Fig. 5. 12 The feasibility analysis of twin transmission according to Schmid factors of twin variants, when the parent crystal is subjected to uniaxial compression. (a) and (b) the loading domain associated with the activation of C_1^I and C_4^I in the parent crystal. (c) The SF associated with C_4^I twin variant in the twinned crystal C_1^I when the crystal is subjected to the loading in the common loading domain. (d) The refined common loading domain according to the feasibility of $C_{1,4}^I$ TTJ's formation. Red indicates domain with positive SF while blue with negative SF. The common loading domain (colour region) and the refined common loading domain (outlined by the dashed line) associated with twin transmission of (e) C_2^I, (f) C_3^I, (g) C_5^I, and (h) C_6^I twin variant into the twinned domain C_1^I.

The loading domain in which two twins can be activated is defined as the common loading domain, which is the overlap red region (the outline of the color region in Fig. 5.12c) by overlapping Fig. 5.12a and b. In the common loading region, we recalculated the SF associated

with the twin C_4^I in the twinned crystal C_1^I. The variation of the SF of C_4^I in C_1^I is plotted in Fig. 5.12c. It seems that twin transmission is possible because of the red region in the common loading domain. When refining the loading domain according to Fig. 5.12d, it is obvious that the common loading domain associated with the transmission of C_4^I into C_1^I has very small SF. Thus, twin transmission is mechanically unfavorable. Using the same analysis, we examined the feasibility of twin transmission associated with other four twin variants C_2^I, C_3^I, C_5^I, and C_6^I, as shown in Fig. 5.12e-h. The outline of the color region shows the common loading domain associated with the positive SFs for both twins in the parent disregarding the formation of $C_{1,j}^I$ TTJs, while the dashed line further refines the common loading domain corresponding to their formation. It is obvious there is no twin transmission because of the near zero or negative SF associated with the transmitted twin in the pre-existing twin. This is in agreement with the experimental results.

5.8 Extended to the analysis of {11$\bar{2}$1} twin-twin junctions

5.8.1 Introduction

As mentioned in Section 3.2, sequential {10$\bar{1}$2} twins are stimulated by {11$\bar{2}$1} twin-twin junctions. The mechanism has been analysed in terms of SF and displacement gradient tensor based accommodation. However, the feature of {11$\bar{2}$1} twin-twin junctions is still unclear. According to the above method, we make a statistical analysis of {11$\bar{2}$1} twin-twin junctions in this section in order to understand the frequency of different types of {11$\bar{2}$1} twin-twin junctions and preferential formation of {11$\bar{2}$1} twin-twin boundaries. This section is based on the experiment in Section 3.2.

5.8.2 Crystallography

There are six {11$\bar{2}$1} twin variants denoted by T_i^{II} (the subscript i = 1…6; the superscript II represents type II extension twin) that the subscript i increases by a counter-clockwise rotation around the *c*-axis of the crystal, as shown in Fig. 5.13a. Three types of twin-twin junctions can happen when two {11$\bar{2}$1} twin variants meet as depicted in Fig. 5.13b-d. In Fig. 5.13b, Type I is defined with the interaction line l_{12} of T_1^{II} and T_2^{II} twin variants (referred to as $T_{i,i+1}^{II}$) parallel to [0$\bar{1}$13]. In Fig. 5.13c, Type II TTJ is generated by T_1^{II} and T_3^{II} twin variants (referred to as $T_{i,i+2}^{II}$). The intersection line l_{13} between the two twin planes is along [1$\bar{2}$13]. In Fig. 5.13d, Type III TTJ is depicted with the interaction line l_{14} of T_1^{II} and T_4^{II} twin variants

(referred to as $T^{II}_{i,i+3}$) along [1$\bar{1}$00]. The intersection lines for three types of TTJs are marked by white dashed lines.

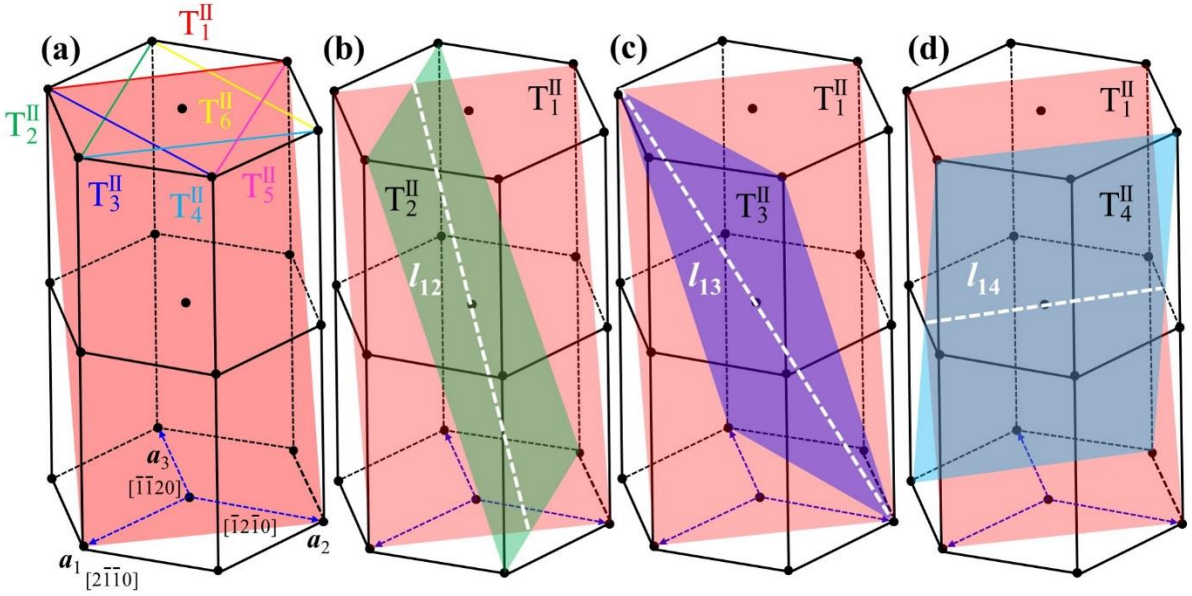

Fig. 5. 13 (a) Six {11$\bar{2}$1} <$\bar{1}\bar{1}$26> (T^{II}_i) twin variants form three types of twin-twin junctions. (b) Type I $T^{II}_{i,i+1}$ with the intersection line along [0$\bar{1}$13]; (c) Type II $T^{II}_{i,i+2}$with the intersection line along [1$\bar{2}$13]; (d) Type III $T^{II}_{i,i+3}$ with the intersection line along [1$\bar{1}$00]. The dashed white lines indicate the intersection line.

Similarly, the TTB in the acute side of the two twinning planes is called TTB_A while the other in the obtuse side as TTB_O. For type I TTJs, TTB_A corresponds to (03$\bar{3}$2) plane in the matrix. When it is expressed into the crystal orthonormal frame of the twins as listed in Table 5.3, TTB_A bonds the (34 1 $\overline{35}$ 12) plane in the T^{II}_1 twin and the ($\overline{34}$ 35 $\bar{1}$ 12) plane in the T^{II}_2 twin. Besides, TTB_O is parallel to the ($\bar{2}$110) in the matrix. TTB_O corresponds to the (12 $\overline{21}$ 9 $\overline{10}$) plane in the T^{II}_1 twin and to the (12 9 $\overline{21}$ 10) plane in the T^{II}_2 twin, and. The planes in the two twins are twisted 34.5° for TTB_A and 0.06° for TTB_O. From the geometry view, the TTB_O interface of Type I TTJs might have lower formation energy than the TTB_A interface because of its small twist angle. For type II TTJs, TTB_A corresponds to ($\bar{1}$010) plane in the matrix. When it is expressed into the crystal orthonormal frame of the twins, TTB_A bonds the (1 $\overline{10}$ 9 $\overline{10}$) plane in the T^{II}_1 twin and the ($\bar{9}$ 10 $\bar{1}$ 10) plane in the T^{II}_3 twin. Besides, TTB_O is parallel to the ($\bar{1}$2$\bar{1}$2) in the matrix. TTB_O corresponds to the (28 $\bar{9}$ $\overline{19}$ $\bar{9}$) plane in the T^{II}_1 twin and to the ($\overline{19}$ $\bar{9}$ 28 $\bar{9}$) plane in the T^{II}_3 twin. The planes in the two twins are twisted 0.07° for TTB_A and 61.33° for TTB_O. From the geometry view, the TTB_A interface of Type I TTJs might have lower formation energy than the TTB_O interface because of its small twist angle. For type III TTJs, TTB_A corresponds to ($\bar{1}\bar{1}$20) plane in the matrix. When it is expressed into the crystal

orthonormal frame of the twins, TTB_A bonds the $(\bar{9}\ \bar{9}\ 18\ \bar{2}\bar{0})$ plane in the T_1^{II} twin and the $(\bar{9}\ \bar{9}\ 18\ 20)$ plane in the T_4^{II} twin. Besides, TTB_O is parallel to the (0002) in the matrix. TTB_O corresponds to the $(22\bar{4}\bar{9})$ plane in the T_1^{II} twin and to the $(\bar{2}\bar{2}4\bar{9})$ plane in the T_4^{II} twin.

Table 5. 3 Crystallographic characters of three types of $\{11\bar{2}1\}$ twin-twin junctions.

TTJs	Intersection line	TTB_A			TTB_O		
		in matrix	in C_1^I	in C_i^I (i=2…4)	in matrix	in C_1^I	in C_i^I (i=2…4)
$T_{i,i+1}^{II}$	$[0\bar{1}13]$	$(03\bar{3}2)$	$(34\ 1\ \bar{3}\bar{5}\ 12)$	$(\bar{3}\bar{4}\ 35\ \bar{1}\ 12)$	$(\bar{2}110)$	$(12\ \bar{2}\bar{1}\ 9\ \bar{1}\bar{0})$	$(12\ 9\ \bar{2}\bar{1}\ 10)$
			Twist 34.5°			Twist 0.06°	
$T_{i,i+2}^{II}$	$[1\bar{2}13]$	$(\bar{1}010)$	$(1\ \bar{1}\bar{0}\ 9\ \bar{1}\bar{0})$	$(\bar{9}\ 10\ \bar{1}\ 10)$	$(\bar{1}2\bar{1}2)$	$(28\ \bar{9}\ \bar{1}\bar{9}\ \bar{9})$	$(\bar{1}\bar{9}\ \bar{9}\ 28\ \bar{9})$
			Twist 0.07°			Twist 61.33°	
$T_{i,i+3}^{II}$	$[1\bar{1}00]$	$(\bar{1}\bar{1}20)$	$(\bar{9}\ \bar{9}\ 18\ \bar{2}\bar{0})$	$(\bar{9}\ \bar{9}\ 18\ 20)$	(0002)	$(22\bar{4}\bar{9})$	$(\bar{2}\bar{2}4\bar{9})$
			Twist 0°			Twist 0°	

5.8.3 Frequency of twin-twin junctions

As mentioned in Chapter 3, we identified 46 $\{11\bar{2}1\}$ TTJs. A typical EBSD pattern is shown in Fig. 5.14a. In the grain indicated by G, two $\{11\bar{2}1\}$ twins (Tw1 and Tw2) meet. In Fig. 5.14b, {0002} poles are reoriented near the centre of the pole figure by Tw1 and Tw2, which are identified to be $(11\bar{2}1)<\bar{1}\bar{1}26>$ and $(\bar{1}2\bar{1}1)<1\bar{2}16>$ with the help of $\{11\bar{2}1\}$ pole figure in Fig. 5.14c, respectively. The bisection planes between $(11\bar{2}1)$ and $(\bar{1}2\bar{1}1)$ planes are $(03\bar{3}2)$ and $(\bar{2}110)$, which are projected in the macroscopic frame as shown in Fig. 5.14d, where the dashed lines represent the trace of the bisection planes. It indicates that the detected TTB marked by a dashed white line in Fig. 5.14a corresponds to TTBo. There are three interesting findings about the detected $\{11\bar{2}1\}$ twin-twin junctions. Firstly, all these detected $\{11\bar{2}1\}$ TTJs belong to Type I ($T_{i,i+1}^{II}$) with the interaction line parallel to $<0\bar{1}13>$ while other two types do not appear. Secondly, the SFs of the two twins forming a TTJ are always the highest and the second highest among all six equivalent variants. Besides, TTB_A of Type I corresponds to $(03\bar{3}2)$ plane in the matrix and TTB_O is parallel to the $(\bar{2}110)$ in the matrix. All the detected TTBs were found to lie in $\{\bar{2}110\}$ planes, which indicates that only TTB_O belonging to Type I happens. In the following part, the only presence of Type I TTJs is examined by using an apparent SF analysis. To understand the preference of TTB_O of Type I over TTB_A, analysis of the dislocation reactions when TTJs form is applied.

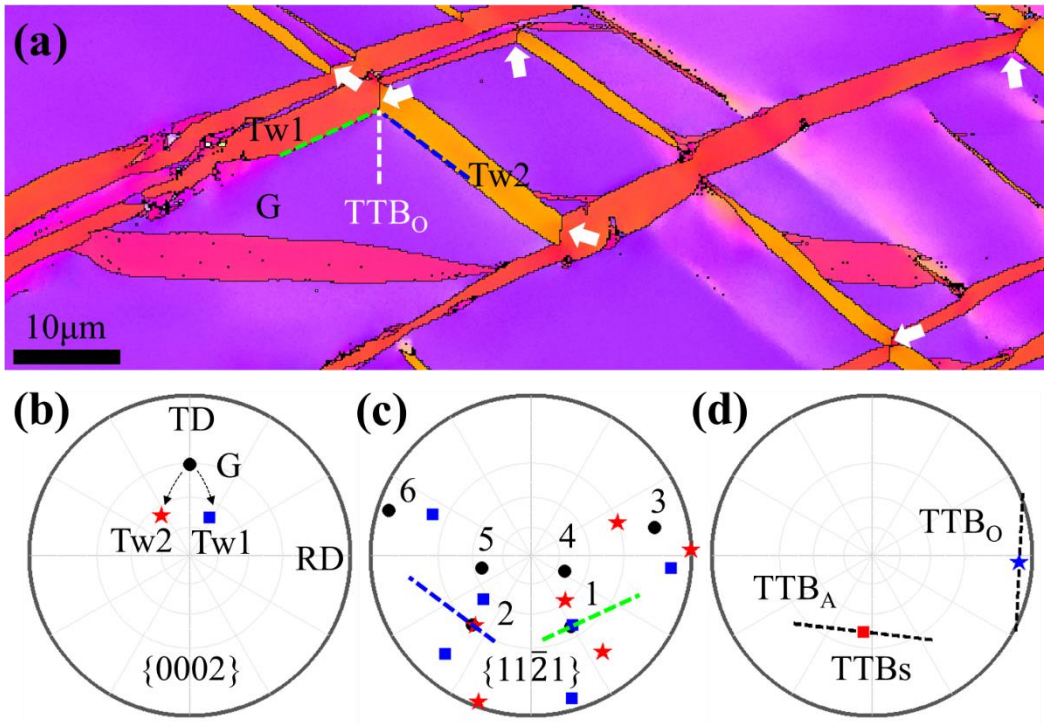

Fig. 5. 14 (a) A typical EBSD map showing {11$\bar{2}$1} twin-twin junctions indicated by white arrows. Black dots, blue squares and red stars represent the grain (G, Euler angles: φ_1=0.3°, Φ=120.8°, φ_2=35.4°), twin 1 (Tw1, Euler angles: φ_1=153.5°, Φ=29.5°, φ_2=44.9°) and twin 2 (Tw2, Euler angles: φ_1=34.6°, Φ=146.2°, φ_2=58.5°), respectively. Pole figures of: (b) {0002} planes, (c) {11$\bar{2}$1} planes and (d) the bisection planes of Tw1 and Tw2.

5.8.4 Discussion

5.8.4.1 Why only Type I appears

According to the macroscopic SF analysis in Section 3.2, all {11$\bar{2}$1} twin variants have the highest or second highest SF. Without loss of generality, an apparent SF analysis is applied here based on the hypothesis that the grain is subjected to uniaxial compression. Firstly, {11$\bar{2}$1} twin variant T_1^{II} is chosen to be one in this study. We determine the loading domain in which the activated twin has the first, or second highest SF among six variants. The result is shown in Fig. 5.15a. Then, similar operation was conducted for twin variants T_2^{II}, T_3^{II}, and T_4^{II}, as plotted in Fig. 5.15b, c, and d, respectively. For a pair of twins that form a TTJ, the common loading domain is determined by overlapping their loading domains. Fig. 5.15e and f show the common loading domain associated with the formation of type I $T_{i,i+1}^{II}$ TTJ. Fig. 5.15g shows the SFs of two twins in the common stress domain associated with type II $T_{i,i+2}^{II}$ TTJ, indicating that no stress loading could satisfy the condition for producing Type II TTJs. Fig. 5.15h and i show the common loading domain associated with the formation of type III $T_{i,i+3}^{II}$ TTJ. It is

noticed that type I TTJ will be activated with high SFs under most loadings in the loading domain.

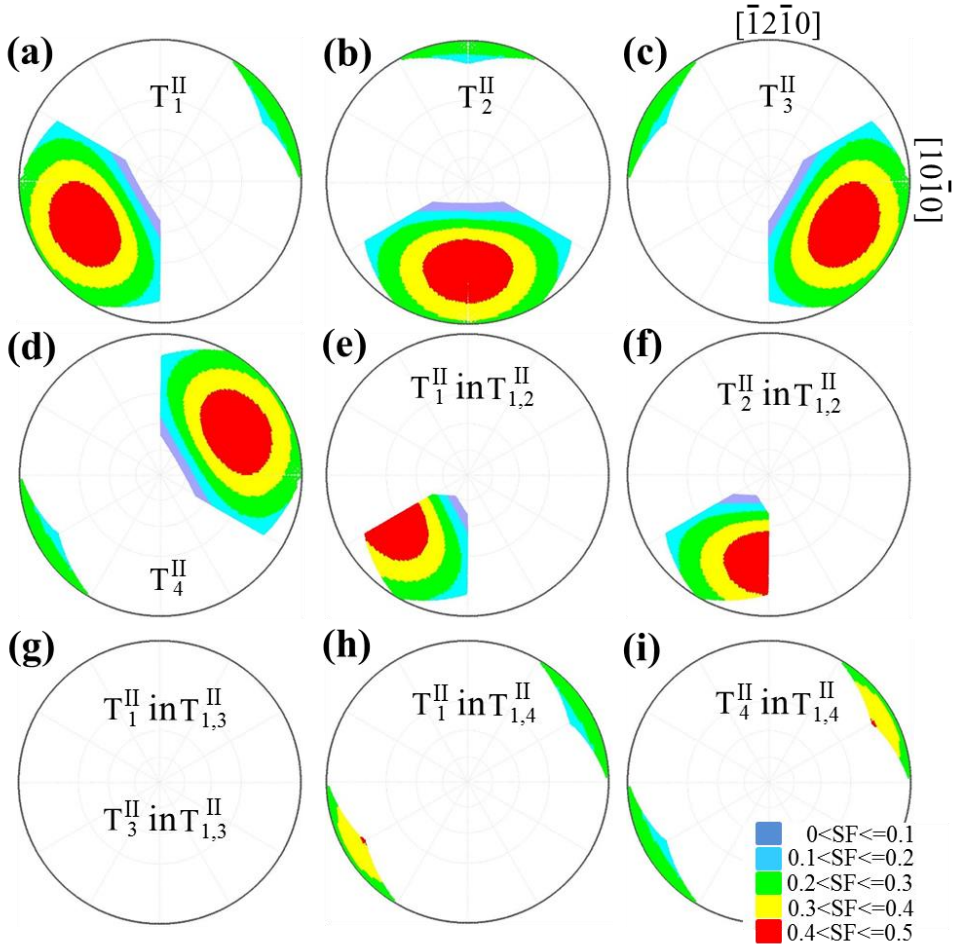

Fig. 5. 15 Loading domains associated with formation of TTJs (a) T_1^{II}, (b) T_2^{II}, (c) T_3^{II}, and (d) T_4^{II}. The common loading domains associated with the formation of TTJs (e) T_1^{II} in $T_{1,2}^{II}$ and (f) T_2^{II} in $T_{1,2}^{II}$, (g) T_1^{II} in $T_{1,3}^{II}$ and T_3^{II} in $T_{1,3}^{II}$, (h) T_1^{II} in $T_{1,4}^{II}$ and (i) T_4^{II} in $T_{1,4}^{II}$.

5.8.4.2 Why only TTBo of Type I is generated

When a twin interacts another one, the twinning dislocations meet and react, forming TTBs [136]. Therefore, the Burgers vector of the resultant dislocations at the TTB is the sum of the twinning dislocations associated with the two twins. For TTB_A associated with T_1^{II}-T_2^{II} TTJ, the Burgers vector of the resultant interface dislocation is:

$$b_t^{T_2^{II}} + b_t^{T_1^{II}} \Rightarrow b_{21}^{A}$$

$$\lambda[1\bar{2}16]+\lambda[\bar{1}\bar{1}26]\Rightarrow 3\lambda[0\bar{1}14] \quad (5\text{-}7)$$

The Burgers vector of the resultant interface dislocation in TTB_O is thus equal to:

$$b_t^{T_2^{II}} - b_t^{T_1^{II}} \Rightarrow b_{21}^{O}$$

$$\lambda[1\bar{2}16]\text{-}\lambda[\bar{1}\bar{1}26] \Rightarrow \lambda[2\bar{1}\bar{1}0] \quad (5\text{-}8)$$

Where, $\lambda=\frac{1}{4(c/a)^2+1}$, 0.09 for titanium. $b_t^{T_2^{II}}$ is the Burgers vector of the impinging twinning dislocation. When T_2^{II} twin meets primary T_1^{II} twin, b_{21}^{A} and b_{21}^{O} represent the Burgers vectors of the resultant boundary dislocations on the acute side and obtuse side, respectively. Similar dislocation reaction was done for other two types of TTJs. The resultant interface dislocations have Burgers vectors: $b_{31}^{A}=3\lambda[10\bar{1}0]$, $b_{31}^{O}=\lambda[1\ \bar{2}\ 1\ 12]$, $b_{41}^{A}=2\lambda[11\bar{2}0]$, $b_{41}^{O}= 12\lambda[0001]$. The elastic energy of these dislocations is proportional to the square of the magnitude of Burgers vector as summarized in Table 5. 4. According to Frank's law [73], the elastic energy of two twinning dislocations associated with C_2^I and C_1^I twins is proportional to $199.44(\lambda a)^2$. The elastic energy for a resultant interface dislocation in TTBs is proportional to $389.88(\lambda a)^2$ for TTB_A and $9(\lambda a)^2$ for TTB_O, respectively. Thus, TTB_O associated with T_1^{II} - T_2^{II} TTJ is energetically preferred than TTB_A.

Table 5. 4 Burgers vectors for three types of $\{11\bar{2}1\}$ twin-twin junctions before and after dislocation reaction.

Junction	b^I	b^A	b^O	$2\|b^I\|^2/(\lambda a)^2$	$\|b^A\|^2/(\lambda a)^2$	$\|b^O\|^2/(\lambda a)^2$
$T_2^{II}\leftrightarrow T_1^{II}$	$\lambda[1\bar{2}16]$	$3\lambda[0\bar{1}14]$	$\lambda[2\bar{1}\bar{1}0]$	199.44	389.88	9.00
$T_3^{II}\leftrightarrow T_1^{II}$	$\lambda[2\bar{1}\bar{1}6]$	$3\lambda[10\bar{1}0]$	$\lambda[1\ \bar{2}\ 1\ 12]$	199.44	27.00	371.88
$T_4^{II}\leftrightarrow T_1^{II}$	$\lambda[11\bar{2}6]$	$2\lambda[11\bar{2}0]$	$12\lambda[0001]$	199.44	36.00	362.88

5.8.5 Summary

In this section, $\{11\bar{2}1\}$ twin-twin junctions (TTJs) are investigated in pure titanium. According to the crystallographic features, six equivalent $\{11\bar{2}1\}$ twin variants (T_i^{II}) can possibly form three types of $\{11\bar{2}1\}$ TTJs, i.e., Type I $T_{i,i+1}^{II}$, Type II $T_{i,i+2}^{II}$, and Type III $T_{i,i+3}^{II}$. A statistical analysis of EBSD patterns reveals that only Type I $T_{i,i+1}^{II}$ TTJs are generated in our experiments without the occurrence of other two types. The SF analysis of the detected $\{11\bar{2}1\}$ TTJs reveal that all active $\{11\bar{2}1\}$ twins have the first or second highest SFs among six variants. According to the experimental result that the active twin variants have the first or second highest SFs, an apparent SF analysis successfully predicts the preference of Type I TTJs in all possible loadings. By using dislocation reactions during the formation of twin-twin boundaries, the line energy associated with the formation of TTB_O in Type I is lower than that of TTB_A.

5.9 Chapter conclusion

In this chapter, we conduct a statistical analysis of $\{11\bar{2}2\}$ twin-twin junctions (TTJs) and characterize the structural features of $\{11\bar{2}2\}$ TTJs. Similar operation is applied to the analysis of $\{11\bar{2}1\}$ TTJs.

Corresponding to the crystallography of $\{11\bar{2}2\}$ twins, three types of $\{11\bar{2}2\}$ TTJs form, Type I $C^{I}_{i,i+1}$, Type II $C^{I}_{i,i+2}$, and Type III $C^{I}_{i,i+3}$. Type III $C^{I}_{i,i+3}$ is associated with the interaction of two co-zone variants. EBSD analysis reveals that type I $C^{I}_{i,i+1}$ TTJs are most popular among three types of TTJs while type III $C^{I}_{i,i+3}$ TTJs are rarely activated. In addition, one twin will block another incoming twin. Thus, no twin transmission happens, instead, twin-twin boundaries (TTBs) form. SF analysis reveals that these activated twins associated with 93% of TTJs have their SFs to be first, second, or third highest among six variants. Such information enables us to explore the frequency of TTJs according to the common loading domain. The result clearly demonstrates that the formation of Type I TTJs would be profuse, while Type III TTJs would be rarely activated. This is in agreement with experimental observations. Consequently, twin transmission across another twin is mechanically unfavourable due to the small resolved shear stress. Thus, twin-twin junctions form. The interesting finding is that TTBs only form on one side of the incoming twin as a TTJ forms. Corresponding to the formation of TTBs based on the interactions of twinning dislocations, we found that interface dislocations in the observed TTBs have lower line energy than those in the un-observed TTBs.

Then, a statistical analysis of $\{11\bar{2}1\}$ TTJs was performed to study their crystallographic features. Six equivalent $\{11\bar{2}1\}$ twin variants (T^{II}_{i}) can possibly form three types of $\{11\bar{2}1\}$ TTJs, i.e., Type I $T^{II}_{i,i+1}$, Type II $T^{II}_{i,i+2}$, and Type III $T^{II}_{i,i+3}$. EBSD results reveal that only Type I $T^{II}_{i,i+1}$ TTJs are detected in our experiments while Types II and III are absent. According to the SF analysis of detected $\{11\bar{2}1\}$ TTJs, all active $\{11\bar{2}1\}$ twins exhibit the first or second highest SFs among six variants, which helps us to investigate the frequency of three types of TTJs in a general method. With the assumption that the twin variants should carry the first or second highest SFs in all possible loadings, an apparent SF analysis successfully predicts the preference of Type I TTJs. Another interesting finding is that only TTB_O belonging to Type I happens while TTB_A is not observed. By the investigation of dislocation reactions to produce corresponding TTBs, the formation of TTB_O in Type I have lower line energy than that of TTB_A.

However, structure analysis is based on crystallographic analysis and meso/macro-scale EBSD characterizations and mechanics analysis, atomic-level structures are lack. Future work will focus on characterizing atomic structures of TTBs and understanding the influence of TTBs on secondary twinning and consequent twinning and de-twinning events by using atomistic simulations and transmission electron microscopes.

Chapter 6 Conclusions and Prospects

Contents

6.1 Conclusions

Sequential {10$\bar{1}$2} twinning stimulated by {11$\bar{2}$1} twin-twin junctions

In this section, we experimentally studied {10$\bar{1}$2} (T_i^I) extension twins stimulated by the {11$\bar{2}$1} (T_i^{II}) twin-twin junctions in rolled pure titanium at room temperature. {10$\bar{1}$2} twins are identified to always form in the obtuse region between T_{i-1}^{II} and T_i^{II}, where the zone axis associated with T_i^I is a shared vector in describing the zone axis of the two primary twins. This new sequential twinning mechanism is confirmed by quasi in-situ EBSD observation. A statistical EBSD analysis reveals that the active {10$\bar{1}$2} twin variants always have the second highest Schmid factor (SF) among six possibilities while the variant with the highest SF is absent. An apparent SF analysis, as the local stress is taken into account, is able to determine that the SF results are applicable in all possible loadings. With the help of displacement gradient accommodation, the preference of the active variant with the second highest SF is explained over the absent one with the highest SF.

Accommodative {10$\bar{1}$2} twinning at high angle grain boundaries

A {11$\bar{2}$2} compression twin adjoining a {10$\bar{1}$2} extension twin (Twin pairs) was found in rolled pure titanium subjected to compression along the normal direction. These twin pairs were observed at high angle grain boundaries (GBs) near 90°. Classical SF analysis is invalid to explain the occurrence of some adjoined {10$\bar{1}$2} twins because they have low even negative SFs. Local accommodation mechanism is applied by expressing the displacement gradient tensor of the {11$\bar{2}$2} twins into twinning reference frames of all potential {10$\bar{1}$2} twins in the neighboring grain. The results show that the active {10$\bar{1}$2} twin is the one that has the largest capacity among all six possibilities to accommodate the shear induced by the {11$\bar{2}$2} twins. The selection of the {10$\bar{1}$2} twin variants is dependent on the accommodation ability of the potential {10$\bar{1}$2} twin variants while it is not controlled by the external stress.

Dislocation mediated variant selection for {10$\bar{1}$2} double twinning

In this section, {10$\bar{1}$2} double twinning inside primary {11$\bar{2}$2} compression twins is investigated in a pure polycrystalline titanium by compression along the normal direction. A detailed analysis of the detected 425 secondary {10$\bar{1}$2} twins has led to the following conclusions:

1. The 36 possible secondary {10$\bar{1}$2} twins inside primary {11$\bar{2}$2} compression twins can be classified into three groups in terms of misorientations between the parents and secondary twins: Group I with a misorientation of 41.34° around axis <5 $\overline{14}$ 3>, Group II with a misorientation of 48.44° around axis <$\bar{5}$503> and Group III with a misorientation of 87.85° around axis <7$\overline{43}$0>. A detailed analysis of the detected 425 indicates that Group II are the most frequent (85.6%), while Group I and III variants are only present in a fraction of 10.6% and 3.8%, respectively.

2. Our SF based analysis shows that 93.4% of the detected secondary twins have normalized SFs larger than 0.8, where principally only a single secondary twin variant is activated in the primary compression twins. A small fraction (4.5%) of the secondary twins was found in the primary twins where two variants were observed. There is a very large fraction of secondary twins (49.3%) which do not obey the Schmid law.

3. An apparent SF analysis also shows that Group III twins have very low SFs, leading to their low experimental frequency. However, the SF criterion has led to nearly equal theoretical frequencies for twin variants of Groups I and II, which is contradictory to the experimental observations.

4. The prevalence of Group II secondary twins over Group I is possible to justify with dislocation dissociations based on the common direction between the primary and secondary twin planes and a prismatic plane. This prismatic-dislocation mediated nucleation mechanism is applicable to both Group II and Group III double twin variants. Even though the geometrical feature also facilitates the activation of Group III double twins, the dislocation reaction presented clearly shows that a prismatic dislocation dissociating into three secondary twining dislocations for Group II twin is energetically favored while a prismatic dislocation dissociating into only one twining dislocation associated with Group III twin is energetically unfavourable. Prismatic-dislocation mediated nucleation mechanism can clarify the preference of Group II over Group I and Group III. With the help of an apparent SF analysis, the stress domains in which only one or two Group II double twin variants can be activated are in agreement with experiments.

Twin-twin junctions

{$11\bar{2}2$} compression twins in Ti were frequently generated in rolled pure titanium. When multiple twin variants are active in the same grain, twin-twin interactions may happen. We conducted a statistical analysis of {$11\bar{2}2$} twin-twin junctions (TTJs). The structural features of {$11\bar{2}2$} TTJs were characterized. Corresponding to the crystallography of {$11\bar{2}2$} twins, three types of {$11\bar{2}2$} TTJs may form, i.e., Type I $C^{I}_{i,i+1}$, Type II $C^{I}_{i,i+2}$, and Type III $C^{I}_{i,i+3}$. EBSD statistics reveals that type I $C^{I}_{i,i+1}$ TTJs are most popular among three types of TTJs while type III $C^{I}_{i,i+3}$ TTJs are rarely activated. No twin transmission happens, instead, twin-twin boundaries (TTBs) form. SF analysis of the detected TTJs reveals that 93% of these activated TTJs have their SFs to be first, second, or third highest among six variants, which enables us to investigate the frequency of TTJs in all possible loadings. An apparent SF analysis clearly demonstrates that the formation of Type I TTJs would be profuse, while Type III TTJs would be rarely activated. Twin transmission across another twin is mechanically unfavorable due to the small resolved shear stress. The interesting finding is that TTBs only form on one side of the incoming twin as a TTJ forms. Corresponding to the formation of TTBs based on the interactions of twinning dislocations, interface dislocations in the observed TTBs have lower line energy than those in the un-observed TTBs. Similar operation was applied to the analysis of {$11\bar{2}1$} (T^{II}_{i}) twin-twin junctions that can also be classified into three types, i.e., Type I $T^{II}_{i,i+1}$, Type II $T^{II}_{i,i+2}$, and Type III $T^{II}_{i,i+3}$. Experimental results reveal that only Type I $T^{II}_{i,i+1}$ TTJs are detected while Types II and III are absent, which can be predicted by using an apparent SF analysis as a consideration of local stress. Dislocation reactions explain the preferred formation of the TTBs in Type I due to its low line energy.

6.2 Prospects

1. Prismatic slip is reported to facilitate the nucleation of specific double twinning variants here. Atomistic simulations and characterizations are still needed to clarify the nucleation of double twins. Even though specific double twinning variants are preferred to be active in primary twins, other rare double twinning variants are also detected. The mechanism for activating the abnormal double twins is still unclear.

2. When a twin interacts another one, the local orientation is modified. The deformation mechanism in the reoriented domains needs further investigations. The generation of double twinning induced by twin-twin interactions is also necessary to be clarified. It is essential to

pay attention to the effect of local stress concentration on activation of twinning and slip by using detailed numerical simulations.

3. The interaction between the dislocation and twinning is little included in this work. The role of dislocation on the propagation of twinning interface also needs detailed investigation.

4. Characterization of twin-twin boundaries should be done at atomic scale as well as its effect on secondary twinning and de-twinning by simulation and high resolution TEM. Besides, the role of twin-twin boundaries should be implemented into the constitutive equations that facilitates the accurate prediction of the stress-strain and work hardening behaviors in response to the external deformation.

Résumé substantiel en français

Analyse cristallographique de la sélection des variants de macles et des jonctions macles-macles dans un titane commercialement pur

Au **chapitre 1**, les modes de glissement et de maclage ont été introduits. Ensuite, une revue de la littérature des études sur le maclage dans les matériaux de la structure cristalline HCP a été résumée de façon à supporter les principaux résultats trouvés.

Au **chapitre 2**, les méthodes de calcul utilisées dans la thèse ont été introduites telles que la transformation du gradient de déplacement d'une macle dans un autre grain, l'analyse des traces et la réorientation de la texture associée à la sélection des variants macles.

Chapitre 3 Le maclage {10$\bar{1}$2} stimulé par des joints macles-macles type {11$\bar{2}$1}

Les 6 variants de la macle de tension {10$\bar{1}$2} et de la macle {11$\bar{2}$1} sont notés T_i^I et T_i^{II} respectivement (voir le tableau 1). L'indice *i* allant de 1 à 6 croit dans le sens horaire autour de l'axe **c** (voir figure 3.1a).

Tableau 1 : Les notations des 6 variants de la macle de tension {10$\bar{1}$2} et de la macle {11$\bar{2}$1}

Variants de la macle {10$\bar{1}$2}<$\bar{1}$011>		Variants de la macle {11$\bar{2}$1}<$\bar{1}\bar{1}$26>	
T_1^I	(10$\bar{1}$2) [$\bar{1}$011]	T_1^{II}	(11$\bar{2}$1) [$\bar{1}\bar{1}$26]
T_2^I	(01$\bar{1}$2) [0$\bar{1}$11]	T_2^{II}	($\bar{1}$2$\bar{1}$1) [1$\bar{2}$16]
T_3^I	($\bar{1}$102) [1$\bar{1}$01]	T_3^{II}	($\bar{2}$111) [2$\bar{1}\bar{1}$6]
T_4^I	($\bar{1}$012) [10$\bar{1}$1]	T_4^{II}	($\bar{1}\bar{1}$21) [11$\bar{2}$6]
T_5^I	(0$\bar{1}$12) [01$\bar{1}$1]	T_5^{II}	(1$\bar{2}$11) [$\bar{1}$2$\bar{1}$6]
T_6^I	(1$\bar{1}$02) [$\bar{1}$101]	T_6^{II}	(2$\bar{1}\bar{1}$1) [$\bar{2}$116]

Les observations faites en EBSD montrent beaucoup de macles stimulées aux jonctions macles-macles comme l'indiquent les flèches blanches sur la figure 3.1b. Les figures de pôles sont utilisées pour identifier les variants de macles. Les macles observées ont une relation du type $T_1^{II}T_2^{II} \rightarrow T_2^I$ par exemple la jonction de la macle T_1^{II} (11$\bar{2}$1) [$\bar{1}\bar{1}$26] avec la macle T_2^{II} ($\bar{1}$2$\bar{1}$1) [1$\bar{2}$16] donne la macle T_2^I (01$\bar{1}$2) [0$\bar{1}$11], soit sous une forme plus générale: $T_{i-1}^{II}T_i^{II} \rightarrow T_i^I$. Des analyses quasi in-situ en EBSD ont été menées pour confirmer ce type de mécanisme de maclage séquentiel.

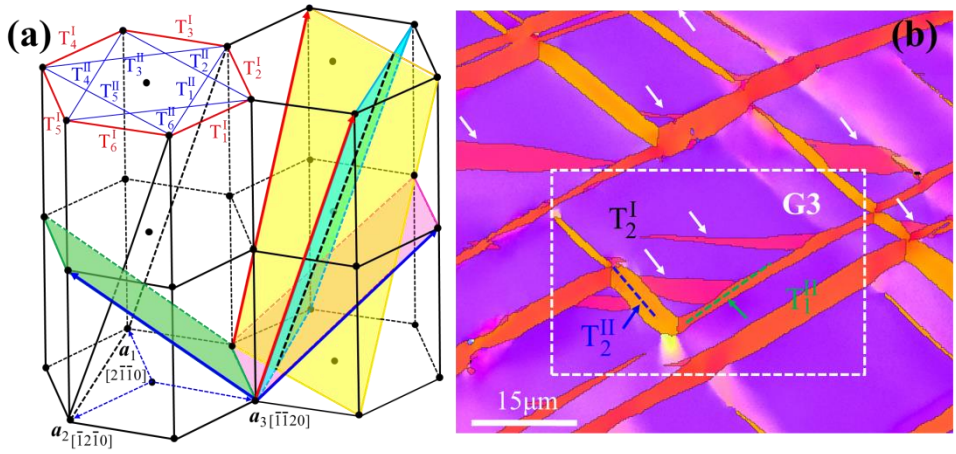

Fig. 3. 1: Cristallographie des macles dans la structure hexagonale. La figure 3a montre les 2 plans de macles $\{11\bar{2}1\}$ (en vert clair T_1^{II} et en jaune T_2^{II}) et les 2 plans de macles $\{10\bar{1}2\}$ (en rose T_2^{I} et en vert T_5^{I}). Les 2 flèches rouges indiquent la direction de cisaillement pour $\{11\bar{2}1\}$, et les flèches bleues pour $\{10\bar{1}2\}$. (b) Image EBSD de macles $\{10\bar{1}2\}$ et de jonctions macles-macles $\{11\bar{2}1\}$ indiquées par les flèches blanches.

3.1 Sélection de l'emplacement des macles séquentielles

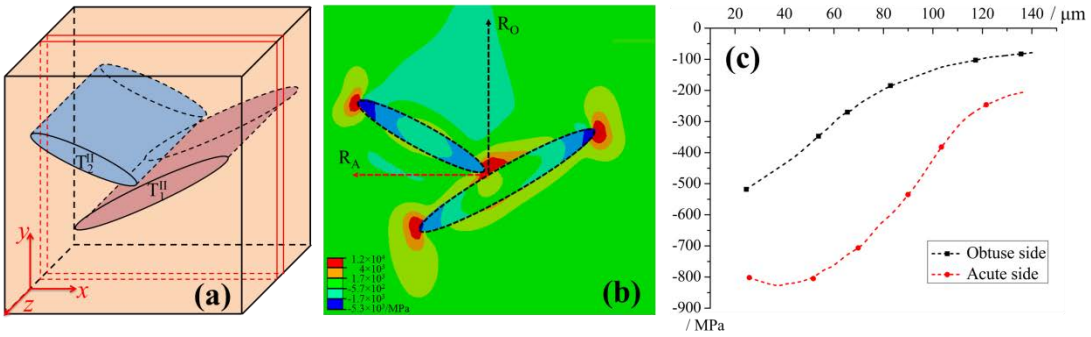

Fig. 3. 2 (a) Schéma du modèle en éléments finis. (b) RSS associées aux 2 variants de macles $\mathbf{T_2^I}$ et $\mathbf{T_5^I}$. (c) Variation de la RSS (MPa, axe vertical) le long des 2 directions RO et RA (μm, axe horizontal). La RSS provient des contraintes résiduelles dues à la jonction macle-macle.

Pour comprendre pourquoi les macles séquentielles sont toujours présentes dans les régions d'angles obtus, nous avons examiné les champs de contraintes dues aux macles primaires en utilisant la méthode des éléments finis (MEF). Dans notre modèle MEF montré sur la figure 3.2a, nous avons schématisé les 2 macles $\{11\bar{2}1\}$ relatives aux variants T_1^{II} et T_2^{II} et elles ont été placés dans une boite 40*40*8. Du fait que l'angle entre les 2 variants de macles c'est-à-dire proche de 90°, la cission résolue (RSS) des 2 variants (T_2^I et T_5^I) est approximativement la même. Seule la RSS associée au variant T_2^I est montré dans la figure 3.2b. La Fig. 3. 7c montre les variations de RSS dans 2 directions le long de la région de l'angle aigu et de l'angle obtus

(notées R_A et R_O respectivement). Le RSS associées à T_2^I et à T_5^I sont négatives (opposées à la direction de maclage). Néanmoins, la RSS due aux contraintes résiduelles est plus faible dans la région obtuse que dans la région aigue.

Sous un chargement, la RSS s'inverse, favorisant ainsi le maclage séquentiel dans la région obtuse.

3.2 Accommodation

Nous avons calculé le tenseur gradient de déplacement associé aux variants T_1^{II} et T_2^{II} dans le repère orthonormé du cristal dans le grain pour savoir si la déformation induite par la macle $\{11\bar{2}1\}$ peut être accommodée par glissements et/ou par d'autres macles dans le grain. Le variant T_2^I peut effectivement accommoder le gradient de déplacement généré par les 2 macles primaires $\{11\bar{2}1\}$. Ainsi, la combinaison du facteur de Schmid et le critère d'accommodation du gradient de déplacement assure la relation suivante : $T_{i-1}^{II} T_i^{II} \rightarrow T_i^I$.

3.3 Résumé du chapitre

Dans ce chapitre, les macles $\{10\bar{1}2\}$ observées ont été stimulées par les jonctions macles-macles $\{11\bar{2}1\}$. Le facteur de Schmid (FS) classique ne permet d'expliquer ce maclage anormal $\{10\bar{1}2\}$. L'explication de la présence de ces macles $\{10\bar{1}2\}$ est donnée par l'accommodation locale (tenseur gradient de déplacement).

Cette étude a donné lieu à deux publications l'une dans Acta Materialia ; l'autre dans Scripta Materalia.

***S. Xu**, M. Gong, C. Schuman, J.-S. Lecomte, X. Xie, J. Wang. Sequential {10$\bar{1}$2} twinning stimulated by other twins in titanium, **Acta Mater**. 132 (2017) 57-68.*

***S. Xu**, C. Schuman, J.-S. Lecomte. Accommodative {10$\bar{1}$2} twins at high angle grain boundaries in rolled pure titanium, **Scr Mater**. 116 (2016) 152-156.*

Chapitre 4 : La sélection des variants du double maclage au moyen des dislocations

Il y a 36 combinaisons possibles de maclage secondaire $\{10\bar{1}2\}$ à partir de la macle primaire $\{11\bar{2}2\}$. Selon la désorientation entre le maclage secondaire et le grain parent, les 36 possibles variants de macles $\{11\bar{2}2\}$-$\{10\bar{1}2\}$ sont regroupés en 3 groupes : Groupe I autour de $<5\bar{1}\bar{4}3>$ avec 41.34°, Groupe II autour de $<\bar{5}503>$ avec 48.44° et Groupe III autour de $<7\bar{4}\bar{3}0>$ avec 87.85° (voir tableau 2). Sur les 425 macles secondaires $\{10\bar{1}2\}$ détectées par EBSD, nous

avons obtenu la statistique suivante : le groupe II rassemble 85.6% du total de cette population et seulement 10.6% et 3.8% de macles secondaires pour le groupe I et III, respectivement. Les variants de macles secondaires appartenant au groupe II sont donc préférentiellement sélectionnés dans les macles primaires.

Tableau 2 : la notation des 3 groupes

Groupe	Axe-angle (minimum)	Nombre de variants
I	<5$\bar{1}$43> 41.34°	12
II	<$\bar{5}$503> 48.44°	12
III	<74$\bar{3}$0> 87.85°	12

4.1 Le facteur de Schmid pour l'évaluation de la macle secondaire {10$\bar{1}$2}

Nous avons calculé le facteur de Schmid normalisé (NSF) c'est-à-dire les valeurs du FS dans un grain sont divisées par le FS le plus élevé. L'analyse du NSF indique que les groupes I et II ont les FS les plus élevés tandis que le groupe III a les FS les plus bas.

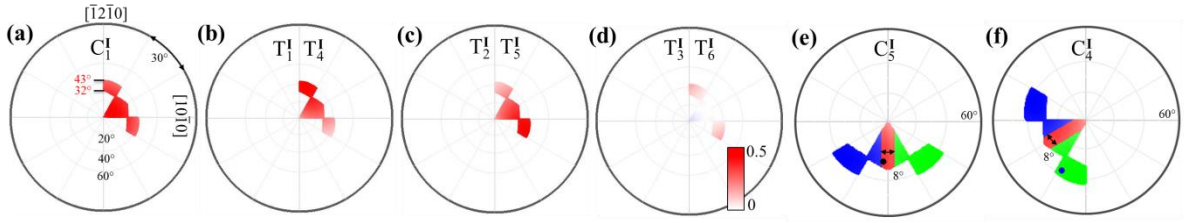

Fig. 4.1 Figures de pôle inverse du FS de différents variants de macles en compression: (a) Domaine de contrainte où le FS de la macle primaire $\mathbf{C_1^I}$ est >0 et le plus haut sur les 6 possibles. Dans ce domaine de contrainte, le FS des macles secondaires $\mathbf{T_1^I}$ et $\mathbf{T_4^I}$ est montré en (b) ; le FS des macles secondaires $\mathbf{T_2^I}$ et $\mathbf{T_5^I}$ en (c) et en (d) le FS des macles secondaires $\mathbf{T_3^I}$ et $\mathbf{T_6^I}$; En (e) la distribution du FS du Groupe II pour les variants $\mathbf{T_i^I}$ et $\mathbf{T_{i+1}^I}$ dans le domaine de chargement associé à la macle $\mathbf{C_5^I}$ et en (f) pour la macle $\mathbf{C_4^I}$. Le vert indique que le FS associé avec le variant $\mathbf{T_i^I}$ est plus grand que le variant $\mathbf{T_{i+1}^I}$. Le bleu indique que le FS associé avec le variant $\mathbf{T_i^I}$ est plus petit que le variant $\mathbf{T_{i+1}^I}$. Le rouge indique que la différence de FS entre les 2 variants est inférieure à 0.05.

Sans perte de généralité, nous avons mené une analyse FS généralisée. Tout d'abord, nous déterminons le domaine de chargement dans lequel la macle primaire C_1^I est active sous compression uniaxiale. La direction de chargement est tracée dans une figure de pôles inverse comme indiqué sur la Fig. 4. 81a ; le domaine (en dégradé de rouge en fonction du FS) est très restreint car on a pris seulement le domaine où le FS est plus grand que 0.3 et où il est le plus grand des 6 variants. Ensuite, le FS des 6 variants de la macle {10$\bar{1}$2} T_j^I (j=*1...6*) sont calculés

et tracés sur les figures 4.1 b-d. Les FS des variants T_3^I et T_6^I du Groupe III ont les plus petits FS par rapport aux autres groupes. Cela pourrait répondre à la plus faible activité du Groupe III, alors que cela ne nous permet pas distinguer l'activité des Groupes II et I. Nous avons également comparé les FS associés à deux variantes de macles équivalentes appartenant au Groupe II. Lorsque la différence des FS associées aux deux variantes du groupe II est inférieure à 0,05, nous les avons traitées de manière égale. De manière correspondante, nous avons re-tracé le domaine de chargement dans les figures 4. 1e et 4.1f pour le groupe II associé aux variants de la macle de contraction primaire C_5^I et C_4^I, respectivement.

4.2 La nucléation basée sur la dissociation de dislocations

Nous avons examiné le mécanisme basé sur la réaction de dislocations, en utilisant les principes développés pour le magnésium (Ref [1]). La caractéristique cristallographique des macles doubles est illustrée sur la figure 4. 2. Le plan bleu désigne la macle primaire et le plan rose représente la macle secondaire. La ligne en pointillée blanche indique l'intersection l_{ij}, entre la macle primaire et la macle secondaire. Les lignes d'intersection des groupes II et III se situent dans un plan prismatique $\{10\bar{1}0\}$, tel que décrit par les lignes en pointillées jaunes. En s'appuyant sur un travail similaire (Ref [1]), nous avons étudié la dissociation ou la réflexion de la dislocation prismatique <**a**> dans le plan de macle primaire avec des dislocations associées à des macles $\{10\bar{1}2\}$.

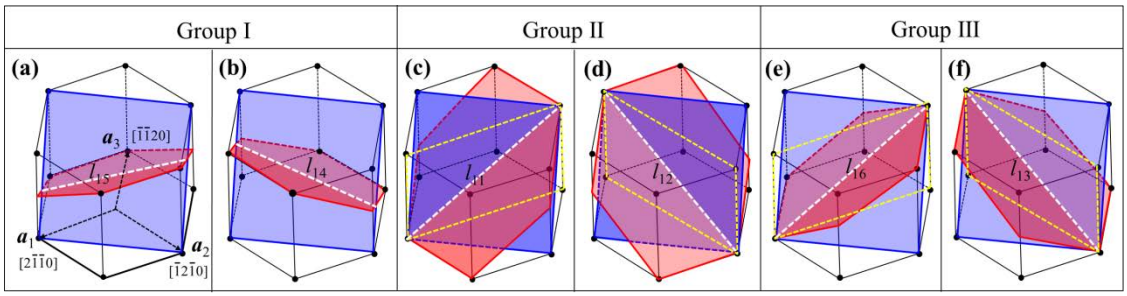

Fig. 4. 2 Cristallographie des macles doubles $\{11\bar{2}2\} \rightarrow \{10\bar{1}2\}$. Le plan bleu montre la macle primaire $\boldsymbol{C_i^I}$, et le plan rose représente la macle secondaire $\boldsymbol{T_i^I}$. la ligne en pointillés blancs indique l'intersection $\boldsymbol{l_{ij}}$ entre $\boldsymbol{C_i^I}$ et $\boldsymbol{T_j^I}$. La ligne en pointillés jaunes représente le plan $\{10\bar{1}0\}$.

Lorsque les dislocations $(10\bar{1}0)[1\bar{2}10]$ s'approchent du joint de macle primaire, elles peuvent se dissocier en dislocations de macle associées avec macles secondaires des groupes II et III. Pour le groupe II, une dislocation b_a, $(10\bar{1}0)[1\bar{2}10]$ pourrait être dissociée en 3 dislocations de macle $3b_t^{(01\bar{1}2)}$, et une dislocation résiduelle b_r^1, ceci en accord avec les loi de Frank. Cependant, une dislocation prismatique $(10\bar{1}0)[1\bar{2}10]$ peut se dissocier en une seule

dislocation de macle du groupe III. Cette dissociation n'est énergétiquement pas favorable (en accord avec les lois de Franck). Si la dislocation b_a entrante est d'abord dissociée en une dislocation de macle $b_t^{(\bar{1}\bar{1}22)}$ sur le premier plan de macle, alors la dislocation résiduelle peut servir de source de nucléation ; seule une dislocation de macle secondaire peut être nucléée (toujours en accord avec les lois de Frank). La dissociation pour le groupe II est énergétiquement favorable alors qu'elle ne l'est pas pour le groupe III. Ce mécanisme n'est pas applicable au groupe I car les macles secondaires intervenant dans ce groupe n'ont pas en commun d'axe de zone comme pour les variants du groupe II. La nucléation des macles via les dislocations explique l'activité préférentielle du groupe II par rapport aux autres groupes.

Afin de confirmer l'activation du glissement prismatique associé à la macle primaire $\{11\bar{2}2\}$ avec les variants de macle $\{10\bar{1}2\}$ du groupe II, un échantillon a été poli et déformé en compression, ensuite des observations des lignes de glissement en électrons secondaires ont été effectuées. Les macles primaires et secondaires (figure 4.3a) ont été identifiées comme étant $(\bar{1}\bar{1}22)[\bar{1}\bar{1}2\bar{3}]$ et $(0\bar{1}12)[01\bar{1}1]$. Ces macles secondaires appartiennent au groupe II. Le glissement prismatique $(10\bar{1}0)$ <**a**> est nécessaire pour la dissociation en accord avec le mécanisme proposé au dessus. Des traces de glissement (figure 4.3a) ont été identifiées comme étant du $(10\bar{1}0)$. Cela satisfait le groupe II. Cependant, le critère de nucléation ne peut pas distinguer la préférence de 2 variants dans un même groupe, ceci est du au fait que les 2 variants doivent avoir approximativement la même RSS.

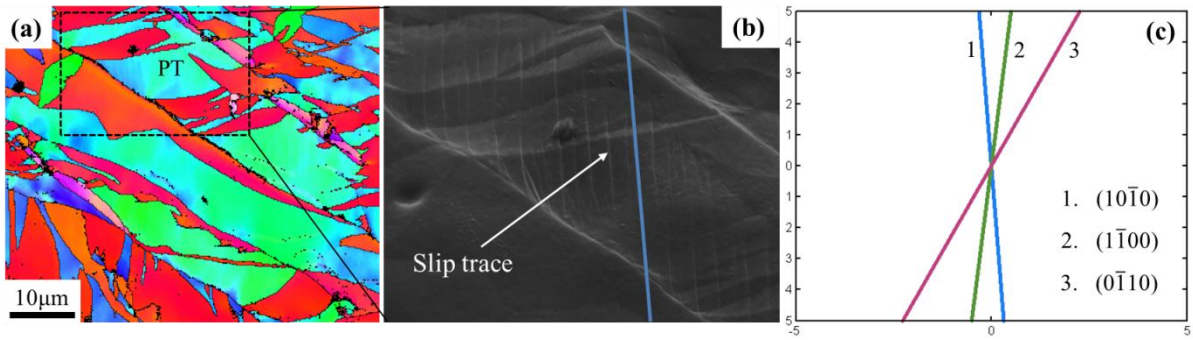

Fig. 4. 3 (a): Carte EBSD d'un échantillon poli et déformé. (b): Grossissement au MEB de la région de a) (c): Orientations des 3 traces possibles du glissement prismatique dans une macle primaire (PT) ; la ligne bleue en b et c correspond à la trace du plan prismatique $(10\bar{1}0)$.

4.3 Sélection entre 2 variants dans le Groupe II

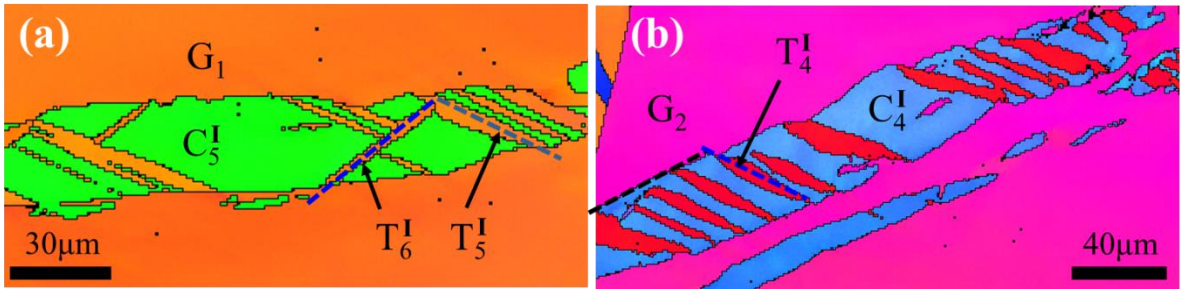

Fig. 4. 4 carte EBSD de (a) 2 macles secondaires $\{10\bar{1}2\}$, (b) une macle secondaire $\{10\bar{1}2\}$ dans une macle primaire de compression $\{11\bar{2}2\}$.

Nous avons étudié le double maclage provenant de la réaction $\{11\bar{2}2\}\rightarrow\{10\bar{1}2\}$. La figure 4.4a montre une cartographie EBSD où la macle primaire $\{11\bar{2}2\}$ contient 2 macles de tension secondaires $\{10\bar{1}2\}$: la macle primaire est notée C_5^I et T_5^I et T_6^I sont les macles secondaires. La direction de chargement est indiquée par un point noir sur la figure 4.1e. Ceci est en accord avec nos prédictions. La figure 4.4b montre une cartographie EBSD où une macle de compression $\{11\bar{2}2\}$ contient une seule macle secondaire de tension $\{10\bar{1}2\}$. Ce variant de macle secondaire appartient au groupe II. Les FS associés à C_4^I et T_4^I sont 0.3222 et 0.473. Le FS de l'autre variant de macle du groupe II , T_5^I est 0.202, ce qui est beaucoup plus petit que celui du T_4^I. Cela explique pourquoi seulement un seul variant apparait.
La direction de chargement est indiquée par un point bleu sur la figure 4.1f.

4.4 Résumé du chapitre

Dans ce chapitre, nous avons étudié la sélection de variant de macle au moyen de dislocations pour le maclage en compression pour un titane commercialement pur. Un groupe spécifique de macle secondaire $\{10\bar{1}2\}$ est préféré. La nucléation au moyen des dislocations est proposée pour l'activation du maclage double, et permet de prédire avec succès le groupe le plus fréquent du maclage double. En combinaison avec une analyse du FS généralisé, le variant de macle utilisé peut être défini parmi les 2 possibilités prévues. Ceci est en accord avec les résultats expérimentaux.
Cette étude a donné lieu à une publications ; l'une dans Acta Materialia.

***S. Xu**, L.S. Toth, C. Schuman, J.-S. Lecomte, M.R. Barnett. Dislocation mediated variant selection for secondary twinning in compression of pure titanium, **Acta Mater**. 124 (2017) 59-70.*

Chapitre 5 : Caractères cristallographiques des joints de macle

Les six variants de macle $\{11\bar{2}2\}$ sont désignés par C_i^I (l'indice i = 1…6; l'indice supérieur I représente la macle de compression $\{11\bar{2}2\}$ (voir tableau 3 et la figure 5.1). L'indice i croit dans le sens horaire lorsque l'on tourne autour de l'axe **c**. Les interactions entre les 2 variants de macle $\{11\bar{2}2\}$ peuvent être classifiées en 3 types, comme résumé dans la figure 5.1 et dans le tableau 4. Quand une macle approche une autre macle, un joint de macle (dans la suite, on le notera TTB pour *Twin-Twin Boundary*) peut être formé et peut être défini géométriquement comme étant l'intersection des 2 plans de macle [2]. Le TTB dans la face aigue est référencé TTB_A, de l'autre coté ; sur la face obtuse : TTB_O.

Tableau 3 : Notation des 6 variants de la macle $\{11\bar{2}2\}<11\bar{2}\bar{3}>$

Les variants de la macle $\{11\bar{2}2\}<11\bar{2}\bar{3}>$ (C_i^I)	
C_1^I	$(11\bar{2}2)\ [11\bar{2}\bar{3}]$
C_2^I	$(\bar{1}2\bar{1}2)\ [\bar{1}2\bar{1}\bar{3}]$
C_3^I	$(\bar{2}112)\ [\bar{2}11\bar{3}]$
C_4^I	$(\bar{1}\bar{1}22)\ [\bar{1}\bar{1}2\bar{3}]$
C_5^I	$(1\bar{2}12)\ [1\bar{2}1\bar{3}]$
C_6^I	$(2\bar{1}\bar{1}2)\ [2\bar{1}\bar{1}\bar{3}]$

Le plan du joint pour chaque type est exprimé dans la matrice et dans les deux macles. Le résultat est montré dans la tableau 4. Il existe un angle de torsion (noté *Twist*) entre les jonctions maclés (notées TTJ) dans les 2 macles.

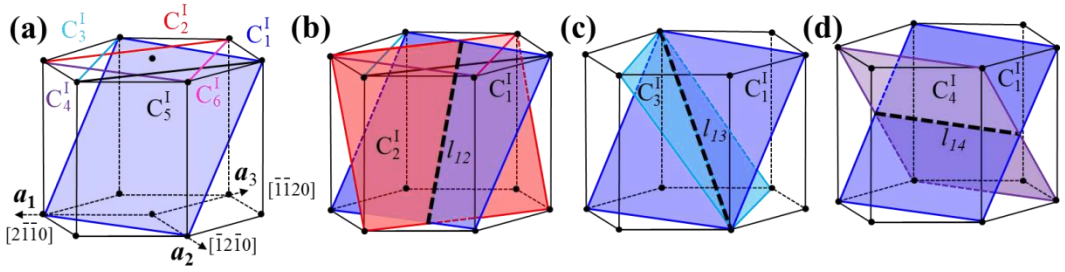

Fig. 5. 4 (a) les 6 variants de macle $\{11\bar{2}2\}$ $<11\bar{2}\bar{3}>$ (notés $\mathbf{C_i^I}$) forment 3 types de jonctions maclées (notées TTJ pour Twin-Twin Junction). (b) le Type I $\mathbf{C_{i,j+1}^I}$ avec la ligne d'intersection $[0\bar{2}23]$; (c) le Type II $\mathbf{C_{i,j+2}^I}$ avec la ligne d'intersection $[2\bar{4}23]$; (d) le Type III $\mathbf{C_{i,j+3}^I}$ avec la ligne d'intersection $[1\bar{1}00]$. La ligne d'intersection est représentée par une ligne noire en gras et en pointillé.

Tableau 4 : La cristallographie des 3 types de jonctions macles-macles {11$\bar{2}$2}

TTJs	Ligne d'Intersection	TTB_A			TTB_O		
		Dans la matrice	dans C_1^I	dans C_i^I (i=2…4)	Dans la matrice	dans C_1^I	dans C_i^I (i=2…4)
$C_{i,i+1}^I$	[0$\bar{2}$23]	(03$\bar{3}$4)	(23 2 $\overline{25}$ 18)	($\overline{23}$ 25 $\bar{2}$ 18)	($\bar{2}$110)	(9 $\overline{12}$ 3 $\overline{10}$)	(9 3 $\overline{12}$ 10)
			Twist 61.8°			Twist 0.17°	
$C_{i,i+2}^I$	[2$\bar{4}$23]	($\bar{1}$010)	(2 $\bar{5}$ 3 $\overline{10}$)	($\bar{3}$ 5 $\bar{2}$ 10)	($\bar{1}$2$\bar{1}$4)	(58 $\bar{3}$ $\overline{55}$ $\bar{6}$)	($\overline{55}$ $\bar{3}$ 58 $\bar{6}$)
			Twist 8.5°			Twist 76.6°	
$C_{i,i+3}^I$	[1$\bar{1}$00]	($\bar{1}\bar{1}$20)	($\bar{3}$ $\bar{3}$ 6 $\overline{20}$)	($\bar{3}$ $\bar{3}$ 6 20)	(0002)	(22$\overline{43}$)	($\overline{22}$4$\bar{3}$)
			Twist 0°			Twist 0°	

5.1 Statistiques de la jonction maclée (TTJ)

Grace aux analyses EBSD, nous avons détecté 243 TTJs. Le Type I représente la majorité de ces TTJs. Deux variantes de macles associées à 93% des TTJs sont parmi les 3 premiers plus grands FS des six variantes. Ces informations nous permettent d'explorer la fréquence des TTJ. La préférence de Type I est contrôlée par le chargement externe.

5.2 Caractérisation de la jonction maclée

En utilisant la méthode mentionnée ci-dessus, les données EBSD ont été appliquées pour détecter si les deux joints de macles peuvent se produire pour chaque type. La caractéristique intrigante associée aux TTJ est que la jonction maclée ne se forme que d'un côté de la macle entrante, car une macle rencontre une autre macle. Pour les TTJ de type I, la figure 5.2a montre un TTJ associé au TTJ $C_{3,4}^I$. Il convient de mentionner que TTBo a été formé parmi tous les TTJ de type I alors que TTBA n'a pas été observé. Pour le type II (figure 5.2b), un TTJ de type II est associé au TTJ $C_{2,6}^I$. Parmi tous les TTJ de type II, il semblait que seul des TTBA sont formés. On peut également remarquer que les macles croissent préférentiellement sur un côté des macles entre elles. Les TTJ de type III sont rarement observés dans les données EBSD. La figure 5.2c montre un TTJ de type III. Il se compose d'une macle C_3^I et d'un C_6^I. Le TTBA a été observé contrairement au TTBO.

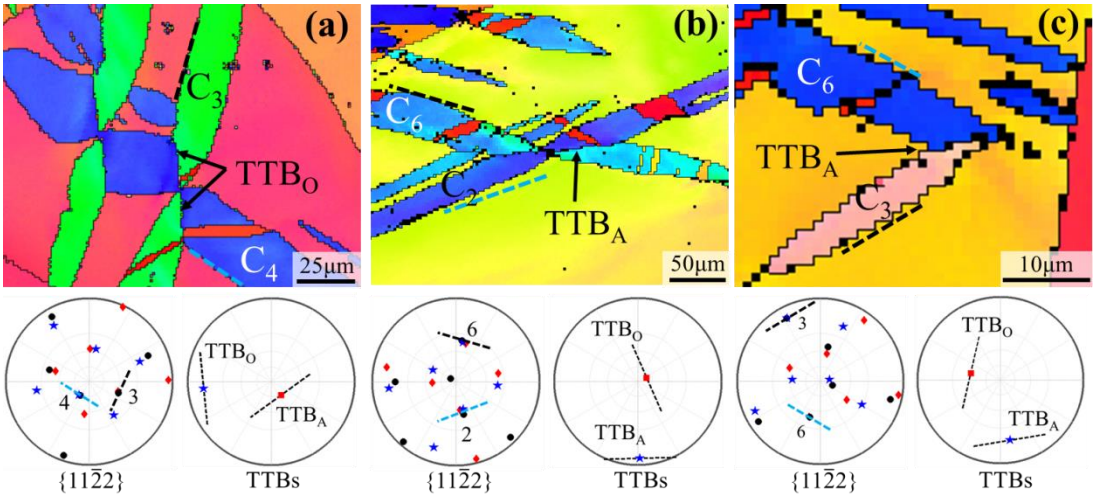

Fig 5.2. Différentes microstructures avec des jonctions maclées : (a) type C_1^I-C_2^I, (b) type C_1^I-C_3^I, (c) type C_1^I-C_4^I. et leurs figures de pôles {11$\bar{2}$2}. Les lignes pointillées dans la figure de pôle {11$\bar{2}$2} indiquent les traces TTB_A et TTB_O associées aux jonctions maclées.

5.3 La formation des joints macles-macles (TTBs)

La formation des TTBs a été décrite comme une réaction des dislocations de maclage. Lorsque deux macles intersectées se développent à travers le glissement des dislocations de macle, ces dislocations de maclage se rencontrent et réagissent, en formant des TTBs. Par conséquent, le vecteur Burgers des dislocations résultantes au TTB est la somme des dislocations de maclage associées aux deux macles. L'énergie élastique de ces dislocations est proportionnelle au carré de la grandeur du vecteur Burgers. Le tableau 5 résume l'énergie élastique de ces dislocations. Selon la loi de Frank [3], le TTBO du Type I est plus favorable que le TTBA en raison de son énergie élastique faible. Cependant, le TTBA des types II et III est plus favorable que TTBO. Les résultats sont en accord avec les expériences.

Tableau 5 : Les vecteurs de Burgers des 3 types de jonction macle-macle {11$\bar{2}$2} avant et après la réaction de dislocations

Jonction	b^I	b^A	b^O	$2\|b^I\|^2/(\lambda a)^2$	$\|b^A\|^2/(\lambda a)^2$	$\|b^O\|^2/(\lambda a)^2$
$C_2^I \leftrightarrow C_1^I$	$\lambda[\bar{1}2\bar{1}3]$	$3\lambda[0\bar{1}12]$	$\lambda[2\bar{1}\bar{1}0]$	63.36	117.72	9.00
$C_3^I \leftrightarrow C_1^I$	$\lambda[\bar{2}11\bar{3}]$	$3\lambda[10\bar{1}0]$	$\lambda[1\bar{2}16]$	63.36	27.00	99.72
$C_4^I \leftrightarrow C_1^I$	$\lambda[\bar{1}\bar{1}23]$	$2\lambda[11\bar{2}0]$	$6\lambda[0001]$	63.36	36.00	90.72

5.4 Résumé du chapitre

Dans ce chapitre, les caractères des joints macles-macles {11$\bar{2}$2} sont introduits dans le titane commercialement pur. Parmi les trois types de joints macles-macles, un seul type est le plus fréquent des macles détectées et la formation d'une seule macle est facilitée. Le premier point sera abordé en utilisant une analyse FS généralisée et la dernière sera discutée à l'aide de la réaction de dislocation.

Ce travail a donné lieu à deux publications l'une déjà acceptée dans Philosophical *Magazine Letters*, l'autre a été soumise à *Materials Science and Engineering A*.

***S. Xu**, M. Gong, X. Xie, C. Schuman, J.-S. Lecomte, J. Wang. Crystallographic characters of {11$\bar{2}$2} twin-twin junctions in titanium, **Philosophical Magazine Letters** (2017), accepted.*
***S. Xu**, C. Schuman, J.-S. Lecomte, P. Moll, L. Peltier. Insights into the preference of {11-21} twin-twin boundaries in pure titanium, **Submitted** (2017).*

Références

[1] I.J. Beyerlein, J. Wang, M.R. Barnett, C.N. Tome. Double twinning mechanisms in magnesium alloys via dissociation of lattice dislocations, Proc R Soc A Math. 468 (2012) 1496-1520.

[2] E. Roberts, P.G. Partridge. The accommodation around {10-12}<-1011> twins in magnesium, Acta Metall 14 (1966) 513-527.

[3] J.P. Hirth, J. Lothe. Theory of dislocations, , New York: McGraw-Hill (1968).

References

[1] B. Hanson. Present and future uses of titanium in engineering, Mater Des. 7 (1986) 301-307.

[2] G. Abouelmagd, H. Büchkremer, E. El-Magd, D. Stöver. Mechanical properties of a TiAl6V4 alloy processed by powder metallurgy, J Eng Mater Technol. 37 (1993) 583-597.

[3] D. Eylon, F. Froes, R. Gardiner. Developments in titanium alloy casting technology, JOM 35 (1983) 35-47.

[4] H. Van Kann. Titanium and titanium alloys, vol. 1. Plenum Press, New York, USA, 1982.

[5] J. Kahles, M. Field, D. Eylon, F. Froes. Machining of titanium alloys, JOM Journal of the Minerals, Metals and Materials Society 37 (1985) 27-35.

[6] O. Ozugwu, M. Wang. Titanium alloys and their machinability, J. Mater. Proc. Tech 68 (1997) 262-274.

[7] H. Chandler. Machining of reactive metals, ASM Handbook. 16 (1989) 844-857.

[8] M. Barnett, Z. Keshavarz, A. Beer, X. Ma. Non-Schmid behaviour during secondary twinning in a polycrystalline magnesium alloy, Acta Mater. 56 (2008) 5-15.

[9] I. Beyerlein, J. Wang, M. Barnett, C. Tomé. Double twinning mechanisms in magnesium alloys via dissociation of lattice dislocations. Proc. R. Soc. A, vol. 468: The Royal Society, 2012. p.1496-1520.

[10] T. Bieler, P. Eisenlohr, C. Zhang, H. Phukan, M. Crimp. Grain boundaries and interfaces in slip transfer, Current Opinion in Solid State and Materials Science 18 (2014) 212-226.

[11] C. Cepeda-Jiménez, J. Molina-Aldareguia, M. Pérez-Prado. Origin of the twinning to slip transition with grain size refinement, with decreasing strain rate and with increasing temperature in magnesium, Acta Mater. 88 (2015) 232-244.

[12] H. El Kadiri, J. Kapil, A. Oppedal, L. Hector, S.R. Agnew, M. Cherkaoui, S. Vogel. The effect of twin–twin interactions on the nucleation and propagation of twinning in magnesium, Acta Mater. 61 (2013) 3549-3563.

[13] J.J. Jonas, S. Mu, T. Al-Samman, G. Gottstein, L. Jiang, Ė. Martin. The role of strain accommodation during the variant selection of primary twins in magnesium, Acta Mater. 59 (2011) 2046-2056.

[14] Y. Liu, N. Li, S. Shao, M. Gong, J. Wang, R. McCabe, Y. Jiang, C. Tomé. Characterizing the boundary lateral to the shear direction of deformation twins in magnesium, Nature communications 7 (2016).

[15] J. Tu, X. Zhang, J. Wang, Q. Sun, Q. Liu, C.N. Tomé. Structural characterization of {10-12} twin boundaries in cobalt, Appl Phys Lett. 103 (2013) 051903.

[16] J. Ye, R.K. Mishra, A.K. Sachdev, A.M. Minor. In situ TEM compression testing of Mg and Mg–0.2 wt.% Ce single crystals, Scr Mater. 64 (2011) 292-295.

[17] I. Beyerlein, R. McCabe, C. Tomé. Effect of microstructure on the nucleation of deformation twins in polycrystalline high-purity magnesium: a multi-scale modeling study, J Mech Phys Solids. 59 (2011) 988-1003.

[18] B. Clausen, C. Tomé, D. Brown, S. Agnew. Reorientation and stress relaxation due to twinning: modeling and experimental characterization for Mg, Acta Mater. 56 (2008) 2456-2468.

[19] H. El Kadiri, C.D. Barrett, M.A. Tschopp. The candidacy of shuffle and shear during compound twinning in hexagonal close-packed structures, Acta Mater. 61 (2013) 7646-7659.

[20] G. Proust, C. Tomé, G. Kaschner. Modeling texture, twinning and hardening evolution during deformation of hexagonal materials, Acta Mater. 55 (2007) 2137-2148.

[21] J. Wang, I. Beyerlein, C. Tomé. An atomic and probabilistic perspective on twin nucleation in Mg, Scr Mater. 63 (2010) 741-746.

[22] J. Wang, I.J. Beyerlein, J.P. Hirth. Nucleation of elementary {-1011} and {-1013} twinning dislocations at a twin boundary in hexagonal close-packed crystals, Model Simul Mater Sci Eng. 20 (2012) 024001.

[23] J. Wang, J.P. Hirth, C.N. Tomé. (-1012) Twinning nucleation mechanisms in hexagonal-close-packed crystals, Acta Mater. 57 (2009) 5521-5530.

[24] J. Wang, R.G. Hoagland, J.P. Hirth, L. Capolungo, I.J. Beyerlein, C.N. Tomé. Nucleation of a (-1012) twin in hexagonal close-packed crystals, Scr Mater. 61 (2009) 903-906.

[25] J. Wang, S. Yadav, J. Hirth, C. Tomé, I. Beyerlein. Pure-shuffle nucleation of deformation twins in hexagonal-close-packed metals, Mater Res Lett. 1 (2013) 126-132.

[26] L. Jiang, J.J. Jonas, R. Mishra, A. Luo, A. Sachdev, S. Godet. Twinning and texture development in two Mg alloys subjected to loading along three different strain paths, Acta Mater. 55 (2007) 3899-3910.

[27] J. Del Valle, F. Carreño, O.A. Ruano. Influence of texture and grain size on work hardening and ductility in magnesium-based alloys processed by ECAP and rolling, Acta Mater. 54 (2006) 4247-4259.

[28] H. Wang, P. Wu, J. Wang. Modeling inelastic behavior of magnesium alloys during cyclic loading–unloading, Int J Plast. 47 (2013) 49-64.

[29] L. Wu, S. Agnew, D. Brown, G. Stoica, B. Clausen, A. Jain, D. Fielden, P. Liaw. Internal stress relaxation and load redistribution during the twinning–detwinning-dominated cyclic deformation of a wrought magnesium alloy, ZK60A, Acta Mater. 56 (2008) 3699-3707.

[30] G. Proust, C.N. Tomé, A. Jain, S.R. Agnew. Modeling the effect of twinning and detwinning during strain-path changes of magnesium alloy AZ31, Int J Plast. 25 (2009) 861-880.

[31] S. Agnew, M. Yoo, C. Tome. Application of texture simulation to understanding mechanical behavior of Mg and solid solution alloys containing Li or Y, Acta Mater. 49 (2001) 4277-4289.

[32] T. Al-Samman, X. Li. Sheet texture modification in magnesium-based alloys by selective rare earth alloying, Mater Sci Eng A. 528 (2011) 3809-3822.

[33] J. Bohlen, M.R. Nürnberg, J.W. Senn, D. Letzig, S.R. Agnew. The texture and anisotropy of magnesium–zinc–rare earth alloy sheets, Acta Mater. 55 (2007) 2101-2112.

[34] C. Cepeda-Jiménez, J. Molina-Aldareguia, M. Pérez-Prado. Effect of grain size on slip activity in pure magnesium polycrystals, Acta Mater. 84 (2015) 443-456.

[35] J.T. Wang, J.Q. Liu, J. Tao, Y.L. Su, X. Zhao. Effect of grain size on mechanical property of Mg–3Al–1Zn alloy, Scr Mater. 59 (2008) 63-66.

[36] B.-Y. Liu, J. Wang, B. Li, L. Lu, X.-Y. Zhang, Z.-W. Shan, J. Li, C.-L. Jia, J. Sun, E. Ma. Twinning-like lattice reorientation without a crystallographic twinning plane, Nature communications 5 (2014).

[37] Q. Yu, Z.-W. Shan, J. Li, X. Huang, L. Xiao, J. Sun, E. Ma. Strong crystal size effect on deformation twinning, Nature. 463 (2010) 335-338.

[38] A.A. Pochettino, N. Gannio, C.V. Edwards, R. Penelle. Texture and pyramidal slip in Ti, Zr and their alloys, Scr Metall. 27 (1992) 1859-1863.

[39] A. Styczynski, C. Hartig, J. Bohlen, D. Letzig. Cold rolling textures in AZ31 wrought magnesium alloy, Scr Mater. 50 (2004) 943-947.

[40] Y.N. Wang, J.C. Huang. Texture analysis in hexagonal materials, Mater Chem Phys. 81 (2003) 11-26.

[41] L. Wang, R. Barabash, Y. Yang, T. Bieler, M. Crimp, P. Eisenlohr, W. Liu, G.E. Ice. Experimental characterization and crystal plasticity modeling of heterogeneous deformation in polycrystalline α-Ti, Metall Mater Trans A. 42 (2011) 626-635.

[42] B. Barkia, V. Doquet, E. Héripré, I. Guillot. Characterization and analysis of deformation heterogeneities in commercial purity titanium, Mater Charact. 108 (2015) 94-101.

[43] J.W. Christian, S. Mahajan. Deformation twinning, Prog Mater Sci. 39 (1995) 1-157.

[44] M. Yoo. Slip, twinning, and fracture in hexagonal close-packed metals, Metallurgical Transactions A 12 (1981) 409-418.

[45] S. Kleiner, P. Uggowitzer. Mechanical anisotropy of extruded Mg–6% Al–1% Zn alloy, Mater Sci Eng A. 379 (2004) 258-263.

[46] S.-G. Hong, S.H. Park, C.S. Lee. Role of {10-12} twinning characteristics in the deformation behavior of a polycrystalline magnesium alloy, Acta Mater. 58 (2010) 5873-5885.

[47] Y. Wang, J. Huang. The role of twinning and untwinning in yielding behavior in hot-extruded Mg–Al–Zn alloy, Acta Mater. 55 (2007) 897-905.

[48] L. Wang, P. Eisenlohr, Y. Yang, T.R. Bieler, M.A. Crimp. Nucleation of paired twins at grain boundaries in titanium, Scr Mater. 63 (2010) 827-830.

[49] A.A. Salem, S.R. Kalidindi, R.D. Doherty. Strain hardening of titanium: role of deformation twinning, Acta Mater. 51 (2003) 4225-4237.

[50] S. Jin, K. Marthinsen, Y. Li. Formation of {11-21} twin boundaries in titanium by kinking mechanism through accumulative dislocation slip, Acta Mater. 120 (2016) 403-414.

[51] L. Capolungo, I. Beyerlein. Nucleation and stability of twins in hcp metals, Phys Rev B. 78 (2008) 024117.

[52] L. Wang, R. Barabash, T. Bieler, W. Liu, P. Eisenlohr. Study of {11-21} Twinning in α-Ti by EBSD and Laue Microdiffraction, Metall Mater Trans A. 44 (2013) 3664-3674.

[53] S. Wang, Y. Zhang, C. Schuman, J.-S. Lecomte, X. Zhao, L. Zuo, M.-J. Philippe, C. Esling. Study of twinning/detwinning behaviors of Ti by interrupted in situ tensile tests, Acta Mater. 82 (2015) 424-436.

[54] F. Xu, X. Zhang, H. Ni, Q. Liu. {11-24} deformation twinning in pure Ti during dynamic plastic deformation, Mater Sci Eng A. 541 (2012) 190-195.

[55] J. Wang, I. Beyerlein, J. Hirth, C. Tomé. Twinning dislocations on {-1011} and {-1013} planes in hexagonal close-packed crystals, Acta Mater. 59 (2011) 3990-4001.

[56] S. Nemat-Nasser, W. Guo, J. Cheng. Mechanical properties and deformation mechanisms of a commercially pure titanium, Acta Mater. 47 (1999) 3705-3720.

[57] G. Gray III. Influence of strain rate and temperature on the structure. Property behavior of high-purity titanium, Le Journal de Physique IV 7 (1997) C3-423-C423-428.

[58] M. Doner, H. Conrad. Deformation mechanisms in commercial Ti (0.5 at. pct oineq) at intermediate and high temperatures (0.3-0.6 tinm), Metall Trans. 4 (1973) 2809-2817.

[59] A.A. Salem, S.R. Kalidindi, R.D. Doherty. Strain hardening regimes and microstructure evolution during large strain compression of high purity titanium, Scr Mater. 46 (2002) 419-423.

[60] A. Salem, S. Kalidindi, S. Semiatin. Strain hardening due to deformation twinning in α-titanium: Constitutive relations and crystal-plasticity modeling, Acta Mater. 53 (2005) 3495-3502.

[61] A.A. Salem, S. Kalidindi, R. Doherty, S. Semiatin. Strain hardening due to deformation twinning in α-titanium: mechanisms, Metall Mater Trans A. 37 (2006) 259-268.

[62] H. Becker, W. Pantleon. Work-hardening stages and deformation mechanism maps during tensile deformation of commercially pure titanium, Computational Materials Science 76 (2013) 52-59.

[63] L. Capolungo, I. Beyerlein, C. Tomé. Slip-assisted twin growth in hexagonal close-packed metals, Scr Mater. 60 (2009) 32-35.

[64] S. Ishioka. Dynamic formation of a twin in a bcc crystal, J Appl Phys. 46 (1975) 4271-4274.

[65] S. Mendelson. Zonal dislocations and twin lamellae in h.c.p. metals, Mater Sci Eng. 4 (1969) 231-242.

[66] J. Wang, H. Huang. Shockley partial dislocations to twin: another formation mechanism and generic driving force, Appl Phys Lett. 85 (2004) 5983-5985.

[67] J. Wang, H. Huang. Novel deformation mechanism of twinned nanowires, Appl Phys Lett. 88 (2006) 203112.

[68] N. Thompson, D. Millard. XXXVIII. Twin formation, in cadmium, The London, Edinburgh, and Dublin Philosophical Magazine and Journal of Science 43 (1952) 422-440.

[69] M. Kronberg. Atom movements and dislocation structures for plastic slip in single crystals of β-uranium, Journal of Nuclear Materials 1 (1959) 85-95.

[70] D. Westlake. Twinning in zirconium, Acta Metallurgica 9 (1961) 327-331.

[71] A. Serra, D. Bacon, R. Pond. The crystallography and core structure of twinning dislocations in hcp metals, Acta Metallurgica 36 (1988) 3183-3203.

[72] R. Pond, J. Hirth. Defects at surfaces and interfaces, Solid State Physics 47 (1994) 287-365.

[73] J.P. Hirth. Theory of dislocations, (1968).

[74] S. Mendelson. Dislocation Dissociations in hcp Metals, J Appl Phys. 41 (1970) 1893.

[75] A. Serra, D. Bacon. Computer simulation of screw dislocation interactions with twin boundaries in HCP metals, Acta Metall. 43 (1995) 4465-4481.

[76] A. Serra, D.J. Bacon. On the generation of twinning dislocations in hcp twin boundaries. Materials Science Forum, vol. 207: Trans Tech Publ, 1996. p.553-556.

[77] A. Serra, R. Pond, D. Bacon. Computer simulation of the structure and mobility of twinning disclocations in HCP Metals, Acta Metall. 39 (1991) 1469-1480.

[78] N.E. Paton, W.A. Backofen. Plastic deformation of titanium at elevated temperatures, Metall MaterTrans B. 1 (1970) 2839-2847.

[79] Y.B. Chun, S.H. Yu, S.L. Semiatin, S.K. Hwang. Effect of deformation twinning on microstructure and texture evolution during cold rolling of CP-titanium, Mater Sci Eng A. 398 (2005) 209-219.

[80] Z. Zeng, S. Jonsson, Y. Zhang. Constitutive equations for pure titanium at elevated temperatures, Mater Sci Eng A. 505 (2009) 116-119.

[81] M. Glavicic, A. Salem, S. Semiatin. X-ray line-broadening analysis of deformation mechanisms during rolling of commercial-purity titanium, Acta Mater. 52 (2004) 647-655.

[82] N. Gurao, R. Kapoor, S. Suwas. Deformation behaviour of commercially pure titanium at extreme strain rates, Acta Mater. 59 (2011) 3431-3446.

[83] D. Chichili, K. Ramesh, K. Hemker. The high-strain-rate response of alpha-titanium: experiments, deformation mechanisms and modeling, Acta Mater. 46 (1998) 1025-1043.

[84] T. Wang, B. Li, M. Li, Y. Li, Z. Wang, Z. Nie. Effects of strain rates on deformation twinning behavior in α-titanium, Mater Charact. 106 (2015) 218-225.

[85] P. Zhou, D. Xiao, C. Jiang, G. Sang, D. Zou. Twin Interactions in Pure Ti Under High Strain Rate Compression, Metall Mater Trans A. 48 (2017) 126-138.

[86] H. Qin, J.J. Jonas. Variant selection during secondary and tertiary twinning in pure titanium, Acta Mater. 75 (2014) 198-211.

[87] H. Qin, J.J. Jonas, H. Yu, N. Brodusch, R. Gauvin, X. Zhang. Initiation and accommodation of primary twins in high-purity titanium, Acta Mater. 71 (2014) 293-305.

[88] N. Bozzolo, L. Chan, A.D. Rollett. Misorientations induced by deformation twinning in titanium, J Appl Crystallogr. 43 (2010) 596-602.

[89] S. Mullins, B. Patchett. Deformation microstructures in titanium sheet metal, Metallurgical Transactions A 12 (1981) 853-863.

[90] A. Roth, M.A. Lebyodkin, T.A. Lebedkina, J.S. Lecomte, T. Richeton, K.E.K. Amouzou. Mechanisms of anisotropy of mechanical properties of α-titanium in tension conditions, Mater Sci Eng A. 596 (2014) 236-243.

[91] W. Tirry, S. Bouvier, N. Benmhenni, W. Hammami, A. Habraken, F. Coghe, D. Schryvers, L. Rabet. Twinning in pure Ti subjected to monotonic simple shear deformation, Mater Charact. 72 (2012) 24-36.

[92] S. Bouvier, N. Benmhenni, W. Tirry, F. Gregory, M. Nixon, O. Cazacu, L. Rabet. Hardening in relation with microstructure evolution of high purity α-titanium deformed under monotonic and cyclic simple shear loadings at room temperature, Mater Sci Eng A. 535 (2012) 12-21.

[93] F. Rosi, C. Dube, B. Alexander. Mechanism of plastic flow in titanium-determination of slip and twinning elements, Trans. Aime 197 (1953) 257.

[94] H. Conrad. Effect of interstitial solutes on the strength and ductility of titanium, Prog Mater Sci. 26 (1981) 123-403.

[95] J. Warwick, N. Jones, K. Rahman, D. Dye. Lattice strain evolution during tensile and compressive loading of CP Ti, Acta Mater. 60 (2012) 6720-6731.

[96] T. Sakai, M. Fine. Failure of Schmid's law in Ti-Al alloys for prismatic slip, Scripta Metallurgica 8 (1974) 541-544.

[97] H. Numakura, Y. Minonishi, M. Koiwa. <-1-123>{10-11} slip in titanium polycrystals at room temperature, Scripta metallurgica 20 (1986) 1581-1586.

[98] N. Stanford, U. Carlson, M. Barnett. Deformation twinning and the Hall–Petch relation in commercial purity Ti, Metall Mater Trans A. 39 (2008) 934-944.

[99] X. Deng, S. Hui, W. Ye, X. Song. Analysis of twinning behavior of pure Ti compressed at different strain rates by Schmid factor, Mater Sci Eng A. 575 (2013) 15-20.

[100] W. Tirry, S. Bouvier, N. Benmhenni, W. Hammami, A.M. Habraken, F. Coghe, D. Schryvers, L. Rabet. Twinning in pure Ti subjected to monotonic simple shear deformation, Mater Charact. 72 (2012) 24-36.

[101] I. Beyerlein, C. Tomé. A dislocation-based constitutive law for pure Zr including temperature effects, Int J Plast. 24 (2008) 867-895.

[102] X. Wu, S.R. Kalidindi, C. Necker, A.A. Salem. Prediction of crystallographic texture evolution and anisotropic stress–strain curves during large plastic strains in high purity α-titanium using a Taylor-type crystal plasticity model, Acta Mater. 55 (2007) 423-432.

[103] P. Partridge. The crystallography and deformation modes of hexagonal close-packed metals, Metall Rev. 12 (1967) 169-194.

[104] M. Battaini, E. Pereloma, C. Davies. Orientation effect on mechanical properties of commercially pure titanium at room temperature, Metall Mater Trans A. 38 (2007) 276-285.

[105] E.O. Hall. The Deformation and Ageing of Mild Steel: III Discussion of Results Proc. Phys. Soc. B 64 (1953) 747-753.

[106] N.J. Petch. The cleavage strength of polycrystals, J. Iron Steel Inst 174 (1953) 25-28.

[107] E. El-Danaf, S.R. Kalidindi, R.D. Doherty. Influence of grain size and stacking-Fault Energy on Deformation Twinning in Fcc Metals, Metall Mater Trans A. 30A (1999) 1223-1233.

[108] M.A. Meyers, O. Vohringer, V.A. Lubarda. The onset of twining in metals: a constitutive description, Acta Mater. 49 (2001) 4025-4039.

[109] M.R. Barnett, Z. Keshavarz, A.G. Beer, D. Atwell. Influence of grain size on the compressive deformation of wrought Mg–3Al–1Zn, Acta Mater. 52 (2004) 5093-5103.

[110] A. Ghaderi, M.R. Barnett. Sensitivity of deformation twinning to grain size in titanium and magnesium, Acta Mater. 59 (2011) 7824-7839.

[111] R.J. Lederich, S.M.L. Sastry, J.E. O'neal, B.B. Rath. The effect of grain size on yield stress and work hardening of polycrystalline titanium at 295 K and 575 K, Mater Sci Eng. 33 (1978) 183-188.

[112] C.N. Tomé, R.A. Lebensohn, U.F. Kocks. A model for texture development dominated by deformation twinning: Application to zirconium alloys, Acta Metall. 39 (1991) 2667-2680.

[113] J. Sun, P. Trimby, F. Yan, X. Liao, N. Tao, J. Wang. Grain size effect on deformation twinning propensity in ultrafine-grained hexagonal close-packed titanium, Scr Mater. 69 (2013) 428-431.

[114] M.D. Uchic, D.M. Dimiduk, J.N. Florando, W.D. Nix. Sample dimensions influence strength and crystal plasticity, Science 305 (2004) 986-989.

[115] J.R. Greer, W.C. Oliver, W.D. Nix. Size dependence of mechanical properties of gold at the micron scale in the absence of strain gradients, Acta Mater. 53 (2005) 1821-1830.

[116] Z.W. Shan, R.K. Mishra, S.A. Syed Asif, O.L. Warren, A.M. Minor. Mechanical annealing and source-limited deformation in submicrometre-diameter Ni crystals, Nat Mater 7 (2008) 115-119.

[117] J. Hirth, J. Wang, C. Tomé. Disconnections and other defects associated with twin interfaces, Prog Mater Sci. 83 (2016) 417-471.

[118] J. Wang, L. Liu, C. Tomé, S. Mao, S. Gong. Twinning and de-twinning via glide and climb of twinning dislocations along serrated coherent twin boundaries in hexagonal-close-packed metals, Mater Res Lett. 1 (2013) 81-88.

[119] B. Xu, L. Capolungo, D. Rodney. On the importance of prismatic/basal interfaces in the growth of twins in hexagonal close packed crystals, Scr Mater. 68 (2013) 901-904.

[120] X. Zhang, B. Li, X. Wu, Y. Zhu, Q. Ma, Q. Liu, P. Wang, M. Horstemeyer. Twin boundaries showing very large deviations from the twinning plane, Scr Mater. 67 (2012) 862-865.

[121] Q. Sun, X. Zhang, Y. Ren, L. Tan, J. Tu. Observations on the intersection between twin variants sharing the same zone axis in deformed magnesium alloy, Mater Charact. 109 (2015) 160-163.

[122] Q. Sun, X. Zhang, J. Tu, Y. Ren, H. Qin, Q. Liu. Characterization of basal-prismatic interface of twin in deformed titanium by high-resolution transmission electron microscopy, Philos Mag Lett. 95 (2015) 145-151.

[123] B.M. Morrow, R.J. McCabe, E.K. Cerreta, C.N. Tomé. Observations of the atomic structure of tensile and compressive twin boundaries and twin–twin interactions in zirconium, Metall Mater Trans A. 45 (2014) 5891-5897.

[124] B. Li, E. Ma. Zonal dislocations mediating twinning in magnesium, Acta Mater. 57 (2009) 1734-1743.

[125] M. Chen, E. Ma, K.J. Hemker, H. Sheng, Y. Wang, X. Cheng. Deformation twinning in nanocrystalline aluminum, Science 300 (2003) 1275-1277.

[126] B. Li, B. Cao, K. Ramesh, E. Ma. A nucleation mechanism of deformation twins in pure aluminum, Acta Mater. 57 (2009) 4500-4507.

[127] X. Wu, J. Narayan, Y. Zhu. Deformation twin formed by self-thickening, cross-slip mechanism in nanocrystalline Ni, Appl Phys Lett. 93 (2008) 031910.

[128] H. El Kadiri, A. Oppedal. A crystal plasticity theory for latent hardening by glide twinning through dislocation transmutation and twin accommodation effects, J Mech Phys Solids. 58 (2010) 613-624.

[129] A. Serra, D.J. Bacon. A new model for {10-12} twin growth in hcp metals, Philos Mag A. 73 (1996) 333-343.

[130] P. Partridge, E. Roberts. The formation and behaviour of incoherent twin boundaries in hexagonal metals, Acta Metallurgica 12 (1964) 1205-1210.

[131] B. Reed-Hill, E. Buchanan. Zig-zag twins in zirconium, Acta Metallurgica 11 (1963) 73-75.

[132] A. Oppedal, H. El Kadiri, C. Tomé, G. Kaschner, S.C. Vogel, J. Baird, M. Horstemeyer. Effect of dislocation transmutation on modeling hardening mechanisms by twinning in magnesium, Int J Plast. 30 (2012) 41-61.

[133] L. Jiang, J.J. Jonas, A.A. Luo, A.K. Sachdev, S. Godet. Influence of {10-12} extension twinning on the flow behavior of AZ31 Mg alloy, Mater Sci Eng A. 445 (2007) 302-309.

[134] Q. Yu, J. Wang, Y. Jiang, R.J. McCabe, C.N. Tomé. Co-zone {-1012} Twin Interaction in Magnesium Single Crystal, Mater Res Lett. 2 (2014) 82-88.

[135] E. Roberts, P. Partridge. The accommodation around {10-12}<-1011> twins in magnesium, Acta Metallurgica 14 (1966) 513-527.

[136] Q. Yu, J. Wang, Y. Jiang, R.J. McCabe, N. Li, C.N. Tomé. Twin–twin interactions in magnesium, Acta Mater. 77 (2014) 28-42.

[137] S. Godet, L. Jiang, A. Luo, J. Jonas. Use of Schmid factors to select extension twin variants in extruded magnesium alloy tubes, Scr Mater. 55 (2006) 1055-1058.

[138] S.H. Park, S.-G. Hong, C.S. Lee. Activation mode dependent {10-12} twinning characteristics in a polycrystalline magnesium alloy, Scr Mater. 62 (2010) 202-205.

[139] K.D. Molodov, T. Al-Samman, D.A. Molodov, G. Gottstein. Mechanisms of exceptional ductility of magnesium single crystal during deformation at room temperature: Multiple twinning and dynamic recrystallization, Acta Mater. 76 (2014) 314-330.

[140] P. Yang, Y. Yu, L. Chen, W. Mao. Experimental determination and theoretical prediction of twin orientations in magnesium alloy AZ31, Scr Mater. 50 (2004) 1163-1168.

[141] J. Jiang, A. Godfrey, W. Liu, Q. Liu. Identification and analysis of twinning variants during compression of a Mg–Al–Zn alloy, Scr Mater. 58 (2008) 122-125.

[142] M. Barnett, Z. Keshavarz, M. Nave. Microstructural features of rolled Mg-3Al-1Zn, Metall Mater Trans A. 36 (2005) 1697-1704.

[143] M. Barnett, M. Nave, C. Bettles. Deformation microstructures and textures of some cold rolled Mg alloys, Mater Sci Eng A. 386 (2004) 205-211.

[144] J. Koike, Y. Sato, D. Ando. Origin of the Anomalous (10-12) Twinning During Tensile Deformation of Mg Alloy Sheet, Mater Trans. 49 (2008) 2792.

[145] K.D. Molodov, T. Al-Samman, D.A. Molodov, G. Gottstein. On the role of anomalous twinning in the plasticity of magnesium, Acta Mater. 103 (2016) 711-723.

[146] C. Schuman, L. Bao, J.S. Lecomte, Y. Zhang, J.M. Raulot, M.J. Philippe, C. Esling. A New Variant Selection Criterion for Twin Variants in Titanium Alloys (Part 2), Adv Eng Mater. 14 (2012) 304-311.

[147] C. Schuman, L. Bao, J. Sébastien Lecomte, Y. Zhang, J. Marc Raulot, M. Jeanne Philippe, C. Esling. A New Variant Selection Criterion for Twin Variants in Titanium Alloys (Part 1), Adv Eng Mater. 13 (2011) 1114-1121.

[148] S. Wang, C. Schuman, L. Bao, J.S. Lecomte, Y. Zhang, J.M. Raulot, M.J. Philippe, X. Zhao, C. Esling. Variant selection criterion for twin variants in titanium alloys deformed by rolling, Acta Mater. 60 (2012) 3912-3919.

[149] S. Mu, J.J. Jonas, G. Gottstein. Variant selection of primary, secondary and tertiary twins in a deformed Mg alloy, Acta Mater. 60 (2012) 2043-2053.

[150] J. Koike. Enhanced deformation mechanisms by anisotropic plasticity in polycrystalline Mg alloys at room temperature, Metall Mater Trans A. 36 (2005) 1689-1696.

[151] W. Hutchinson, M. Barnett. Effective values of critical resolved shear stress for slip in polycrystalline magnesium and other hcp metals, Scr Mater. 63 (2010) 737-740.

[152] J. Koike, T. Kobayashi, T. Mukai, H. Watanabe, M. Suzuki, K. Maruyama, K. Higashi. The activity of non-basal slip systems and dynamic recovery at room temperature in fine-grained AZ31B magnesium alloys, Acta Mater. 51 (2003) 2055-2065.

[153] Z.-Z. Shi, Y. Zhang, F. Wagner, P.-A. Juan, S. Berbenni, L. Capolungo, J.-S. Lecomte, T. Richeton. On the selection of extension twin variants with low Schmid factors in a deformed Mg alloy, Acta Mater. 83 (2015) 17-28.

[154] K. Amouzou, T. Richeton, A. Roth, M. Lebyodkin, T. Lebedkina. Micromechanical modeling of hardening mechanisms in commercially pure α-titanium in tensile condition, Int J Plast. 80 (2016) 222-240.

[155] A. Churchman. The slip modes of titanium and the effect of purity on their occurrence during tensile deformation of single crystals. Proceedings of the Royal Society of London A: Mathematical, Physical and Engineering Sciences, vol. 226: The Royal Society, 1954. p.216-226.

[156] H. Li, D. Mason, T. Bieler, C. Boehlert, M. Crimp. Methodology for estimating the critical resolved shear stress ratios of α-phase Ti using EBSD-based trace analysis, Acta Mater. 61 (2013) 7555-7567.

[157] S. Zaefferer. A study of active deformation systems in titanium alloys dependence on alloy composition and correlation with deformation texture, Mater Sci Eng A. 344 (2003) 20-30.

[158] B. Barkia, V. Doquet, J.-P. Couzinié, I. Guillot, E. Héripré. In situ monitoring of the deformation mechanisms in titanium with different oxygen contents, Mater Sci Eng A. 636 (2015) 91-102.

[159] J. Gong, A.J. Wilkinson. Anisotropy in the plastic flow properties of single-crystal α titanium determined from micro-cantilever beams, Acta Mater. 57 (2009) 5693-5705.

[160] C. Zambaldi, Y. Yang, T.R. Bieler, D. Raabe. Orientation informed nanoindentation of α-titanium: Indentation pileup in hexagonal metals deforming by prismatic slip, J Mater Res. 27 (2012) 356-367.

[161] M.J. Philippe, M. Serghat, P.V. Houtte, C. Esling. Modelling of texture evolution for materials of hexagonal symmetry — II. application to zirconium and titanium α or near α alloys, Acta Metall. 43 (1995) 1619-1630.

[162] N. Benmhenni, S. Bouvier, R. Brenner, T. Chauveau, B. Bacroix. Micromechanical modelling of monotonic loading of CP α-Ti: Correlation between macroscopic and microscopic behaviour, Mater Sci Eng A. 573 (2013) 222-233.

[163] D. Gloaguen, G. Oum, V. Legrand, J. Fajoui, S. Branchu. Experimental and theoretical studies of intergranular strain in an alpha titanium alloy during plastic deformation, Acta Mater. 61 (2013) 5779-5790.

[164] M. Knezevic, R.A. Lebensohn, O. Cazacu, B. Revil-Baudard, G. Proust, S.C. Vogel, M.E. Nixon. Modeling bending of α-titanium with embedded polycrystal plasticity in implicit finite elements, Mater Sci Eng A. 564 (2013) 116-126.

[165] H. Bunge, C. Esling, J. Muller. The influence of crystal and sample symmetries on the orientation distribution function of the crystallites in polycrystalline materials, Acta Crystallographica Section A: Crystal Physics, Diffraction, Theoretical and General Crystallography 37 (1981) 889-899.

[166] É. Martin, L. Capolungo, L. Jiang, J.J. Jonas. Variant selection during secondary twinning in Mg–3%Al, Acta Mater. 58 (2010) 3970-3983.

[167] S. Xu, M. Gong, C. Schuman, J.-S. Lecomte, X. Xie, J. Wang. Sequential {10-12} twinning stimulated by other twins in titanium, Acta Mater. 132 (2017) 57-68.

[168] S. Xu, C. Schuman, J.-S. Lecomte. Accommodative {10-12} twins at high angle grain boundaries in rolled pure titanium, Scr Mater. 116 (2016) 152-156.

[169] B. Beausir, J.-J. Fundenberger. Université de Lorraine - Metz, 2015, ATOM - Analysis Tools for Orientation Maps, http://atom-software.eu/".

[170] J.-J. Fundenberger, B. Beausir. Université de Lorraine - Metz, 2015, JTEX - Software for Texture Analysis, <http://jtex-software.eu/>.

[171] D. Tromans. Elastic anisotropy of HCP metal crystals and polycrystals, Int. J. Res. Rev. Appl. Sci 6 (2011) 462-483.

[172] R. Xin, C. Guo, Z. Xu, G. Liu, X. Huang, Q. Liu. Characteristics of long {10-12} twin bands in sheet rolling of a magnesium alloy, Scr Mater. 74 (2014) 96-99.

[173] M. Arul Kumar, I.J. Beyerlein, R.J. McCabe, C.N. Tome. Grain neighbour effects on twin transmission in hexagonal close-packed materials, Nat Commun 7 (2016) 13826.

[174] T. Hama, H. Nagao, A. Kobuki, H. Fujimoto, H. Takuda. Work-hardening and twinning behaviors in a commercially pure titanium sheet under various loading paths, Mater Sci Eng A. 620 (2015) 390-398.

[175] L. Bao, Y. Zhang, C. Schuman, J.-S. Lecomte, M.-J. Philippe, X. Zhao, C. Esling. Multiple twinning in pure hexagonal close-packed titanium, J Appl Crystallogr. 46 (2013) 1397-1406.

[176] R. Xin, Y. Liang, C. Ding, C. Guo, B. Wang, Q. Liu. Geometrical compatibility factor analysis of paired extension twins in extruded Mg–3Al–1Zn alloys, Mater Des. 86 (2015) 656-663.

[177] C.F. Gu, L.S. Toth, M. Hoffman. Twinning effects in a polycrystalline magnesium alloy under cyclic deformation, Acta Mater. 62 (2014) 212-224.

[178] R. Lebensohn, C. Tomé. A study of the stress state associated with twin nucleation and propagation in anisotropic materials, Philos Mag A. 67 (1993) 187-206.

[179] S. Xu, L.S. Toth, C. Schuman, J.-S. Lecomte, M.R. Barnett. Dislocation mediated variant selection for secondary twinning in compression of pure titanium, Acta Mater. 124 (2017) 59-70.

[180] L.S. Toth, P. Gilormini, J.J. Jonas. Effect of rate sensitivity on the stability of torsion textures, Acta Metall 36 (1988) 3077-3091.

[181] L. Capolungo, P.E. Marshall, R.J. McCabe, I.J. Beyerlein, C.N. Tomé. Nucleation and growth of twins in Zr: A statistical study, Acta Mater. 57 (2009) 6047-6056.

[182] R.A. Lebensohn, C.N. Tomé. A study of the stress state associated with twin nucleation and propagation in anisotropic materials, Philos Mag. 67 (1993) 187-206.

[183] P.A. Juan, S. Berbenni, M.R. Barnett, C.N. Tomé, L. Capolungo. A double inclusion homogenization scheme for polycrystals with hierarchal topologies: application to twinning in Mg alloys, Int J Plast. 60 (2014) 182-196.

[184] I.J. Beyerlein, J. Wang, M.R. Barnett, C.N. Tome. Double twinning mechanisms in magnesium alloys via dissociation of lattice dislocations, Proc R Soc A Math. 468 (2012) 1496-1520.

[185] W.B. Hutchinson, M.R. Barnett. Effective values of critical resolved shear stress for slip in polycrystalline magnesium and other hcp metals, Scr Mater. 63 (2010) 737-740.

[186] S. Xu, M. Gong, X. Xie, C. Schuman, J.-S. Lecomte, J. Wang. Crystallographic characters of {11-22} twin-twin junctions in titanium, Philosophical Magazine Letters (2017) **Accepted**.

[187] S. Xu, C. Schuman, J.-S. Lecomte, P. Moll, L. Peltier. Insights into the preference of {11-21} twin-twin boundaries in pure titanium, **Submitted** (2017).

[188] E. Roberts, P.G. Partridge. The accommodation around {10-12}<-1011> twins in magnesium, Acta Metall 14 (1966) 513-527.

[189] J. Wang, I.J. Beyerlein. Atomic structures of symmetric tilt grain boundaries in hexagonal close packed (hcp) crystals, Model Simul Mater Sci Eng. 20 (2012) 024002.

Publication list

1. Publications in international journals

[1] **S. Xu**, M. Gong, C. Schuman, J.-S. Lecomte, X. Xie, J. Wang. Sequential $\{10\bar{1}2\}$ twinning stimulated by other twins in titanium, **Acta Mater**. 132 (2017) 57-68.

[2] **S. Xu**, L.S. Toth, C. Schuman, J.-S. Lecomte, M.R. Barnett. Dislocation mediated variant selection for secondary twinning in compression of pure titanium, **Acta Mater**. 124 (2017) 59-70.

[3] **S. Xu**, C. Schuman, J.-S. Lecomte. Accommodative $\{10\bar{1}2\}$ twins at high angle grain boundaries in rolled pure titanium, **Scr Mater**. 116 (2016) 152-156.

[4] **S. Xu**, C. Schuman, J.-S. Lecomte. Selection criterion for $\{11\bar{2}2\}$ twinning in rolled pure titanium, **MRS Advances** (2017) 1-7.

[5] **S. Xu**, M. Gong, X. Xie, C. Schuman, J.-S. Lecomte, J. Wang. Crystallographic characters of $\{11\bar{2}2\}$ twin-twin junctions in titanium, **Philosophical Magazine Letters** (2017) **Accepted**.

[6] **S. Xu**, C. Schuman, J.-S. Lecomte, P. Moll, L. Peltier. Insights into the preference of {11-21} twin-twin boundaries in pure titanium, **Submitted** (2017).

2. Contributions to international conferences

[1] **S. Xu**, C. Schuman, J.-S. Lecomte. **Presentation**. "Accommodative $\{10\bar{1}2\}$ twins in pure titanium", **2016 MRS Fall meeting** in Boston, USA, 11.2016.

[2] **S. Xu**, C. Schuman, J.-S. Lecomte, T.M. Liu. **Poster**. **Anisotropy and Texture 2015**, European Days in Metz, France.

Appendix

The Taylor Viscoplastic Polycrystal Model

Taylor proposed in 1938 that all the crystals that constitute the polycrystal deform exactly the same way as the sample (concerning the plastic part of the deformation). This model can be formulated by the condition that the local velocity gradient $\underline{\underline{l}}^{(g)}$ ('grain') is equal to the macroscopic one, $\underline{\underline{L}}$:

$$\underline{\underline{l}}^{(g)} = \underline{\underline{L}} \quad .$$

This condition assures the compatibility between grains. Expressing the fully imposed strain rate tensor in vector form ($\dot{\varepsilon}_i$), we can write the so-called "strain-equation" with the help of the Schmid-orientation tensor ($M_i^{(s)}$, also in vector form) and the slips on the slip systems ($\dot{\gamma}_r^{(s)}$):

$$\dot{\varepsilon}_i = \sum_{s=1}^{N} M_i^{(s)} \dot{\gamma}_r^{(s)} \quad .$$

Now the constitutive relation for viscoplastic slip is used:

$$\dot{\gamma}_r^{(s)} = \dot{\gamma}_r^{(0)} \frac{\tau^{(s)}}{\tau_0^{(s)}} \left| \frac{\tau^{(s)}}{\tau_0^{(s)}} \right|^{\frac{1}{m}-1} ,$$

where $\tau^{(s)}$ is the resolved shear stress on slip system (s). The latter is obtained from the stress state $\underline{\sigma}$ (also in vector form) as:

$$\tau^{(s)} = \underline{\sigma} \cdot \underline{M}^{(s)} \quad .$$

So the strain-equation becomes:

$$\dot{\varepsilon}_i = \dot{\gamma}_r^{(0)} \sum_{s=1}^{N} M_i^{(s)} \frac{\underline{\sigma} \cdot \underline{M}^{(s)} \left| \underline{\sigma} \cdot \underline{M}^{(s)} \right|^{\frac{1}{m}-1}}{\left(\tau_0^{(s)}\right)^{\frac{1}{m}}} \quad .$$

This equation can be solved by the Nawton-Raphson technique to obtain $\underline{\sigma}$. Knowing $\underline{\sigma}$, the slip distribution is also given by:

$$\dot{\gamma}_r^{(s)} = \dot{\gamma}_r^{(0)} \frac{\underline{\sigma} \cdot \underline{M}^{(s)}}{\tau_0^{(s)}} \left| \frac{\underline{\sigma} \cdot \underline{M}^{(s)}}{\tau_0^{(s)}} \right|^{\frac{1}{m}-1} .$$

The slip distribution permits to obtain the lattice rotation.

The macroscopic stress state $\underline{\underline{\sigma}}$ is calculated by an integration of the local stress state within the total volume V of the polycrystal:

$$\underline{\underline{\sigma}} = \frac{1}{V} \int \underline{\underline{\sigma}}^{(g)} dV \quad .$$

When the stress state is constant in a grain, it0 becomes a simple summation:

$$\underline{\underline{\sigma}} = \sum_{g=1}^{n} \underline{\underline{\sigma}}^{(g)} f^{(g)} \quad ,$$

where $f^{(g)} = \frac{\int_g dV}{V}$ represents the volume fraction of grain g and n is the total number of grains.